Transition Metal Complexes and Their Applications in Energy Conversion

PUTTOCK, EMMA,VICTORIA

Transition Metal Complexes and Their Applications in Energy Conversion

Emma Victoria Puttock

A thesis submitted in partial fulfilment of the requirements for the degree of Doctor of Philosophy

Department of Chemistry

June 2017

Abstract

The rich coordination chemistry of transition metals renders them of interest for broad applications in energy conversion. For example, there is increasing interest in molecular light absorbers such as dye-sensitized photoelectrochemical solar cells (DSSCs) and hybrid inorganic/organic devices. Additionally, the properties of light emitting molecules are the subject of intense research, with applications in organic light emitting diodes (OLEDs) and photosensitisers of energy- and electron-transfer for solar energy conversion.

This thesis can be broadly separated into two sections; (1) the study of a macrocyclic cobalt complex and its potential as a catalyst for the conversion of protons into H_2 and (2) the synthesis and study of transition metal complexes as phosphorescent dopants for OLEDs.

In part 1, the synthesis and characterisation of a series of cobalt compounds coordinated by the macrocyclic biquinazoline ligand, Mabiq, is presented. The solution and solid-state structures of the compounds were examined, alongside the electronic structures of paramagnetic **2** and **3**. Electrochemistry data reveals that the reduction of **4** is possible to form a formally Co^0 species, which shows promise in its activity with respect to H_2 production.

In part 2, the synthesis and characterisation of a range of mono- and bimetallic Pt(II) and Ir(III) complexes is presented. A series of readily synthesised tridentate proligands and their resulting complexes is presented that include pseudo-cyclometallating units to allow for mild reaction conditions. The complexes are weakly emissive, with PLQYs in the range 0.1 – 4%, attributed to varying rates of non-radiative decay. Two successful strategies in decreasing non-radiative decay are reported: the replacement of the chloride ancillary ligand with a stronger field acetylide ligand and the development of tetradentate proligands to improve the rigidity of the square planar complexes. The synthesis of hydrazone-based proligands, which offer two N^N^O-coordination sites bridged by a central pyrimidine ring is also reported. Coordination of a second Ir(III) centre results in a 6-fold enhancement of the PLQYs.

Declaration

The research described herein was undertaken in the Department of Chemistry at Durham University between May 2013 and May 2017. All of the work is my own, unless expressly stated otherwise. No part of it has previously been submitted for a degree at this or any other university.

Statement of Copyright

Acknowledgements

I have thoroughly enjoyed my time at Durham University and a large part of that can be attributed to all the people who I have encountered over the past four years. Firstly, I'd like to thank my supervisor, Prof. J. A. Gareth Williams, for all the support and guidance throughout my PhD studies.

I'd like to acknowledge and thank the EPSRC, Department of Chemistry, Durham University, the CDT in Energy and the DEI for financial support to undertake this research.

Members of the Williams group, both past and present, have been a great source of support and friendship, it has been a pleasure to work with you all. A special shout out goes to Raminder Mulla for listening to me rant all the times I was sure I was losing my mind, Edward Walter for always seeing the bright side of life and most of all to Melissa Walden for providing inumerous belly laughs (yenbapko) and true friendship.

Much of this work could not have been achieved without the input and assistance of other people. I'd like to thank all of the members of support staff within the department of Chemistry, from those who provide the NMR, mass spectrometry, crystallography and HPLC service to the glassblowers and those who provide tea. It would be remiss of me not to mention Miriam and all of her kind words over the years.

Finally, I'd like to mention my family and loved ones. Thank you, all of you, for supporting me and believing in me throughout. I couldn't have done it without you.

Abbreviations

ASAP	Atmospheric solids analysis probe mass spectrometry
B3LYP	Becke, 3-parameter, Lee-Yang-Parr hybrid exchange-correlation energy functional
bpy	2,2'-bipyridine
br	Broad
BuLi-LiDMAE	Butyllithium-lithium dimethylaminoethanol
COD	1,5-cyclooctadiene
COSY	Correlation spectroscopy
CT	Charge transfer
CV	Cyclic voltammetry
DCM	Dichloromethane
DCTB	Trans-2-[3-(4-tert-Butylphenyl)-2-methyl-2-propenylidene]malononitrile
DFT	Density functional theory
DMF	Dimethylformamide
DMFDMA	N,N-dimethylformamide dimethyl acetal
$dmgBF_2^-$	(difluoroboryl)dimethylglyoximatio anion
DMSO	Dimethylsulfoxide
DOSY	Diffusion-ordered spectroscopy
dpybH	1,3-di(2-pyridyl)-benzene
dpyxH	1,3-di(2-pyridyl)-4,6-dimethylbenzene
DSSC	Dye-sensitised solar cell
EPA	diethyl ether, isopentane and ethanol 2/2/1 by volume
EPR	Electron paramagnetic resonance
ESI	Electrospray ionisation
EQE	External quantum efficiency
ES-MS	Electrospray ionization mass spectrometry
Et	Ethyl
Hbpca	bis(2-pyridylcarbonyl)amide

HER	Hydrogen evolution reaction
HOMO	Highest occupied molecular orbital
HMBC	Heteronuclear multiple-bond correlation spectroscopy
HPLC	High performance liquid chromatography
HSQC	Heteronuclear single-quantum correlation spectroscopy
HRMS	High resolution mass spectroscopy
Hthpy	2-(2-thienyl)pyridine
IC	Internal conversion
ILCT	Intraligand charge transfer
IR	infrared
ISC	Intersystem crossing
LANL2DZ	Los Alamos National Laboratory 2-double-zeta basis set
LC	Ligand centered
LEEC	Light-emitting electrochemical cell
LMCT	Ligand-to-metal charge transfer
LUMO	Lowest unoccupied molecular orbital
MALDI	Matrix assisted laser desorption/ionisation
MC	Metal centered
Me	Methyl
MeCN	Acetonitrile
MLCT	Metal-to-ligand charge transfer
mp.	Melting point
MW	Microwave
NHE	Normal hydrogen electrode
NIR	Near-infrared
NMR	Nuclear magnetic resonance
NOESY	Nuclear overhauser effect spectroscopy
OER	Oxygen evolution reaction
OLED	Organic light emitting diode
ORTEP	Oak Ridge thermal ellipsoid plot

phbpyH	6-phenyl-2,2’-bipyridine
PLQY	Photoluminescence quantum yield
PMMA	Poly(methylmethacrylate)
ppyH	2-phenylpyridine
PSII	Photosystem Two
QY	Quantum yield
RT	Room temperature
S_0	Singlet ground state
SCE	Standard calomel electrode
sh	Shoulder
SOC	Spin-orbit coupling
S_n	N^{th} singlet excited state
SQUID	superconducting quantum interference device
TD-DFT	Time-dependent density functional theory
TFA	Trifluoroacetic acid
THF	Tetrahydrofuran
TLC	Thin-layer chromatography
T_n	N^{th} triplet excited state
TOF	Time of flight
TON	Turnover number
tpymt	2,4,6-tris(2-pyrimidine)-1,3,4-triazine
tpyt	2,4,6-tris(2-pyridyl)-1,3,4-triazine
UV	Ultraviolet

Table of Contents

Part I - Cobalt Complexes Containing a Redox Active Macrocyclic Biquinazoline Ligand

Our children will enjoy in their homes electrical energy too cheap to meter.... Transmutation of the elements, unlimited power, ability to investigate the working of living cells by tracer atoms, the secret of photosynthesis about to be uncovered, these and a host of other results, all in about fifteen short years.

Lewis Strauss – 1954

1.1 Introduction

1.1.1 The Current Energy Crisis

As the modern world develops, so does its need for energy. Alongside our growing population and technological advances, the global demand for energy is steadily increasing. In 1993 the world's energy consumption was 9.5 TW, in 2011 this increased by 48% to 14 TW.[1] It is estimated that by 2050 our demand for energy will increase at least two-fold due to population and economic growth and will have tripled by 2100.[2] This increase in demand for energy comes not only from our expanding population, which is set to increase to 9.4 billion by 2050, but from the rising standard of living in areas across the globe.[2]

Our reliance on finite resources, such as fossil fuels, has led to our reserves depleting at an alarming rate. It is well documented[1–5] that our current energy resources are insufficient to meet our growing appetite. Our current reserves of oil and natural gas are set to become critically low in 40 years. Despite being our most plentiful source of fossil fuels, even our coal reserves are only projected to last 114 years if we continue at our current rate of production.[6] Continuing to irreversibly burn our fossil fuels at this rate has implications beyond energy production; these reserves have a huge host of useful industrial applications. Oil is used for lubricants, dyes, plastics and synthetic rubber, natural gas is used in ammonia, glass and plastic production and coal is used to make creosote oil, benzene, toluene, ammonium nitrate, soap, aspirin and solvents.[3] A further hot topic in the employment of fossil fuels as an energy source is the consequence on the environment. Although the real consequences of increased greenhouse gases cannot be accurately predicted, it is now generally accepted that human activities are largely causing climate change by releasing CO_2 and other heat-trapping gases into the atmosphere.[7] Society, with its ever increasing awareness of the strains we place on the environment, demands a solution that is both sustainable and 'green'.

Solar power is the most plentiful resource available to humankind and a large amount of focus has been placed on this energy source. More energy from sunlight hits the earth in 1 hour, than all of the energy consumed by humans in an entire year.[8] Even taking into account that 19% of solar power is absorbed by clouds and 30% is reflected back into space, the available power is still 5000 times the current world energy needs.[3]

A key challenge in the exploitation of solar energy is the ability to store and dispatch energy upon demand. Society relies on a continual energy supply and solar energy is

intermittent due to variable atmospheric conditions, therefore an inexpensive storage mechanism is needed for solar energy to become our primary energy supply.[2] A viable approach to this is to develop a process which can capture and convert solar energy through the formation of chemical bonds, i.e., to generate high-energy molecules as nature accomplishes in a photosynthetic process. Current schemes aim to split water into oxygen and a fuel such as hydrogen, methanol or other hydrocarbons.[8] This is by no means a new idea, indeed the first instance may be credited to science fiction: Jules Verne, "Vingt mille lieues sous les mers: Tour dumonde sous-marin" (twenty thousand leagues under the sea), 1870.[9]

Hydrogen is an odourless, colourless, tasteless and non-poisonous gas which produces water when burned. Hydrogen has already proven a useful fuel, an interesting example being in the space program, providing electrical power to shuttles and allowing the crew to consume the water by-product![10] Hydrogen is a useful 'feedstock' to a variety of industrial activities and has the potential to become a fuel sufficient to energize virtually every aspect of society; from homes to electrical utilities to business and industry.[11] There is often a perception of danger surrounding hydrogen fuel cells that can give pause to sceptics[12] but for more than half a century hydrogen has been used, stored and transported in the U.S. industrial sector. Like any fuel, safe handling procedures have made this possible.[13]

The production of hydrogen from solar energy devices is a sought-after process, as hydrogen can be produced by using solar energy to split water molecules into H_2 and O_2 in a process termed 'artificial photosynthesis'. The chemical community has stepped up to the challenge, and many have joined the race to produce cost-effective, efficient and robust catalysts for artificial photosynthesis.

1.1.2 Artificial Photosynthesis

Interest in photosynthesis stems from the fact that all of the raw materials and power needed for the synthesis of biomass are available in almost unlimited amounts. In natural photosynthesis, the energy of the sun is harnessed; water is split into oxygen, protons and electrons. The oxygen is released into the environment and the electrons are used to reduce CO_2 to sugar and other molecules, creating an energy store which we release when we burn fuels such as fossil and biomass; thus creating a renewable cycle (Scheme 1.1).[14]

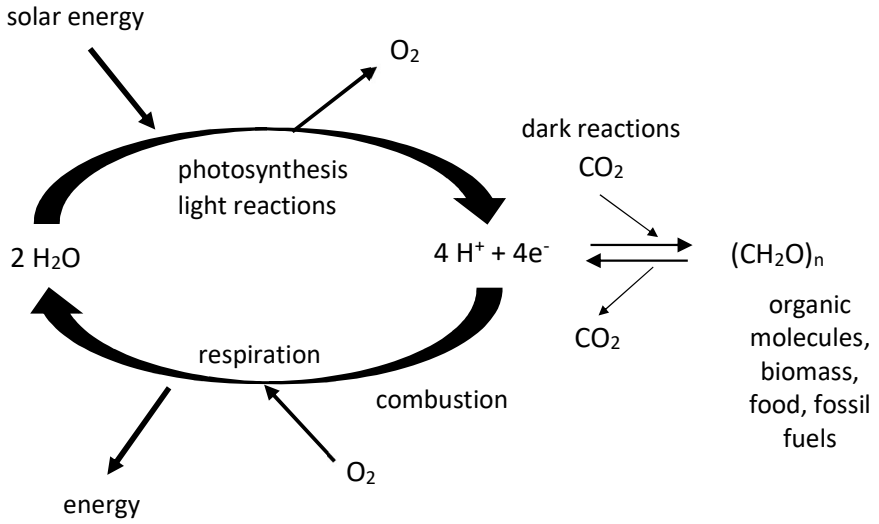

Scheme 1.1: A representation of the energy flow in the biological cycle of photosynthesis and respiration.[14]

In artificial photosynthesis, the protons and electrons are recombined to produce hydrogen. The splitting of water requires two individual multi-electron redox processes; water oxidation to dioxygen (or the oxygen evolution reaction, OER) and proton reduction to dihydrogen (or the hydrogen evolution reaction, HER)[15] as displayed in Scheme 1.2.

$$2H_2O \xrightarrow[\text{catalyst}]{h\nu} O_2 + 4H^+ + 4e^-$$

$$4H^+ + 4e^- \xrightarrow[\text{catalyst}]{} 2H_2$$

Scheme 1.2: Water oxidation and proton reduction equations.

This process is highly desirable as 4.92 eV is stored when two water molecules are split into two molecules of H_2 and one of O_2.[15] However, in order to achieve water splitting sizable kinetic and thermodynamic energy barriers must be overcome.[8] These barriers are overcome in nature by a very complex series of reactions which are still not fully understood.[14]

One example of a water oxidation catalyst used in natural photosynthesis is Photosystem Two (PSII). PSII is a multi-subunit complex embedded within the thylakoid membrane inside chloroplasts of green plants. Due to its importance to understanding the water splitting reaction there has been a wide range of techniques used to probe the mechanisms involved and also to determine the structure of the catalytic centre (Figure 1.1).[16]

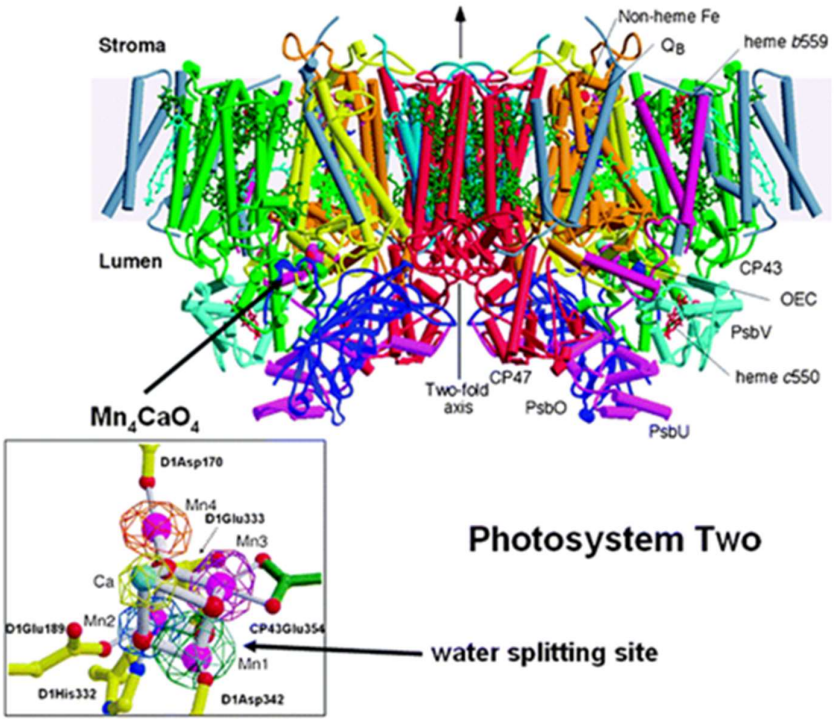

Figure 1.1: A side view of PSII, inset with the oxygen evolving centre, CaMn4. PSII consists of two monomers, related by a two-fold rotation axis. The protein subunits shown in orange and yellow compose the reaction centre.[1]

PSII is nature's oxygen evolution catalyst and many groups strive to synthesise oxygen-evolving catalysts. In an artificial system, successful water oxidation will be followed by proton reduction to form dihydrogen. To reduce a proton using a single electron has an energy cost of 2.3V vs NHE. A $H^{\bullet}$ radical is formed, which can be reduced using a second electron to yield H_2 with the release of 2.3V. Thus, the reaction is overall thermoneutral, but there is a need for a catalyst to lower the energetic requirements of the first reduction.[2]

1.1.3 Hydrogen Evolution Catalysts

The photocatalytic evolution of hydrogen is an area of artificial photosynthesis that has enjoyed its share of success and great developments in the past 10 years.[9] The HER is a well-studied reaction, a driving force of this being the key role hydrogen plays in many industrial reactions.[17] Many advances have been made in the drive for noble-metal-free molecular catalysts for light-driven hydrogen evolution. The catalytic performances of the noble-metal group for hydrogen production are unrivalled, but the limited supply and high

[1] *Reprinted with permission from Science, 2004, 303, 1831, Copyright (2004), American Association for the Advancement of Science.*

costs of noble metals would not sustain a wide-scale production of such devices. In biology, the hydrogenase enzymes are able to catalyse both proton reduction and hydrogen oxidation with efficiencies comparable to platinum particles.[18] Hydrogenases are large molecules (98 kDa) that contain a buried bimetallic active site composed of only nickel and iron. These are situated in a sulphur- and carbon-rich environment.[19] There are two distinct types of hydrogenases, according to the identity of their binuclear active sites, either Fe-Fe or Ni-Fe (Figure 1.2).[18]

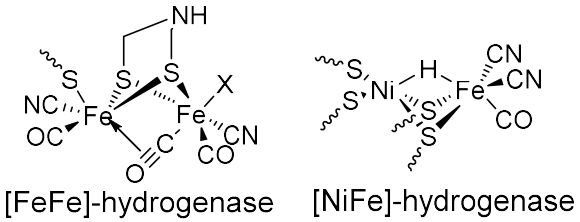

Figure 1.2: Structure of the active sites of the hydrogenases. X = H^-, H_2O or H_2.

By examining these structures and pathways, a bio-inspired catalysis approach has been undertaken to generate functional models of hydrogenases, that make use of first-row transition metals.[18] In recent years, intense work has been directed at biomimetic models of the Fe-only hydrogenase; retaining the sulfur environment, the nature and number of metal ions as well as the diatomic carbonyl and cyanide ligands found at the active site. The activities displayed by some compounds are noteworthy[20] but generally there is a lack of functioning hydrogenase mimics,[8] suggesting that the large protein environment of the hydrogenases plays a significant role in activity and that simply replicating the active site alone will not succeed. Moreover, biomimics can suffer from instability as they generally lack chelating ligands, which help stabilise the coordination sphere during catalysis.[20]

A different approach to replicating the hydrogenases ability is therefore required to successfully develop a proton reduction catalyst. The HER at metal electrodes has been well studied and the generally accepted mechanism in acidic media consists of three steps. The first step is the discharge step where a proton is adsorbed to the surface of the electrode:

$$H^+_{(aq)} + e^- \longrightarrow H_{(ads)}$$

This is followed by recombination of two H_{ads} to generate H_2 and/or by protonation of H_{ads} coupled to a single electron transfer:

$$2H_{ads} \longrightarrow H_2$$

$$H_{ads} + H^+_{(aq)} + e^- \longrightarrow H_2$$

The strength of the proton adsorption to the metal plays a key role in determining the catalytic activity of the metal electrode. The strength of the M–H bond against the log of the current exchange density for several metals is displayed in Figure 1.3.[2] Metals on the left side of the volcano peak, which form relatively weak bonds, exhibit a slow initial adsorption rate and hence the rate of hydrogen evolution is limited. The metals that lie on the right side of the volcano peak form very strong M–H bonds and hence the final desorption step and evolution of hydrogen is limited.

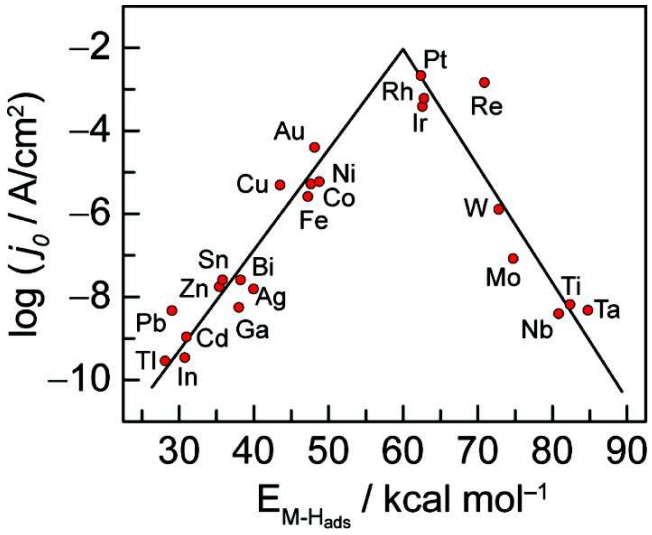

Figure 1.3: Volcano curve displaying the relationship between M–H bond strength and the current exchange density.[2]

The metals situated at the peak of the volcano plot have the optimum M–H bond strength for efficient adsorption and desorption and therefore are the pre-eminent hydrogen evolution catalysts. However, these metals are rare and expensive and so, as previously discussed, their implementation is not viable on a wide scale.

In an effort to move away from precious metals, numerous studies have focused on metals such as Co, Fe and Ni in mono, bi- or multi-metallic systems in order to tune the strength of the M-H bond and thereby increase electrocatalytic activity. These molecular

[2] *Reprinted with permission from J. Electroanal. Chem., 1972, 39, 163, Copyright (1972), Elsevier B.V.*

catalysts are bio-inspired rather than biomimetic, taking inspiration from biological systems and exploiting this knowledge to design original catalysts.

First row transition metals are earth-abundant and inexpensive, but can facilitate multi-electron reactions due to the availability of multiple oxidations states. A synthetic approach allows chemists to exploit in creative ways the versatile and modular character of coordination chemistry to develop efficient photosensitizers.[18] The intention would be to replace the platinum electrode with a molecular complex able to catalyse the reaction, i.e., to lower the activation potential for hydrogen evolution.[21]

Despite having no biological relevance in terms of water splitting and being significantly less abundant than Fe, Ni or Mn[22], cobalt has received considerable attention in the field over the past 10 years.[23] Its catalytic power for hydrogen evolution was recognised some time ago and to date numerous efficient systems have been reported.[23]

1.1.4 Mechanism of Hydrogen Evolution

There has been considerable experimental and theoretical investigation into the mechanism of cobalt-catalysed hydrogen evolution. Naturally, understanding the fundamental mechanisms of electrocatalytic hydrogen evolution will assist in the design of better catalysts.[24] It is generally accepted that the mechanism begins with the reduction of Co^{II} to Co^{I} which is then protonated to form Co^{III}-H (Scheme 1.3).[15]

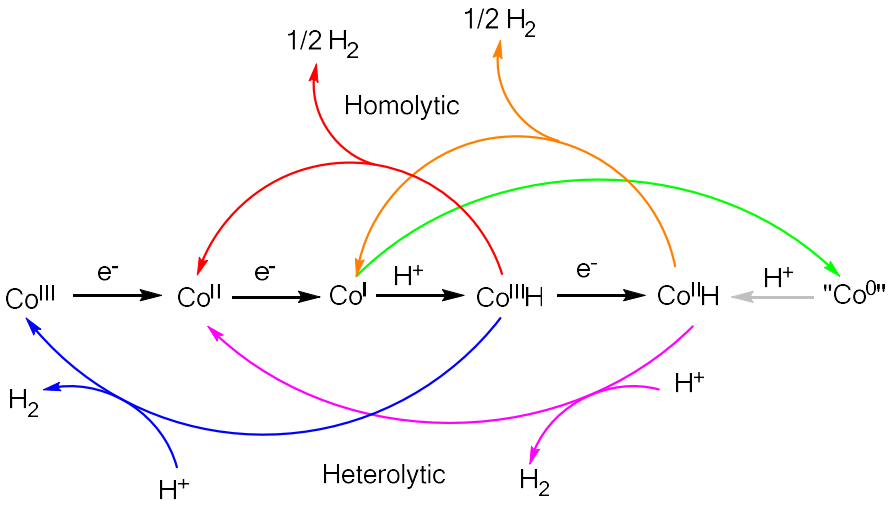

Scheme 1.3: H_2 evolution pathways[3]

[3] Adapated *with permission from Acc. Chem. Res., 2009, 42, 1995-2004, Copyright (2009), American Chemical Society.*

Hydrogen evolution then can occur via a homolytic or heterolytic pathway. The Co^{III}-H can react in a bimolecular step with another Co^{III}-H to eliminate H_2 (homolytic, bimetallic pathway, red) or it can be protonated, generating H_2 and a Co^{III} species which can then be reduced (heterolytic, monometallic pathway, blue).[15] A further possibility is the reduction of Co^{III}-H to yield Co^{II}-H, which can then react via a similar homolytic (orange) or heterolytic (purple) pathway. A final possibility is that the Co^{I} species is not protonated but reduced to a Co^{0} species which is then protonated to form Co^{II}-H and can react in the manner stated above.[15]

The different pathways available to cobalt-catalysed evolution would imply different optimum operating conditions.[24] Baffert et. al. (2007) carried out in-depth analysis of the mechanism of hydrogen evolution by the complex $[Co(dmgBF_2)_2L]$ ($dmgBF_2^-$ = (difluoroboryl)dimethylglyoximatio anion, L = CH_3CN, DMF, H_2O). They concluded that the pathway followed is also reliant on the strength of the acid used as the proton source. They listed three possible mechanisms, involving: (i) Co^{III}-H as the active species, (ii) both Co^{III}-H and Co^{II}-H as intermediates and (iii) Co^{II}-H as the active species (Scheme 1.4).[21]

Hydrogen evolution proceeds via pathway (i) if the acid used is strong enough to protonate both Co^{I} and Co^{III}-H species, meaning a heterolytic pathway is more probable. With lower strength acids, Co^{III}-H cannot be protonated and therefore is further reduced to Co^{II}-H which then can react via parallel homolytic and heterolytic pathways. Finally, very weak acids (e.g. Et_3NH^+) are unable to protonate the Co^{I} species, and hence require further reduction of the Co^{I} species to a "Co^{0}" species before protonation can occur. This leads to a Co^{II}-H intermediate which evolves hydrogen through parallel homolytic and heterolytic pathways.[21]

Detailed mechanistic work has suggested that the homolytic pathway predominates and the heterolytic pathway is only competitive at low catalyst or high acid concentrations. The low-barrier homolytic pathway is generally limited by diffusion of two hydride species together in solution, which could be elimated by the covalent linking of cobalt centres in a single catalyst.[15] Recent work by Dempsey et. al. (2010) examined the mechanism of hydrogen evolution from a photogenerated hydridocobaloxime and reported that reaction via protonation of Co^{II}-H is favoured under certain conditions, such as in solution where Co^{III}-H is in low concentrations.[25]

Overall, the pathway can be optimised by both judicious choice of operating conditions and careful design of the cobalt catalyst.

Mechanism (i)

$[Co^{II}(dmgBF_2)_2L] + e^- \rightleftharpoons [Co^{I}(dmgBF_2)_2L]^-$

$[Co^{I}(dmgBF_2)_2L]^- + H^+ \rightleftharpoons [Co^{III}H(dmgBF_2)_2L]$

$[Co^{III}H(dmgBF_2)_2L] + H^+ \rightleftharpoons [Co^{III}(dmgBF_2)_2L]^+ + H_2$

$[Co^{III}(dmgBF_2)_2L]^+ + e^- \rightleftharpoons [Co^{II}(dmgBF_2)_2L]$

Mechanism (ii)

$[Co^{II}(dmgBF_2)_2L] + e^- \rightleftharpoons [Co^{I}(dmgBF_2)_2L]^-$

$[Co^{I}(dmgBF_2)_2L]^- + H^+ \rightleftharpoons [Co^{III}H(dmgBF_2)_2L]$

$[Co^{III}H(dmgBF_2)_2L] + e^- \rightleftharpoons [Co^{II}H(dmgBF_2)_2L]^-$

$[Co^{II}H(dmgBF_2)_2L]^- + H^+ \overset{\text{heterolytic}}{\rightleftharpoons} [Co^{II}(dmgBF_2)_2L] + H_2$

$2[Co^{II}H(dmgBF_2)_2L]^- \overset{\text{homolytic}}{\rightleftharpoons} 2[Co^{I}(dmgBF_2)_2L]^- + H_2$

Mechanism (iii)

$[Co^{II}(dmgBF_2)_2L] + e^- \rightleftharpoons [Co^{I}(dmgBF_2)_2L]^-$

$[Co^{I}(dmgBF_2)_2L]^- + e^- \rightleftharpoons [Co(dmgBF_2)_2L]^{2-}$

$[Co(dmgBF_2)_2L]^{2-} + H^+ \rightleftharpoons [Co^{II}H(dmgBF_2)_2L]^-$

$[Co^{II}H(dmgBF_2)_2L]^- + H^+ \overset{\text{heterolytic}}{\rightleftharpoons} [Co^{II}(dmgBF_2)_2L] + H_2$

$2[Co^{II}H(dmgBF_2)_2L]^- \overset{\text{homolytic}}{\rightleftharpoons} 2[Co^{I}(dmgBF_2)_2L]^- + H_2$

Scheme 1.4: Possible mechanisms for hydrogen evolution based on acid strength

1.1.5 Cobalt Catalysts for Hydrogen Evolution

Most of the catalytically active cobalt systems are square-planar macrocyclic or pseudo-macrocyclic complexes, such as **1** and other cobaloxime derivatives **2-4** (Figure 1.4).[22] Cobaloximes have been extensively studied and were initially proposed as models of the B_{12} co-enzyme, but have now acquired an independent research field because of their rich coordination chemistry and potential application in organic synthesis.[26] Cobaloximes have the general formula $RCo(L)_2B$, where R is an organic group σ-bonded to

cobalt, B is an axial base *trans* to the organic group and L is a monoanionic dioxime ligand (e.g. glyoxime (gH), Dimethylglyoxime (dmgH), diphenylglyoxime (dpgH)).[27]

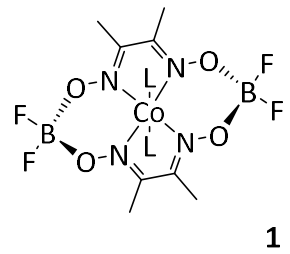

1

$[Co(dmgBF_2)_2L_2]$
(L = H_2O, CH_3CN, DMF)

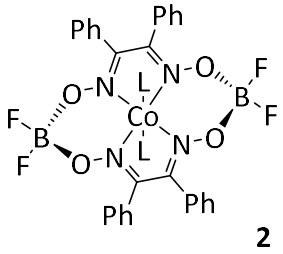

2

$[Co(dpgBF_2)_2L_2]$
(L = H_2O, CH_3CN, DMF)

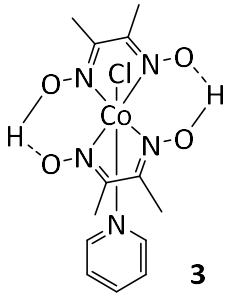

3

$[Co(dmgH)_2pyCl]$

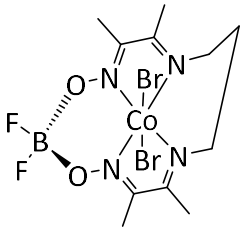

4

$[Co(do_2)_2BF_2pnBr_2]$

Figure 1.4: Structures of some cobaloximes. *(dmg = dimethylglyoxime, dpg = diphenylglyoxime, do = N^2,$N^{2\prime}$-propanediylbis(2,3-butandione 2-imine 3-oxime).*

It is proposed that the fine combination of soft ligands found at the active site of hydrogenases helps in making the iron centre both nucleophilic and easily reducible which stabilises an open coordination site for substrate binding. As some of these features can be found in cobaloximes, these compounds are interesting potential electrocatalysts for hydrogen evolution in terms of both cost and working potential.[20] In the reduced Co(I) state the cobaloximes are powerful nucleophiles which can be protonated to yield cobalt(III)-hydride species which can evolve dihydrogen either through protonation or binuclear reductive elimination.[28]

One of the first examples of catalytic activity for hydrogen evolution using a cobaloxime was reported by P. Connolly and J. Espenson in 1986. The Co^{II} macrocycle $Co^{II}(dmgBF_2)_2$ (Figure 1.5) was mixed with acidic solutions (pH 2) of $EuCl_2/CrCl_2$ and shown to evolve copious amounts of H_2. It was noted that a trace amount of catalyst caused the

reaction to proceed until the supply of MCl_2 was exhausted, suggesting a mechanism involving electron donation from Cr^{2+}/Eu^{2+} (Scheme 1.5).[29]

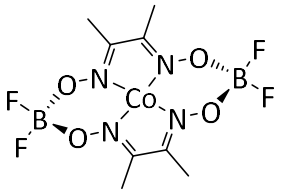

Figure 1.5: Co^{II} macrocycle $Co^{II}(dmgBF_2)_2$ investigated by P. Connolly and J. Espenson.

$$Cl^- + Cr^{2+} + Co^{II}(dmgBF_2)_2 \rightleftharpoons [Cr\text{-}Cl\text{-}Co(dmgBF_2)_2]^+$$

$$[Cr\text{-}Cl\text{-}Co(dmgBF_2)_2]^+ \longrightarrow Co^{I}(dmgBF_2)_2^- + CrCl^{2+}$$

$$Co(dmgBF_2)_2 + H^+ \longrightarrow HCo^{III}(dmgBF_2)_2$$

$$2HCo(dmgBF_2)_2 \xrightarrow{\text{Homolytic}} 2Co(dmgBF_2)_2 + H_2$$

$$HCo(dmgBF_2)_2 + H^+ \xrightarrow{\text{Heterolytic}} H_2 + Co^{III}(dmgBF_2)_2^+$$

$$Co^{III}(dmgBF_2)_2^+ + Cr^{2+} + Cl^- \longrightarrow CrCl^{2+} + Co(dmgBF_2)_2$$

Scheme 1.5: Proposed mechanism of hydrogen elimination.

The proposed mechanism begins with the formation of a bridged intermediate [Cr-Cl-Co$(dmgBF_2)_2]^+$, which enables an inner-sphere electron transfer from Cr^{II} to Co^{II}. This electron transfer has slightly unfavourable thermodynamics and therefore is thought to be responsible for a slow overall rate of catalysis.[29]

In 2005, Hu *et al.* reasoned that this system might be well suited to electrocatalytic hydrogen evolution, as the $Co^{II/I}$ transition may be rapid and the process should occur at relatively positive potentials. He further reasoned that modification of the diglyoxime framework should allow tuning of the $Co^{II/I}$ redox potential and hence the potential at which hydrogen evolution occurs. Hu *et al.* investigated two related complexes, **5** and **6** which can be seen in Figure 1.6.[30] It was established that both **5** and **6** serve as catalysts for hydrogen evolution, with complex **6** mediating hydrogen evolution at -0.28 V vs. SCE in CH_3CN. This was one of the most positive potentials recorded at the time (until that date others were the range of -1 V to -2 V in organic solvents).

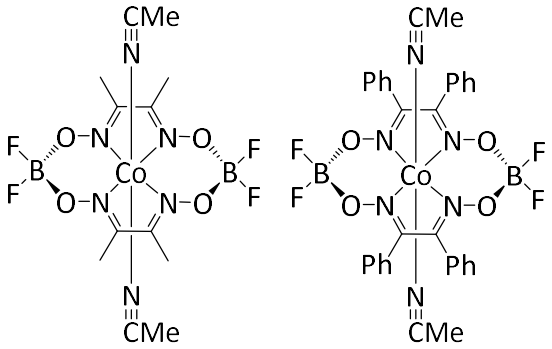

*Figure 1.6: Complex **5** and **6** studied by Hu et al.*

A recent breakthrough in hydrogen evolution catalysed by cobalt cobaloxime based complexes is the work by Kaeffer *et al.* (2015)[31] which contributes to the development of a second generation of catalysts utilising cobalt diamine-dioxime complexes. These tetradentate ligands (see Figure 1.7) form cobalt complexes which are more stable to hydrolysis under strongly acidic conditions than the first generation cobaloximes. H_2 evolution involves the oxime bridge as a protonation site, reproducing the mechanism in the active sites of hydrogenase enzymes, allowing modest overpotentials at a wide range of acid-base conditions in non-aqueous solutions.

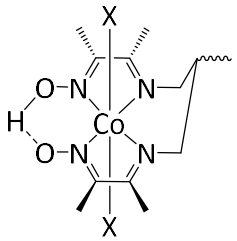

Figure 1.7: Cobalt Diimine-Dioxime complex (X = Br, Cl, …).

Another promising candidate in the field of cobalt hydrogen evolution are Co(II)-octahedral complexes with polypyridyl ligands. The first catalyst of this nature, **7** (Figure 1.8), was reported by Chang and co-workers.[32] This tetradentate system was designed to stabilise the Co^{II} centre while allowing two open coordination sites on which binding and catalysis may occur.

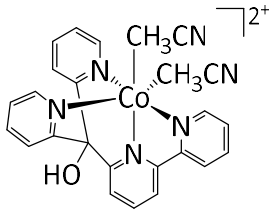

7

Figure 1.8: Tetradentate polypyridyl Co^{II} complex reported by Chang and co-workers.

Chang and co-workers found this system was able to electrocatalytically reduce protons to hydrogen and again implicated a Co^{I} species in the catalytic cycle. However, the catalyst is not soluble in water in the millimolar range and subsequently second generation complexes have looked at modifying the ligand in order to address this problem.[33] A number of polypyridyl catalysts have since been reported and the robustness of the coordination sphere towards reduction, hydrolysis and ligand exchange under reductive conditions has allowed light-driven hydrogen evolution under fully aqueous conditions.[23]

Interestingly, a number of ligand-assisted catalytic processes are emerging for this class of compounds. Ligand-centred redox processes have been characterised for complexes **8** and **9a-b** (Figure 1.9), with ligands bearing redox-active moieties in the backbone.[34,35]

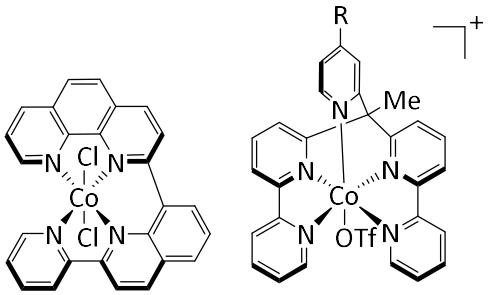

8 **9a R = H** **9b R = CF_3**

Figure 1.9: Complexes bearing redox active moieties in the ligand backbone.

The cyclic voltammograms of **8** and **9a-b** both reveal a Co^{II}/Co^{I} couple and two further reduction processes assigned as ligand-centred. In electrocatalytic studies, the Co^{II}/Co^{I} couple is still observed at all pH values and hydrogen evolution occurs at more cathodic potentials, likely triggered by a ligand-centred reduction process. These redox active moieties are thought to stabilise the reduced cobalt centre through π-back-bonding,

shifting the Co^{II}/Co^{I} couple to a more positive potential and reducing the nucleophilicity of the Co^{I} state.

Great progress has been made in the last few decades on catalytic hydrogen evolution by Co complexes, showing earth-abundant metals are a viable approach to artificial photosynthesis. Of course, challenges still remain in the development of materials for solar driven hydrogen evolution. Many systems suffer from low aqueous solubility, stability or do not exhibit sufficiently high turnover numbers (TON) at low catalyst concentrations. Due to the wealth of studies into water splitting with cobalt, this field is reaching maturity and it is reasonable to say that a fully molecular photoelectrocatalytic system for water splitting will be a reality in the near future.[22]

1.1.6 Current Strategy

In an attempt to develop a cost-effective H_2-producing catalyst, research during the first part of my doctoral studies was focused on metal complexes containing the N_4-macrocyclic biquinazoline ligand, HMabiq (Scheme 1.6). This ligand offers two binding sites for metals and a key part of the research has focused on the development of cobalt complexes where either one or both of these sites are occupied.

This potential hydrogen evolution catalyst has several benefits. Firstly, the use of cobalt eradicates the need for expensive metals such as platinum, helping meet the demand for a cost-effective catalyst. This builds upon the considerable promise that has been shown by cobaloxime catalysts, which feature macrocyclic cavities with cobalt centres.

Secondly, the HMabiq ligand is able to participate in redox processes by storing and donating electrons as needed. The redox non-innocence of the HMabiq ligand has been established previously,[36,37] the π* orbitals of the diketiminate unit are capable of accepting one electron.

Most ligands used in inorganic chemistry are not redox-active, the energy needed to oxidize or reduce them by one electron is much greater than the energy needed to change the oxidation state at the metal; hence changes in the electronic structure occur at the metal. "Non-innocence", as it is often known, can occur when ligands have energetically accessible levels that allow redox reactions to change their charge state. Thus, the ligands are 'redox active'.[38] The coordination between a metal $M^{y/y+1}$ and a redox active ligand ($RAL^{x/x-1}$) may either exist as a resonance situation with delocalised valences, or as an equilibrium between two different redox isomeric species:

$$(RAL)^{x}M^{y} \longleftrightarrow (RAL)^{x-1}M^{y+1} \qquad \text{resonance}$$

$$(RAL)^{x}M^{y} \rightleftharpoons (RAL)^{x-1}M^{y+1} \qquad \text{redox isomers}$$

During reactions, non-innocent ligands can cooperate with the metal centre and react synergistically to facilitate chemical processes. The ligand is able to act as an electron sink, allowing the metal to store and accept electron density while retaining its original oxidation state, avoiding unfavourable, high energy states of the metal. The employment of redox active ligands opens up a whole new range of reactions which would otherwise

not be possible for first row transition metals. Multi-electron reactions, such as hydrogen evolution, tend to be catalysed most effectively by precious metals since they typically undergo $2e^-$ oxidation state changes, whereas common metals tend to undergo $1e^-$ reactions. It is therefore thought that redox active ligands allow base metals to mimic precious metals, by combining 1e- redox change at the ligand with a $1e^-$ redox change at the metal, for an overall oxidation change of $2e^-$ (Scheme 1.6).[39] The use of the redox active Mabiq ligand may bypass the unfavourable Co^0 species which is implicated in the hydrogen evolution mechanism, allowing for reactivity to be seen even with weak acids.

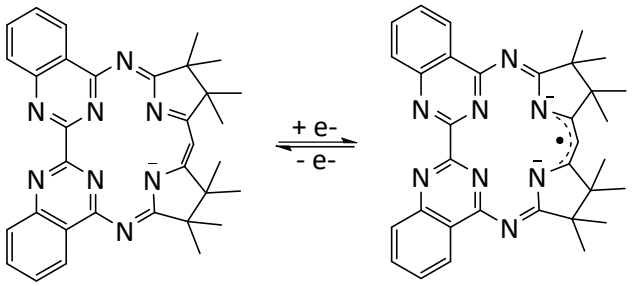

Scheme 1.6: $1e^-$ reduction of Mabiq ligand.

Finally, the second binding site provided by HMabiq may allow us to add a sensitiser to the system. A particularly interesting system which used this method was described by Hawecker *et al.* in 1983. Hydrogen evolution was achieved in organic or aqueous organic media using the photosensitiser/relay-catalyst/donor system of $Ru(bipy)_3Cl_2$/$Co(dmgH)_2$/tertiary amine. The photosensitiser allowed visible light irradiation to drive the hydrogen evolution, producing the most active photochemical process that had been reported at the time. The overall hydrogen generation process was proposed to involve two catalytic cycles; the photochemical ruthenium cycle and the thermal cobalt cycle, as well as two irreversible reactions; the formation of hydrogen and the oxidative decomposition of the tertiary amine. A schematic representation of the reactions is given in Scheme 1.7.[40]

The feasibility of efficient hydrogen production is displayed by this work, and has spurred on the search for stable components, photosensitisers of larger spectral domain and alternative electron donor species.[40]

The addition of a sensitizer would allow us to harness solar energy directly, making our system solar driven. This is an exciting feature which may allow us to create a system

that can drive H_2 evolution and oxygen formation with the only inputs being water and sunlight.

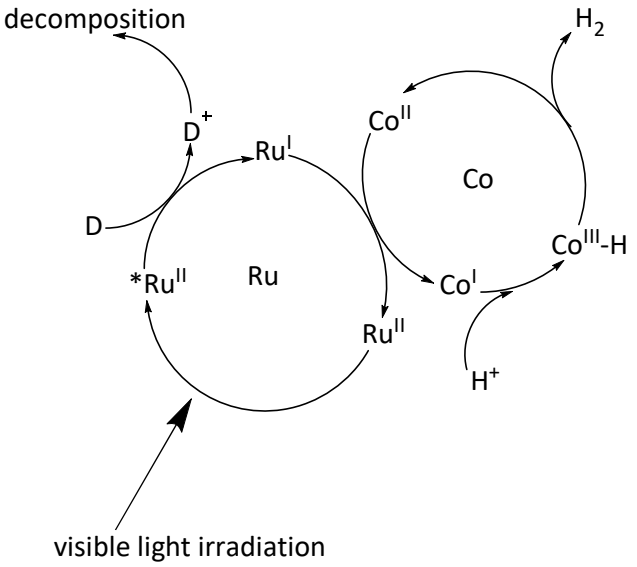

Scheme 1.7: Schematic representation of photochemical hydrogen generation in the ruthenium(II)-cobaloxime supramolecular complex reported by Hawecker et al. D = tertiary amine.

1.2 Results and discussion

1.2.1 Synthesis of Cobalt Mabiq complexes

The target macrocyclic ligand, HMabiq, was synthesised according to the synthesis previously published by E. Müller et. al[37], as shown in Scheme 1.8.

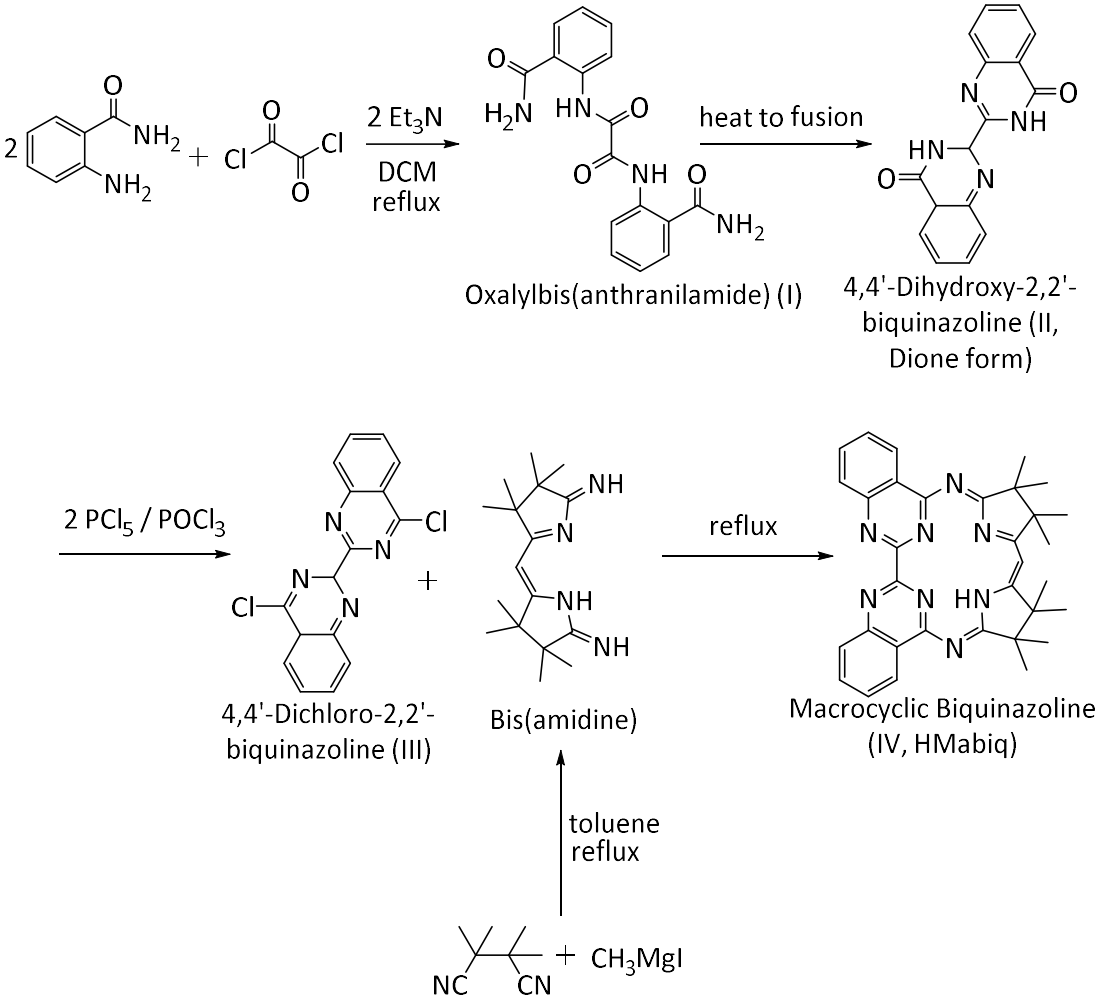

Scheme 1.8: HMabiq Synthesis

Following successful synthesis of the HMabiq ligand, a series of Co-Mabiq complexes was synthesised, as detailed in Scheme 1.9. Complex **1** and **2** were first synthesised by Priyabrata Banerjee. Complex **3** was first synthesised by Liam Drennen.

The Co^{III} complex $Co(Mabiq)Cl_2$ (**1**) was initially synthesised in the presence of hydrogen peroxide as an oxidant, following the protocol established for the synthesis of $Co(Mabiq)(CN)_2$.[37] However, carrying out the reaction in an aerated CH_2Cl_2 solution resulted in higher product yields. **1** is dark brown in colour in the solid form, dissolving readily in DCM and less so in MeOH to form an amber solution. The diamagnetic nature of

1 is confirmed by the ^{1}H NMR spectrum which displays no broadening of peaks compared to those on the spectrum of the free ligand (Figure 1.10). Furthermore, there is an upfield shift of both the aromatic protons and the diketiminate C-H proton when compared to the spectrum of the free HMabiq ligand, which can be attributed to the coordination of the Co^{III} ion on the macrocyclic cavity.

Although von Zelewskys's original motivation for the synthesis of HMabiq was to design a bimetallic complex with photocatalytic properties, the binuclear complexes targeted by both von Zelewsky and Hess were never reported.[36,37] We have successfully generated both monometallic Co^{II} complex Co(Mabiq)Cl (**2**) and the bimetallic Co^{II} complex Co_2(Mabiq)Cl_3 (**3**) which can be formed with one or two equivalents of anhydrous $CoCl_2$, respectively. Both **2** and **3** are dark green in colour, with **2** dissolving readily in DCM and less so in MeOH whereas **3** is only soluble in MeOH.

The Co^{I} complex Co(Mabiq) (**4**) can be formed on reduction of **2** using 1 equivalent of cobaltocene in THF. **4** is a deep purple colour and dissolves readily in THF. The ^{1}H NMR spectrum (Figure 1.10) shows a further upfield shift of the diketiminate C-H proton signal, which now appears at 7.54 ppm. This shift is significantly higher than that of the corresponding signal in the spectrum of the Co^{III}-, Fe^{II}-, and Zn^{II}-Mabiq complexes.[36]

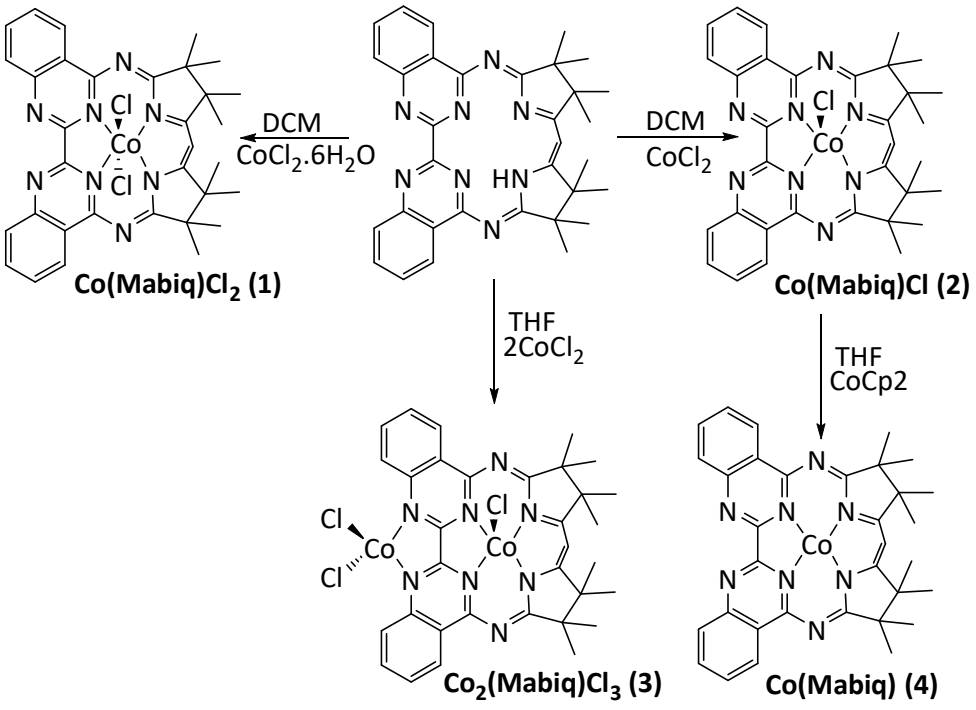

Scheme 1.9: Synthesis of cobalt complexes.

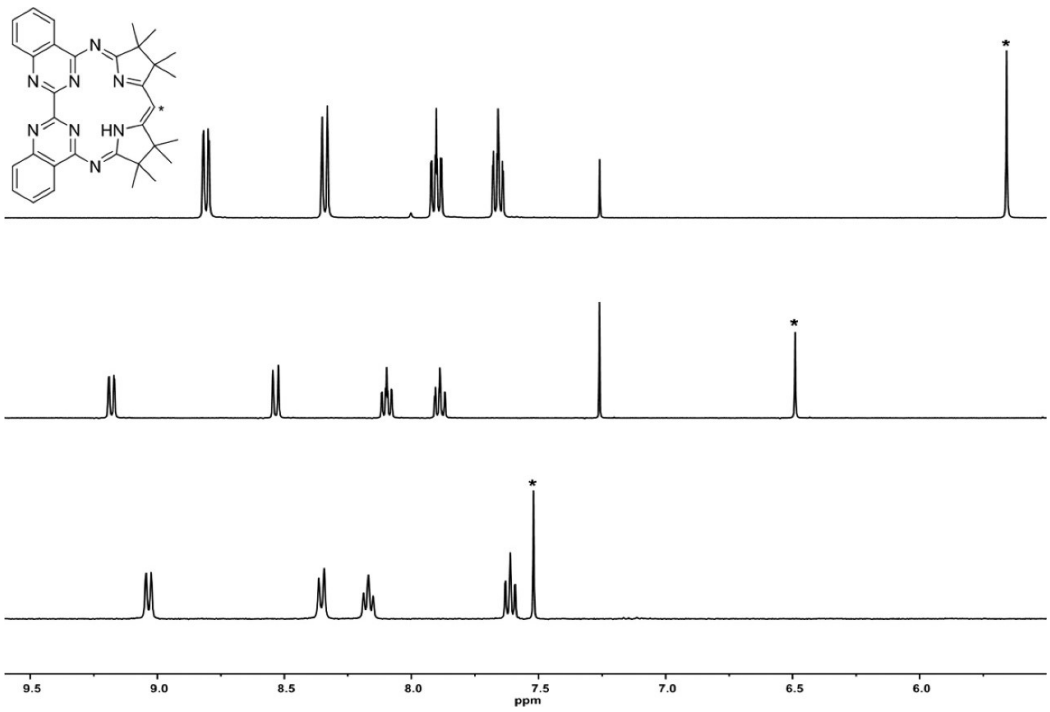

*Figure 1.10: ^{1}H NMR spectra of HMabiq (top, $CDCl_3$), **1** (middle, $CDCl_3$), and **4** (bottom, THF-d_8), showing the aromatic protons and the diketiminate proton (*).*[41]

1.3 Characterisation of Cobalt Mabiq Complexes

1.3.1 Solution State Characterisation

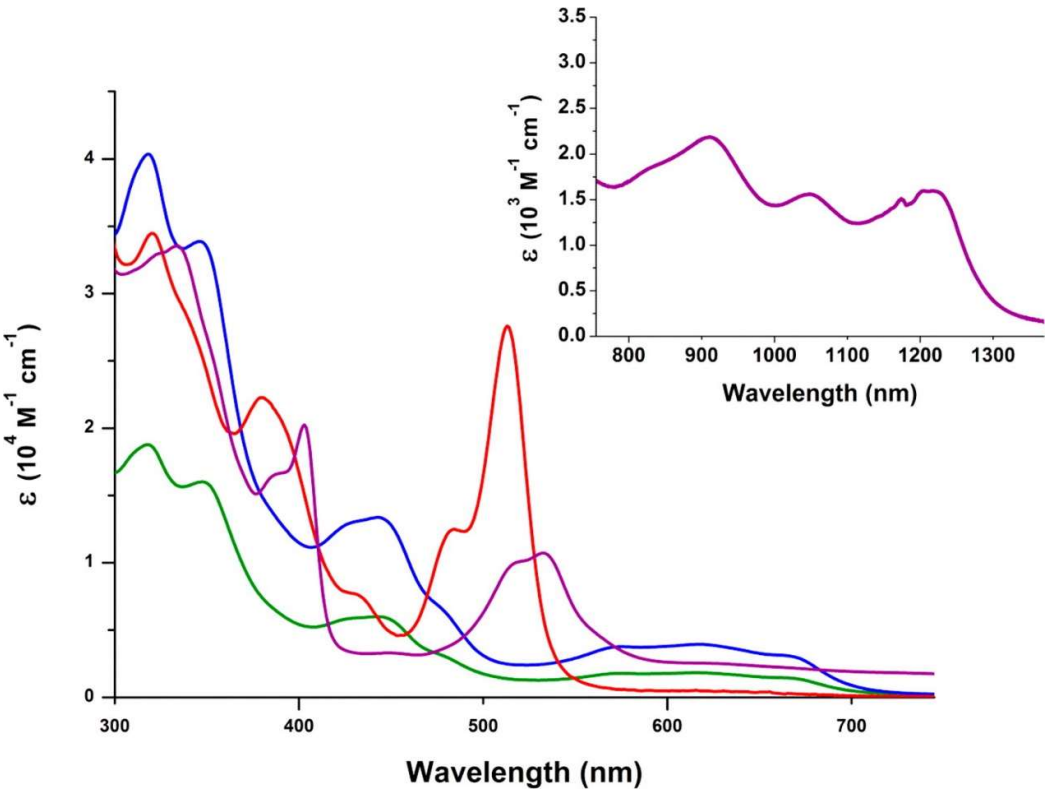

*Figure 1.11: Electronic absorption spectra of **1** (red, CH_2Cl_2), **2** (green, CH_3OH), **3** (blue, CH_3OH), and **4** (purple, THF). Inset: NIR region of the spectrum of **4**.*[41]

Absorption bands at λ_{max} = 484 and 514 nm can be seen in the UV-Visible electronic absorption spectrum of **1** (Figure 1.11). These features are reminiscent of those seen for Co(Mabiq)CN_2 (λ_{max} = 502 and 536 nm) and Zn(Mabiq)Cl (λ_{max} = 471 and 502 nm).[36,37] von Zelewsky attributed these features in the visible region to Mabiq π-π* transitions by comparing the low energy features to those of dicyanocobalamin, and the energy of the lowest energy absorption band is related to the net charge of the coordinated central atom, with increasing charge resulting in a move to higher energy.[37] This conclusion appears to be consistent with the position of these absorptions bands in the above spectra and Fe^{III}(Mabiq)Cl_2 (λ_{max} = 524 nm).

The trio of peaks which can be seen in **2** and **3** (λ_{max} = 576, 618 and 668 nm) are assigned as charge-transfer bands due to their high molar extinction coefficients, distinguishing them from spin-forbidden metal centred d-d transitions. Remarkably, the

solution absorption spectra of **2** and **3** are only distinguishable by their extinction coefficients. The spectra are superimposable and exhibit identical transitions (Figure 1.11). The similarity in the two spectra may be an indication that the outer $CoCl_2$ moiety is labile and therefore dissociates in solution.

In order to further explore the dissociation of $CoCl_2$ from **3**, the solid-state UV-Vis for **2** and **3** were recorded, as can be seen in Figure 1.12. We can see that the spectrum of **3** maintains its trio of peaks, whereas the spectrum of **2** appears to have retained two of the three. The λ_{max} of both **2** and **3** are at a lower energy than in the solution state.

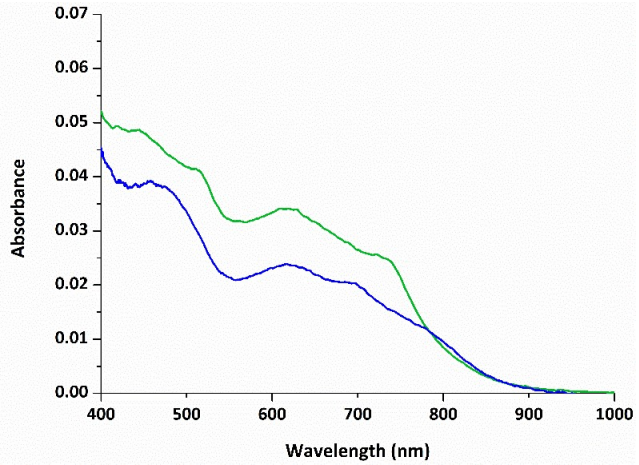

*Figure 1.12: Solid state electronic spectra of **2** (green) and **3** (blue).*

Further to this, the solid-state IR spectra (Figure 1.13) exhibit several distinctive bands in the fingerprint region. The differences in the spectra confirms that in the solid state there are clear differences between **2** and **3**.

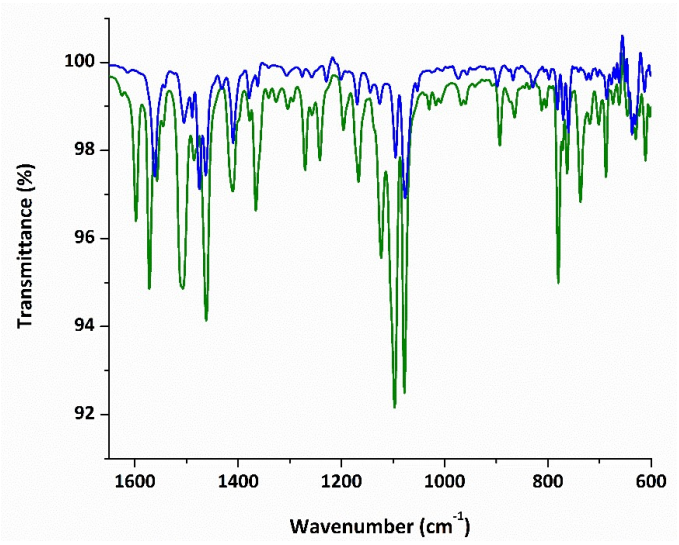

*Figure 1.13: Comparison of IR spectra of **2** (green) and **3** (blue).*

The UV-Visible absorption spectrum of low-valent Co(Mabiq) **4** in THF exhibits the π-π* transitions (λ_{max} = 392 and 403 nm) as seen for **1** and discussed earlier, as well as absorption bands at λ_{max} = 523 and 533 nm as seen for **2** and **3** which are again assigned to metal-to-ligand charge transfer. In addition, multiple features can be seen in the NIR region (inlaid, Figure 1.11), which closely resembles the absorption bands seen for Co^{I} cobalamin.[42] In the superreduced vitamin B_{12} the low-energy transitions are assigned as Co 3d -> corrin π* excitations, with the relevant π* orbitals localised on the diketimate group of the corrin ring. It is proposed that a similar Co -> Mabiq transition involving the π* orbitals on the diketimate group may account for these transitions in the spectrum of **4**.

1.3.2 Solid State Structures

Co(Mabiq)Cl_2 (1)

Crystals of **1** were obtained via slow evaporation of a solution of crude product in DCM, with >90% yields. The structure obtained for **1** from X-ray diffraction of a suitable crystal is shown in Figure 1.14.

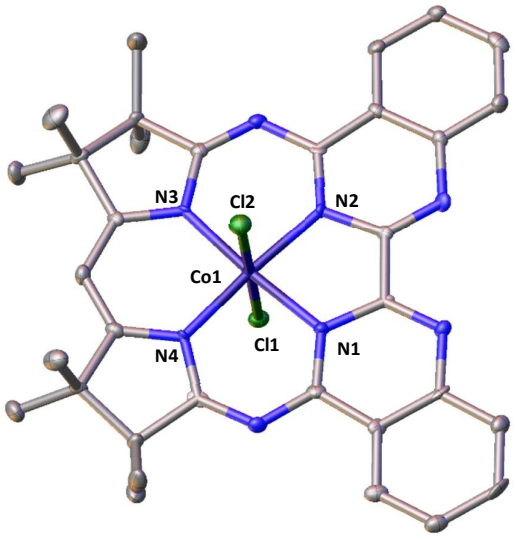

*Figure 1.14: Molecular structure of **1**. Hydrogen atoms and solvent molecules omitted for clarity. T = 120K.*

*Table 1.1: Selected bond lengths and bond angles for Complex **1**.*

Bond Lengths (Å)		*Bond Angles (°)*	
Co1-Cl1	2.2640(12)	Cl2-Co1-Cl1	179.1(5)
Co1-Cl2	2.2451(12)	N1-Co1-N2	83.8(13)
Co1-N1	1.920(3)	N2-Co1-N3	91.6(13)
Co1-N2	1.928(3)	N3-Co1-N4	92.7(13)
Co1-N3	1.902(3)	N4-Co1-N1	92.0(13)
Co1-N4	1.891(3)		

Complex **1** displays a Co^{III} ion coordinated by four nitrogen atoms in the macrocyclic cavity. The coordination about the metal is pseudooctahedral; the Co^{III} ion lies within the plane of the macrocyclic N-donors with two axial chloride ligands. The cobalt ion in the macrocyclic cavity is asymmetrically coordinated, with a slightly longer bond (1.92 Å) to the bipyrimidine nitrogen atoms in comparison to the shorter (1.90 Å) bond to the pyrrole nitrogen atoms (Table 1.1). This is a phenomenon noted in the related complex $[Co^{III}(Mabiq)(CN)_2]$[37], which is attributed to the different donor strength/basicity of the two

types of nitrogen donors, although it could be due to the different bite angles. One CH_2Cl_2 molecule per Co is located in the crystal structure of **1**.

Co(Mabiq)Cl_2 (2)

Crystals of **2** were obtained via slow evaporation of a solution of crude product in DCM. The structure obtained for **2** from X-ray diffraction of a suitable crystal is shown in Figure 1.15.

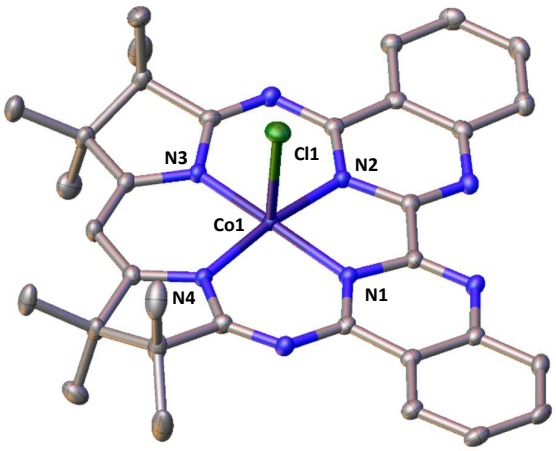

*Figure 1.15: Molecular structure of **2**. Hydrogen atoms and solvent molecules omitted for clarity. T = 120K.*

*Table 1.2: Selected bond lengths and bond angles for Complex **2**.*

Bond Lengths (Å)		*Bond Angles (°)*	
Co1-Cl1	2.4458(7)	N1-Co1-N2	84.2(9)
Co1-N1	1.918(2)	N2-Co1-N3	91.3(9)
Co1-N2	1.911(2)	N3-Co1-N4	92.5(9)
Co1-N3	1.892(2)	N4-Co1-N1	92.2(9)
Co1-N4	1.891(2)		

Complex **2** displays a Co^{II} ion situated within the macrocyclic cavity. The coordination about the metal is square pyramidal; the Co^{II} ion sits 0.114 Å above the N_4-plane that compromises the macrocyclic cavity. As with **1**, the cobalt ion in the macrocyclic cavity is asymmetrically coordinated. The M-N distances show little variation, although there is a slight decrease in the bond length to the pyrrole nitrogen's in comparison to **1**, as expected due to the increase in metal-to-ligand π-backbonding of Co^{II} vs. Co^{III} centre

(Table 1.2). Solvent molecules are located in the structure in a ratio of two CH_2Cl_2 per Co molecule.

Co_2(Mabiq)Cl_3 (3)

Crystals of **3** were obtained via vapour diffusion of ether into a solution of the crude product in MeOH, although the crystal structure was too disordered for the data to be refined to a publishable level. The structure obtained for **3** from X-ray diffraction of a suitable crystal is shown in Figure 1.16.

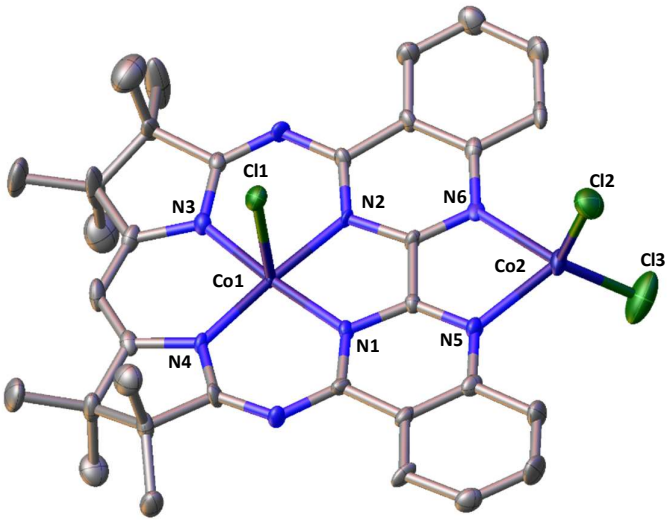

*Figure 1.16: Molecular structure of **3**. Hydrogen atoms and solvent molecules omitted for clarity. T = 120K.*

*Table 1.3: Selected bond lengths and bond angles for Complex **3**.*

Bond Lengths (Å)		*Bond Angles (°)*	
Co1-Cl1	2.541(2)	N1-Co1-N2	85.3(2)
Co1-N1	1.933(6)	N2-Co1-N3	90.6(3)
Co1-N2	1.923(6)	N3-Co1-N4	94.0(3)
Co1-N3	1.906(6)	N4-Co1-N1	90.1(3)
Co1-N4	1.896(6)	N5-Co2-N6	81.3(2)
Co2-Cl2	2.216(3)	Cl4-Co2-Cl5	120.6(12)
Co2-Cl3	2.231(3)	Cl4-Co2-N5	111.7(16)
Co2-N5	2.069(6)		
Co2-N6	2.061(6)		

Complex **3** displays a Co^{II} ion coordinated by four nitrogen atoms in the macrocyclic cavity. The coordination about the inner Co is again square pyramidal whereas the coordination about the outer Co^{II} is tetrahedral, although this is slightly distorted. As in **1** and **2**, the cobalt ion in the macrocyclic cavity of **3** is asymmetrically coordinated.

Co(Mabiq) (4)

Crystals of **4** were obtained via vapour diffusion of ether into a solution of the crude product in THF. The structure obtained for **4** from X-ray diffraction at the Diamond Light Source is shown in figure 18.

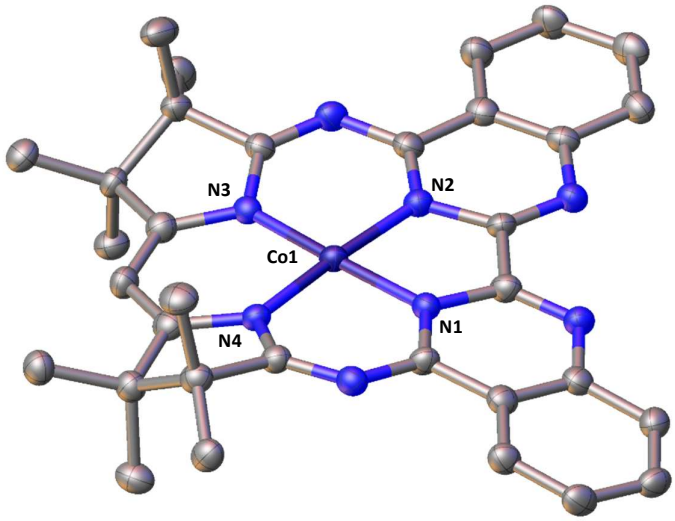

*Figure 1.17: Molecular structure of **4**. Hydrogen atoms and solvent molecules omitted for clarity. T = 120K.*

*Table 1.4: Selected bond lengths and bond angles for Complex **4**.*

Bond Lengths (Å)		*Bond Angles (°)*	
Co1-N1	1.877(3)	N1-Co1-N2	84.8(13)
Co1-N2	1.878(3)	N2-Co1-N3	91.2(13)
Co1-N3	1.857(3)	N3-Co1-N4	92.6(13)
Co1-N4	1.864(3)	N4-Co1-N1	91.4(13)

The coordination about the metal in **4** is square planar; the Co^{I} ion sits within the plane of the macrocyclic N-donor atoms. As with the other complexes, the cobalt ion in the macrocyclic cavity is asymmetrically coordinated. The M-N distances are the shortest of the four complexes, going against the expected trend of decreasing bond lengths with each reduction; this is attributed to π-backbonding from the electron rich Co^{I}. It is interesting to

note the bond lengths of the diketiminate unit; the average C-C bond distance is slightly shorter than seen in the previous complexes, whereas the C-N bonds are considerably longer. This effect has been observed previously, with similar bond distances seen in the reduced Fe^{II}(Mabiq$^{\bullet}$) complex.[36] This calls into question the most accurate description of the low-valent complex **4**: whether Co^{I}(Mabiq) or Co^{II}(Mabiq$^{\bullet}$).

The dihydropyrrole rings in all four complexes are considerably puckered; the sum of the five bond angles are on average in the range of 533-535° instead of the ideal 547.5°.[37] The rings are the least puckered in **3**, which has angles of 533° and 538° whereas they are the most puckered in **4** having angles of 529° and 531°. In the case of all four complexes, the sum of the six angles in each of the pyrimidine rings is 720°, showing them all to be completely flat.[37] However, there are varying degrees of distortion of the bipyrimidine unit among the compounds, with **4** again being the most distorted with a difference of ~6° in coplanarity between to two pyrimidine groups. In all four complexes the bond lengths of the diketiminate unit lie in between the theoretical values for single and double bonds[43], indicating a fully conjugated system.

1.3.3 Electronic Structure

The electronic structures of paramagnetic complexes **2** and **3** were examined using EPR spectroscopy[4] and SQUID magnetometry[5].

The solid-state magnetic susceptibility data of **2** was measured from 2 – 300 K and the results are shown in Figure 1.18 as a plot of magnetic moment vs. temperature. The data affords a temperature independent magnetic moment of 1.88 μ_B, consistent with an $S = {}^1/_2$ ground state for the Co^{II} complex. The low spin assignment is confirmed by the X-band EPR spectrum recorded in a CH_2Cl_2/toluene solution at ambient temperature (Figure 1.19), which produces an eight-line hyperfine splitting of the electron-spin resonance. When measured at 30 K, the frozen solution spectrum has a richly detailed hyperfine structure (Figure 1.20). The magnitude of the g anisotropy supports a five-coordinate low-spin Co^{II} and is markedly different from that of a four-coordinate species.[41]

The solid-state magnetic susceptibility data of **3** was measured from 2 – 300 K and the results are shown in Figure 1.21 as a plot of magnetic moment vs. temperature. The data affords a temperature independent magnetic moment of 4.3 μ_B from 50 – 300 K, which decreases below 50 K to a value of $\mu_{eff} \sim 3.8\ \mu_B$. The data supports the presence of two Co^{II} ions in **3** with $S = {}^1/_2$ and $S = {}^3/_2$ ground states (the spin only value is $\mu_{eff} = 4.24\ \mu_B$ for g = 2). The fluid-solution EPR spectrum of **3** in methanol essentially identical to that of **2**; the hyperfine pattern can arise from a single spin only, presumably that of the $S = {}^1/_2$ Co^{II} ion (Figure 1.22). When measured at 10 K, the frozen solution spectrum consists of a broad signal at ~120 mT attributed to an $S = {}^3/_2$ and a second signal at ~300 mT is consistent with the assumed spin doublet observed at room temperature (Figure 1.23). This spectrum is additional evidence for the dissociation of the bimetallic **3** in solution; the high-field signal at 120 mT is generated by dissociation of the high-spin Co^{II}.

[4] Measurements and analysis performed by Dr. Stephen Sproules at the University of Glasgow.
[5] Measurements performed by Andreas Göbels and analysis by Dr. Eckhard Bill at the MPI for Bioinorganic Chemistry.

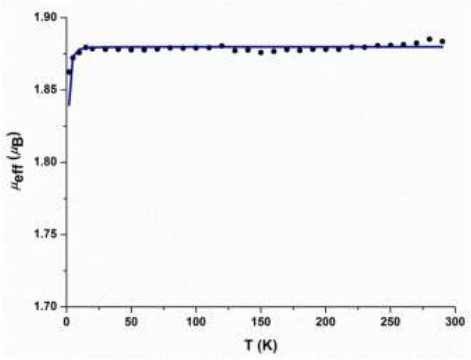

*Figure 1.18: Temperature dependence of the magnetic moment μ_{eff}, μ_B, (2 – 300 K, 1T) of a crystalline sample of **2**. S_1 = ½; g_1 = 2.17; TIP = 61 x 10^{-6} cm^3 mol^{-1}.*

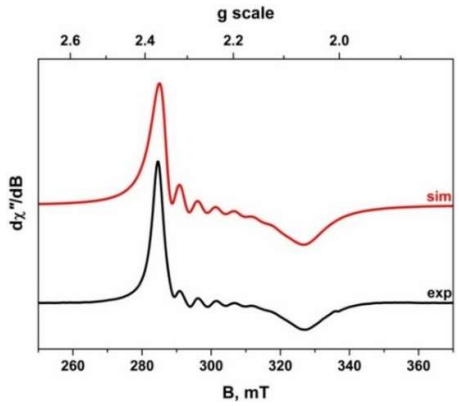

*Figure 1.19: X-band EPR spectrum of **2** recorded in CH_2Cl_2/toluene at 293 K (experimental conditions: frequency, 9.4338 GHz; modulation, 0.7 mT; power, 20 mW). Experimental spectrum shown in black and simulation depicted by the red trace: g_{iso} = 2.204; A_{iso} = 55 × 10^{-4} cm^{-1}.*

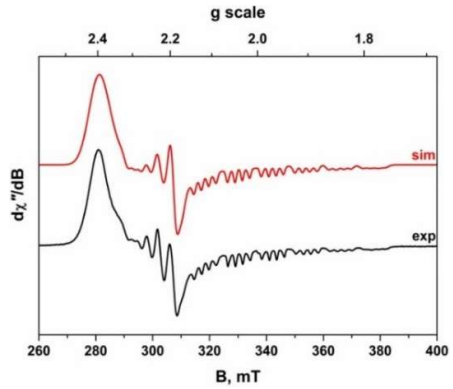

*Figure 1.20: X-band EPR spectrum of **2** recorded in CH_2Cl_2/toluene at 30 K (experimental conditions: frequency, 9.3668 GHz; modulation, 0.5 mT; power, 0.63 mW). The experimental spectrum is shown in black and the simulation depicted by the red trace: g = (2.280, 2.280, 2.002); $A\{^{59}Co\}$ = (35, 36, 111) × 10^{-4} cm^{-1}; $A\{^{35,37}Cl\}$ = (0, 0, 25) × 10^{-4} cm^{-1}.*

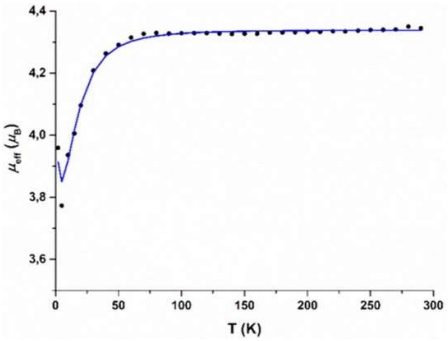

*Figure 1.21: Temperature dependence of the magnetic moment μ_{eff}, μ_B, of a powdered sample of **3**. $S_1 = {}^3/_2$; $S_2 = {}^1/_2$; $g_1 = 2.05$; $g_2 = 2.0$; $J_{12} = 0.47\ cm^{-1}$; $|D_2| = 20.37\ cm^{-1}$; $TIP = 1500 \times 10^{-6}\ cm^3\ mol^{-1}$.*

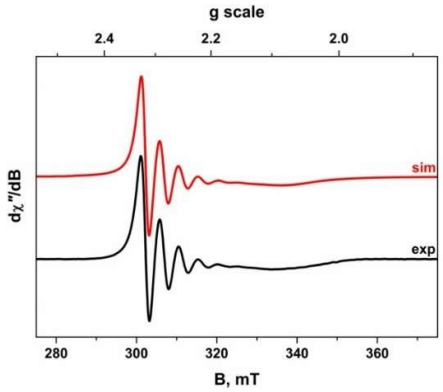

*Figure 1.22: X-band EPR spectrum of **3** recorded in CH_3OH at 293 K (experimental conditions: frequency, 9.8079 GHz; modulation, 0.4 mT; power, 20 mW). Experimental spectrum shown in black and simulation depicted by the red trace: $g_{iso} = 2.196$; $A_{iso} = 49 \times 10^{-4}\ cm^{-1}$.*

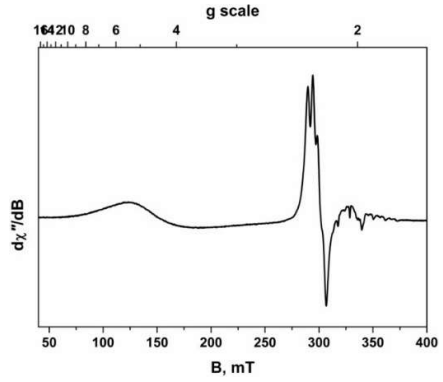

*Figure 1.23: X-band EPR spectra of **3** recorded in CH_3OH/toluene at 10 K (experimental conditions: frequency, 9.3352 GHz; modulation, 0.6 mT; power, 0.63 mW). Experimental data are depicted by the solid line. Simulation of an $S = {}^3/_2$ spectrum of a tetrahedral Co^{II} centre with $D >> h\nu$ is shown by the dashed line: $g = (2.35, 2.35, 2.58)$; $E/D = 0.03$; $W = (450, 450, 1000) \times 10^{-4}\ cm^{-1}$; $\sigma_{E/D} = 0.22$.*

1.3.4 Electrochemistry

The cyclic voltammograms (CV) for complexes **1**-**4** are shown in Figure 1.24.

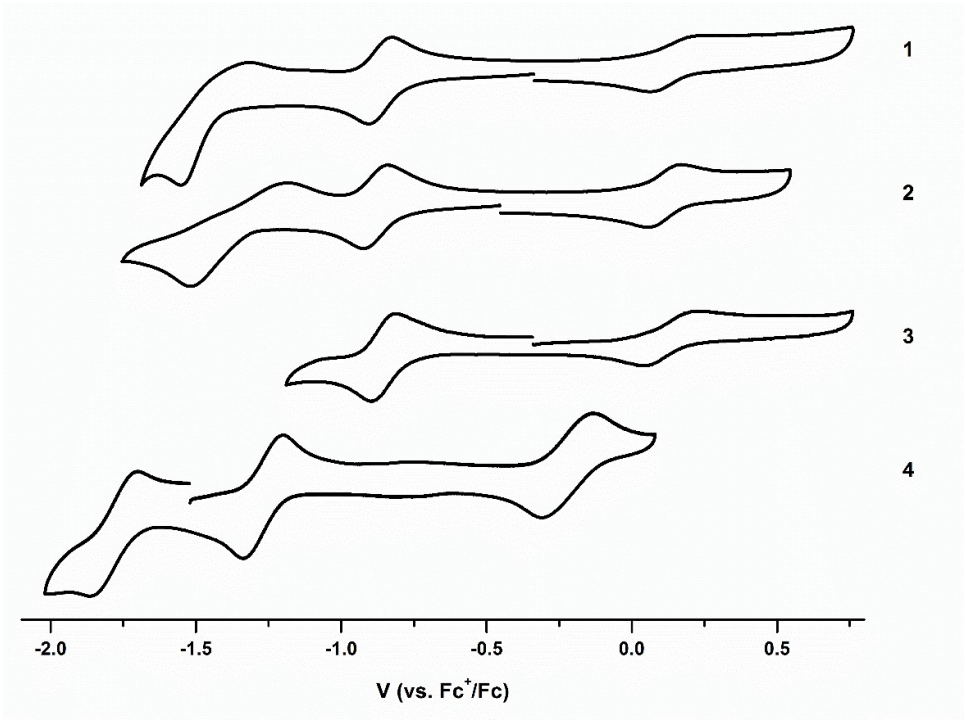

*Figure 1.24: CVs of **1**–**4** (0.2 V s^{-1}; 0.1 M $[N(n\text{-}Bu)_4]PF_6$; that of **4** in THF and all others in CH_3OH).*

The CV's for **1** and **2** are remarkably similar and show three individual redox processes. An irreversible redox couple can be seen at $E_{1/2}$ = ~0.1 V which is assigned to the Co^{III}/Co^{II} couple. Although on first glance the redox couple may appear to be reversible, a peak separation of 280 mV and 190 mV and a peak current ratio of 1.08 and 1.47 for **1** and **2** respectively rules out this assignment.[44] The redox couple at $E_{1/2}$ = ~0.1 V is followed by a reversible one electron reduction at $E_{1/2}$ = ~-0.9 V and a second irreversible reductive event at E_a = ~-1.5 V (Table 1.5).

All three redox events can be seen in the CV of **4** but are shifted to more negative potentials. Interestingly, all three events are fully reversible showing that the presence of the axial ligand clearly has a substantial effect on the electrochemical properties. The peak-to-peak separation for these redox processes is 125 – 150 mV; however, the peak-to-peak separation for the $Fc^{+/0}$ couple was also determined to be 134 mV in THF. The reversible nature of the redox events observed for complex **4** is further confirmed by peak currents in the range of 0.9 – 1.

Ligand centred reduction has been observed for the Zn- and Fe-Mabiq complexes and occurred at potentials of -0.9 V and -1.5 V, respectively.[36] The second redox process in the CVs of **1**, **2** and **4** may therefore formally correspond to the Co^{II}/Co^{I} couple but could also be attributed to a Co^{II}(Mabiq$^{\bullet}$) species. Thus, the ensuing redox event would likely entail the formation of Co^{I}(Mabiq$^{\bullet}$), where both the metal and the ligand are one-electron reduced, rather than the formal Co^{0} species.

*Table 1.5: Reduction Potentials (V vs $Fc^{+/0}$) of **1**-**4** (the Oxidation State Represents the Formal Metal Valency)*

	$E_{1/2}$ (Co^{III}/Co^{II})	$E_{1/2}$ (Co^{II}/Co^{I})	$E_{1/2}$ (Co^{I}/Co^{0})
1	0.14	-0.86	E_a = -1.53; E_c = -1.33
2	0.11	-0.88	E_a = -1.51; E_c = -1.22
3	0.12	-0.85	
4	-0.22	-1.27	-1.78

The CV for the bimetallic **3** displays only two individual redox processes; though the presence of an additional Co^{II} ion appears to have little other discernible effect. The potentials of the Co^{III}/Co^{II} and Co^{II}/Co^{I} couples are in line with those seen for **1** and **2**. The redox event assigned to the Co^{I}/Co^{0} couple is no longer present and scanning at potentials more negative than -1.2 V led to the appearance of new redox waves (Figure 1.25). Redox deactivation by a neighbouring metal ion has been reported previously[45] and may be occurring in this system. However, if $CoCl_2$ is indeed dissociating from the ligand as postulated from the solution-state characterisation, this would also complicate the electrochemistry. At present, we cannot confirm the solution-state composition of **3** and are unable to draw any further conclusions from the CV.

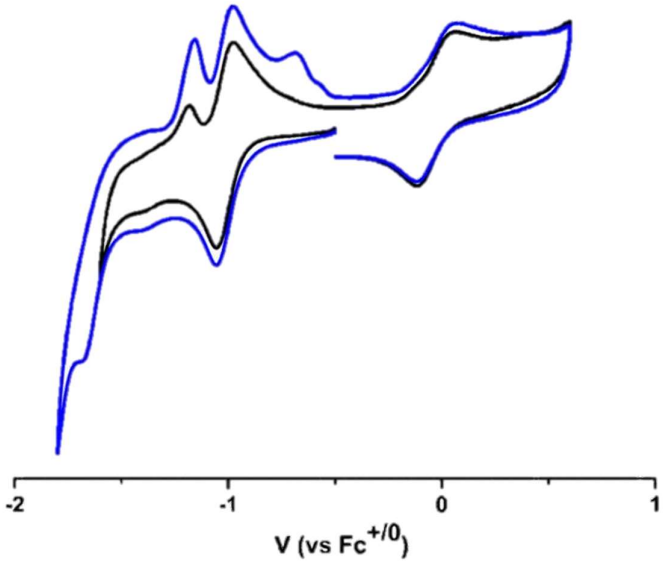

*Figure 1.25: CV of **3** in CH_3OH, showing the effect of scanning at potentials <-1.2V; 0.2 V s^{-1}; 0.1 M $[N(n\text{-}Bu)_4]PF_6$.*

The use of cyclic voltammetry enables electrolysis to provide electrons rather than chemical reductants and restricts the system to very few components. Cyclic voltammetry is a fascinating technique as catalytic turnover reactions lead to deviations from the ideal reversible behaviour of the redox curves, which allow qualitative and quantitative information to be inferred. This includes but is not limited to; the amount of H_2 evolved, the turnover numbers (TONs) per mole and mechanistic information such as the rate-determining step.

When a proton source is added to a solution of a molecular catalyst, an increase of the anodic current accompanied by the loss of the reverse oxidation peak is indicative of a catalytic wave.[46] Molecular cobalt complexes have been studied extensively as catalysts for electrochemical H_2 production, with formation of a Co^{I} species and subsequently a Co^{III}-H intermediate as a typical mechanism. To this end, we have used cyclic voltammetry to explore the potential of these complexes as hydrogen evolution catalysts, focusing on the Co^{II}/Co^{I} couple.

The effect of adding a proton source to **1** was observed by cyclic voltammetry (Figure 1.26). A current increase is observed on addition of trifluoroacetic acid (TFA). At 1 equivalent, there is an increase of the anodic current with no loss of the cathodic current, whereas with increasing equivalents we see a broadening of the anodic peak accompanied by an increase in current, a reduction of the return wave and a new cathodic peak. It may

be that a catalytic wave (although there is no true loss of the return wave) is being obscured by the appearance of a new redox couple, likely Co^{III}-H/Co^{II}-H. This phenomenon has been observed previously by Hu *et al.,* who reported the appearance of a new quasi-reversible wave when investigating catalytic hydrogen production with the complex $Co(dmfBF_2)_2(CH_3CN)_2$.[47]

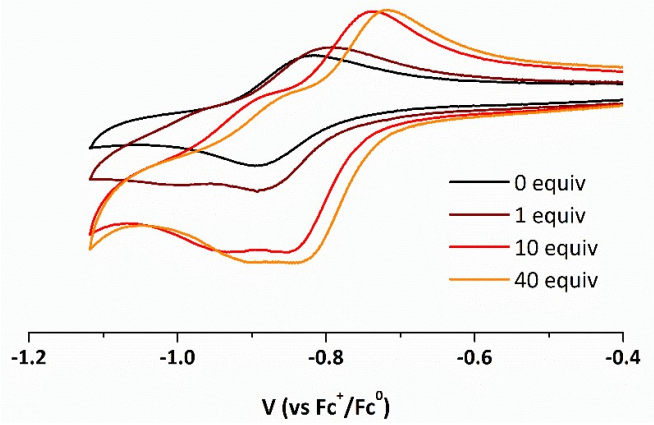

*Figure 1.26: Cyclic voltammogram for **1** increasing equivalents of trifluoroacetic acid. Glassy carbon electrode, 0.5mM solution in CH_3OH; 0.2 V s^{-1}; 0.1 M $[N(n\text{-}Bu)_4]PF_6$.*

When increasing equivalents of tosic acid are added to a DCM solution of **2**, a similar effect can be observed (Figure 1.27).

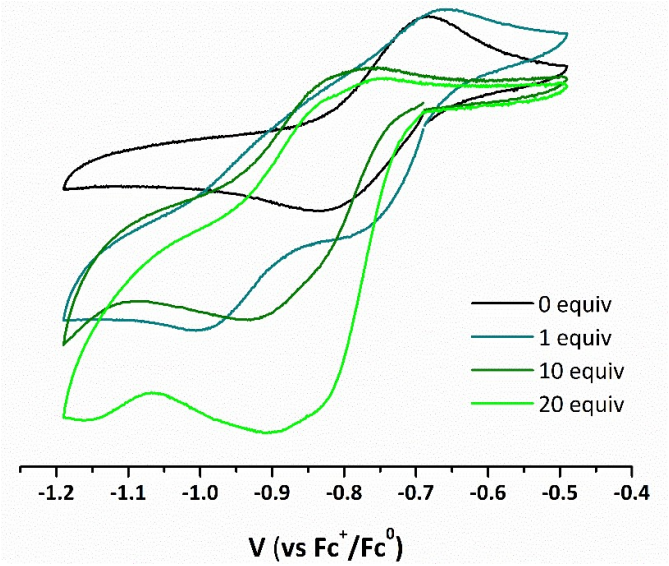

*Figure 1.27: Cyclic voltammogram for **2** with increasing equivalents of tosic acid. Glassy carbon electrode, 0.5mM solution in DCM; 0.2 V s^{-1}; 0.1 M $[N(n\text{-}Bu)_4]PF_6$.*

On addition of one equivalent of tosic acid, a new reduction event can be seen at E_a = ~-1.0 with the retention of the Co^{II}/Co^{I} couple. With increasing equivalents, a

broadening of the reduction event is observed with an appreciable loss of the return wave. Again, although less pronounced, this may be indicative of a catalytic wave with more than one process occurring.

Typically, electrolysis is performed at a potential less negative than that of the direct electrochemical reduction.[48] However, this is not the case seen here; the apparent catalytic wave appears at a potential more negative than that of the Co^{II}/Co^{I} couple. Similar behaviour was observed by Razavet *et al*. who reported catalytic hydrogen production with the complex $[Co(dmgH)_2(py)Cl]$. This complex displayed a catalytic wave with high acid concentrations at more negative potentials than the Co^{II}/Co^{I} reversible wave. Razavet *et al*. assigned this catalytic wave to proton electroreduction.[20]

It is worth noting that the presence of axial chloride in both **1** and **2** may be interfering with the catalytic process; in order for Co^{III}-H to be formed a vacant coordination site must be available for coordination.

The effect of adding acid to **3** was also measured by cyclic voltammetry; no catalytic activity was observed (Figure 1.28). Although an increase of the anodic current is observed, this is also accompanied by an increase in the cathodic current. This does not indicate the irreversible loss of hydrogen as is seen for complex **1** and **2** but rather suggests that a new reversible Co(II/I) species may be formed in solution.

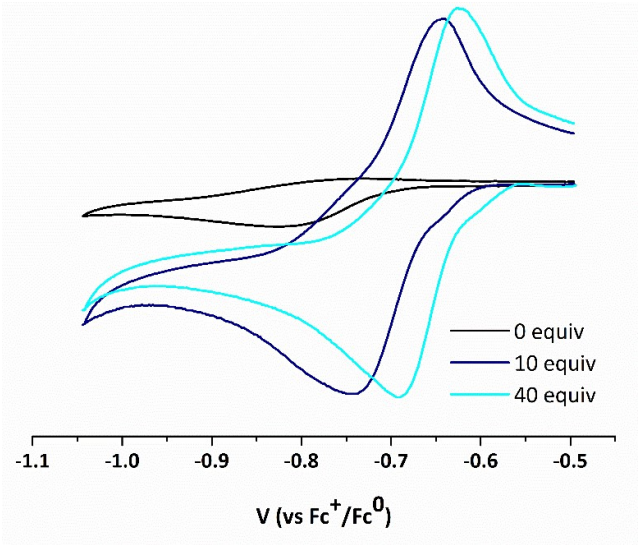

*Figure 1.28: Cyclic voltammogram for **3** with increasing equivalents of tosic acid. Glassy carbon electrode, 0.5mM solution in CH_3OH; 0.2 V s^{-1}; 0.1 M $[N(n\text{-}Bu)_4]PF_6$.*

In order to explore the behaviour of **4** on addition of a proton source, the complex was first oxidised using $FeCp_2^*PF_6$ to form the complex $[Co^{II}(mabiq)]PF_6$ (**4-ox**). This allowed us to obtain a Co^{II} complex of Mabiq without the complication of axial chloride.

The effect of adding a proton source to **4-ox** can be seen in Figure 1.29. Addition of increasing equivalents of triflic acid triggers the appearance of a new catalytic irreversible anodic wave near the Co^{II}/Co^{I} couple. The Co^{II}/Co^{I} couple appears to be completely lost and there is no evidence of additional redox couples forming at this concentration. Due to time constraints, only very preliminary experiments were carried out on **4-ox** but this is a promising result and suggests that the axial chloride anions do indeed cause the complicated processes occuring in both **1** and **2**.

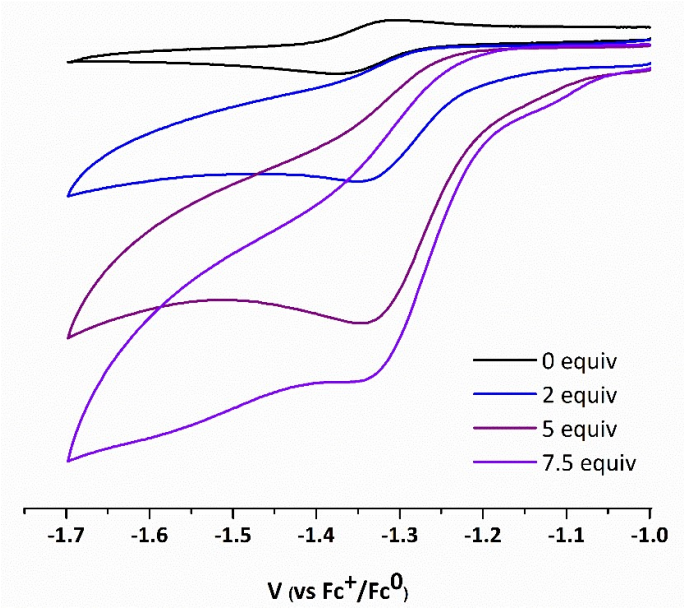

*Figure 1.29: Cyclic voltammogram for **4-ox** with increasing equivalents of triflic acid. Glassy carbon electrode, 0.5mM solution in CH_3OH; 0.2 V s^{-1}; 0.1 M $[N(n\text{-}Bu)_4]PF_6$.*

1.4 Conclusions and Further Work

The molecular structure of HMabiq is such that it is able to bind through the four nitrogen donors in the macrocyclic cavity, allowing the isolation of a three-electron series of monometallic compounds **1**, **2**, and **4**.

Despite the functionalities of Mabiq appearing well suited to the coordination of a second metal ion, this phenomenon was previously unreported. Complex **3** offers the first evidence of the ability of HMabiq to bind to a second metal. Based on the solution-state spectroscopic data, we conclude that the outer $CoCl_2$ moiety is only weakly bound and readily removed from the bipyrimidine unit.

Electrochemical data confirms the ability of monometallic Co(Mabiq) compounds to be further reduced yielding formally Co^0 monoanionic species, likely resulting from the reduced form of the macrocycle. The removal of all axial chloride anions in complex **4** introduces full electrochemical reversibility into the system.

Preliminary studies into the suitability of these complexes as hydrogen evolution show promising results. Complex **1** and **2** show promising activity towards proton sources with both complexes exhibiting a current increase, however neither cyclic voltammogram appears clear cut with broad peaks and the emergence of new redox couples. Removing the axial chloride anions again appears to improve the system, the addition of a proton source to the cyclic voltammogram of complex **4-ox** displayed the typical behaviour for total catalysis and was uncomplicated by broadening or additional redox couples.

An unfortunate feature of complex **4** and indeed **4-ox** is the increase in air sensitivity of these complexes. Complex **1** is air stable and while complex **2** shows some air sensitivity it is stable for a period of days. Complex **4** however is extremely air sensitive and is affected by air on a sub-second timescale. It may be beneficial to replace the chloride anion with a more labile ligand and hence increase the ease of access to the coordination site rather than removing the chloride anion altogether.

The cyclic voltammetry of complex **3** only exhibited two redox couples, assigned to the Co^{III}/Co^{II} and Co^{II}/Co^{I} couple. This is a somewhat surprising result; due to the lability of the outer $CoCl_2$ moiety we expected to see behaviour similar to that of complex **2**. Disappointingly, the addition of a proton source to the CV of **3** showed no evidence of

catalytic activity. It is possible that at the higher concentrations of cyclic voltammetry there is little to no loss of the outer $CoCl_2$ moiety.

Now that the ability of HMabiq to coordinate two metal ions has been verified, exploration of this phenomenon is warranted. The effect of coordination of a second metal ion may be explored by the complexation of Zn into the macrocyclic cavity followed by the coordination of $CoCl_2$ into the bipyrimidine unit. Modification to enhance the chelating ability of the external unit may be advantageous to this end.

Part 2 – New Tridentate and Tetradentate Ligands for Photoactive Metal Complexes

PHOSPHORESCENCE. Now there's a word to light your hat to… to find that phosphorescence, that light within, that's the genius behind poetry.

Emily Dickinson

2 Introduction

Since 1959 and the first report of phosphorescence resulting from a charge transfer state in the transition metal complex $[Ru(bpy)_3]^{2+}$, interest in photoactive metal complexes has grown exponentially.[49] This explosion of interest has been driven by the many applications these complexes offer; phosphors for organic light-emitting devices (OLEDs) and light-emitting electrochemical cells (LEECs), light-harvesting units or 'dyes' for dye-sensitised solar cells (DSSCs) and energy and/or electron donors in artificial photosynthesis to name but a few.[50–53] The past two decades have seen thousands of transition-metal complexes synthesised and extensive studies have been reported on their photochemistry.[54] The factors that govern the luminescence efficiencies of heavy metal complexes are now better understood; high-efficiency emission and systematic colour tuning are possible with a wide range of ligands.[55] This review will consider the factors governing the luminescent properties of a compound and the strategies for the rational design of highly emissive transition-metal complexes.

2.1 Luminescence

When light energy is absorbed by a molecule to form an excited electronic state, the molecule tends to try to lower its energy back to the ground state. Generally this is achieved by transferring the energy into vibrations and rotations known as non-radiative decay.[56] However, in some molecules the energy may be lost radiatively, as a photon of light, in a process known as photoluminescence. This mode of decay of the excited state can be broadly divided into two categories: fluorescence and phosphorescence.

Fluorescence is the emission of light from a spin-allowed transition, i.e. from an excited state whose spin multiplicity is the same as that of the ground state (e.g. $S_1 \rightarrow S_0$). Emission from this pathway is relatively fast, being characterised by a high radiative rate constant k_r^s of the order of 10^8-10^9 s^{-1}, leading to emission lifetimes in the nanosecond range.[57] When a molecule has been promoted to a singlet excited state, intersystem crossing (ISC) can occur, changing the spin multiplicity to a triplet excited state. Emission from this state is a spin-forbidden process ($\Delta S \neq 0$), referred to as phosphorescence. For purely organic molecules, the rate constant for this process is as low as 0.1-100 s^{-1} but incorporation of a heavy metal (such as platinum or iridium) into a molecule increases spin-orbit coupling (SOC), which relaxes the spin selection rule and increases the rate constant of phosphorescence. Radiative decay through this pathway is still significantly slower than

fluorescence, leading to longer emission lifetimes on the order of microseconds. The pertinent states related to this process are represented with a classical Jabłoński diagram (Figure 2.1), first proposed by Professor Alexander Jabłoński in 1935.[58]

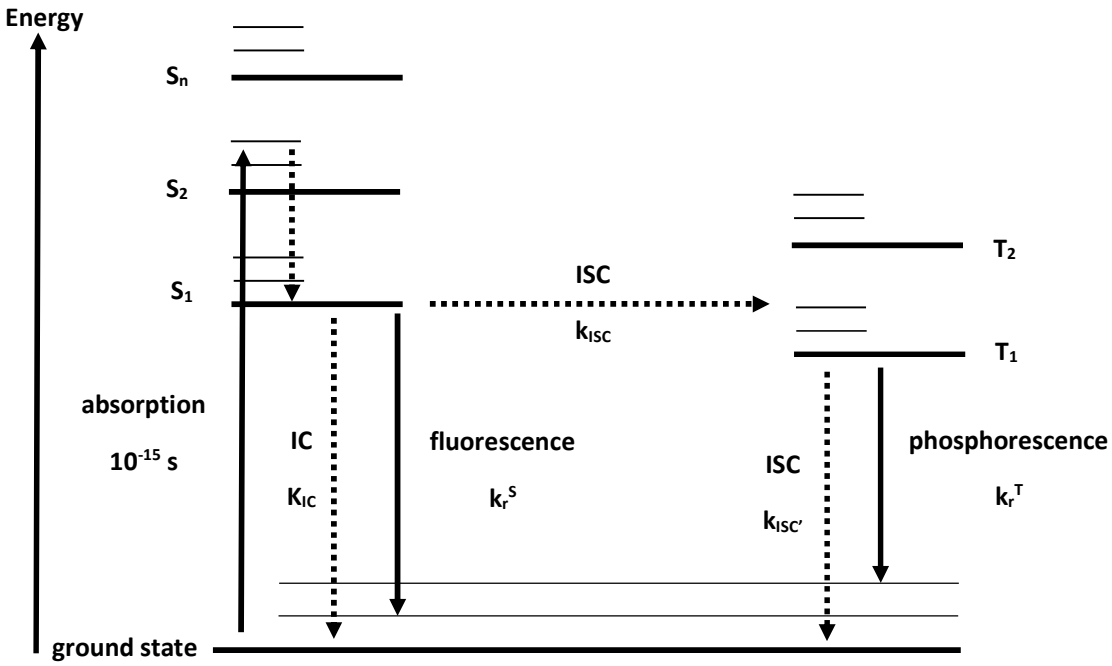

Figure 2.1: A simplified Jabłoński diagram illustrating the rate constants for key processes. 'IC' represents internal conversion followed by vibrational relaxation; 'ISC' represents intersystem crossing followed by vibrational relaxation.

2.1.1 Quantum Yield

The efficiency of emission from a given excited state is quantified in terms of the photoluminescence quantum yield, ϕ_{lum}, which is simply the ratio of the number of photons emitted to the number of photons absorbed (assuming all the absorbed light led to the emitting state). This is determined by the relative rate constants of radiative decay (k_r) and non-radiative decay (k_{nr}), according to equation 2.1.

$$\Phi_{lum} = \frac{n_E}{n_A} = \frac{k_r}{k_r + k_{nr}} \quad (2.1)$$

Triplet states are generally not populated directly through absorption of light due to the spin selection rule; rather the T_1 state is formed indirectly from the S_1 state through ISC. However, for complexes with small ligands and heavy metals, ISC is usually much faster

than the rate of emission from the singlet excited state and so equation 2.1 can often still be applied.

2.1.2 Electronic Transitions

In an organometallic compound, the molecular orbitals can be crudely approximated as either metal- or ligand-based. This results in the excited state generally being described as one of four transitions: metal centred (MC), metal-to-ligand charge transfer (MLCT), ligand-to-metal charge transfer (LMCT) and ligand centred (LC). These are illustrated schematically in Figure 2.2. It is important to note that although broadly classified in these states, if they are similar in energy, mixing of the states can occur and emission may be the result of a combination of transitions.

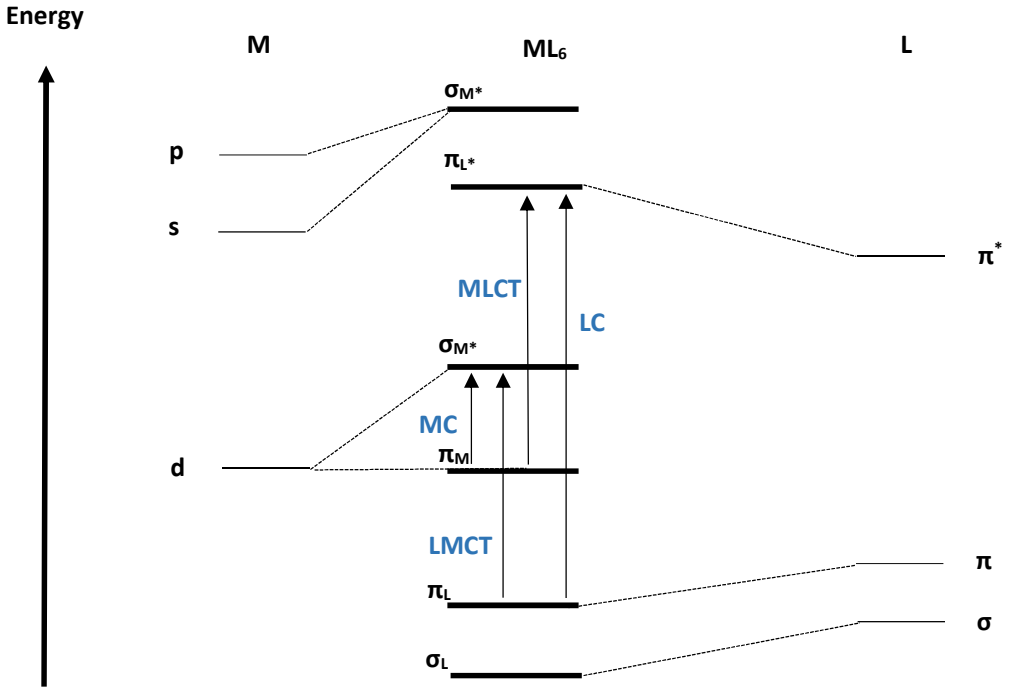

Figure 2.2: An energy level diagram to illustrate the various possible excited states of octahedral metal complexes.

2.1.3 Promoting Luminescence

It is clear that in order to design molecules which are brightly luminescent, a high k_r and low k_{nr} value are desirable. The phosphorescence quantum yield also depends on the efficiency of formation of the triplet state, which is determined by the magnitude of the rate constant of ISC. The high-spin orbit coupling of a heavy metal nucleus facilitates both the ISC process and emission from the triplet state. As a result, the degree of metal

character in the excited state is important in determining the efficiency of emission; k_r should be highest for excited states with a high degree of metal character, e.g. MLCT states.

However, a d-d (MC) excited state with solely metal character typically leads to population of antibonding orbitals, causing an elongation of M-L bonds and significant distortion of the molecule in the excited state and therefore a large k_{nr} due to the isoenergetic crossing point lying at thermally accessible energies (Figure 2.3a). Bearing this in mind, a careful balance of energy levels must be achieved; if the MLCT state and the d-d states are quite close in energy, the d-d states can be thermally populated, i.e. if ΔE is comparable to kT (Figure 2.3b). This offers a non-radiative decay pathway and renders a complex non-emissive at room temperature.

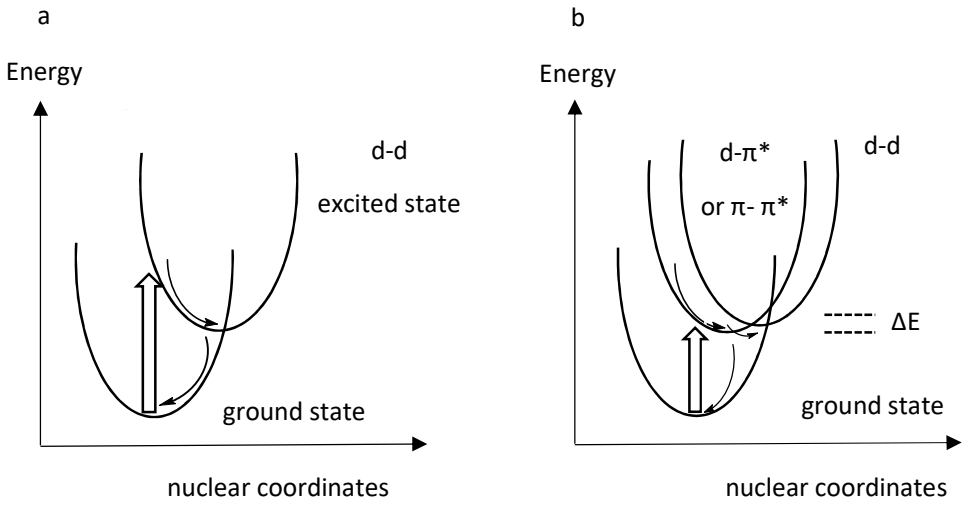

Figure 2.3: (a) The displaced potential energy surface of the d-d excited state formed by population of an antibonding metal centred orbital. (b) The d-d state can provide a thermally activated decay pathway for other, lower-lying excited states if ΔE is comparable to kT. Thick arrows represent absorption of light; thin ones indicate vibrational relaxation and non-radiative decay.

Therefore, we can conclude that the most emissive complexes will be those in which (1) the lowest lying excited state is not a MC d-d state and (2) the energy gap between the lowest lying excited state and the d-d state is large enough to prevent thermally activated decay.

The higher spin-orbit coupling of the third-row metals promotes $S_1 \rightarrow T_1$ intersystem crossing and promotes the $T_1 \rightarrow S_0$ phosphorescence process, making metals such as Pt and Ir a popular choice for emissive complexes. However, caution must be taken to ensure that the metal ion 'participates' in the excited state; the relative energies of MLCT

and LC states depend on the combination of ligand, metal and metal oxidation state. We shall now consider some of the main classes of Pt(II) and Ir(III) complexes that are luminescent under ambient temperatures. After reviewing some important and informative early examples, we will focus on advances from the past few years.

2.2 Platinum(II) complexes of aromatic bidentate ligands

There are many Pt(II) complexes based on the $Pt(N^N)X_2$ structure where N^N is a bidentate diamine ligand such as bipyridine or phenanthroline and their derivatives. X must provide a strong ligand-field to ensure the d-d state is not the lowest energy or thermally accessible from a lower-lying CT or LC state. For example, those where X = Cl are rarely significantly emissive.

An early example of a luminescent bidentate Pt(II) complex was reported by Kunkely *et. al.* where X = -C≡N in the complex $Pt(dpphen)(CN)_2$, **1** (Figure 2.4).[59] The strong-field cyanide lowers the energy of the highest-occupied metal-centred orbitals and raises the vacant d_{x2-y2} orbitals, such that the $Pt(N^N)(CN)_2$ emits from the π-π* state. The complex emits green light centred at 520 nm in dilute CH_2Cl_2 solution. At higher concentrations an association to an excimer takes place. The excimer emits at lower energy, with emission of red light centred at 615 nm. The excimer is reported as being characterised by a metal-metal bond which promotes dimerization and emission originates from the interaction of an excited monomer with a ground-state monomer.

Organometallic carbon derivatives that incorporate Pt-aryl bonds have also seen success. The high degree of covalency in Pt-C bonds and a good match between the energies of the highest filled metal and ligand-based orbitals frequently leads to the excited state having a significant degree of MLCT character.[53] The bis-mesityl complex, **2** (Figure 2.4), reported by Dungey *et al.* emits at 660nm in dilute toluene solution from a ^{3}MLCT state. The colour of emission from these complexes can be readily tuned, for example related compounds containing perfluorinated aryl rings, reported by Nishida *et al.,*[60] emit at substantially blue shifted wavelengths compared to the mesityl compound **2**. This is rationalised by the electron-withdrawing influence of the fluorine substituents in lowering the energy of the metal-centred HOMO.

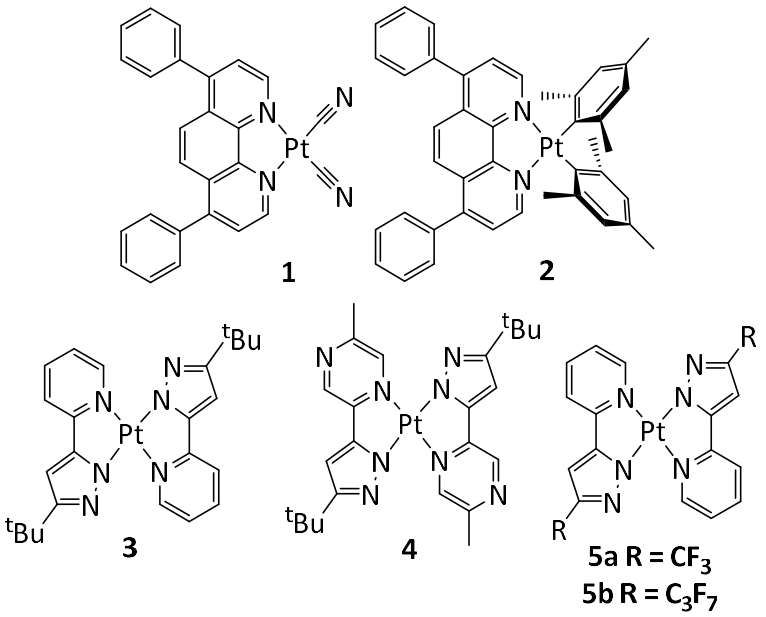

Figure 2.4: Representative Pt(II) complexes with bidentate ligands.

A further success in the preparation of luminescent bidentate Pt(II) complexes comes from the use of 'pseudo-cyclometallates'. This replaces the neutral two-electron 'L' donors such as pyridines and quinolines by heterocycles such as pyrazoles, indazoles, imidazoles and triazoles. These systems can either coordinate via a neutral nitrogen atom or through deprotonation of a 'pyrrolic' nitrogen. In the latter case, the coordination offered to the metal is essentially analogous to that of a cyclometallating ligand; hence 'pseudo-cyclometallating'. These ligands again exert a strong ligand field, giving a beneficial effect on luminescence. An interesting example of this type of ligand was reported by Chi and co-workers when exploring the chemistry of Pt(II) with a series of 3-(2-pyridyl)pyrazole, 3-(pyrazyl)pyrazole and 3-(2-pyridyl)triazole ligands.[61] It was noted that PLQY in solution varied widely according to the substituents on the ring; the *tert*-butyl substituted complexes **3** and **4** are amongst the most efficient Pt(II) emitters known (ϕ = 0.82 and 0.86, respectively), whereas the analogues **5a** and **5b** display very weak emission under the same conditions (Figure 2.4).

Another important class of Pt(II) bidentate complexes are those which incorporate a bidentate N^C cyclometallating ligand. The coordination pattern for Pt(II) complexes of this type may be type I or type II (Figure 2.5). Type I contains a bidentate cyclometallating ligand with two monodentate ligands and type II contains two bidentate ligands with at least one being cyclometallating. Depending on the nature of the ligands, the complexes can either be neutral or ionic.

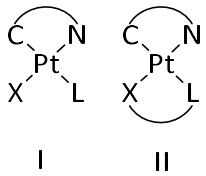

Figure 2.5: Types of cyclometallated Pt(II) complexes.

In general, the emission of type I complexes tend to be inferior to type II complexes and are instead typically used as intermediates in the preparation of type II complexes.[62] The archetypal complex is one based upon 2-phenylpyridine (Hppy) and its analogues, modifications of which are mainly focused on colour tuning and improving PLQY. An interesting example of this modification is a series of lepidine-based ligands reported by Velusamy *et al.*[63] The complexes **6** - **12** (Figure 2.6) contain 1 lepidine-based ligand and one O^O acac ligand and emit in the orange-to-red region with a wide range of PLQYs (ϕ_{PL} = 0.15 – 0.99) (Table 2.1). The O^O ligand is easily introduced and normally does not influence the excited state energy significantly, so that the properties are essentially those associated with the N^C ligand.[57] Electron-withdrawing substituents in the aryl ring lower the HOMO, leading to a shift to the blue, whereas extending the conjugation in the heterocycle shifts the emission to the red.

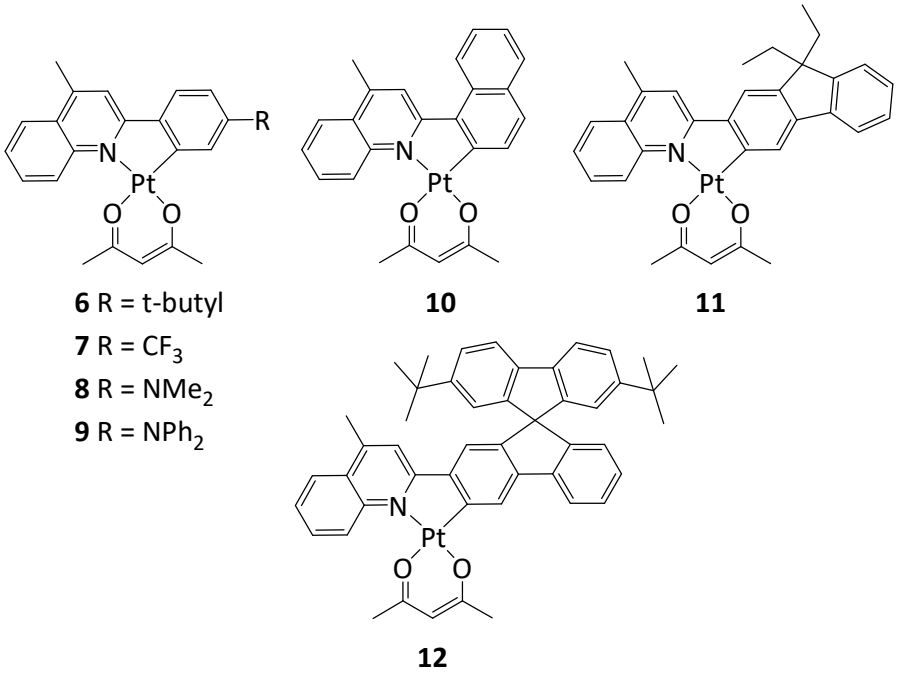

6 R = t-butyl
7 R = CF_3
8 R = NMe_2
9 R = NPh_2

10

11

12

Figure 2.6: Lepidine-based Pt(II) complexes.

Table 2.1: Data for Lepidine-based Pt(II) Complexes in degassed toluene at 298 K.

	Emission (nm)	Q.Y.
6	619	0.35
7	617	0.70
8	597	0.87
9	593	0.99
10	641	0.15
11	600	0.74
12	588	0.60

Schiff bases have provided a C^N cyclometallated alternative to 2-phenylpyridine; these complexes usually show intense phosphorescence in the solid state which is less efficient in solution.[64] Komiya *et al.* reported a series of complexes bearing iminophenyl and iminophenoxy ligands, with an absolute quantum efficiency up to 0.29 in the crystalline state (Figure 2.7).[64] The complexes show extraordinarily wide chromogenic change; emission occurs over a range of 99nm when simply introducing methoxy groups at different positions on the rings ($R^1 – R^4$).

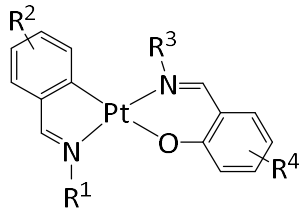

13

Figure 2.7: Cyclometallated Pt(II) complexes based on Schiff base ligands.

2.3 Platinum(II) complexes of aromatic tridentate ligands

In an effort to further increase PLQY, researchers have turned their attention to tridentate ligands. The d-d excited states of Pt(II) complexes with bidentate ligands are susceptible to distortion away from the D_{4h} symmetry of the ground state towards a D_{2d} symmetry, in which the plane of the bidentate ligand is twisted relative to that containing the other two ligands.[65] As discussed previously, excited state distortion is associated with an increase in non-radiative decay causing an adverse effect on PLQYs. Tridentate ligands which are able to bind via three sites rather than two in a planar conformation should inhibit such distortion owing to a more rigid binding.

2.3.1 N^N^N-Coordinated Ligands

The N^N^N-coordinated platinum terpyridyl complex of Pt(II) $[Pt(tpy)Cl]^+$ (**14**, Figure 2.8) was first synthesised by Morgan *et al.* in 1934.[66] The photophysical properties were not explored until the 1990s when it was found that room temperature luminescence was not observed. The coordination bite angle around Pt(II) is smaller than the favourable 180° about the N-Pt-N.[67] This strain results in a weaker ligand field compared to that which is expected, such that the anti-bonding d_{x2-y2} orbital lies at a similar energy to the ligand π*. In order to enable room temperature luminescence, the ligand field strength must be increased to raise the d_{x2-y2} orbital so it can no longer be populated, or the MLCT radiative excited state lowered to an extent where population of the d_{x2-y2} orbital is no longer possible.

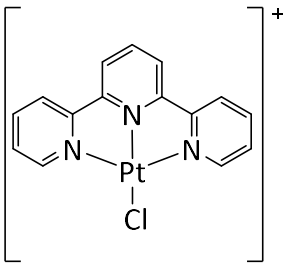

14

Figure 2.8: Terpyridyl Pt(II) complex, $[Pt(tpy)Cl]^+$.

Systematic exploration of substituent effects has led to the preparation of $[Pt(tpy)Cl]^+$ derivatives that are luminescent at room temperature. Introduction of substituents in the 4 position of the central pyridine ring was shown to produce luminescent compounds by McMillin *et al.*[68] As shown in Figure 2.9, the introduction of the electron-withdrawing substituent inhibits thermal population of the d-d excited states by lowering the MLCT state further than the d-d states and increasing the energy gap. The introduction of an electron-donating substituent stabilises the MLCT state in relation to the deactivating d-d states, due to the lone pairs on the substituents conjugating with the π-system of the terpyridine ligand. A new π-π* state is formed with intra-ligand charge-transfer (ILCT) character which increases the gap between the emissive and non-radiative states.

Replacement of the chloride ancillary ligand with a stronger-field ligand can also increase ligand field splitting, increasing the energy of the d-d states and reducing the likelihood of their population. A good example of this is an acetylide ligand and a wide range of emissive complexes based on $[Pt(tpy)(-C\equiv C-R)]^+$ have been reported.[69–71] Other studies

have shown that increasing the size of the chelate ring from a 5 to 6 membered can relieve ring strain in the system, giving a bite angle closer to 180° which gives a stronger ligand field and promotes the d-d energy.[72]

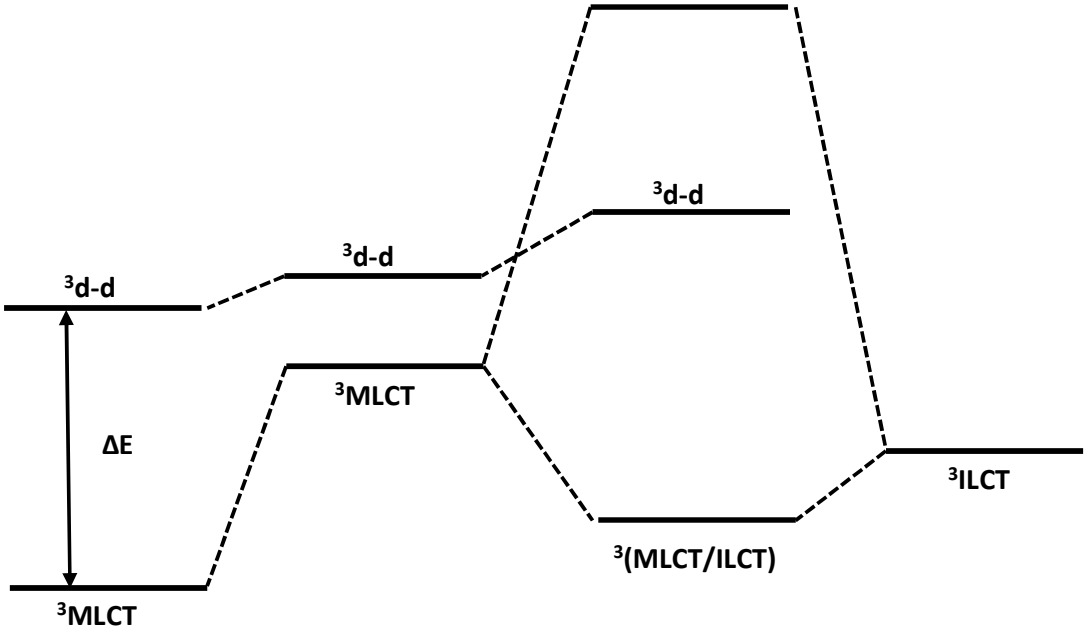

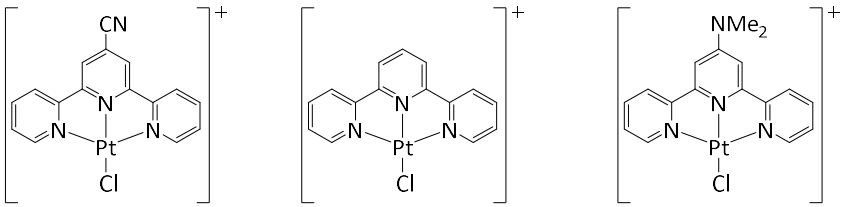

15 16 17

Figure 2.9: Molecular orbital diagram for the proposed excited state energies of 4-substituted Pt(II) tpy complexes for electron-withdrawing and electron-donating substituents.[6]

2.3.2 N^N^C-Coordinated Ligands

Replacing one of the nitrogen atoms in the terpyridine ligand by a cyclometallating aryl ring has a profound effect on the luminescence. Constable *et al.* first reported the cycloplatinated complex of 6-phenyl-2,2'-bypridine (phbpyH) shown in Figure 2.10[73]. In contrast to $[Pt(tpy)Cl]^+$, the N^N^C complex **18** shows modest room temperature luminescence (λ_{max} = 565 nm, ϕ_{PL} = 0.025)[74]. The strong σ-donating power of the deprotonated carbon and the extended π-system creates a very strong ligand field, increasing the energy difference between the d-d states and MLCT states.

[6] *Adapted with permission from Coord. Chem. Rev., 2002, 229, 113, Copyright (2002), Elsevier Science B.V.*

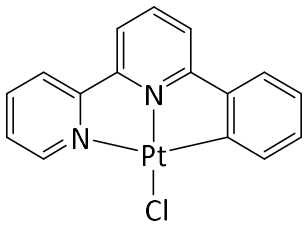

18

Figure 2.10: N^N^C-coordinated complex Pt(phbpy)Cl.

Che and co-workers have provided an in-depth study into the cyclometallated Pt(II) complex with the N^N^C-coordinating ligand, 6-phenyl-2,2'-bypridine (phbpyH) and its derivatives, providing around 30 examples with σ-alkynyl ligands in the fourth coordination site rather than chloride.[75] Most of the reported complexes were emissive in solution at room temperature and emission was attributed to a ^{3}MLCT($d_{Pt} \rightarrow \pi^*_{NNC}$) state. Structural modification of the N^N^C ligand and the acetylide can be used to influence the emission properties, tuning the colour emitted from green-yellow to saturated red. For example, electron-withdrawing substituents on the acetylide ligand shift the emission maxima to higher energy as the metal-based HOMO is lowered in energy (Figure 2.11). Introduction of substituents into the 4-position of the pyridyl rings is also an effective method of colour tuning, whilst substituents on the cyclometallating phenyl ring were found to have very little influence. However, changing from phenyl to thienyl or furanyl rings led to substantial red shift due to the more electron-rich nature of these heterocycles (Figure 2.12).[57]

Interestingly, Harris *et al.* found a decrease in emission efficiency by increasing the size of one of the 5-membered chelate rings to a 6-membered ring (Figure 2.13).[76] Although this change brings the complex closer to the ideal square planar geometry for a Pt(II) complex, the accompanying increase in flexibility of the molecule has a detrimental effect on the quantum efficiency.

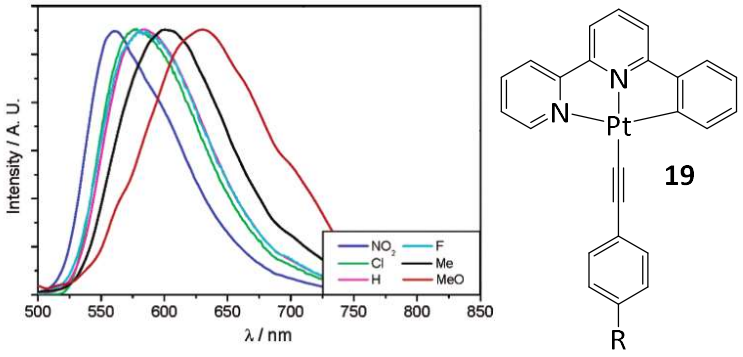

Figure 2.11: Normalised emission spectra for N^N^C-Pt(II) complex with various R substituents shown. Spectra were taken at 298 K in DCM solution.[7]

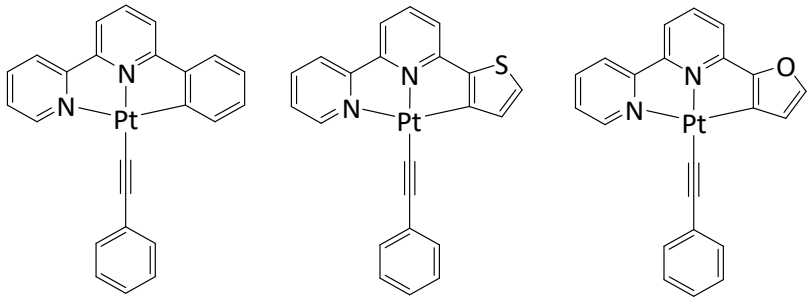

20	**21**	**22**
λ_{max} = 582 nm	λ_{max} = 615 nm	λ_{max} = 640 nm
ϕ_{lum} = 0.04	ϕ_{lum} = 0.05	$\phi_{lum} \leq 10^{-3}$
τ = 0.4 µs	τ = 1.0 µs	$\tau \leq$ 0.1 µs

Figure 2.12: Structures and emission properties of N^N^C-coordinated Pt(II) complexes with various cyclometallated heterocycles. Measurements taken at 298 K in DCM solution.[75]

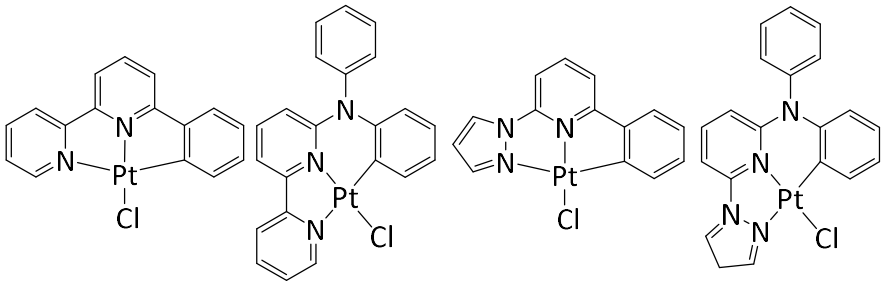

18	**23**	**24**	**25**
λ_{max} = 565 nm	λ_{max} = 615 nm	λ_{max} = 504, 540 nm	λ_{max} = 523 nm
ϕ_{lum} = 0.025	ϕ_{lum} = 0.001	ϕ_{lum} = 0.035	$\phi_{lum} \leq$ 0.001

Figure 2.13: Structures and emission properties of N^N^C-coordinated Pt(II) complexes reported by Harris et al. Measurements taken at 298 K in DCM solution.[76]

[7] Adapted with permission from J. Am. Chem. Soc., 2004, 126, 4958–4971. Copyright (2004) American Chemical Society.

2.3.3 N^N^O-Coordinated Ligands

The aryl ring of N^N^C Pt(II) complexes can be replaced by a phenolate, giving a range of luminescent [(N^N^O)PtX] complexes (where X = Cl, Br, I or -C≡C-Ph and Y = H, Me or t-Bu; Z=H or F) as reported by Kwok *et al.* (Figure 2.14).[77] For complex **26**, broad orange-red emission (λ_{max} = 593-618 nm) originates from triplet excited state with mixed ^{3}MLCT and ^{3}[l → π*(diamine)] (l = lone pair/phenoxide) parentage. Unfortunately, the PLQYs were too low to be measured; this was attributed to quenching by DMF.

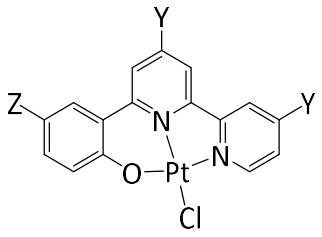

26

Figure 2.14: N^N^O-coordinated Pt(II) complex.

2.3.4 N^C^N-Coordinated Ligands

Changing the position of the cyclometallating ring can lead to significant differences in the chemistry and properties of Pt(II) complexes. The N^C^N-coordinated complex (Figure 2.15) was first reported by Cárdenas *et al*. in a study investigating the complexation chemistry of 1,3-di(2-pyridyl)-benzene with Pt(II) and Pd(II).[78] Williams *et al.* carried out the first photophysical study of the Pt(II) complex **27** (Y = Z = H) and reported intense luminescence; ϕ_{lum} = 0.60 and τ = 7.2 μs in degassed DCM.[79] This is an order of magnitude higher than the isomeric N^N^C-coordinated compound Pt(phbpy)Cl. The unexpectedly high luminescence is attributed to the Pt-C bond in Pt(dpyb)Cl being significantly shorter than in Pt(phbpy)Cl, and hence the ligand-field strength being higher. The emission is highly structured and is scarcely shifted upon cooling to 77K, indicating emission from a primarily LC π-π* state, the contribution of the metal is nevertheless sufficient to promote efficient triplet emission.

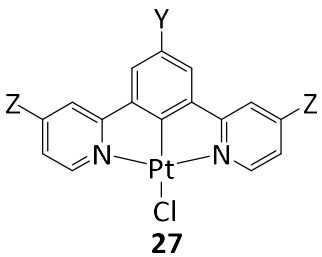

27

Figure 2.15: N^C^N-coordinated Pt(dpyb)Cl

The N^C^N-coordinated complex offers a versatile approach to colour tuning of emission.[55] DFT calculations reveal that the HOMO spans across the cyclometallating ring, the metal and the chloride co-ligand whereas the LUMO is localised on the pyridine rings. This accounts for the influence of substituents at the 4-position of the phenyl ring on emission energy. For example, the introduction of electron-donating aryl groups shifts the emission increasingly to the red while a blue shift is caused by electron-withdrawing groups (Figure 2.16).[51]

It is interesting to note that the complex incorporating the strongly electron-donating pendant R = -$C_6H_4NMe_2$ displays a broad, structureless emission band with a high degree of positive solvatochromism not displayed by the other complexes (Figure 2.16). This behaviour suggests a switch in the nature of the lowest-energy excited state towards one of primarily ILCT, due to the high degree of stabilisation of the emissive excited state.

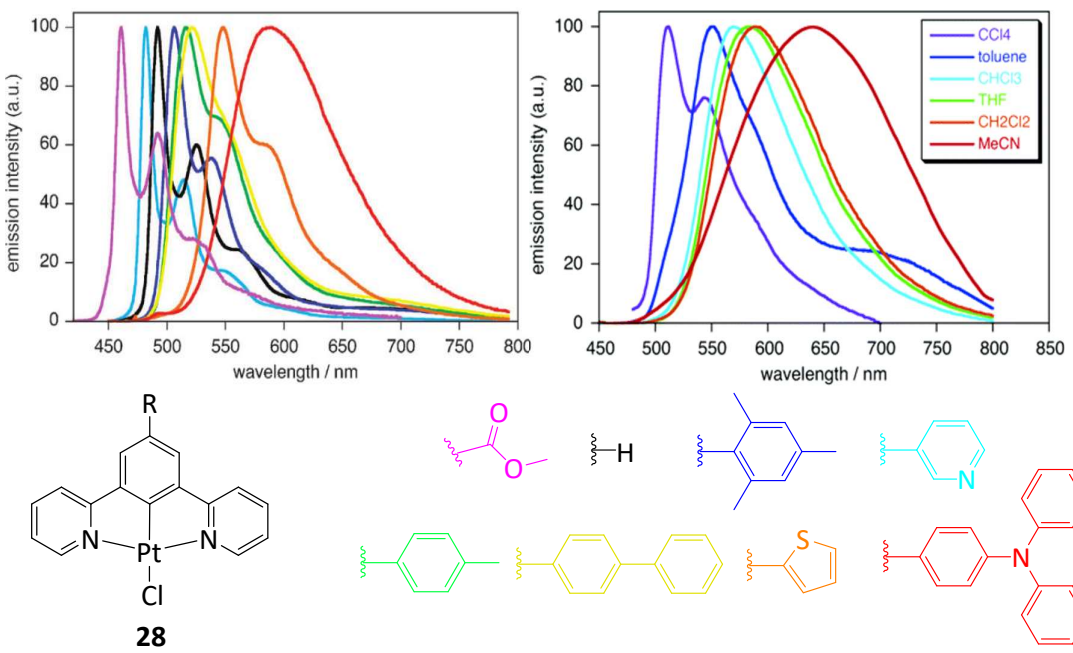

Figure 2.16: Normalised emission spectra of the Pt(dpyb)Cl complexes measured in DCM at 298 K (right) and emission spectra of R = -$C_6H_4NMe_2$ in solvents of differing polarity at 298 K (left).[8]

Increasing the two 5-membered chelate rings of the complex to two 6-membered chelates was found to have a dramatic effect on emission efficiency (Figure 2.17, far right complex). The resulting complex **30**, reported by Williams and co-workers, was found to have severely diminished emission despite having a bite angle close to the desired 180°.[72]

[8] *Reprinted with permission from Inorg. Chem., 2005, 44, 9690–9703, Copyright (2005) American Chemical Society.*

The PLQY was reduced to 1.6% in DCM from 60% and the λ_{max} was shifted to 645 from 491 nm. Williams and co-workers attributed this to emission originating from a predominately LC triplet state, making the radiative transition less allowed.

Interestingly, inserting an amino linker between the pyridine and phenyl units gives a modest increase in emission efficiency: complex **29** (Figure 2.17) emits green light with a 65% PLQY, despite the shift of λ_{max} to a longer wavelength of 506 nm.[80] As seen for other Pt(II) complexes, substitution of the chloride ligand for an acetylide monodentate ligand can also lead to somewhat superior PLQY for the resulting complexes.

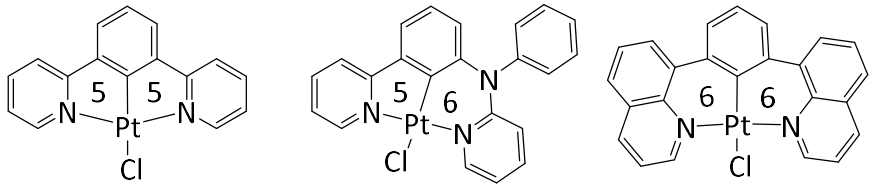

27 **29** **30**

Figure 2.17: Chelate ring sizes of N^C^N-coordinated Pt(II) complexes.

2.3.5 C^N^C-Coordinated Ligands

The introduction of a second cyclometallating ring to produce Pt(II) complexes based on 2,6-diphenylpyridine (**31**, Figure 2.18) are only weakly emissive in solution, although modest PLQYs have been achieved with the introduction of thiophene, fluorene and carbazole groups as anionic carbon donors.[81]

Kui *et al.* reported a series of such modified ligands (Figure 2.19) and observed emission in solution at room temperature with λ_{max} at 564 – 619 nm and ϕ = 0.02 – 0.26.[81] Emission was attributed to excited states with mixed ^{3}MLCT and ^{3}IL character.

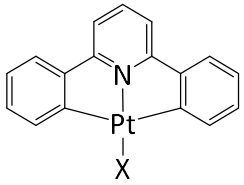

31 X = DMSO

Figure 2.18: Bis-cyclometallated Pt(II) complex based on 2,6-diphenylpyridine.

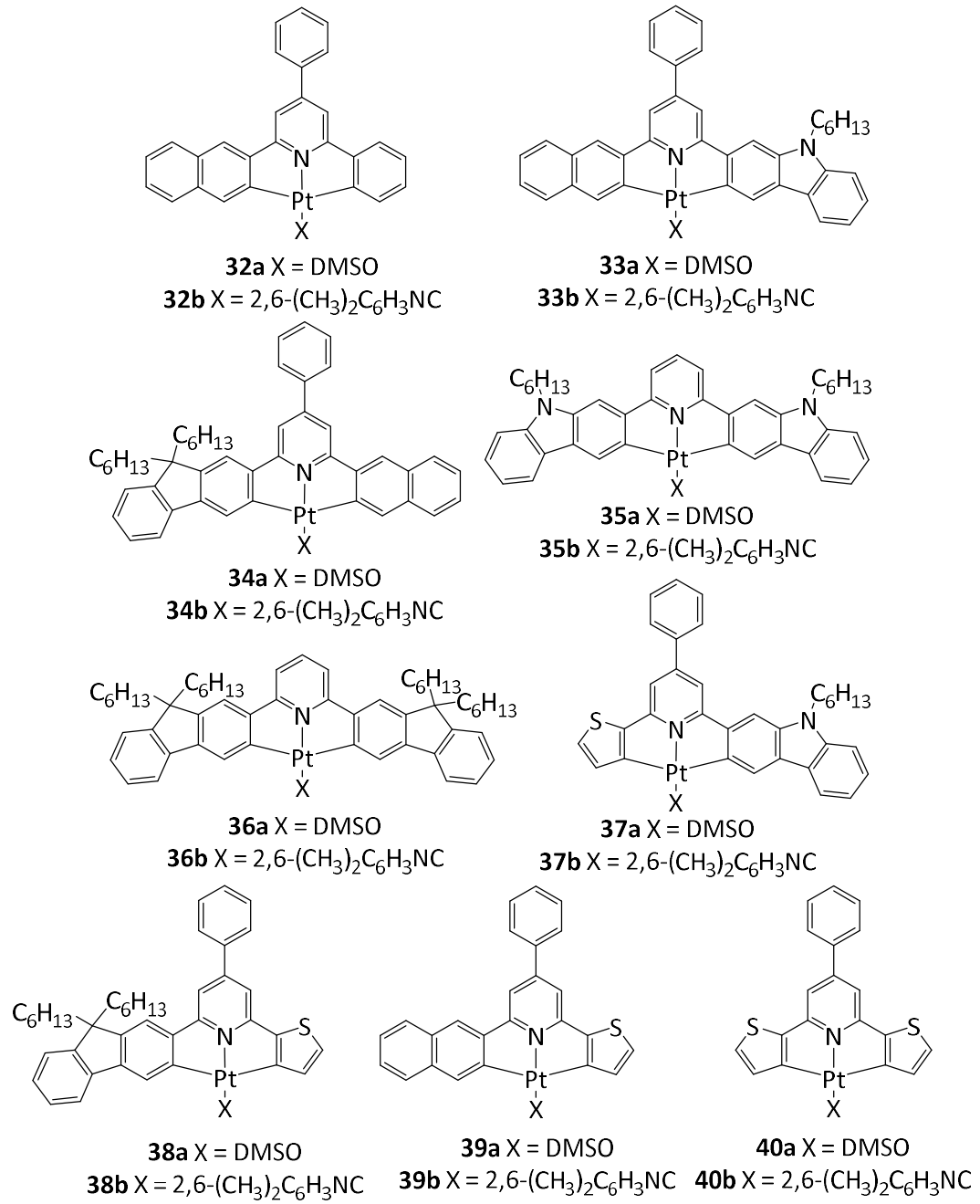

Figure 2.19: Pt(II) C^N^C-coordinated complexes reported by Kui et al.

2.4 Platinum(II) complexes of aromatic tetradentate ligands

In efforts to develop suitable triplet emitters to be used in OLEDs, the development of phosphorescent Pt(II) complexes with tetradentate ligands is a rapidly growing field. Inspiration for this class of emitters was the unfavourable photophysical properties displayed by bis-bidentate bis-cyclometallated Pt(II) complexes such as *cis*-[Pt(ppy)$_2$], (non-emissive at room temperature) and *cis*-[Pt(thpy)$_2$] (Hthpy = 2-(2-thienyl)pyridine), which is emissive but unstable towards sublimation. The poor PLQYs displayed by such complexes

are at least in part attributed to the flexibility of the complexes.[62] The rigidity can be improved by linking the two ligands together to form a ligand which can offer tetradentate coordination and a structure closer to planarity might be anticipated. Depending on how the C-Pt and N-Pt bonds are arranged, there is a possibility of four different coordination patterns as shown in Figure 2.20.

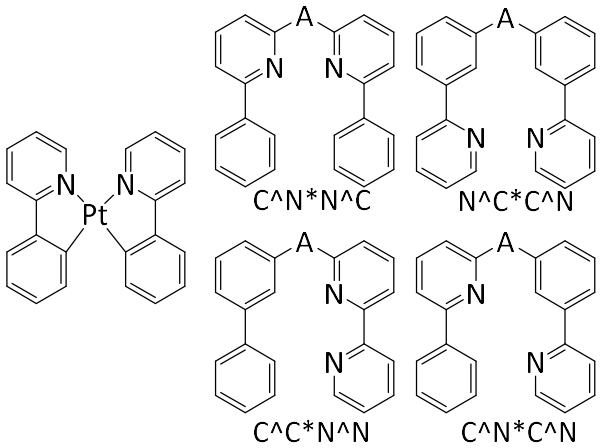

Figure 2.20: Schematic representation of various coordination modes.

In 2009, Feng *et al.* investigated the first *bis*-cyclometallated tetradentate platinum complexes, preparing C^N*N^C complexes **41** and **42** (Figure 2.21).[82] Both complexes emitted at λ_{max} = 492nm with PLQYs of 0.54 (**41**) and 0.58 (**42**). Vezzu *et al.* later showed the effect of functionalisation by using an amine linker to offer high modularity in ligand design.[83] Interestingly, DFT calculations show the HOMO is based on the phenyl rings and the metal while the LUMO is localised on the pyridine rings (Figure 2.22). The complexes **43** and **44** both showed high PLQYs of 0.74 and 0.75, respectively, although the emission wavelength was blue shifted from λ_{max} = 512 nm to λ_{max} = 488 nm with the presence of fluorine in the complex.

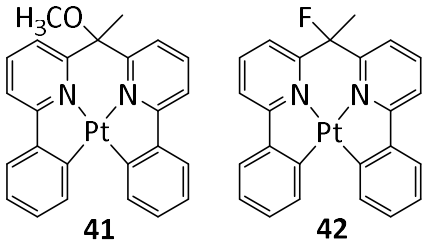

*Figure 2.21: C^N*N^C Pt(II) complexes **41** and **42**.*

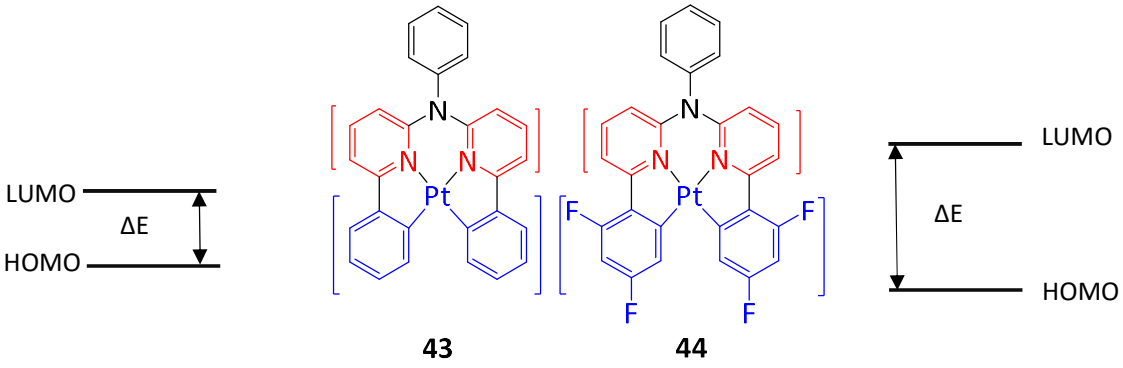

*Figure 2.22: ΔE comparison between Pt(II) complexes **43** and **44**.*

Vezzu *et al.* also studied the influence of the coordination pattern on the photophysical properties, reporting a series of N^C*C^N Pt(II) complexes (**45** – **48**, Figure 2.23).[84] DFT calculations showed the HOMO was again localised on the phenyl rings and the metal and the LUMO localised on the pyridine/pyrazole rings. Replacement of the pyridine rings by pyrazole rings causes a bathochromic shift from λ_{max} = 613 nm to λ_{max} = 474 – 516 nm (Figure 2.24). The more electron rich pyrazole raises the LUMO level causing the blue shift in complexes **46** – **48**.

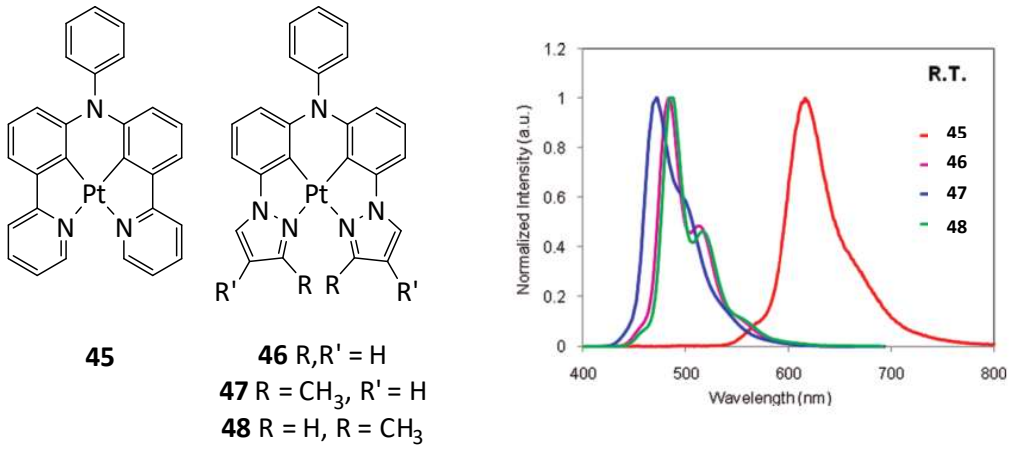

*Figure 2.23: N^C*C^N Pt(II) complexes. Room temperature emission spectra of **45** – **48** in degassed THF at 298K.*[9]

In 2013, Huo *et al.* investigated the C^C*N^N coordination pattern with complexes containing a pyridyl ring and a pyrazole ring (complexes **49** and **50**, Figure 2.24).[85] Careful design of the proligand scaffold was required to restrict rotation, due to the preferential formation of C^N^N-coordinated complexes. Complex **49** is weakly emissive in the red

[9] *Adapted with permission from Inorg. Chem., 2010, 49, 5107–5119. Copyright 2010 American Chemical Society.*

region (λ_{max} = 660 nm, ϕ_{PL} = 0.001), but **50** emits bright yellow light in DCM at 298K (λ_{max} = 555 nm, ϕ_{PL} = 0.17). This increase in PLQY is unsurprising, PLQYs are generally highest in the green region; they fall off towards the blue because of the role of higher-lying states and towards the red because of vibrational deactivation. The emission is attributed to a primarily ligand centred transition (ILCT) with admixture of MLCT.

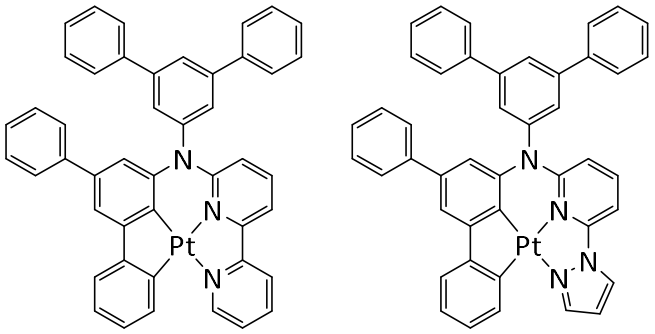

49 **50**

*Figure 2.24: C^C*N^N Pt(II) complexes **49** and **50**.*

Pseudo-cyclometallation has also seen some success in the preparation of tetradentate complexes. Oxygen ligands on their own are usually unsuitable for forming stable complexes with the soft Pt(II) ion but stable complexes can be formed when combined with other ligands such as diimines.[57] Shagisultanova reported in 1998 that the well-known proligand, N,N'-bis(salicylidine)-1,2-ethylenediamine or salen forms a highly luminescent Pt(II) complex, **51** (Figure 2.25).[86] The emissive state is assigned to one of d(Pt)/π(O)→π*(Schiff base) character, giving a PLQY of 0.19 in MeCN. Che and co-workers explored the luminescence of the related ligand based on dpphen appended with ortho-phenoxy groups, finding the resulting Pt(II) complex, **52** (Figure 2.25) to be superior in terms of solution PLQY, reporting an impressive ϕ_{PL} = 0.6 in MeCN.

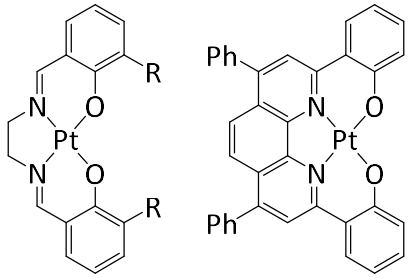

51 R = H **52**

Figure 2.25: Pseudocyclometallated Pt(II) complexes.

Charge neutral O^C^C^N complexes, where the two carbon donors are from neutral carbene species, were recently reported by Li *et al* (Figure 2.26).[87] Complexes **53** to **57** emit in the region λ_{max} = 443 – 461 nm with ϕ_{PL} = 3 – 18%. Complex **58** however does not emit at room temperature, owing to severe structural distortion in the T_1 excited-state and the resulting increase in k_{nr}, revealed by DFT calculations.

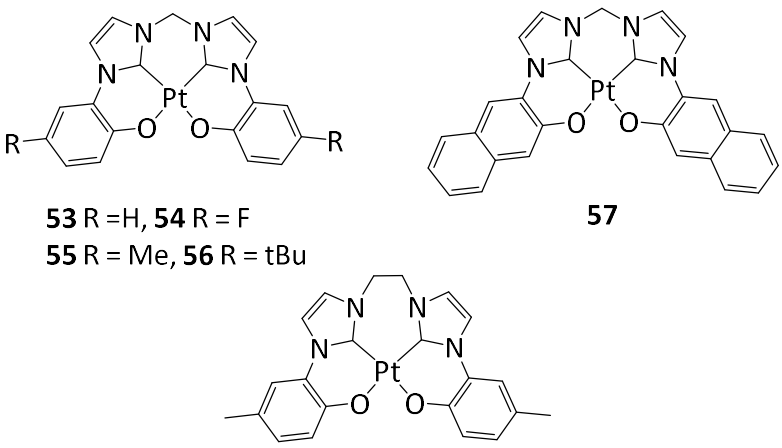

*Figure 2.26: Pt(II) complexes **53** – **58** bearing a tetradentate O^C^C^O ligand.*

Impressive PLQYs have been reported by Kui *et al.* for a series of O^N^C^N-coordinated Pt(II) complexes, which feature one 6-membered metallacycle and two 5-membered metallacycles (Figure 2.27).[88] All complexes displayed green-blue emission, with high PLQYs, ϕ_{lum} = 0.72 to 0.93 and long luminescence lifetimes (τ = 11 to 28 μs).

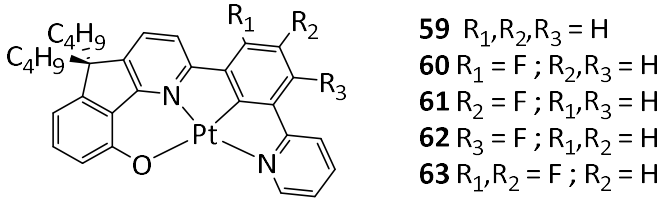

*Figure 2.27: Tetradentate Pt(II) O^N^C^N complexes **59** – **63**.*

A number of closely related O^N^C^N-coordinated Pt(II) complexes with two 6-membered metallacycles and one 5-membered metallacycle have been reported by Cheng *et al.*, utilising a bridging tertiary amine (**64**) or a biphenyl group with a spiro linkage (**65**) (Figure 2.28).[89] Both complexes are efficient emitters; **64** emits at 551 nm with a PLQY of 0.9 and **65** emits at 517 nm with a PLQY of 0.8. The emission is tentatively assigned to excited states having mixed ^{3}MLCT and ^{3}[l → π*(N^C^N)] (l = lone pair of phenoxide) parentage.

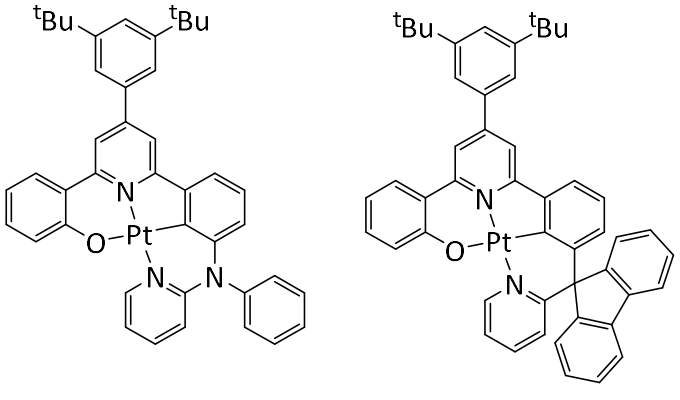

64 **65**

Figure 2.28: O^N^C^N-coordinated Pt(II) complexes with two 6-membered metallacycles and one 5-membered metallacycle.

2.5 Iridium(III) complexes of aromatic ligands

Although once less studied than the other platinum group metals, iridium has become of intense interest in the past 20 years.[90] Most studies have focused on tris-bidentate complexes; the complex $[Ir(ppy)_3]$ (**66**) (Figure 2.29) and its derivatives have been at the centre of many OLED studies. The related cationic systems, of which $[Ir(ppy)_2(bpy)]^+$ (**67**) is representative (Figure 2.29), have also seen much interest; with applications in light-emitting electrochemical cells (LEECs), as probes and sensors for biomolecules and as photocatalysts for water splitting.[90] The area has been extensively reviewed and the reader can refer to a number of comprehensive reviews listed in the references.[91–95]

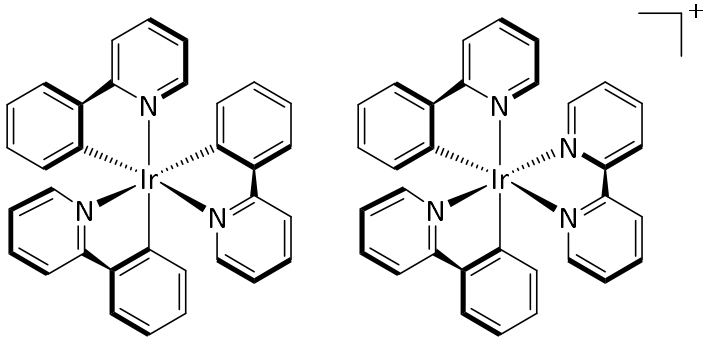

66 **67**

Figure 2.29: Two key tris-bidentate Ir(III) complexes; fac-$[Ir(N^C\text{-}ppy)_3]$ (left) and $[Ir(N^C\text{-}ppy)_2(N^N\text{-}bpy)]^+$.

Despite the increase in interest, only a limited number of groups world-wide have studied Ir(III) complexes with tridentate ligands. As discussed for Pt(II) complexes,

tridentate ligands can lead to different properties and excited states when compared with bidentate analogues. Interestingly, for Ir(III) complexes, C_2-symmetrical tridentate ligands produce achiral complexes as opposed to the tris-bidentate complexes which are intrinsically chiral; the latter form as a racemic mixture of Λ and Δ isomers.

In contrast with the archetypical $[Pt(tpy)Cl]^+$, the parent complex $[Ir(tpy)_2]^+$ (**68**, Figure 2.30) shows structured emission with maxima at 458, 491 and 523 nm and a PLQY of 0.02 – 0.06 depending on counter anion and solvent.[96] The highly structured emission profile, with a vibrational spacing of ~1400 cm^{-1} that is typical of coupling with aromatic C=C vibrations, is characteristic of emission from states with relatively little involvement of the metal and the emission is attributed to LC π-π* excited states.[90] The preparation and purification of these complexes was described as 'ardous' in the first reports; this difficult chemistry was once a hallmark of Ir(III) complexation chemistry.[90] However, an optimised synthesis of these complexes has been developed and the milder, stepwise route allows for the introduction of two differently substituted terpyridines into the coordination sphere.[97] Taking inspiration from the method commonly used for the preparation of asymmetric terpyridine complexes of Ru(III), tpy is reacted with $IrCl_3.nH_2O$ in ethylene glycol to give $[Ir(tpy)Cl_3]$ as an intermediate, which is then reacted with a second tridentate ligand to produce the target complex (Scheme 2.1).

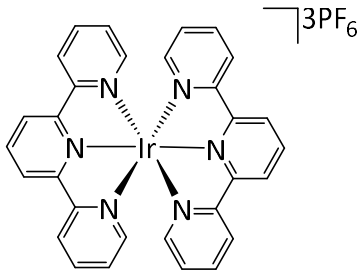

68

Figure 2.30: $[Ir(tpy)_2](PF_6)_3$

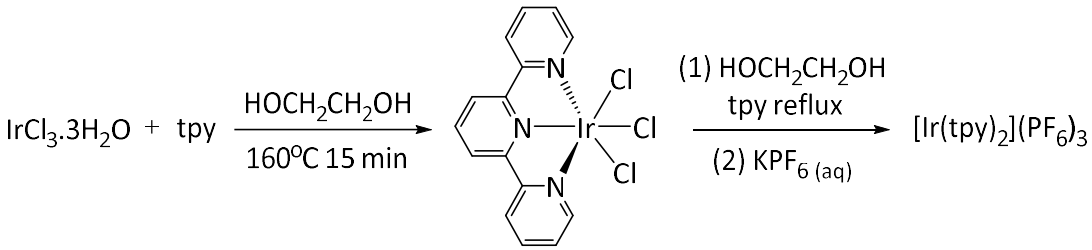

Scheme 2.1: The synthesis of $[Ir(tpy)_2](PF_6)_3$ via $[Ir(tpy)Cl_3]$.

Cyclometallation has also proven successful in the chemistry of Ir(III) with tridentate ligands. Wilkinson *et al.* sought to introduce 1,3-di(2-pyridyl)benzene (dpyb) into the

coordination sphere of Ir(III) to bind in an N^C^N fashion (Figure 2.31, binding mode I).[98] However, reaction of dpybH with $IrCl_3.3H_2O$ resulted primarily in complexation through binding mode II. Interestingly, cyclometallation at the C^4 position is kinetically favoured over reaction at the more hindered C^2 position. This can be overcome by using the xylene derivative, 1,3-di(2-pyridyl)-4,6-dimethylbenzene (dpyxH), to block cyclometallation in binding mode II and give the chloro-bridged dimer $[Ir(dpyx)Cl(\mu\text{-}Cl)]_2$, **69** (Scheme 2.2, centre). Reaction of the intermediate dimer with a wide range of proligands successfully forms a diverse selection of bis-tridentate Ir(III) complexes with varied coordination spheres, as seen in Scheme 4.3.

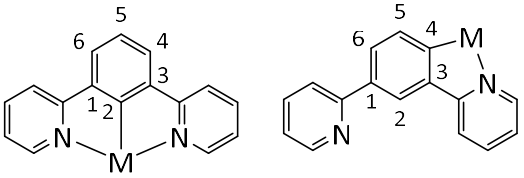

Figure 2.31: N^C^N and N^C binding modes of dpyb.

The emission colour of these Ir(III) bis-tridentate complexes can be tuned in an analogous manner to the Pt(II) complexes discussed, and the selection of these chelates mainly focuses on achieving diverse emission colour.

Introduction of one cyclometallating ligand alongside tpy, as in the case of **70** and **71**, does not favourably affect the emission properties; indeed, these complexes display only very weak emission, on the order of $\phi = <10^{-4}$.[90] DFT calculations reveal that the metal character of the lowest energy excited state is not significantly increased; the HOMO is localised on the N^C^N ligand with a small contribution from the metal and the LUMO is localised on the N^N^N ligand, again with a small contribution from the metal.[90] As discussed in previous sections, given the small contribution of metal character to the excited state, the radiative rate constant k_r is expected to be small.

The introduction of a second cyclometallating carbon atom, as seen for complexes **72** and **73**, increases the PLQY appreciably. These complexes, with a *cis* arrangement of the cyclometallating carbons in *different* ligands, have PLQYs of 0.023 (**73**) and 0.063 (**72**). An interesting difference in such complexes emerges, according to whether the carbon atoms are mutually *cis* or *trans* to one another. In the case of complexes containing *trans* cyclometallated carbons within the *same* ligand, such as complexes **79** and **80** (Figure 2.32),

we observe a decrease in the radiative rate constant by at least an order of magnitude, giving rather small radiative rate constants on the order of 10^4 s^{-1}. This difference is again explained by DFT calculations, showing that the *cis* complex HOMO and LUMO has some contribution from the metal whereas in the *trans* complex the HOMO and LUMO are located on the ligands. Despite this difference in radiative rate constant, the PLQYs of the two classes remain remarkedly similar, presumably because the non-radiative decay constants increase by a roughly comparable factor.[90]

The introduction of a third anionic ligand into the coordination sphere has a dramatic effect on the PLQY, giving a uniformly beneficial effect. This effect can primarily be attributed to the increase in radiative rate constant k_r.[90] The PLQYs of such complexes exceed 0.2 in almost all cases.

Bernhard and co-workers reported the related homoleptic complex $[Ir(phbpy)_2]^+$ (**81**, Figure 2.33), which has a similar coordination environment to that of the highly versatile $[Ir(C^N)_2(N^N)]^+$ (**82**, Figure 2.33).[99] Complex **81** has an increased excited-state lifetime (τ) of 548 ns compared to the 385 ns lifetime of complex **82**; this longer lifetime is attributed to the increased rigidity of complex **81**. It is interesting to note that the deviation from octahedral geometry resulting from the use of the tridentate ligand in complex **81** lowers the PLQY (ϕ = 3.9%) from that of complex **82** (ϕ = 7.3%).

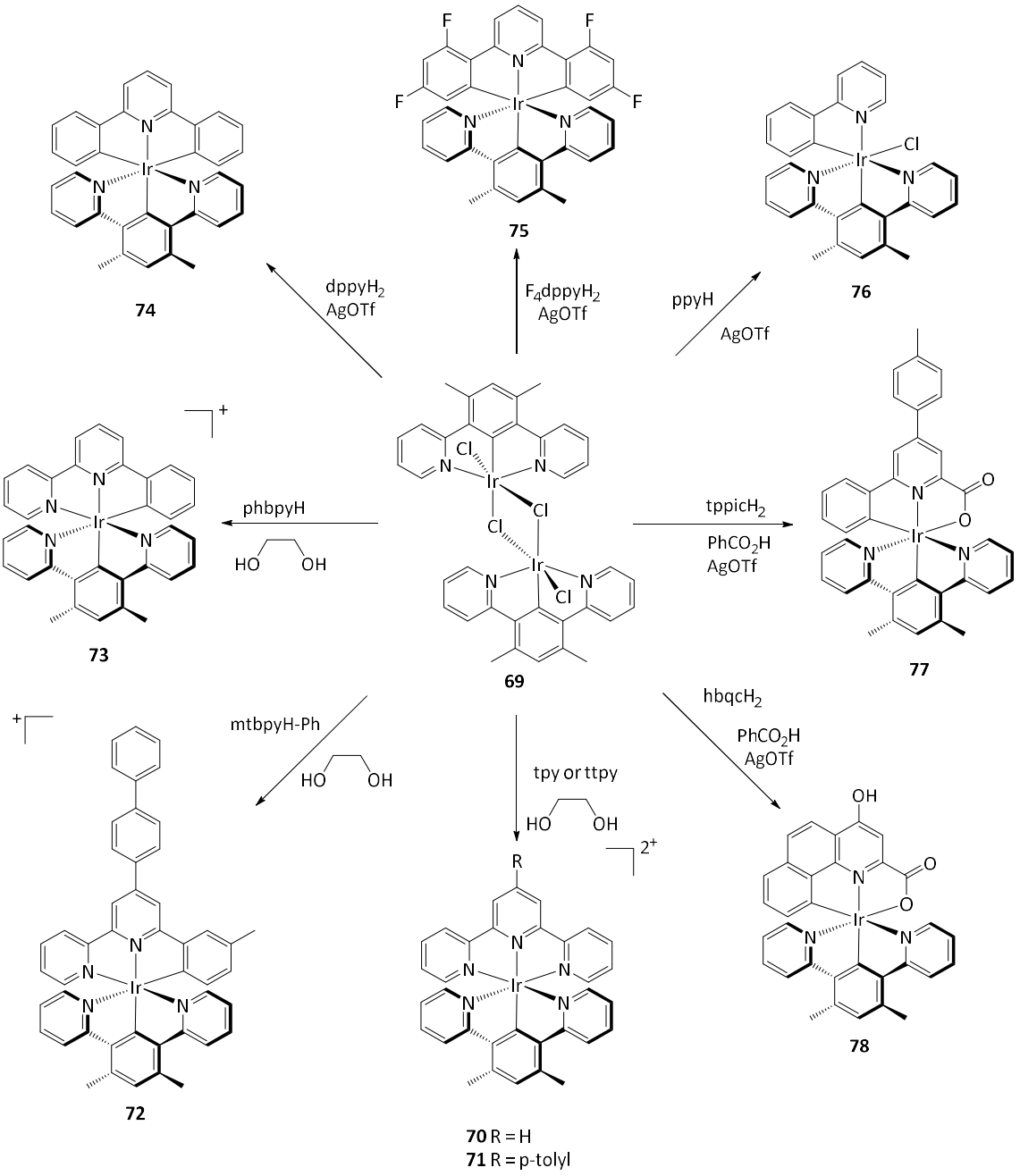

Scheme 2.2: Structures of a range of Ir(III) complexes containing the N^C^N-bound dpyx ligand.

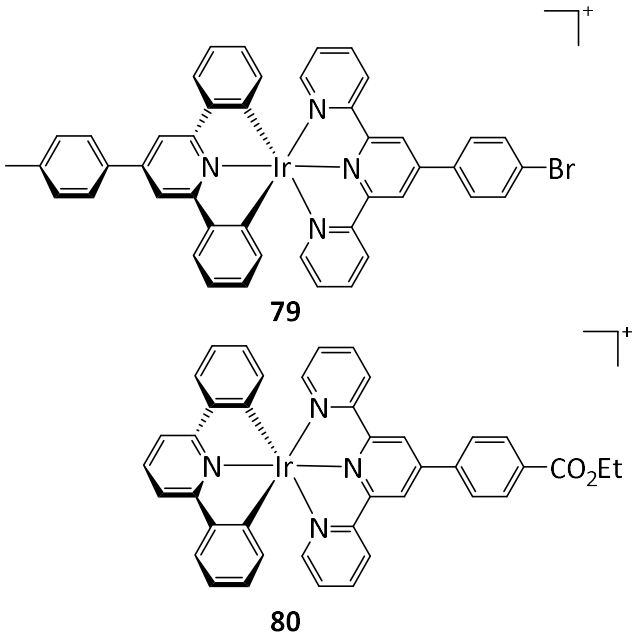

79

80

Figure 2.32: Examples of trans bis-cyclometallated complexes containing the C^N^C-coordinating ligand, 2,6-diphenylpyridine (bottom) or one of its derivatives (top).

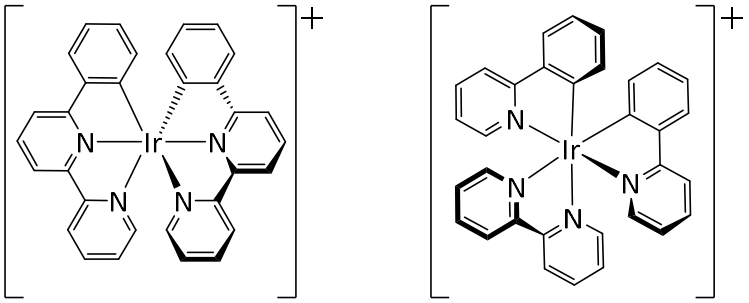

81

82

Figure 2.33: $[Ir(phbpy)_2]^+$ and the related $[Ir(ppy)_2(bpy)]^+$.

2.6 Concluding Remarks

In conclusion, this review has sought to highlight the factors that influence the excited state energies of luminescent Pt(II) and Ir(III) complexes. The continued design and development of these complexes has shown the importance of radiative decay versus non-radiative decay. Ligand design plays a crucial role in controlling the excited state properties and new synthetic strategies will play an increasingly valuable role. Cyclometallating chelates have shown considerable promise in the assembly of luminescent metal complexes and provide a promising route to achieving high PLQYs across a broad spectrum of emission wavelengths.

3 Synthesis of Mononuclear Pt(II) and Ir(III) complexes

3.1 Background and objectives of the work

In the field of luminescent Pt(II) complexes, it has been found that tri-/tetradentate ligands can sometimes offer advantages over bidentate analogues in that they rigidify the square-planar Pt(II) complexes, reducing non-radiative excited-state decay and thus enhancing luminescence.[100] Bidentate complexes can undergo a distortion from square planar towards tetrahedral in the excited state, a process not open to a complex with a tri/tetradentate ligand. However, the synthesis of such multidentate ligands is often arduous, relying on costly metallo-organic precursors, Pd(0) catalysts, and extensive column chromatography.[52]

As discussed in Chapter 2, anionic, tridentate proligands such as 1,3-di(2-pyridyl)benzene (dpybH) have been shown to form complexes with outstanding luminescence efficiencies – the Pt(II) complexes of these ligands are amongst the brightest platinum emitters known.[52] In contrast to Pt(II), Ir(III) binds to dpybH at the C_4 position, giving bidentate coordination (Figure 3.1). Appropriate ligand modification must be used to block this reaction and direct the metalation to the C_2 position to give N^C^N coordination.[52]

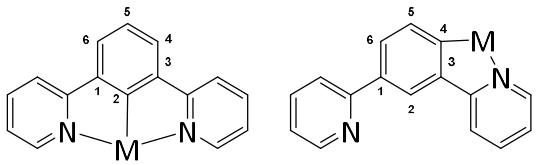

Figure 3.1: N^C^N and N^C binding modes of dpybH.

The combination of σ-donating nitrogen atoms and π-accepting heterocycles leads to relatively low energy charge-transfer (CT) states and thus helps to ensure these complexes absorb and emit in the visible region. The closely related N^N^C-binding ligand 6-phenyl-2,2'-bipyridine (phbpyH) also shares these properties but the different position of the cyclometallating phenyl ring can lead to significant differences in coordination chemistry and properties.

The work presented in this chapter focuses on the quest for highly luminescent Pt(II) and Ir(III) complexes using tridentate ligands that are more readily synthesised. We have developed a series of ligands which retain the key desirable features of dpybH and phbpyH

(imparting rigidity on resulting complexes) but removes the need for cross coupling in their formation. We have also included pseudo-cyclometallating units in order to retain the favourable properties whilst dispensing of the need for the harsh conditions required for cyclometallation (Figure 3.2).

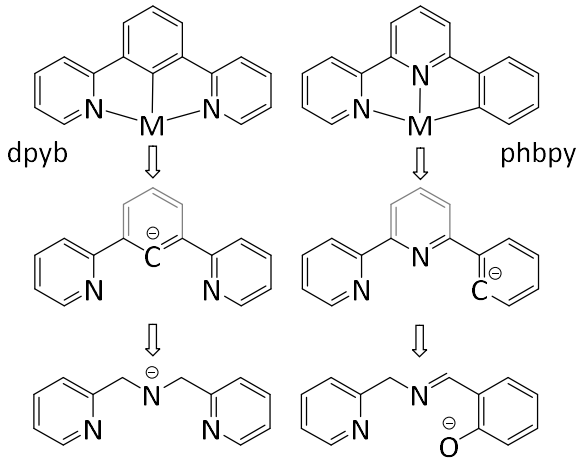

Figure 3.2: The conceptual link between dpyb and phbpy ligands and those reported in this chapter offering an anion N^N$^-$^N and N^N^O$^-$ donor set.

We have also explored tetradentate analogues of some of these tridentate ligands. As discussed in chapter 2, an increasing number of complexes with tetradentate ligands in the literature have shown greatly increased emission efficiencies, probably owing to the greater rigidity.[53] It is also well reported that the chloride ligand in tridentate Pt(II) complexes is somewhat labile and can be replaced with other ligands.[53] This may call into question the nature of these complexes in solution, especially in coordinating solvents.

3.2 Synthesis of tridentate ligands

3.2.1 N^N^O ligands

Imine-based N^N^O Ligands

Since their discovery by Hugo Schiff in 1864[101], Schiff bases have been extensively studied as an important class of ligands for metal coordination, with ligands based on the famous tetradentate proligand N,N'-bis(salicylidene)-1,2-ethylenediamine (H_2Salen) having been studied in a number of research areas (Figure 3.3).[102] Such ligands feature a combination of imine nitrogen and phenolic oxygen donors. However, study of this important class of ligands remains surprisingly limited in terms of excited state chemistry.[103] The small amount of research that has examined Schiff base complexes for

photochemical applications[102–108] has largely focused on complexes of the H_2Salen parent ligand and its analogues.

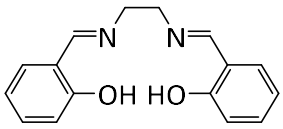

Figure 3.3: Proligand H_2Salen.

Schiff bases are formed by a condensation reaction between an aldehyde and a primary amine, requiring very mild conditions and no catalysis. Imine formation is traditionally carried out in an anhydrous organic solvent, which helps to push the equilibrium towards the condensation product.[109]

We sought to prepare new proligands offering an N^N^O^- coordination set, in which the central N atom would be an imine. Such ligands can be considered analogues of N^N^C^- cyclometallation ligands such as phbpy, but their synthesis should be achievable through Schiff base chemistry rather than requiring C-C bonding forming cross-coupling. Preparation of proligands HL^1, HL^2 and HL^4 have been described previously.[110,111] The synthetic route to HL^1 – HL^4 is depicted in Scheme 3.1. The proligands were prepared in the absence of solvent using a 'melt'. The aldehyde and amine were mixed and heated with stirring to 65°C under vacuum and the reaction progress was monitored by ^{1}H NMR; a near unity conversion was observed. Due to the sensitivity of the product to hydrolysis, the ligands were used directly for complexation without any formal isolation or characterisation.

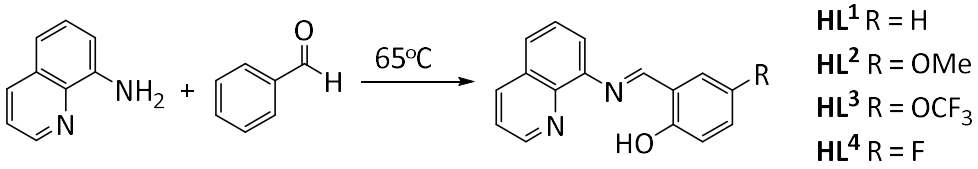

Scheme 3.1: Synthetic route to Imine bridged N^N^O^- proligands HL^1-HL^4.

Hydrazone-based N^N^O Ligands

Given the susceptibility of the imine-based N^N^O proligands to hydrolysis, we reasoned that a hydrazone linker might offer an attractive alternative to generate a more hydrolytically stable analogue (Scheme 3.2). Preparation of proligands HL^5 and some of its derivatives have been reported previously.[112] The synthetic routes to HL^5 – HL^{13} are

depicted in Scheme 3.2. The ligand precursor, 2-hydrazinopyridine, was prepared in an 85% yield by refluxing 2-bromopyridine and hydrazine hydrate to yield a pale orange solid. The proligand, HL^5, was prepared by reaction of the precursor and salicyladehyde, in methanol, at reflux for 30 minutes. A wide number of substitutions can be made on the phenol; the series of ligands HL^6 to HL^{13} were prepared in the same way as HL^5, using the appropriate salicylaldehyde. The reaction invariably produces a fine powder which can be isolated in good yield by filtration without need for further purification.

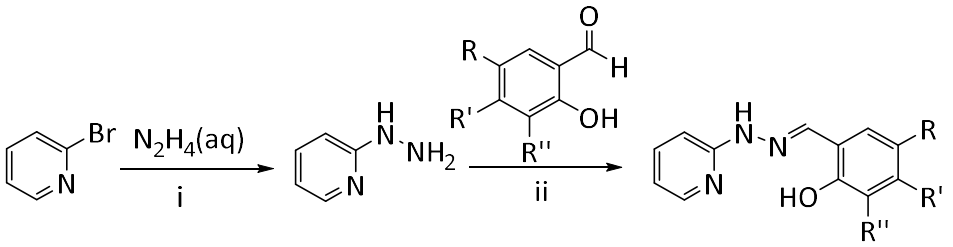

HL^5 R,R',R'' = H (82%)
HL^6 R' = Me, R, R'' = H (61%)
HL^7 R, R'' = Cl, R' = H (89%)
HL^8 R = NO_2, R', R'' = H (79%)
HL^9 R = F, R', R'' = H (51%)
HL^{10} R = Cl, R', R'' = H (70%)
HL^{11} R' = OH, R, R'' = H (44%)
HL^{12} R = OMe, R', R'' = H (58%)

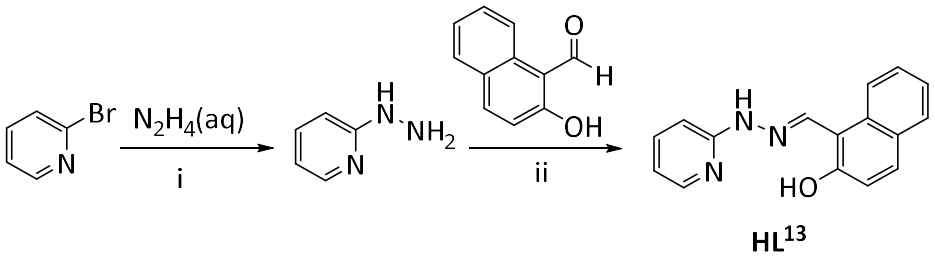

HL^{13}

Scheme 3.2: Synthetic routes to hydrazone bridged N^N^O ligands, HL^6-HL^{13}. Conditions: (i) 110°C, 4 h; (ii) 70°C, MeOH, 1 h.

Condensation of a hydrazine and an aldehyde results in a significant upfield shift of the N=C-H proton in the ^{1}H NMR spectra. For instance, the O=C-H proton in salicylaldehyde has a chemical shift of 9.89 ppm (in $CDCl_3$), while the N=C-H proton in HL^5 has a shift of 7.94 ppm (in $CDCl_3$). The aromatic protons and the phenolic proton are largely unaffected.

Crystals of HL^5 were obtained by slow evaporation of the methanol filtrates from the reaction (Figure 3.4). The structure obtained confirms the identity of the compound; interestingly there is hydrogen bonding within the molecules (N3–H1, 1.904 Å) and to

neighbouring molecules (N1–H2, 2.185 Å) but the packing adopted by this molecule shows no evidence of π-π interactions between the sheets.[113]

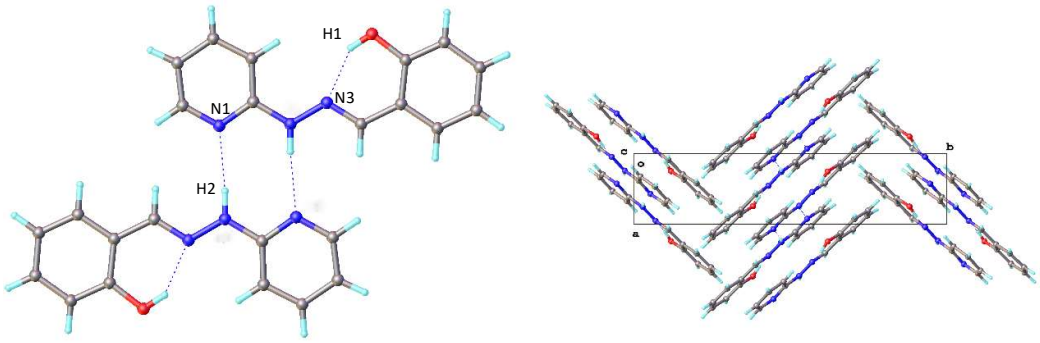

Figure 3.4: Crystal structure and illustration of the packing adopted by HL[5]. Crystallised from MeOH. T = 120 K.

We have also explored the replacement of the N-H functionality with a N-Me moiety (Scheme 3.3). The ligand precursor, 2-(1-methylhydrazinyl)pyridine is prepared in an analogous manner to 2-hydrazinopyridine, by refluxing 2-bromopyridine and methylhydrazine. The resulting yellow oil was used to prepare proligand HL[14] by reaction with salicylaldehyde. Again, a range of substitutions can be made on the phenol by employing different salicylaldehydes. In this case, we also prepared some derivatives incorporating different substituents on the pyridine ring by preparing the appropriate pyridylhydrazines.

Condensation of a methylhydrazine and an aldehyde again results in a significant upfield shift of the N=C-H proton in the ^{1}H NMR spectra. For instance, in HL[14] this proton resonates at 7.80 ppm in $CDCl_3$ compared to 9.89 ppm for salicylaldehyde. The aromatic and phenolic protons are largely unaffected nor is there a significant shift of the N-Me protons.

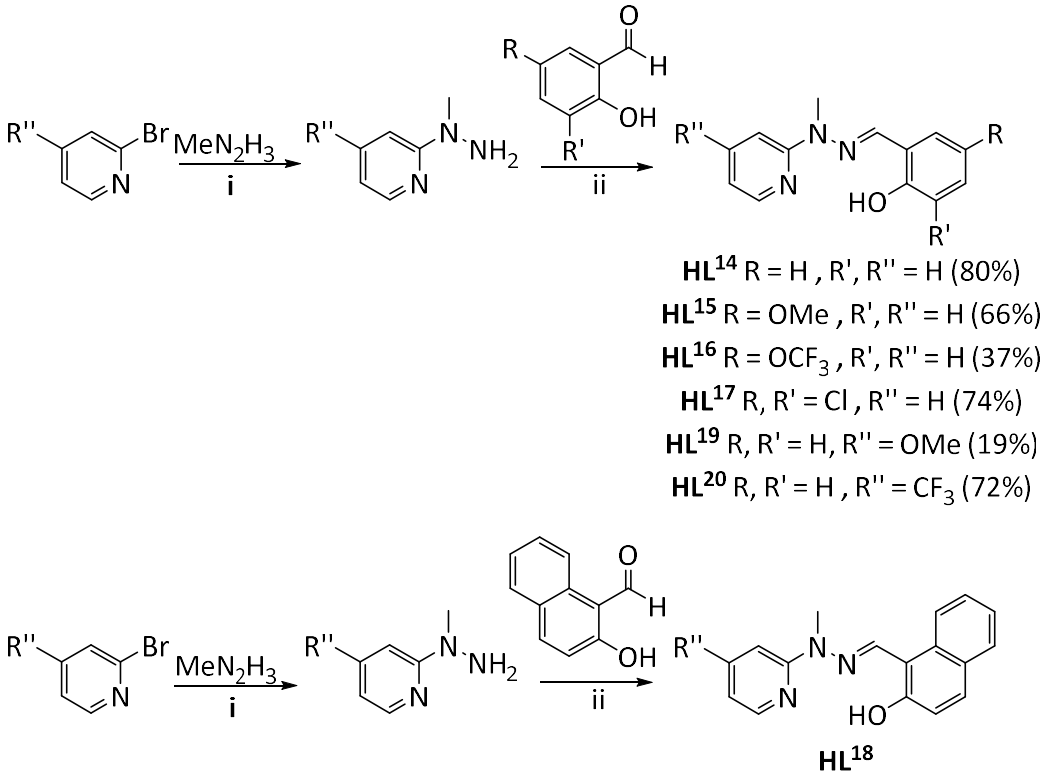

Scheme 3.3: Synthetic routes to h*ydrazone N-Me bridged N^N^O ligands, HL[14]-HL[20].*

Conditions: (i) 110°C, 4 h; (ii) 70°C, MeOH, 1 h.

Pyrazole Based N^N^O Ligand

The N-N=C unit of the above proligand is reminiscent of part of a pyrazole ring. In order to explore the effect of rigidification of this part of the structures the pyrazole-based proligand HL[21] (Figure 3.5) was targeted.

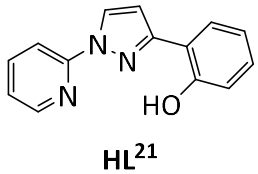

Figure 3.5: Pyrazole bridged N^N^O ligand, HL[21].

In order to synthesise HL[23], we first prepared the intermediate 3-(dimethylamino)-1-(2-hydroxyphenyl)prop-2-enone (Scheme 3.4, **a**) by replicating the synthesises reported by Li *et al.*[114] 2-Hydroxyacetophenone and N,N-dimethylformamide dimethyl acetal (DMFDMA) were heated to 70°C in DMF for 30 minutes. The desired product 'a' was obtained by precipitation from saturated brine.

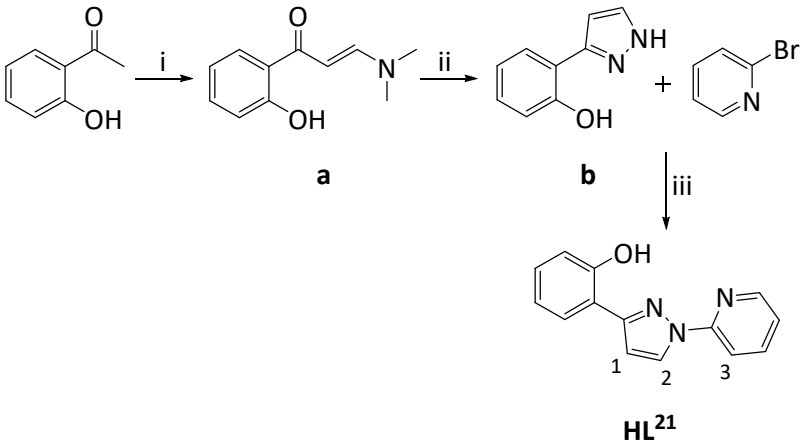

HL[21]

Scheme 3.4: Synthetic route to HL[21]. Conditions: (i) DMFDMA, DMF, 75°C, 30 min; (ii) $N_2H_4.H_2O$, EtOH, reflux, 6 h; (iii) CuI, trans-1,2-diaminocyclohexane, K_2CO_3, 1,4-dioxane, reflux, 24 h

Intermediate **b** was then synthesised by replicating the synthesis reported by Seubert *et al.*[115] Hydrazine monohydrate and intermediate **a** were dissolved in ethanol and refluxed for 6 hours to afford the pure product after work up in a 62% yield.

Proligand HL^{21} was subsequently obtained from 'b' by using the general conditions for the copper-diamine catalysed N-arylation of pyrazoles reported by Buchwald and co-workers.[116] A mixture of intermediate 'b' (1.0 equiv), 2-bromopyridine (1.2 equiv), trans-1.2-cyclohexanediamine (20 mol%), CuI (5 mol%) and K_2CO_3 (2.1 equiv) in anhydrous 1,4-dioxane was degassed via 3 freeze-pump-thaw cycles before being refluxed for a period of 24 hours. The reaction gave HL^{21} in a 55% yield. As observed by Buchwald and co-workers,[116] the reaction selectively forms the product in which the less hindered nitrogen is arylated. The ^1H and ^{13}C NMR study of the structure of pyrazoles reported by Yranzo and co-workers makes the identification of the H^1 and H^2 trivial (refer to Scheme 3.4 for numbering); H^2 is consistently downfield from H^1.[117] ^1H-^1H NOESY is useful for determining which protons are close to each other in space rather than through bonds; the NOESY spectrum shows a correlation between H^2 and H^3 confirming arylation of the less hindered nitrogen.

3.2.2 N^N^N ligands

Due to the higher QYs typically exhibited by N^C^N-coordinated dpyb complexes compared to their N^N^C-coordinated phbpy analogues, we were eager to explore closely related ligands which offered a central position for the anionic ligating atom.

Hydrazide-based N^N^N Ligands

2-Picolinoylhydrazides which possess a coordinating substituent at the C(imine) atom (Scheme 3.5) could be promising candidates for the design of N^N$^-$^N ligands, with a number of different donor atoms in the molecule. The ligand synthesis has been described previously.[118] The commercially available ethyl 2-picolinate was completely converted into the intermediate 2-picolylhydrazine 'a' by refluxing with hydrazine monohydrate in ethanol. HL^{22} was then synthesised by the reaction of equimolar amounts of 2-picolylhydrazine and 2-pyridine carboxaldehyde in methanol at reflux for 2 hours before cooling to ambient temperature. The product was unsuitable for separation by column chromatography due to streaking of the compound but successive recrystallization from DCM/Hexane afforded the target compound in a 44% yield.

There are two possible isomers of the proligand HL^{22}, the *E* and Z forms. These isomers are expected to have different capabilities for binding to metals, owing to the relative arrangement of the donor atoms; the Z-form is able to bind in the desired tridentate fashion. As previously reported by Hecht and co-workers, the reaction invariably produces the highly pure E-isomer.[118] Compounds containing a carbon-nitrogen C=N double bond may undergo photochemical and thermal *cis-trans* isomerisation;[119] we anticipate this isomerisation will occur during complexation of the proligand.

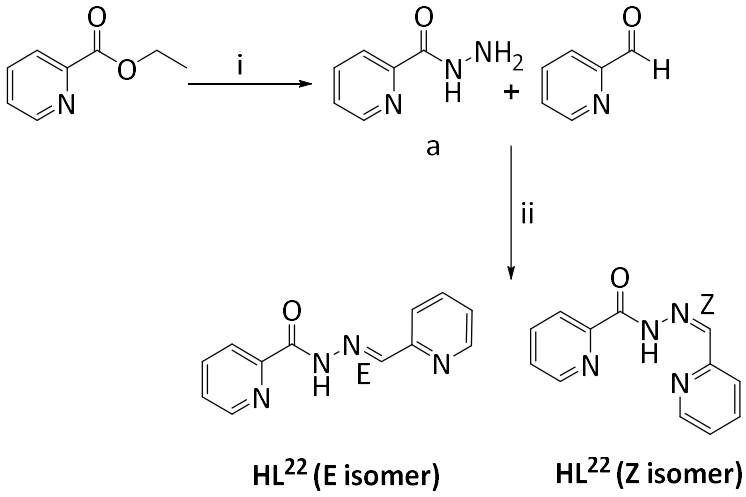

Scheme 3.5: Synthesis of hydrazide-based N^N^N proligand, HL^{22}. Conditions:(i) N_2H_4, EtOH, reflux, 12 h; (ii) MeOH, reflux, 2 h.

Imide and Amide-based Ligands

In order to further explore the possibility of N^N$^-$^N ligands without the conformational ambiguity of E/Z isomers, we turned our attention to the synthesis of both imide and amide ligands (Figure 3.6).

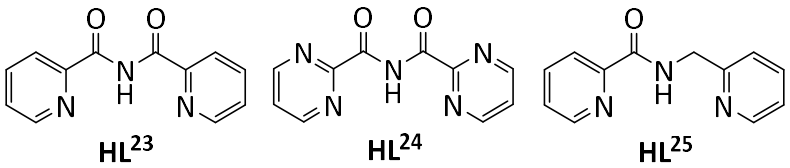

Figure 3.6: Imide and Amide based N^N^N ligands, HL^{23} – HL^{25}

The first structurally characterised imide complex was reported in 1976 by Lerner and Lippard.[120] Since then, many studies have focused on imide coordination chemistry with the ligand bis(2-pyridylcarbonyl)amide (Hbpca, HL^{23}) and related ligands such as Hbpcam (HL^{24}) for applications such as; catalysts for the reduction of carbon dioxide, building blocks for the construction of single molecule magnets and to generate polymeric complexes with interesting structural features including ladders, helicates and clusters.[121121,122] As noted for hydrazide bridged ligands, there are a number of different donor atoms in the molecule allowing for some interesting coordination chemistry.

HL^{23} and HL^{24} were originally obtained as unexpected products of metal-catalysed hydrolysis of 2,4,6-tris(2-pyridyl)-1,3,4-triazine (tpyt) and its pyrimidine analogue (tpymt) (Scheme 3.6).

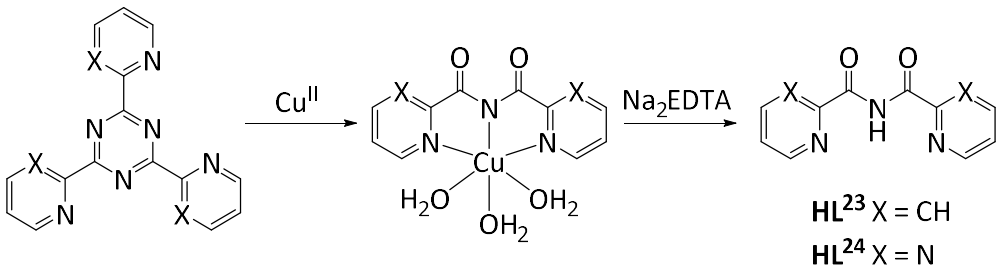

Scheme 3.6: Route by which HL^{25} and HL^{26} were originally obtained.

Tpyt is easy readily obtained from commercial sources but this is not the case for the pyrimidine analogue, tpymt. The first reported synthesis of tpymt (X = N) was by Case and Koft in 1959, with a yield of less than 6% on standing of 2-cyanopyrimidine for several months.[123] This disappointing result prevented extensive studies of this ligand until much later, when in 1976 Lerner and Lippard reported a crude yield of 84% by the trimerization of 2-cyanopyrimidine.[120] The pyrimidine was heated in a sealed vessel at 150°C for 48 h;

the solidified product was then ground to a fine powder and washed with ether to remove any unreacted starting material. A laborious purification followed, reducing the yield to 65%. We replicated this synthesis with great success, the trimerization proceeded with a yield of 80% and after washing with ether the crude material was of sufficient purity that no further purification was required.

Although tpyt and tpymt are stable in boiling water and hydrochloric acid, their hydrolysis is extensively promoted by Cu^{II} salts resulting in the formation of copper complexes of HL^{25} and HL^{26}. $Cu(NO_3)_2.3H_2O$ is added to a suspension of tpyt or tpymt in water and the resulting green slurry is refluxed for a period of two hours. Slow evaporation of the solvent results in bright blue, needle like crystals. The free ligand can then be isolated by treating the Cu^{II} complexes with Na_2EDTA to scavenge the metal. On examination of the crystal structures of the Cu^{II} complexes, it was initially proposed that coordination causes an angular strain which allows nucleophilic attack at the carbon atoms of the triazine ring by water resulting in hydrolysis.[124] However, a later study coordinated tpyt to rhodium(III) and ruthenium(II) but only the Ru(II) complex generated the hydrolysis product despite the angular strain being comparable in across the Cu(II), Ru(II) and Rh(III) complexes. These results allowed further investigation into the nature of the hydrolysis and established that an electron-withdrawing effect was the major factor responsible for metal ion promoted hydrolysis.[122]

The synthesis of the amide bridged ligand HL^{25} has been reported previously.[125] The synthetic route to HL^{25} is depicted in Scheme 3.7. Ethyl 2-picolinate and 2-picolylamine were dissolved in anhydrous 1,4-dioxane and heated in a microwave reactor at 180°C for 1 hour. The crude material was extracted into DCM and purified by column chromatography to give the desired product in a 45% yield.

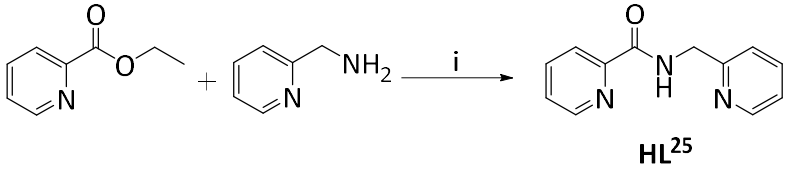

HL^{25}

Scheme 3.7: Synthetic route to HL^{25}. Conditions: (i) 1,4-dioxane, MW 180°C, 1 h.

3.3 Synthesis of tetradentate ligands

3.3.1 C^N^N^O ligands

Hydrazone-based Ligands

Due to the readily synthesised nature and the ease of substitution around the heterocyclic rings of the hydrazone bridged ligands discussed in section 3.2.1, we chose to extend this system into a series of tetradentate proligands (Figure 3.7). HL^{26} and HL^{27} offer a C^N^N^O^- coordination set, whilst HL^{28} is isomeric with HL^{26}, giving a N^C^N^O^- coordination set.

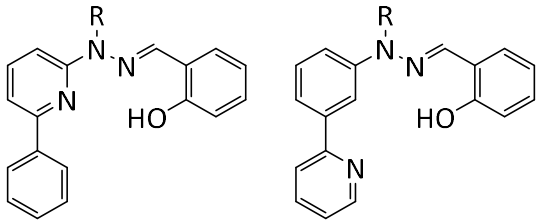

HL^{26} R = H **HL^{28} R = H**
HL^{27} R = Me

Figure 3.7: Hydrazone bridged tetradentate ligands HL^{26}-HL^{28}

The synthesis of proligands HL^{26} and HL^{27} proved to be relatively straightforward due to the activated nature of the 2- and 4- positions of a pyridine towards nucleophilic substitution (Scheme 3.8).[126] This allows a hydrazine unit to be readily installed into the pyridine ring of the phenyl pyridine precursor.

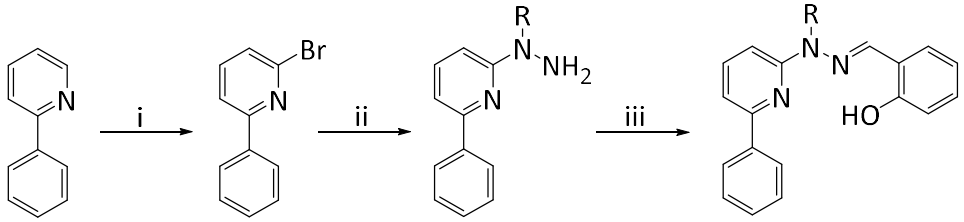

Scheme 3.8: Synthetic route for HL^{26} and HL^{27}. R = H or Me. Conditions: (i) BuLi-LiDMAE, CBr_4, hexane, 0°C; (ii) N_2H_4 (R = H) or MeN_2H_3 (R = Me), reflux, 22 h; (iii) salicylaldehyde, methanol, 70°C, 5 h.

The synthesis of proligands HL^{26} and HL^{27} is a multistep procedure, beginning with the commercially available 2-phenyl pyridine. We successfully replicated the synthesis reported by Gros *et al.*,[127] by halogenating the commercially available 2-phenylpyridine, beginning with lithiation with BuLi-LIDMAE in hexane at 0°C and then carried out condensation with the electrophile CBr_4 to give the desired 2-bromo-6-phenylpyridine.

Column chromatography successfully isolated the pure product in a 62% yield. 2-bromo-6-phenylpyridine was then converted to the desired ligands HL^{26} and HL^{27} in the same manner as the analogous tridentate proligands.

The proligand HL^{28} proved much more synthetically challenging due to the unreactive nature of the benzene ring towards nucleophilic substitution.[126] Unlike HL^{26} and HL^{27}, the hydrazine intermediate cannot be formed by simple nucleophilic substitution on a bromobenzene. We initially proposed the synthetic route outlined in Scheme 3.9.

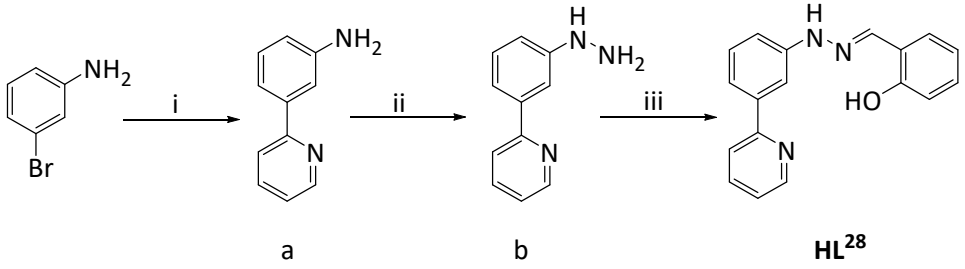

Scheme 3.9: Proposed synthetic route for HL^{28}. Conditions: (i) LiCl, 3-bromoaniline, 2-(tributylstannyl)pyridine, $Pd(PPh_3)_4$, toluene, reflux, 24 h; (ii) $NaNO_2$, HCl, $SnCl_2$, H_2O, 0°C, 1 h; (iii) salicylaldehyde, methanol, 70°C, 5 h.

We successfully synthesised intermediate 'a', 3-(2-pyridinyl)benzenamine, using Stille cross coupling conditions. A mixture of LiCl, 3-bromoaniline, 2-(tributylstannyl)pyridine and $Pd(PPh_3)_4$ in toluene was degassed via 3 freeze-pump-thaw cycles and then refluxed under an inert atmosphere for 48 hours. The crude product was purified by column chromatography which yielded the desired product in an 80% yield.

We next attempted to form the hydrazine intermediate 'b' via diazotisation and reduction by $SnCl_2$ of the diazo intermediate, however we encountered difficulties with side products and instability of the product. This is perhaps somewhat unsurprising, since Lednicer and co-workers encountered similar difficulties when preparing polycyclic aromatic hydrazines via this procedure and there are few examples in the literature of these derivatives.[128]

In order to synthesise the desired ligand HL^{28} we instead proposed the alternative pathway in Scheme 3.10, in which the pyridine ring is incorporated in the last step and the diazotisation is carried out on 3-bromoaniline.

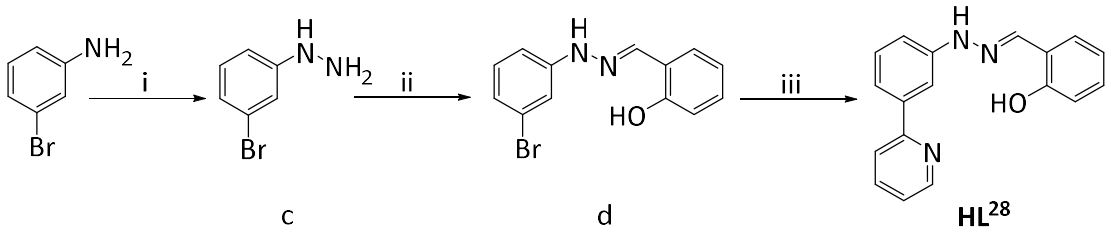

Scheme 3.10: Alternative synthesis of HL[28]. Conditions: (i) $NaNO_2$, HCl, $SnCl_2$, H_2O, 0°C, 1 h; (ii) salicylaldehyde, methanol, 70°C, 5 h; (iii) LiCl, 3-bromoaniline, 2-(tributylstannyl)pyridine, $Pd(PPh_3)_4$, toluene, reflux, 24 h.

The hydrazine intermediate 'c' was successfully synthesised although we did encounter some difficulties with product stability and so the crude material was used without further purification to form the hydrazone bridged intermediate 'd' in a 60% yield. HL[28] was then successfully synthesised using Stille cross coupling conditions, in the same manner as discussed previously, to give the purified product in a 19% yield.

Pyrazole-based Ligands

In order to further investigate the effects on rigidifying the ligand scaffold we turned our attention to extending the N^N^O pyrazole bridged proligand reported earlier into a tetradentate proligand of the type C^N^N^O (Figure 3.8).

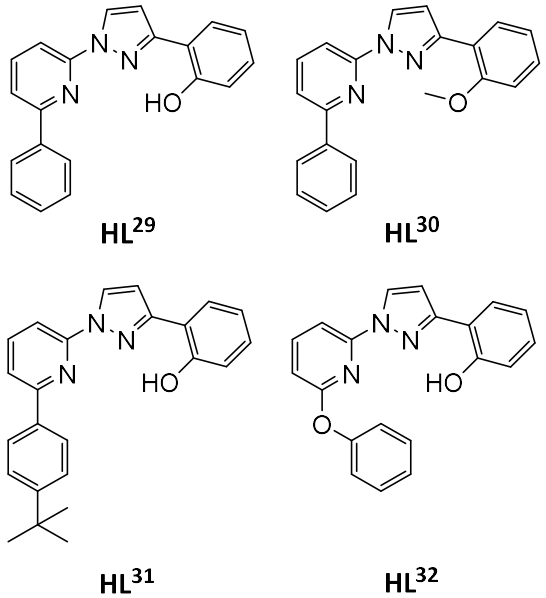

Figure 3.8: Pyrazole bridged ligands HL[29]-HL[32].

The synthesis of proligands HL^{29}-HL^{31} was achieved via the synthetic route depicted in Scheme 3.11. The appropriate pyrazole intermediate 'a' was prepared using the conditions reported by Develay *et al.*[129] (discussed in section 3.2.1) and the appropriate 2-bromo-6-phenyl pyridine analogue was prepared using the conditions reported by Gros *et al*.[127] (discussed earlier in this section).

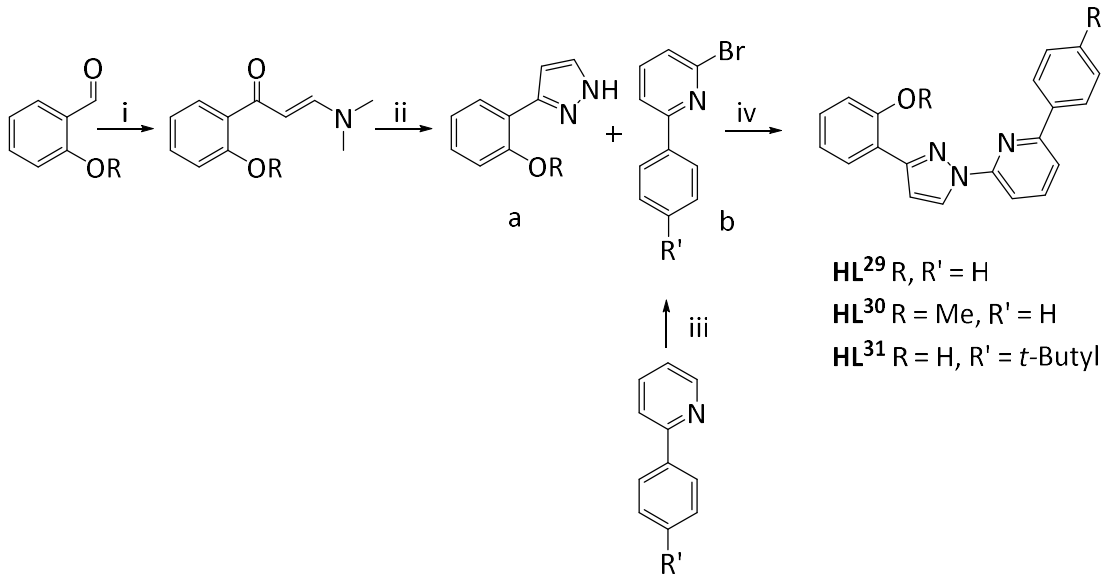

Scheme 3.11: Synthetic route for HL^{29} – HL^{30}. Conditions: (i) DMFDMA, DMF, 75°C, 30 min; (ii) $N_2H_4.H_2O$, EtOH, reflux, 6 h; (iii) BuLi-LIDMAE, CBr_4, hexane, 0°C; (iv) CuI, trans-1,2-diaminocyclohexane, K_2CO_3, 1,4-dioxane, reflux, 24 h.

For the synthesis of HL^{31}, the 2-bromo-6-tert-butyl pyridine starting material was not readily available. This was instead prepared from 2-bromopyridine and 4-tert-butylphenyl boronic acid using Suzuki cross-coupling conditions (Scheme 3.12). A mixture of 2-bromopyridine, 4-tert-butylphenylboronic acid, sodium carbonate and $Pd(PPh_3)_4$ in toluene/water/ethanol (4:4:1) was degassed via freeze-pump-thaw and refluxed for 24 hours. The crude product was purified by column chromatography to give the desired compound in a 90% yield.

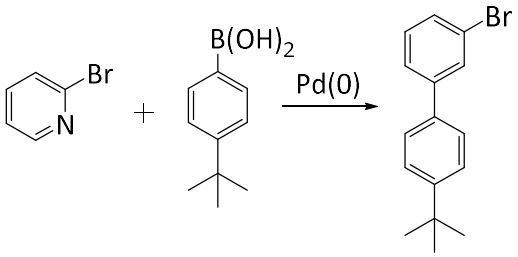

Scheme 3.12: Synthetic route to 2-bromo-6-tert-butyl pyridine.

Synthesis of proligand HL^{32} was achieved via a 2-bromo-6-phenoxypyridine intermediate 'b' (Scheme 3.13).

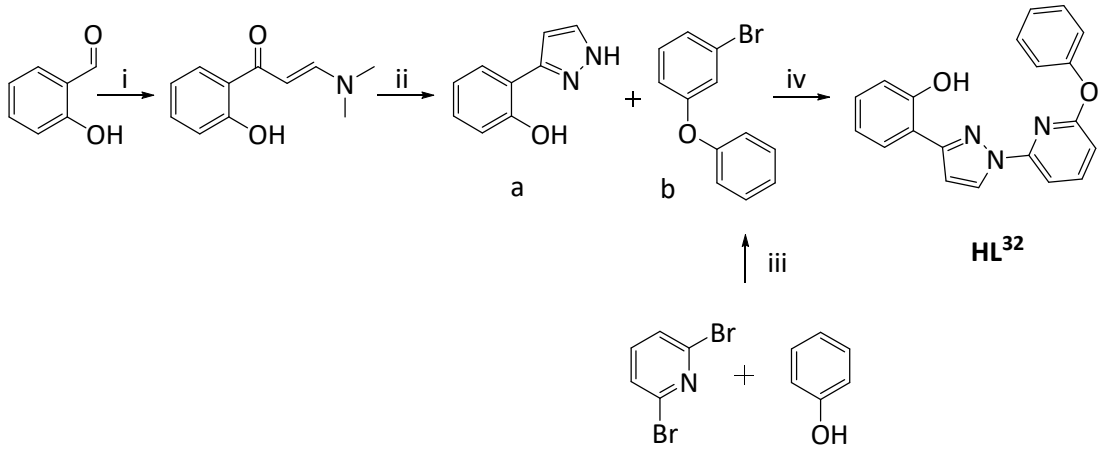

Scheme 3.13: Synthetic route for HL^{32}. (i) DMFDMA, DMF, 75°C, 30 min; (ii) $N_2H_4.H_2O$, EtOH, reflux, 6 h; (iii) NaH, DMF, 0 - 100°C, 12 h; (iv) CuI, trans-1,2-diaminocyclohexane, K_2CO_3, 1,4-dioxane, reflux, 24 h.

The 2-bromo-6-phenoxypyridine intermediate was prepared following the procedure reported by Arai *et al.*[130] A mixture of phenol (3 equivs.), NaH (3 equivs.) and DMF was stirred over ice for 10 minutes, before slow addition of a solution of 2,6-dibromopyridine (1 equiv.) in DMF. The solution was stirred overnight at 100°C before work up and purification to give the desired compound in an 89% yield.

The copper catalysed coupling of HL^{32} proceeded with relatively poor yields, a maximum yield of 30% was achieved. This is presumably due to the deactivating influence of the oxygen and the lower reactivity of bromo compared to iodo substrates.

Small crystals, suitable for X-ray diffraction, were obtained of HL^{29} and HL^{30} (Figure 3.9). The structures obtained confirm the identities of the compounds. Interestingly both structures contain antiparallel π-π linked dimers. In HL^{29} there is hydrogen bonding between the phenolic OH and the pyrazole N which is absent in HL^{30} (OMe in place of OH), this has resulted in a 180° rotation of the pyrazole.

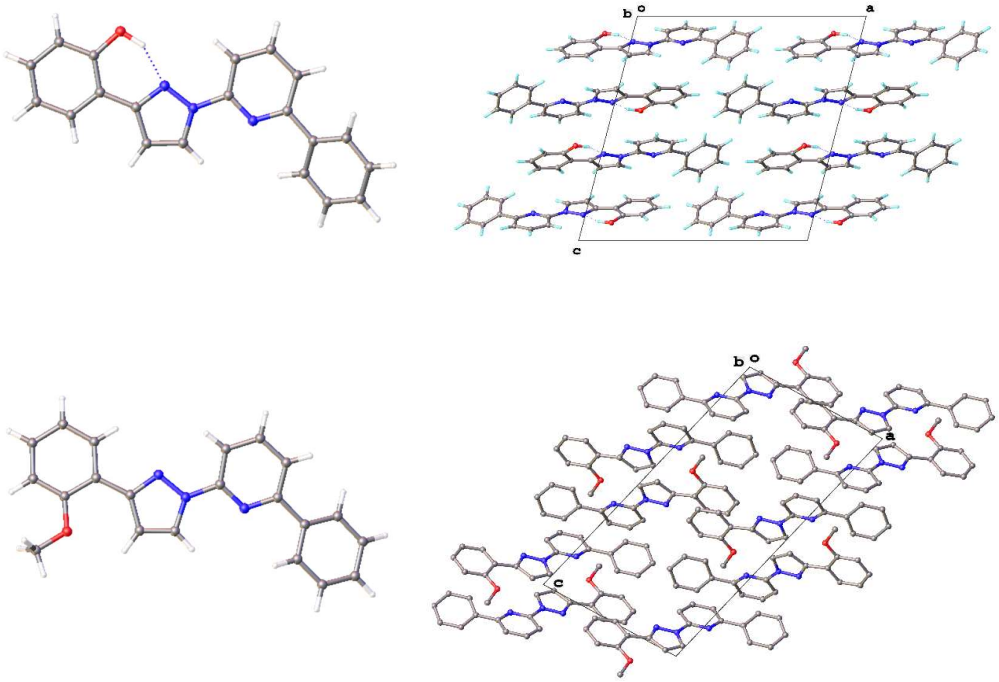

Figure 3.9: Crystal structure and packing of HL[29](above) and HL[30](below). T = 120 K.

3.3.2 C^N^N^N ligands

Again, due to the more favourable emission properties of dpybH complexes over phbpyH complexes we were eager to explore closely related ligands which offer a different position for the pseudo-cyclometallating atom whilst rigidifying the system into a tetradentate ligand.

Owing to the exciting properties of the hydrazine bridged ligands offering multiple coordination modes, we chose to extend this system into a tetradentate ligand. The ligand HL[33] was synthesised via the route shown in Scheme 3.14.

The intermediate ester, methyl-6-phenyl-2-pyridine carboxylate 'a', was synthesised by a Suzuki cross-coupling in 94% yield. The ester was then reacted with hydrazine monohydrate to give quantative conversion into the hydrazine intermediate. Finally, the hydrazine intermediate was reacted with an equimolar amount of 2-pyridine carboxyaldehyde to give a 17% yield of HL[33] after successive recrystallizations.

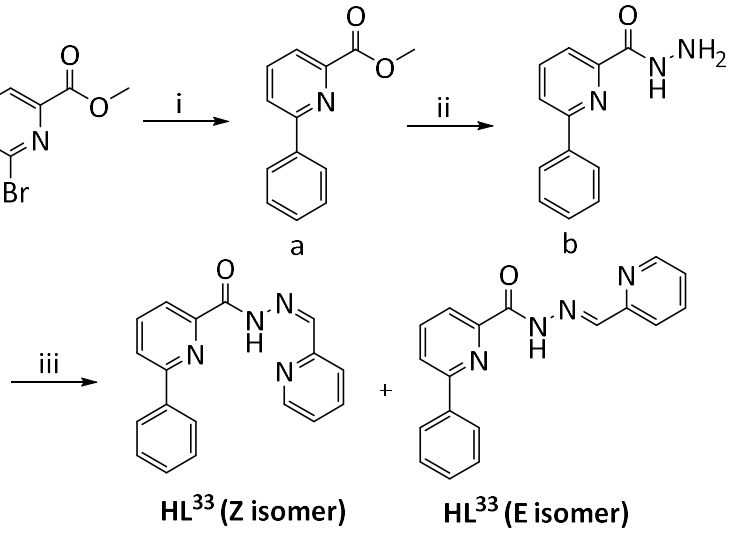

Scheme 3.14: Synthetic route to ligand HL^{33}.

^{1}H NMR of the isolated product showed the presence of both the Z- and E- isomer, in approximately a 3:1 (Z:E) mixture (Figure 3.10). Inspection of the ^{1}H NMR spectrum reveals the N-H proton in the Z isomer resonates at 15.97 ppm ($CDCl_3$) vs. 11.21 ppm ($CDCl_3$) in the E isomer. This behaviour observed for the related ligand quinoline-2-carbaldehyde (pyridine-2-carbonyl)-hydrazone reported by Mori *et al.*[131], a significant downfield chemical shift was observed for the N-H proton in the Z-isomer; a chemical shift of 16.76 ppm ($CDCl_3$) compared to 11.24 ppm in the E-isomer.

The Z and E isomer were successively separated using HPLC, although we were only able to obtain enough of the Z isomer for characterisation (Figure 3.11). These species can interconvert in solution; evidence of the E isomer beginning to form in the purified HL^{35} (Z isomer) sample was observed when the ^{1}H NMR spectra was collected again after one week standing in the presence of light.

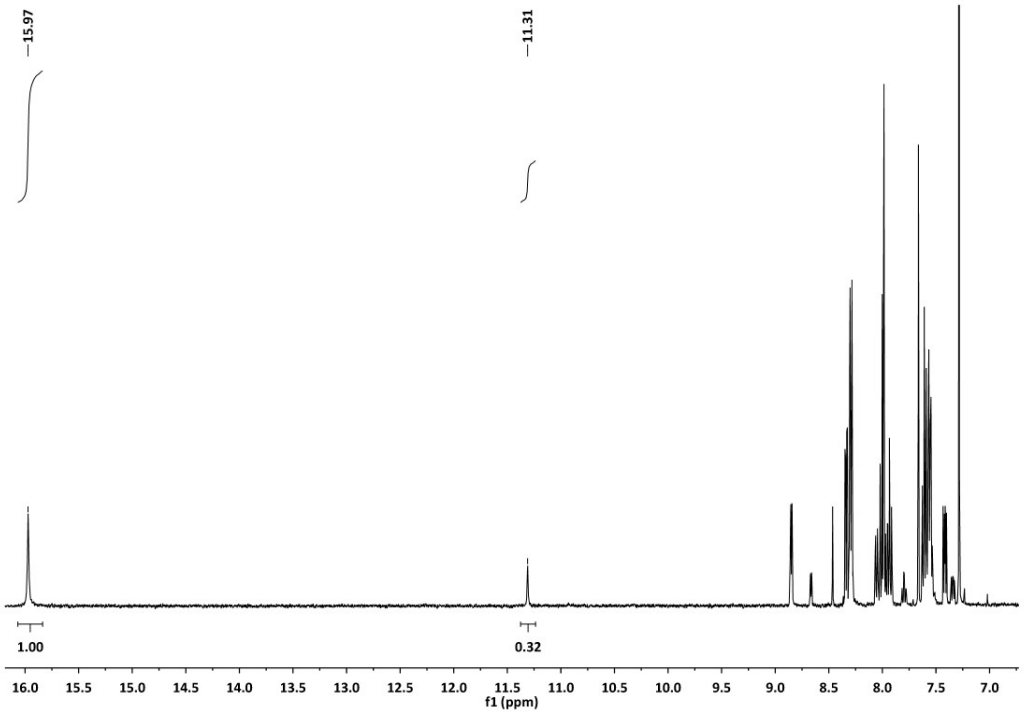

Figure 3.10: 400 MHz 298K ^{1}H NMR spectrum of the as-prepared HL^{33}showing a roughly 3:1 mixture of the Z and E isomers.

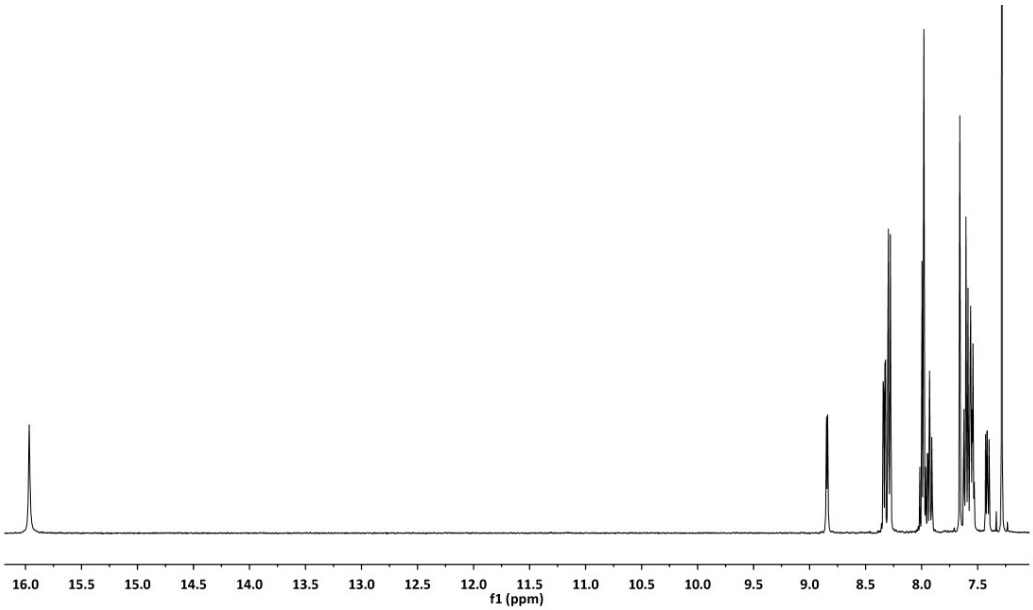

Figure 3.11: 400 MHz 298K ^{1}H NMR Spectrum of HL^{33} (Z isomer) in $CDCl_3$ separated from the mixture of isomers by HPLC.

3.4 Synthesis of Pt(II) complexes of Tridentate Ligands

3.4.1 Synthesis of N^N^O complexes

Imine-based Ligands

The Pt(II) complexes of ligands L^1-L^4 were all prepared by reaction of the corresponding proligands HL^1-HL^4 with dichloro(1,5-cyclooctadiene)platinum(II) ($Pt(COD)Cl_2$) (Figure 3.12).

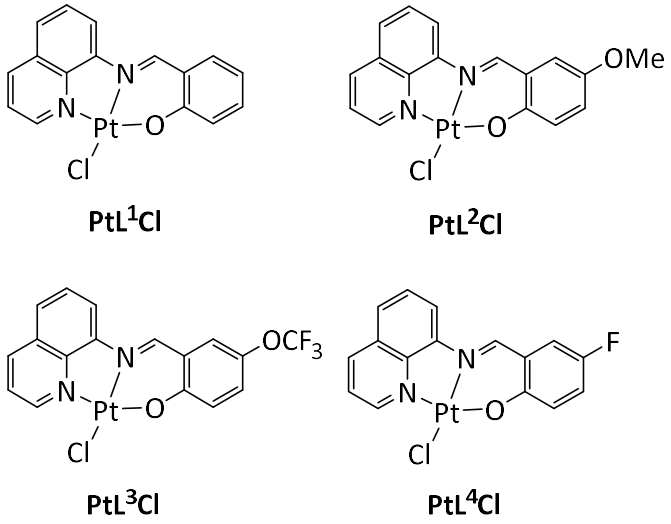

Figure 3.12: Pt(II) complexes of imine based N^N^O ligands.

$Pt(COD)Cl_2$ is widely used as an entry point to other Pt(II) complexes since the 1,5-cycloocatdiene moiety is readily displaced by other ligands.[132] $Pt(COD)Cl_2$ can be obtained from commercial sources but it is easily prepared within the laboratory from K_2PtCl_4 and 4 equivs. of 1,5-cyclooctadiene.[133]

Due to the susceptibility towards hydrolysis of the imine bridged N^N^O ligands, the complex was prepared directly from the corresponding crude proligand without any formal isolation. The ligands were prepared by a melt (as discussed in 3.2.1), after 2 hours under vacuum at 65°C the vessel was filled with argon and a mixture of $Pt(COD)Cl_2$, anhydrous NEt_3 (excess) and anhydrous acetonitrile was added. The mixture was refluxed overnight and the precipitated products were collected by filtration with no purification required.

The identity of the complexes was confirmed by ^1H and ^{13}C NMR spectroscopy and electrospray ionisation (ESI) mass spectrometry. Successful complexation of the ligand

showed the absence of the OH proton in the ^{1}H NMR spectrum and high-resolution mass spectrometry also confirmed the identity of the species.

Small crystals of PtL^{1}Cl suitable for X-ray diffraction, were obtained by slow evaporation of DCM (Figure 3.12). The structure contains one molecule of DCM per PtL^{1}Cl. A summary of important bond lengths and angles is shown in Table 3.1. PtL^{1}Cl shows a nearly planar environment around the Pt atom with only very slight twisting out of the plane (max displacement = 0.018 Å), in fact the whole molecule is essentially planar. The Pt-Cl bond is elongated with respect to the other bonds (2.3264(14) Å), the Pt-O and Pt-N(qui) bonds are approximately equal (1.992(4) and 1.998(5) Å, respectively) and the central Pt-N(imine) bond is somewhat shorter at 1.971(5) Å. Related species of the type [Pt(typ)Cl]$^{+}$ display a very similar structure: an elongated Pt-Cl bond (average 2.303 Å), Pt-N_{cis} bonds approximately equal at 2.02 Å and the Pt-N_{trans} being slightly shorter at 1.93 Å.

The PtL^{1}Cl molecules form pair-wise Pt···Pt interactions which leads to head-to-tail orientation of dimers with a short/long Pt···Pt distance of 3.600 and 5.618 Å, respectively. The interplanar separation between ligands for PtL^{1}Cl of 3.564 Å is sufficiently close for π-π interactions to occur.[113]

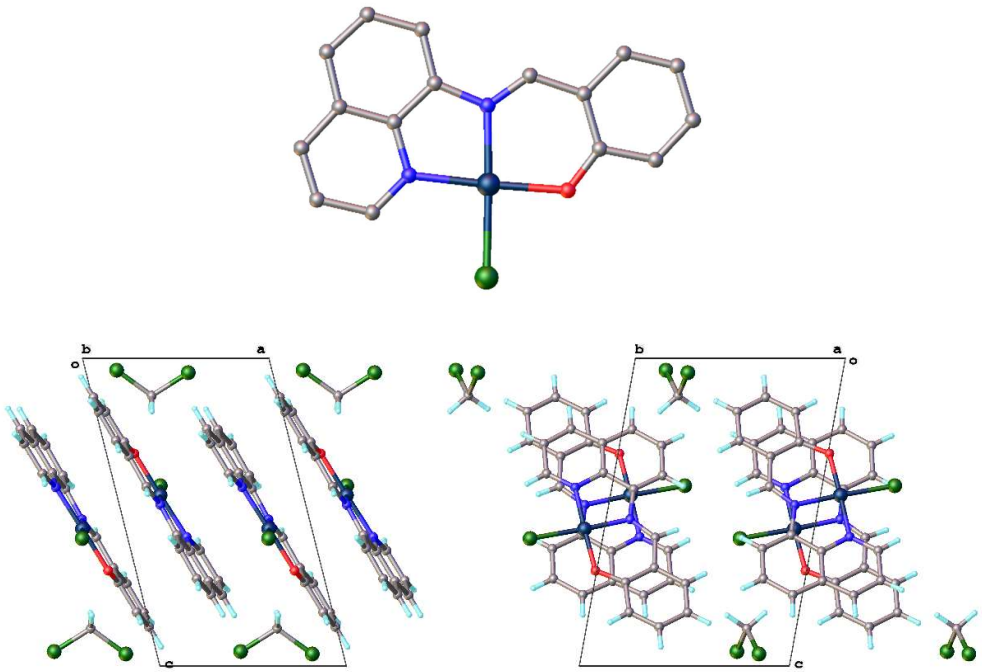

Figure 3.12: Crystal structure and packing of Pt(L^{1})Cl. T = 120 K.

Table 3.1: Selected bond lengths and bond angles for PtL[1]Cl.

Bond Lengths (Å)		*Bond Angles (°)*		*Distances (Å)*	
Pt-$N_{(qui)}$	1.998(5)	N-Pt-O	177.43(19)	Pt···Pt	3.600
Pt-$N_{(imine)}$	1.971(5)	N-Pt-Cl	178.12(15)	Pt···Pt	5.618
Pt-O	1.992(4)	N-Pt-N	82.8(2)		
Pt-Cl	2.3264(14)	N-Pt-O	94.85(18)		
C=N	1.299(7)				
C-N	1.433(7)				

Substitution of the chloride ancillary ligand for one which exerts a stronger ligand-field would be expected to raise the energy of destabilising d-d states, which involve the population of the strongly anti-bonding $d_{x^2-y^2}$ orbital, displacing them to higher energies not accessible at room temperature.[72] Substitution of this ligand for an acetylide group is a well reported strategy for improving the emission efficiency of a range of Pt(II) and Ir(III) complexes.[72,134–139]

The chloride ancillary ligand of PtL[1]Cl was substituted for an acetylide using the technique reported by Cárdenas and co-workers for N^N^C-coordinated Pt(II) complexes.[134] The chemical structure of the new complex PtL[1]C≡C-Ar is shown in Figure 3.13. A mixture of PtL[1]Cl, acetylene, CuI and excess NEt_3 were stirred in anhydrous DCM at 40°C for 48 hours under argon. The resulting mixture was filtered and the crude product purified by column chromatography to give the desired product in a 49% yield as a red solid.

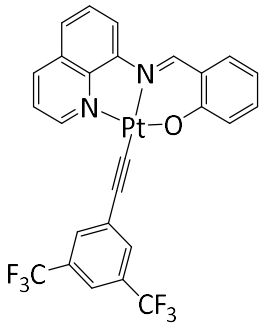

Figure 3.13: The chemical structure of PtL[1]C≡C-Ar

The identity of the complex was confirmed by ^1H and ^{13}C NMR spectroscopy and electrospray ionisation (ESI) mass spectrometry. Crystals suitable for X-ray diffraction were obtained from cooling a concentrated DMSO solution (Figure 3.14). The structure contains two molecules of DMSO per PtL[1]C≡C-Ar. A summary of important bond lengths and angles

is shown in Table 3.2. As with PtL^1Cl we observe an essentially planar environment around Pt, with only a maximum displacement of 0.005 Å from the N^N^O plane. The Pt-C≡C-Ar bond is much shorter than the Pt-Cl bond in PtL^1Cl (1.966(3) vs. 2.3264(14) Å) and the Pt-N(imine) bond opposite is noticeably longer at 2.013(2) vs 1.971(5) Å, presumably due to the stronger *trans* influence exerted by the acetylide. The Pt-O and Pt-N(qui) bonds remain essentially unchanged. Related species of the type $[Pt(typ)C{\equiv}C\text{-}Ar]^+$ displays a very similar effect on the structure when the chloride ligand is replaced with an acetylide, a lengthening on the $Pt\text{-}N_{trans}$ bond (1.93 to 1.97 Å) and a shortening of the $Pt\text{-}C_2Ar$ bond with respect to the Pt-Cl bond (2.303 to 1.98 Å).[140]

The molecules once again form pair-wise Pt···Pt interactions which leads to head-to-tail orientation of dimers with a short/long Pt···Pt distance of 3.587 and 7.216 Å, respectively. The interplanar separation between ligands for $PtL^1C{\equiv}C\text{-}Ar$ of 3.457 Å is sufficiently close for π-π interactions to occur.[113]

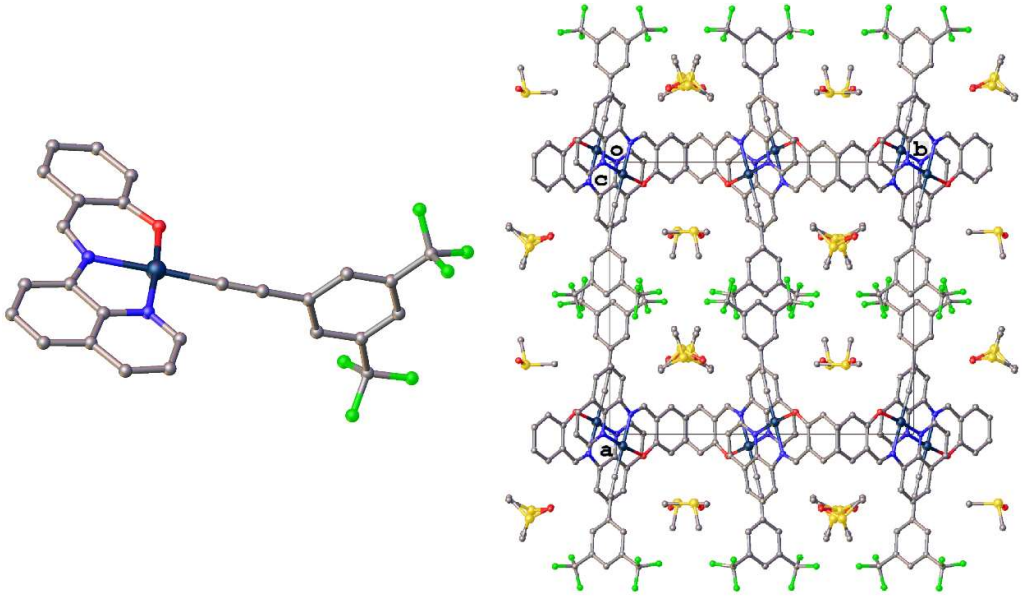

Figure 3.14: Crystal structure and packing of $PtL^1C{\equiv}C\text{-}Ar$. T = 120 K.

Table 3.2: Selected bond lengths and bond angles for $PtL^1C{\equiv}C\text{-}Ar$

Bond Lengths (Å)		*Bond Angles (°)*		*Distances (Å)*	
$Pt\text{-}N_{(qui)}$	1.9925(19)	N-Pt-O	175.83(8)	Pt···Pt	3.587
$Pt\text{-}N_{(imine)}$	2.013(2)	N-Pt-Cl	178.47(9)	Pt···Pt	7.216
Pt-O	1.9970(16)	N-Pt-N	82.01(8)		
$Pt\text{-}C_2Ar$	1.966(3)	N-Pt-O	93.83(8)		
C=N	1.299(3)				
C-N	1.419(3)				

Hydrazone-based Ligands

The Pt(II) complexes of ligands L^5-L^{13} were all prepared by reaction of the corresponding proligands HL^5-HL^{13} with K_2PtCl_4 (Figure 3.15).

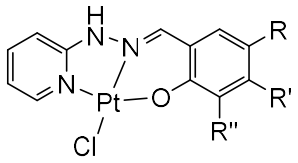

PtL^{5}Cl R, R', R'' = H (60%)
PtL^{6}Cl R, R'' = H, R' = Me (58%)
PtL^{7}Cl R, R'' = Cl, R' = H (61%)
PtL^{8}Cl R = NO_2, R', R'' = H (75%)
PtL^{9}Cl R = F, R', R'' = H (73%)
PtL^{10}Cl R = Cl, R', R'' = H (75%)
PtL^{11}Cl R, R'' = H, R' = OH (36%)
PtL^{12}Cl R = OMe, R', R'' = H (72%)

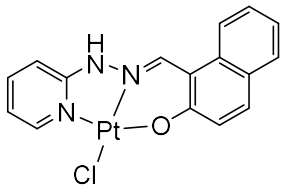

PtL^{13}Cl (68%)

Figure 3.15: Pt(II) complexes of hydrazone (N-H) based N^N^O ligands.

The synthesis of PtL^1Cl, PtL^8Cl and $PtL^{10}Cl$ have been reported previously.[141] The complexes PtL^5Cl – $PtL^{13}Cl$ were synthesised by refluxing the corresponding proligand and K_2PtCl_4 in an EtOH:H_2O mixture for a period of 2 hours. The resulting mixture was cooled to ambient temperature and filtered to yield the crude product. The target complex was obtained by recrystallization in hot DMF in all instances.

The identity of the complexes was confirmed by ^1H and ^{13}C NMR spectroscopy and electrospray ionisation (ESI) mass spectrometry. Complexation causes a small down field shift of the N=C-H proton; for instance, HL^5 has a shift of 8.29 ppm (DMSO-d_6), while in the complex PtL^5Cl the imine proton resonates at 8.61 ppm (DMSO-d_6). Upon complexation, the N-H proton is shifted significantly upfield and becomes very broad. For instance, the N-H proton resonates at 10.50 ppm (DMSO-d_6) in the proligand HL^5 while the N-H proton resonates at 13.73 ppm (DMSO-d_6) in the corresponding PtL^5Cl. Crystals suitable for X-ray diffraction were obtained from the DMF recrystallization in the case of PtL^6Cl and $PtL^{12}Cl$ and from a solution of PtL^8Cl in DMSO. The crystal structure and packing can be seen in Figure 3.16 and a summary of important bond lengths and angles in Table 3.3. PtL^6Cl has one molecule of DMF in the crystal structure and PtL^8Cl has one unit of DMSO whereas $PtL^{12}Cl$ has no solvent molecules in the crystal structure.

Table 3.3: Selected bond lengths, bond angles and distances for PtL^6Cl, PtL^8Cl and $PtL^{12}Cl$

		PtL^6Cl	*PtL^8Cl*	*$PtL^{12}Cl$*
Bond Lengths (Å)	Pt-$N_{(py)}$	1.995(4)	1.992(4)	1.994(2)
	P-$N_{(imine)}$	1.953(4)	1.951(4)	1.941(2)
	Pt-O	1.981(3)	1.993(3)	1.9903(18)
	Pt-Cl	2.3097(13)	2.2947(12)	2.303(7)
Bond Angles (°)	N-Pt-O	175.64(16)	175.38(15)	175.69(7)
	N-Pt-Cl	178.25(13)	177.33(12)	177.61(6)
	N-Pt-N	81.62(17)	81.22(17)	81.13(9)
	N-Pt-O	94.04(16)	94.42(16)	94.57(8)
Distances (Å)	Pt···Pt	5.948	5.07	5.222

We observe an essentially planar environment around Pt in all of the structures, with a maximum of 0.027 Å displacement from the N^N^O plane in PtL^8Cl and as little as 0.002 Å in $PtL^{12}Cl$. There appears to be little to differentiate between the complexes with regards to bond lengths and angles. The central Pt-N(imine) bond is shorter than observed for the analogous N^N^O imine bridged Pt(II) complexes discussed earlier (~1.948 vs. 1.971 Å in PtL^1Cl), there is also a shortening of the Pt-Cl bond (~2.304 vs. 2.326 Å in PtL^1Cl) although it is less significant. It is noteworthy that the hydrazone bridged complex is closer to the values reported for related species of the type $[Pt(typ)Cl]^+$ than the imine bridged complex. The Pt-Cl bond is elongated (average 2.303 Å), Pt-N_{cis} bonds approximately equal at 2.02 Å and the Pt-N_{trans} being slightly shorter at 1.93 Å.

In all structures, there is once again a head-to-tail orientation of molecules although with distances of >4 Å in all cases there is no Pt···Pt interactions. The interplanar separation between ligands for PtL^8Cl of 3.746 Å is sufficiently close for π-π interactions to occur,[113] however the distance in PtL^6Cl (4.648 Å) and $PtL^{12}Cl$ (4.358 Å) is too large for π-π interactions to occur.

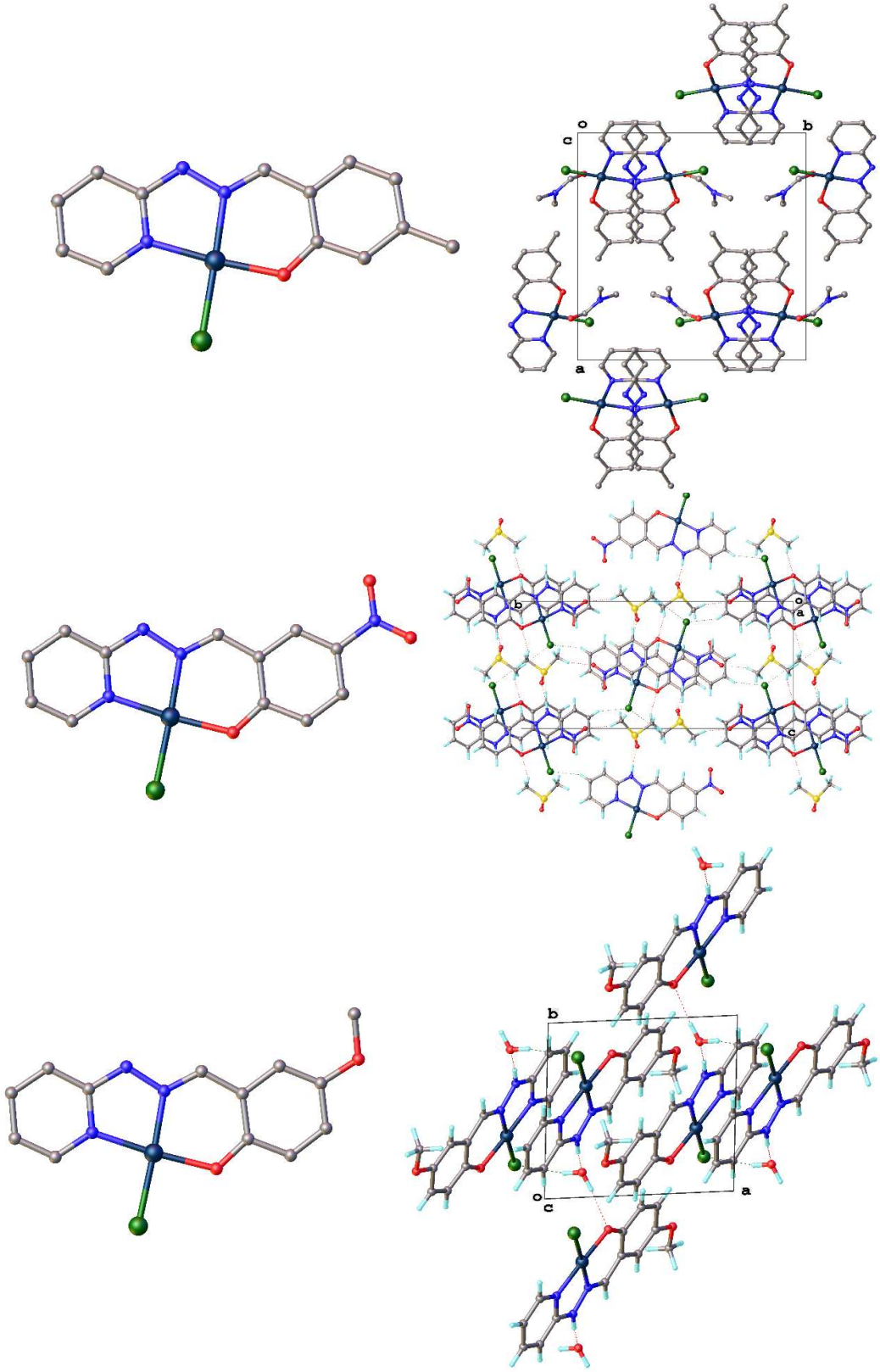

Figure 3.16: Crystal structure and packing of Pt(L^7)Cl (top), Pt(L^9)Cl (middle) and Pt(L^{13})Cl (bottom). T = 120 K.

The Pt(II) complexes of the N-Me hydrazone based ligands L^{14}-L^{20} (Figure 3.17) were all prepared by reaction of the corresponding proligands HL^{14}-HL^{20} with K_2PtCl_4 using the same procedure as for the preparation of complexes PtL^4Cl – $PtL^{13}Cl$.

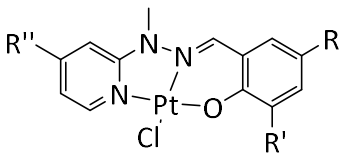

$PtL^{14}Cl$ R, R', R'' = H (82%)
$PtL^{15}Cl$ R = OMe , R', R'' = H (43%)
$PtL^{16}Cl$ R = OCF_3 , R', R'' = H (43%)
$PtL^{17}Cl$ R, R' = Cl , R'' = H (32%)
$PtL^{19}Cl$ R, R' = H, R'' = OMe (32%)
$PtL^{20}Cl$ R, R' = H , R'' = CF_3 (42%)

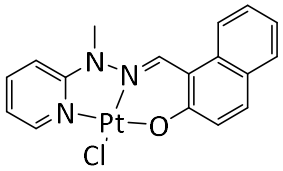

$PtL^{18}Cl$ (35%)

Figure 3.17: Pt(II) complexes of hydrazone (N-Me) based N^N^O ligands.

The identity of the complexes was confirmed by ^1H and ^{13}C NMR spectroscopy and electrospray ionisation (ESI) mass spectrometry. Complexation causes a larger down field shift of the N=C-H proton than seen for the N-H complexes; for instance, the N=C-H proton in HL^{14} resonates at 8.05 ppm (DMSO-d_6) which shifts to 8.94 ppm upon complexation (compared to PtL^5Cl which shifts from 8.29 to 8.61 ppm). Crystals suitable for X-ray diffraction were obtained from the DMF recrystallization of $PtL^{14}Cl$, $PtL^{17}Cl$ and $PtL^{19}Cl$. The crystal structure and packing can be seen in Figure 3.18 and a summary of important bond lengths and angles in Table 3.4. $PtL^{17}Cl$ has one molecule of DMF in the crystal structure whereas $PtL^{14}Cl$ and $PtL^{19}Cl$ have no solvent molecules in the crystal structure.

Table 3.4: Selected bond lengths, bond angles and distance for $PtL^{14}Cl$, $PtL^{17}Cl$ and $PtL^{19}Cl$

		$PtL^{14}Cl$	*$PtL^{17}Cl$*	*$PtL^{19}Cl$*
Bond Lengths (Å)	Pt-$N_{(py)}$	1.9883(14)	1.977(2)	1.986(3)
	P-$N_{(imine)}$	1.9518(13)	1.960(2)	1.956(3)
	Pt-O	1.9758(12)	1.9852(19)	1.99(2)
	Pt-Cl	2.3047(4)	2.3071(8)	2.3105(9)
Bond Angles (°)	N-Pt-O	176.61(5)	176.49(8)	176.28(11)
	N-Pt-Cl	177.59(4)	177.05(6)	177.60(9)
	N-Pt-N	81.02(6)	80.92(9)	81.07(13)
	N-Pt-O	95.58(5)	95.57(8)	95.42(11)
Distances (Å)	Pt···Pt	5.117	4.398	4.733

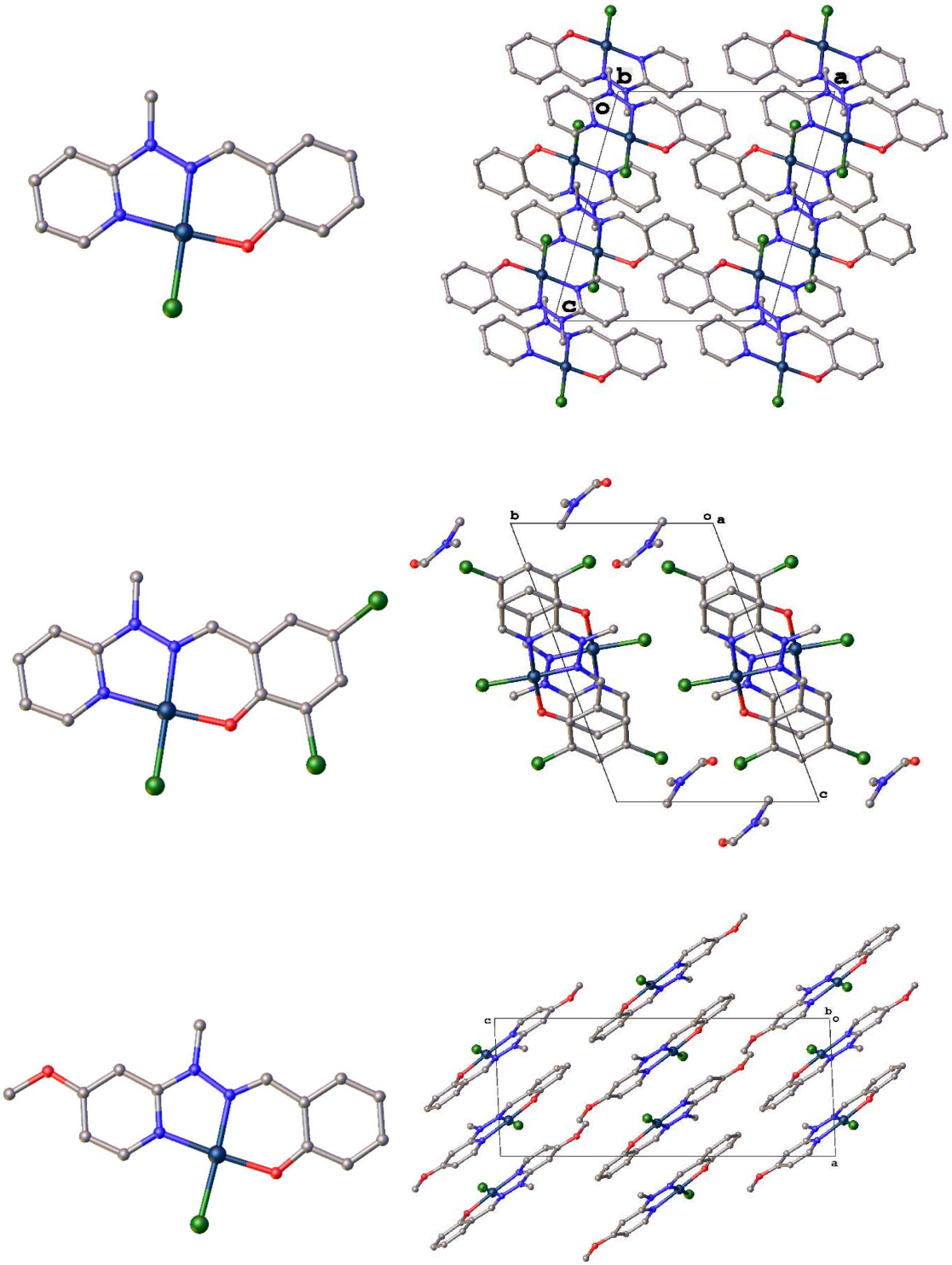

Figure 3.18: Crystal structure and packing of $PtL^{14}Cl$ (top), $PtL^{17}Cl$ (middle) and $PtL^{19}Cl$ (bottom). T = 120 K.

We observe an essentially planar environment around Pt in all of the structures, with a maximum of 0.022 Å displacement from the N^N^O plane in $PtL^{19}Cl$, 0.002 Å in $PtL^{17}Cl$ and zero displacement in $PtL^{14}Cl$. Again, there appears to be little to differentiate

between the complexes with regards to bond lengths and angles, although the central Pt-N(imine) bond is slightly longer than seen for the N-H complexes (~1.956 vs. 1.948 Å).

In all structures, there is once again a head-to-tail orientation of molecules, although with distances of >4 Å in each of the complexes there is no Pt···Pt interactions. The interplanar separation between the tridentate ligands in $PtL^{14}Cl$ is too large for π-π interactions to occur, however the interplanar separation between ligands for $PtL^{17}Cl$ (3.595 Å) and $PtL^{19}Cl$ (3.652 Å) are sufficiently close for π-π interactions.[113]

The chloride ancillary ligand of $PtL^{14}Cl$ was substituted for an acetylide using the technique reported by Cárdenas and co-workers for N^N^C-coordinated Pt(II) complexes.[134] The chemical structure of the new complex $PtL^{14}C{\equiv}C$-Ar is shown in Figure 3.19. A mixture of $PtL^{14}Cl$, acetylide, CuI and excess NEt_3 were stirred in anhydrous DCM at 40°C for 48 hours under argon. The resulting mixture was filtered and the crude product purified by column chromatography to give the desired product in a 38% yield as a yellow solid.

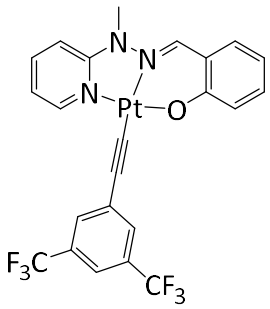

Figure 3.19: The chemical structure of $PtL^{14}C{\equiv}C$-Ar

The identity of the complex was confirmed by ^1H and ^{13}C NMR spectroscopy and electrospray ionisation (ESI) mass spectrometry.

Pyrazole-based Ligands

The Pt(II) complex of ligand L^{21} was prepared by reaction with of the proligand HL^{21} with K_2PtCl_4 (Figure 3.20) using the method reorted by Mohan *et al.*[141] HL^{21} and K_2PtCl_4 were refluxed in a EtOH:H_2O mixture for a period of 2 hours. The resulting mixture was cooled to ambient temperature and filtered to give the pure complex in a 90% yield.

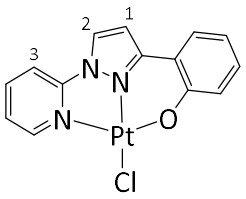

Figure 3.20: Pt(II) complex of pyrazole bridged N^N^O ligand L^{21}

The identity of the complex was confirmed by ^{1}H and ^{13}C NMR spectroscopy and electrospray ionisation (ESI) mass spectrometry. Successful complexation of the ligand showed the absence of the OH proton in the ^{1}H NMR spectrum and high resolution mass spectrometry also confirmed the identity of the species. There is a down field shift of the pyrazole protons H^1 and H^2, which resonate at 7.83 and 9.43 ppm in DMSO-d_6, respectively. These protons resonate at 7.19 (H^1) and 8.72 ppm (H^2) in DMSO-d_6 in the proligand HL^{21}.

3.4.2 Synthesis of N^N^N complexes

Hydrazide bridged Ligands

The Pt(II) complex of ligand L^{22} was prepared by reaction with $Pt(COD)Cl_2$ in an analogous manner to that reported by Mori *et al.*[142] HL^{22}, $Pt(COD)Cl_2$ and excess NEt_3 were refluxed in MeCN for a period of 48 hours before filtration to yield a dark purple solid. ^{1}H NMR revealed this as a mixture of two Pt(II) complexes which could be separated by column chromatography. The proposed structures can be seen in Figure 3.21.

The complexes a-$PtL^{22}Cl$ and b-$PtL^{22}Cl$ were isolated in a 35% and 40% yield, respectively. The complex a-$PtL^{22}Cl$ is burnt orange in colour and is appreciably soluble in DCM, chloroform and DMSO, whereas b-$PtL^{22}Cl$ is a dark purple solid with limited solubility in DCM, chloroform and DMSO.

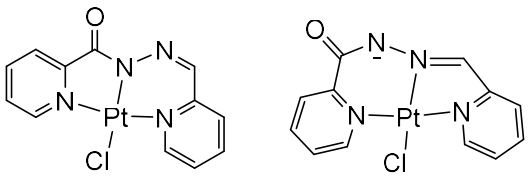

a-$PtL^{22}Cl$ **b-$PtL^{22}Cl$**

Figure 3.21: Pt(II) complexes of hydrazide bridged N^N^N ligand H^{22}

The formation of the complexes indicates that E to Z isomerisation occurs during the reaction, although no isomerisation occurs at room temperature for the free ligand, suggesting that the Pt(II) ion assists the E to Z conversion of the ligand. This assisted

isomerisation was also reported by Mori *et al.* for related compounds [PdCl-(Z-L-κ^2N,N')] and [$PdCl_2$(E-HL'-κ^2N,N')] where L = quinoline-2-carbaldehyde (pyridine-2-carbonyl)hydrazone.[142]

The introduction of platinum satellites can clearly be seen in the ^{1}H NMR spectrum of a-PtL^{22}Cl (Figure 3.22). On comparison with the ^{1}H NMR spectrum of HL^{22}, an upfield shift can be observed for the N=C-H imine proton in a-PtL^{22}Cl, from 8.38 ppm ($CDCl_3$) to 7.60 ppm; interestingly in b-PtL^{22}Cl complexation does not cause a shift of this proton (Figure 3.23).

The complex b-PtL^{22}Cl is the kinetically formed product and in solution is gradually converted under room light to yield a-PtL^{22}Cl. Mori *et al.* reported that this process took several days for the Pd(II) complex of L^{22} and suggested both thermal and photochemical coordination structure conversion in solution could take place via the proposed mechanism show in Figure 3.24.[142]

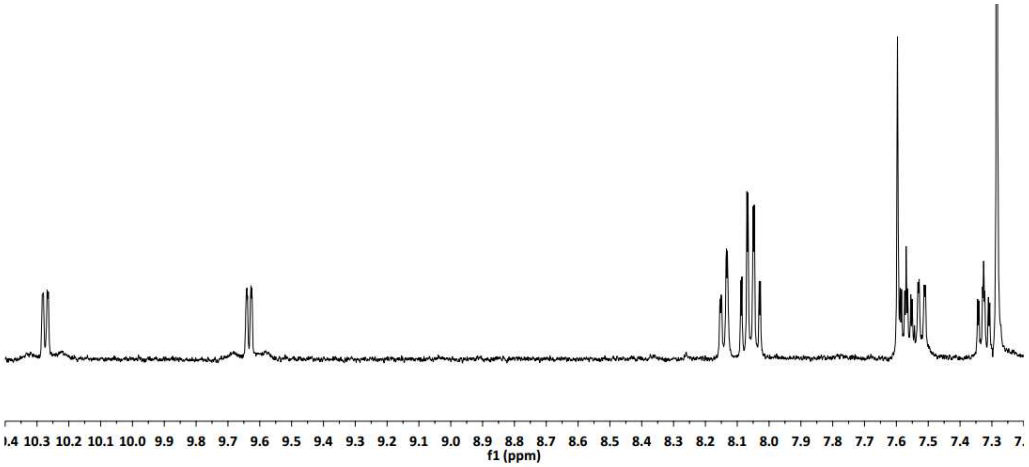

Figure 3.22: 400 MHz 298 K ^{1}H NMR spectrum of a-PtL^{22}Cl in $CDCl_3$.

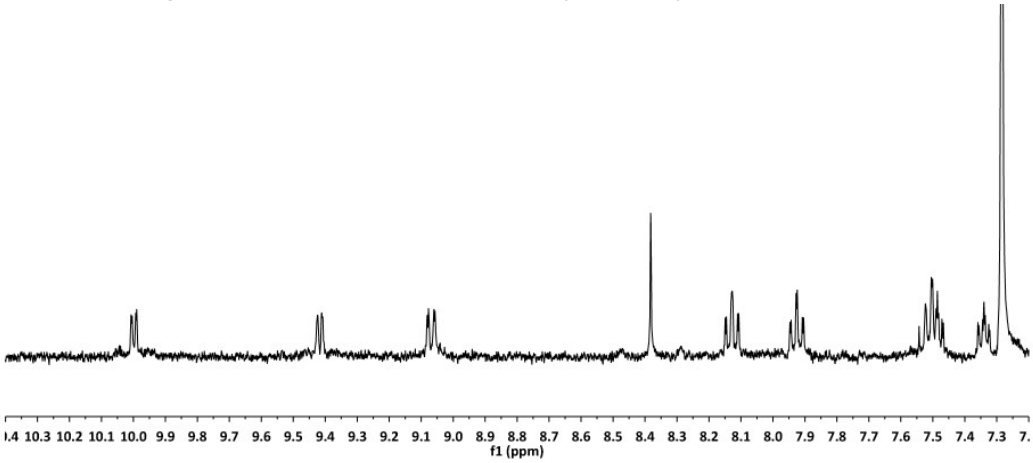

Figure 3.23: 400 MHz 298 K ^{1}H NMR spectrum of b-PtL^{22}Cl in $CDCl_3$.

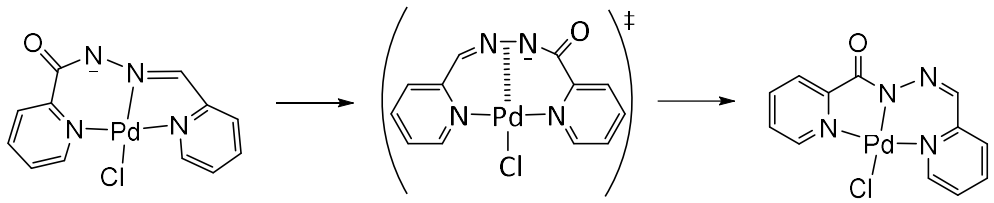

Figure 3.24: Plausible mechanism for photochemical structure conversion.

Imide and Amide-based Ligands

The Pt(II) complexes of ligands L^{23} and L^{25} were prepared by reaction of the corresponding proligand with $Pt(COD)Cl_2$ (Figure 3.25). The synthesis of $PtL^{23}Cl$ has been reported previously.[143] The Pt(II) complexes of L^{25} and L^{27} were synthesised by reaction with $Pt(COD)Cl_2$ with NEt_3 in MeCN. This proceeded in yields of 65% and 40%, respectively, with no need for purification in either instance. The identity of the complexes was confirmed by ^1H and ^{13}C NMR spectroscopy and electrospray ionisation (ESI) mass spectrometry.

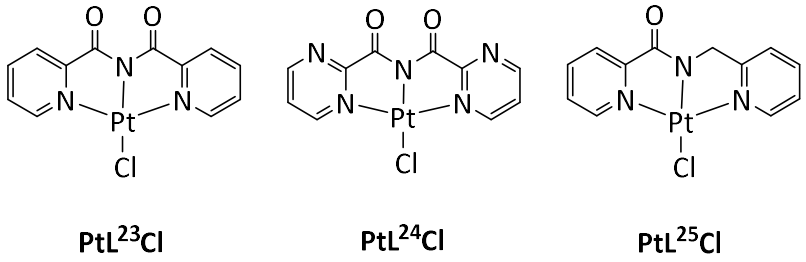

$PtL^{23}Cl$ **$PtL^{24}Cl$** **$PtL^{25}Cl$**

Figure 3.25: Chemical structure of imide and amide-based complexes

An alternative route was required for the Pt(II) complex of L^{24}. We used the conditions reported by Lippert and co-workers, originally for the synthesis of $PtL^{23}Cl$ (with lower yields of around 50%).[143] HL^{26} and K_2PtCl_4 were heated at 60°C for a period of 24 hours. The resulting mixture was filtered, and the filtrates extracted into DCM to give an orange solid. The resulting material was extremely insoluble in all common organic solvents. Analysis of the ^1H NMR in DMSO-d_6 at 80°C showed an approximate 3:1 ratio of ligand to complex and a small amount of aromatic impurity (Figure 3.26). The crude product was recrystallized in hot DMSO to give the target complex as a bright yellow solid.

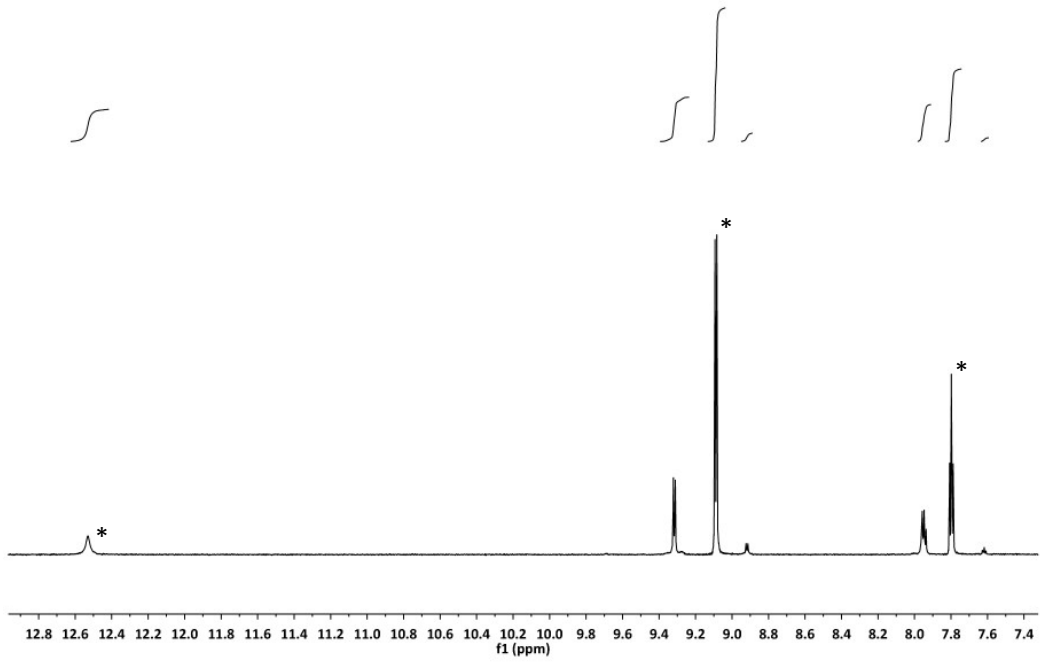

*Figure 3.26: 400 MHz 353 K ^{1}H NMR of the crude product PtL^{24}Cl in DMSO-d_6. The ligand protons are indicated by *.*

3.5 Synthesis of Pt(II) Complexes of Tetradentate Ligands

3.5.1 Synthesis of C^N^N^O complexes

Hydrazone-based Ligands

The Pt(II) complex of L^{27} (Figure 3.27) was synthesised using the well reported method of cyclometallation in acetic acid with K_2PtCl_4.[78,79,129,144,145] HL^{29} and K_2PtCl_4 were refluxed in acetic acid for 3 days before cooling to ambient temperature. Filtration resulted in the crude product which was purified by DMF recrystallization to give the desired product in a 30% yield.

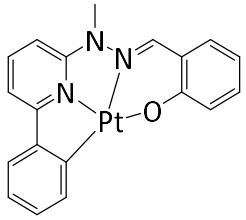

Figure 3.27: Chemical Structure of PtL^{27}

It is interesting to note that the crude ^{1}H NMR revealed the possible formation of a dimer alongside the desired PtL^{27} complex (Figure 3.28).

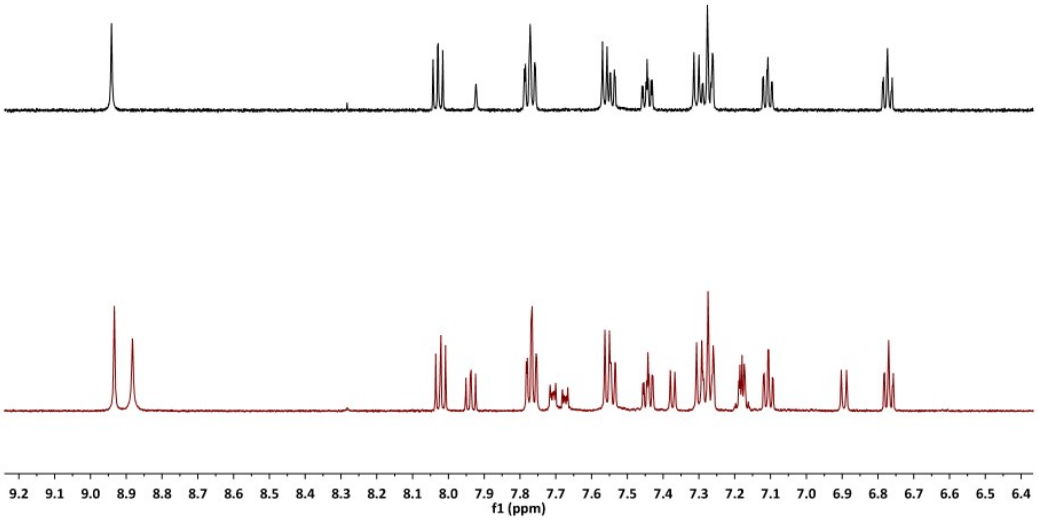

Figure 3.28: 400 MHz 298 K ^{1}H NMR spectrum of PtL^{27} (above) and the crude product (below) in DMSO-d_6

DOSY NMR spectroscopy (diffusion-ordered spectroscopy) was used in order to shed light on the species present (Figure 3.29). DOSY seeks to separate the NMR signals of different components of a mixture according to their diffusion coefficient which is inversely related to the molecular weight/size.[146]

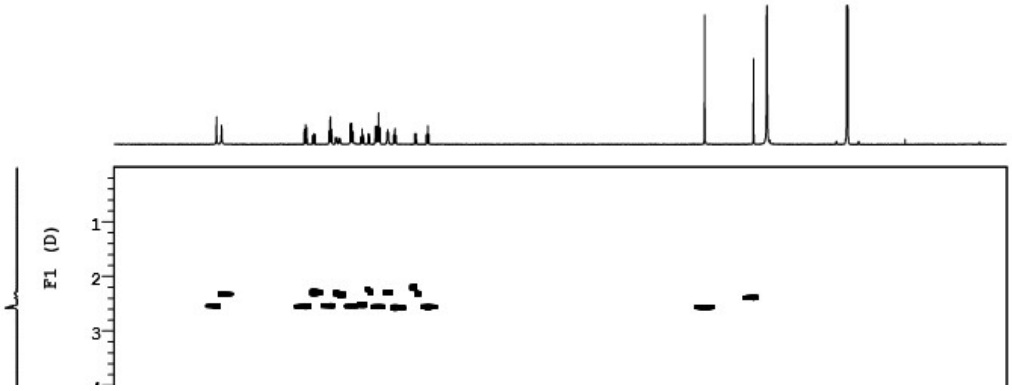

Figure 3.29: DOSY NMR spectrum of the crude product.

Comparison of the DOSY and the ^{1}H NMR spectrum suggests that the isolated PtL^{27} has the smaller molecular weight of the two species, since it has the higher diffusion coefficient. We note that the two species otherwise appear very similar, with each ^{1}H NMR signal of PtL^{27} having a closely related signal of similar splitting and chemical shift.

Crystals suitable for X-ray diffraction were obtained from the DMF recrystallization of PtL^{27}. The structure contains one molecule of DMF per PtL^{27}. The crystal structure and packing can be seen in Figure 3.30 and a summary of important bond lengths and angles in Table 3.5. We observe an essentially planar environment around Pt, with only a 0.01 Å displacement from the C^N^N^O plane. The square planar geometry of the Pt(II) is quite distorted, presumably due to the steric constraints of the ligand. We note the central Pt-$N_{(imine)}$ bond (2.024(4) Å) is longer than seen for any of the tridentate complexes, likely due to the strong trans influence of the cyclometallated phenyl ring. The Pt-$N_{(py)}$ bond is significantly shorter than observed for the analogous tridentate complex $PtL^{14}Cl$ (1.924(4) vs 1.9758(12)).

To the best of our knowledge, there are no reports of a C^N^N^O tetradentate Pt(II) complex in the literature.[147] We instead note the similarities to the C^N^N^C tetradentate complex reported by Vezzu *et al.* (Figure 3.31).[84] They report a Pt-C bond length of 2.004 Å which is very similar to the Pt-C bond length of 2.007(5) Å observed in PtL^{27} however the Pt-N bond length is somewhat longer at 2.051 Å than the observed 2.019 Å for Pt-$N_{(py)}$ in PtL^{27}.

The molecules are again aligned in a head-to-tail orientation, with no evidence of π-π stacking and Pt···Pt distances of > 4Å indicating there is no Pt···Pt interactions.

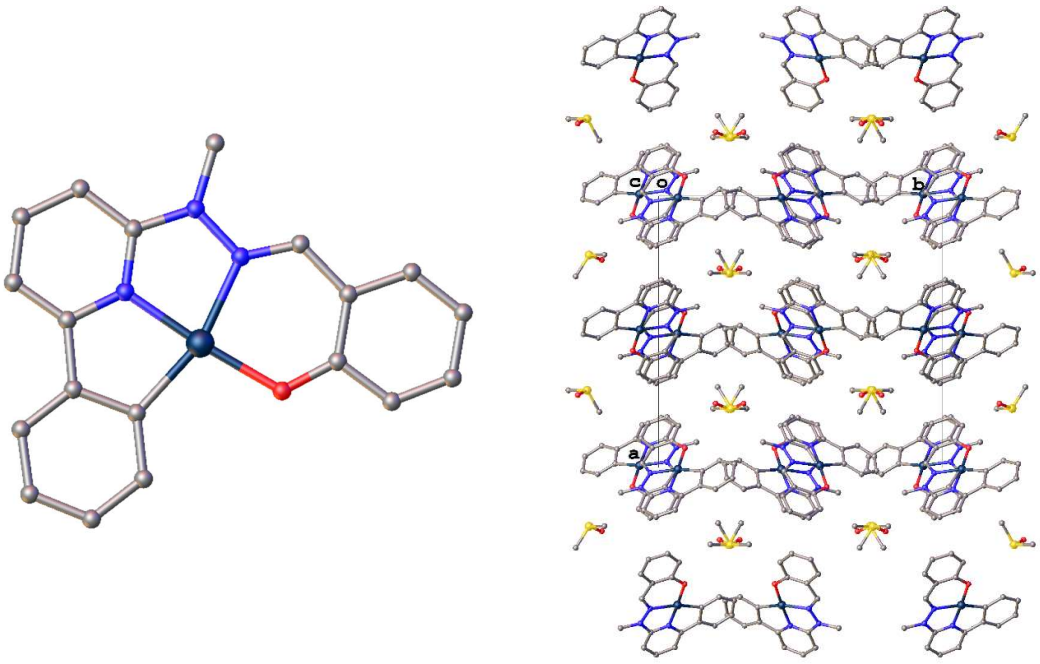

Figure 3.30: Crystal structure and packing of PtL^{27}. T = 120 K.

Table 3.5: Selected bond lengths, bond angles and distances for PtL[27]

Bond Lengths (Å)		*Bond Angles (°)*		*Distances (Å)*	
Pt-$N_{(py)}$	1.924(4)	$N_{(py)}$-Pt-O	176.00(17)	Pt···Pt	4.54
Pt-$N_{(imine)}$	2.024(4)	$N_{(imine)}$-Pt-C	162.8(2)		
Pt-O	2.006(4)	N-Pt-N	80.86(19)		
Pt-C	2.007(5)	$N_{(imine)}$-Pt-O	95.15(17)		
		C-Pt-$N_{(py)}$	82.0(2)		
		C-Pt-O	101.9(2)		

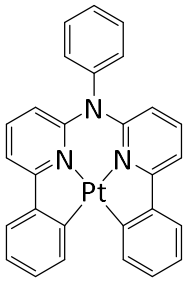

Figure 3.31: Chemical Structure of C^N^N^C complex reported by Vezzu et al.

Repeated attempts to synthesis Pt(II) complexes of L^{26} and L^{28} were unsuccessful. Due to the instability of the N-H hydrazone bridge towards acid[148], we were unable to cyclometalate in acetic acid. We attempted to use the conditions reported by Williams *et al.*[79] for cyclometallation: an aqueous solution of K_2PtCl_4 was added to a solution of HL^{26} in acetonitrile and the aerated mixture was refluxed for 3 days. Unfortunately, this method yielded only the ligand and some decomposition products. We also attempted synthesis using the common starting material for cycloplatination $PtCl_2(DMSO)_2$ in toluene[145] however similar results were obtained. Due to the instability of the N-H hydrazone bridged ligands no further attempts were made to synthesise these complexes.

Pyrazole-based Ligands

We synthesised the Pt(II) complexes of L^{29}-L^{32} by reacting K_2PtCl_4 and the corresponding proligand in acetic acid for 3 – 5 days. Characterisation of the complexes revealed a surprising tridentate complexation mode for all four of the ligands (Figure 3.32).

Inspection of the ^{1}H NMR of $PtL^{29}Cl$ shows the presence of the OH proton, indicating that the oxygen is not coordinated to the Pt(II) (Figure 3.33). We investigated the effect of adding sodium *tert*-butoxide to the ^{1}H NMR sample in order to deprotonate the OH and encourage coordination (Figure 3.33). We initially believed the loss of the OH proton and resulting shift of some signals in the ^{1}H NMR spectrum to be a consequence of formation

of the tetradentate complex rather than simply deprotonation. Mass spectroscopy was unable to shed light upon this phenomenon; due to the lability of the chloride ancillary ligand we often observe the $[M\text{-}Cl]^+$ ion rather than $[M]^+$.

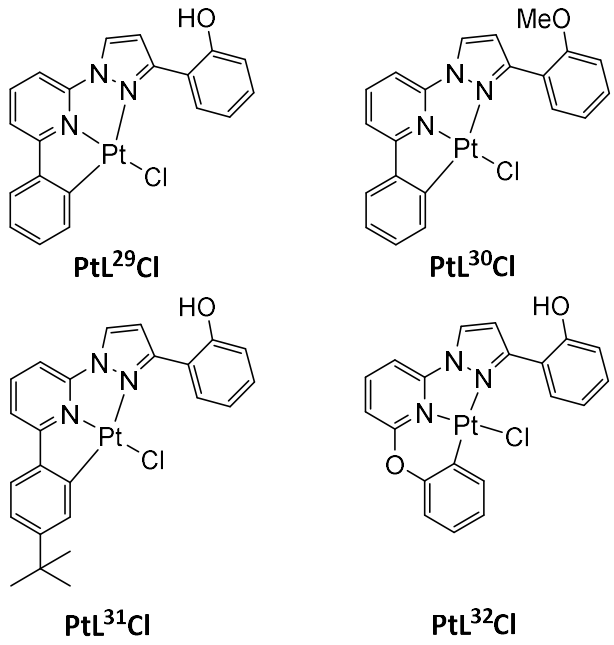

Figure 3.32: Chemical structures of $PtL^{29}Cl$ – $PtL^{32}Cl$.

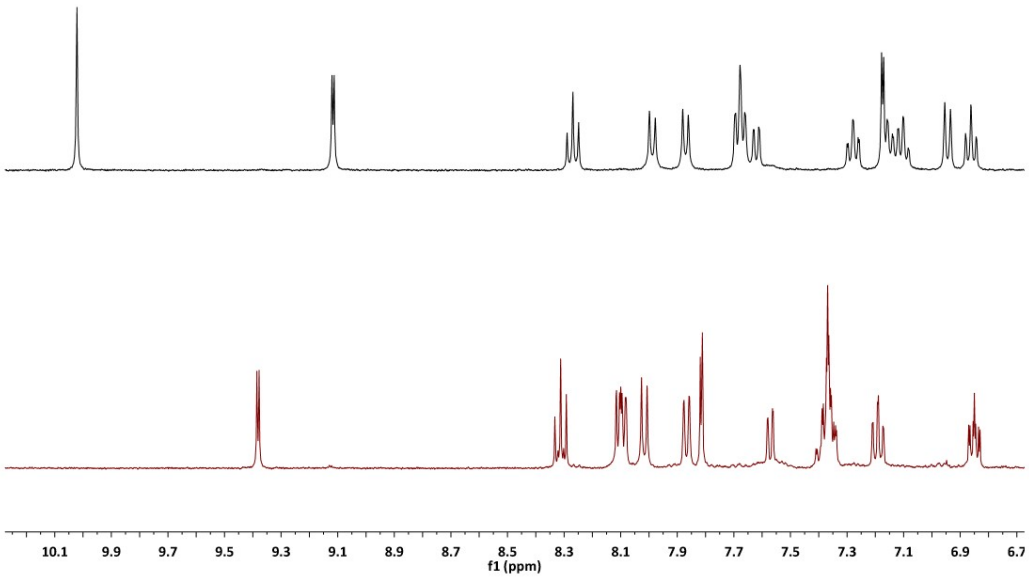

Figure 3.33: 400 MHz 298K ^{1}H NMR of $PtL^{29}Cl$ before (top) and after (bottom) adding sodium t-butoxide in DMSO-d_6.

In order to rationalise this unexpected behaviour, we synthesised the related complex $PtL^{30}Cl$. This would allow us to characterise the complex where coordination through the O-Me is not anticipated and relate this to the $PtL^{29}Cl$ complex. The ^{1}H NMR

looks remarkedly similar to the $PtL^{29}Cl$ spectrum (Figure 3.34). We also observe the $[M\text{-}Cl]^+$ ion in the mass spectrum for $PtL^{30}Cl$.

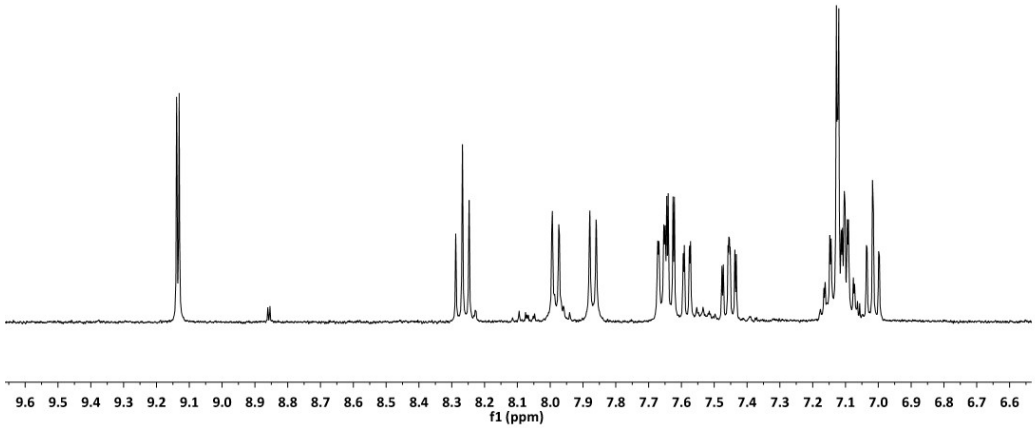

Figure 3.34: 400 MHz 298 K ^1H NMR spectrum of $PtL^{30}Cl$ in DMSO-d_6.

Due to the insoluble nature of complex $PtL^{29}Cl$ we synthesised the related complex $PtL^{31}Cl$, the t-butyl substituent was anticipated to increase the solubility of the complex allowing us to probe the coordination of the Pt(II) further.

Crystals suitable for X-ray diffraction were obtained from the acetic acid filtrates of the reaction mixture. The structure contains three molecules of acetic acid per $PtL^{31}Cl$. The crystal structure and packing can be seen in Figure 3.35 and a summary of important bond lengths and angles in Table 3.6. We observe an essentially planar environment around Pt, with only a 0.036 Å displacement from the C^N^N plane. The square planar geometry of the Pt(II) is significantly distorted as indicated by the small bite angle of C-Pt-$N_{(pyrazole)}$ (160.3(2)°), presumably due to the steric constraints of the ligand. We note the similarities to the tridentate N^N^C pyrazole Pt(II) complex reported by Harris *et al.*[149] (Figure 3.36). The Pt-C bond (1.973(6) Å) is comparable to that reported by Harris *et al.* (1.989 Å) and the Pt-C bond (2.007(5) Å) in PtL^{27}. The Pt-$N_{(pyrazole)}$ which is *trans* to the Pt-C is bond is significantly longer (2.163(5) Å) than the Pt-$N_{(py)}$ bond (1.961(5) Å), indicating the strong structural *trans* effect.

The molecules take a head-to-tail orientation and there is evidence of π-π interactions with an interplanar distance of 3.754 Å. There is no Pt···Pt interaction. The phenol ring is perpendicular to coordination plane.

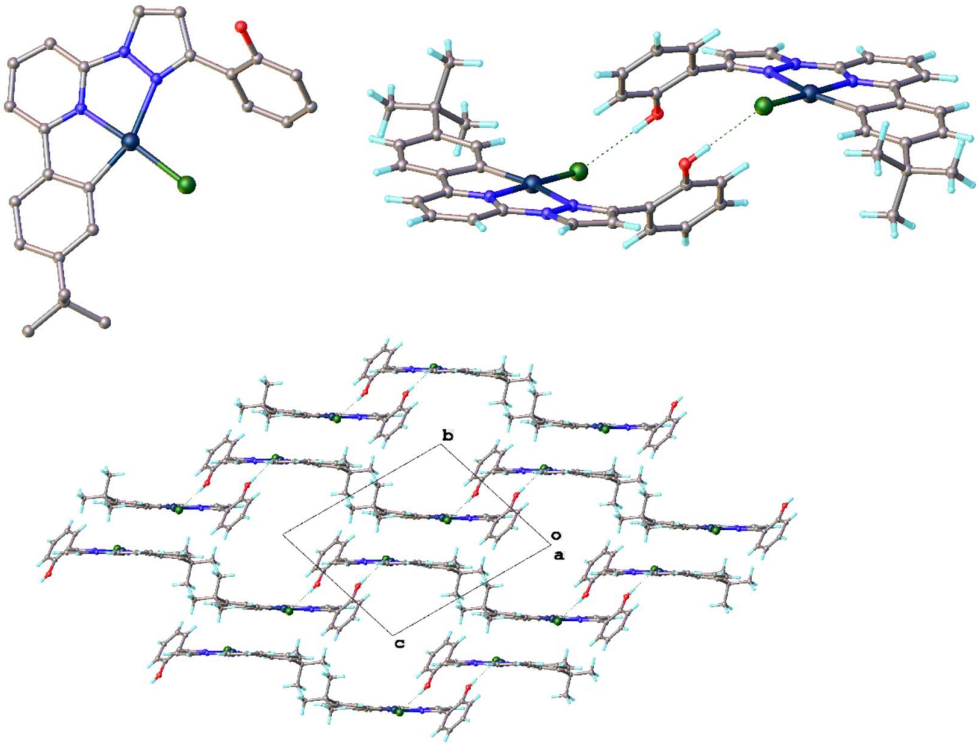

Figure 3.35: Crystal structure and packing of PtL[31]Cl. T = 120 K.

Table 3.6: Selected bond lengths, bond angles and distances for PtL[31]Cl

Bond Lengths (Å)		*Bond Angles (°)*		*Distances (Å)*	
Pt-$N_{(py)}$	1.961(5)	C-Pt-$N_{(pyrazole)}$	160.3(2)	Pt···Pt	5.208
Pt-$N_{(pyrazole)}$	2.163(5)	$N_{(py)}$-N-Cl	175.40(14)		
Pt-C	1.973(6)	C-Pt-$N_{(py)}$	81.8(2)		
Pt-Cl	2.3027(14)	N-Pt-N	78.62(19)		

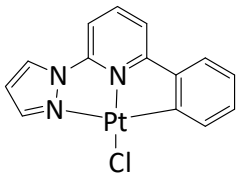

Figure 3.36: Chemical Structure of N^N^C Pt(II) complex reported by Harris et al.

In order to encourage coordination of the O-H moiety in PtL[29]Cl we removed the chloride ancillary ligand using silver triflate (AgOTf). A downfield shift can be observed in the ^{1}H NMR spectrum of the resulting product, however we note the presence of the O-H proton suggesting the Pt(II) is still not coordinated (Figure 3.37).

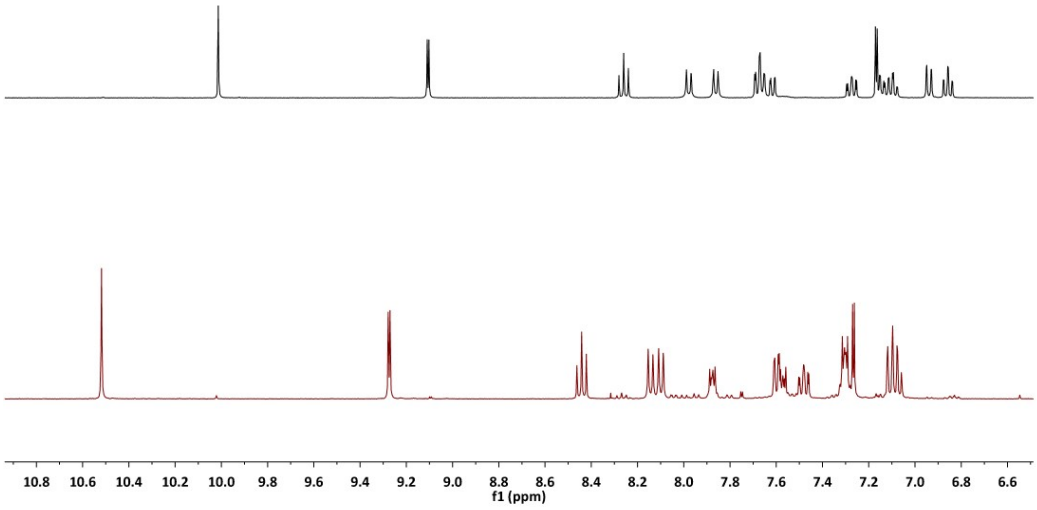

Figure 3.37: 400 MHz 298 K ^{1}H NMR spectrum of PtL^{29}Cl (top) and [PtL^{29}]OTf (bottom) in DMSO-d_6.

Crystals suitable for X-ray diffraction were obtained from the slow evaporation of an acetone solution. The crystal structure and packing can be seen in Figure 3.38 and a summary of important bond lengths and angles in Table 3.7. We note the successful removal of the chloride ancillary ligand, although we observe its replacement with an acetone molecule rather than binding of the O-H moiety. There is an essentially planar environment around Pt, with only a 0.019 Å displacement from the C^N^N plane. The square planar geometry of the Pt(II) remains significantly distorted as indicated by the small bite angle of C-Pt-$N_{(pyrazole)}$ (161.3(3)°). We observe some notable differences in bond lengths from PtL^{31}Cl; the Pt-C bond is longer (1.995(8) vs. 1.973(6) Å), the opposite bond Pt-$N_{(pyrazole)}$ is shorter (2.109(6) vs. 2.163(5) Å), the Pt-$O_{(acetone)}$ is 2.055(5) Å, which is significantly shorter than the Pt-Cl bond in PtL^{31}Cl (2.3027(14) Å) and the Pt-$N_{(py)}$ is also shorter (1.942(7) vs. 1.961(5) Å).

The molecules take a head-to-tail orientation and there is evidence of π-π interactions with an interplanar distance of 3.657 Å. There is no Pt···Pt interaction. The phenol ring is again perpendicular to coordination plane.

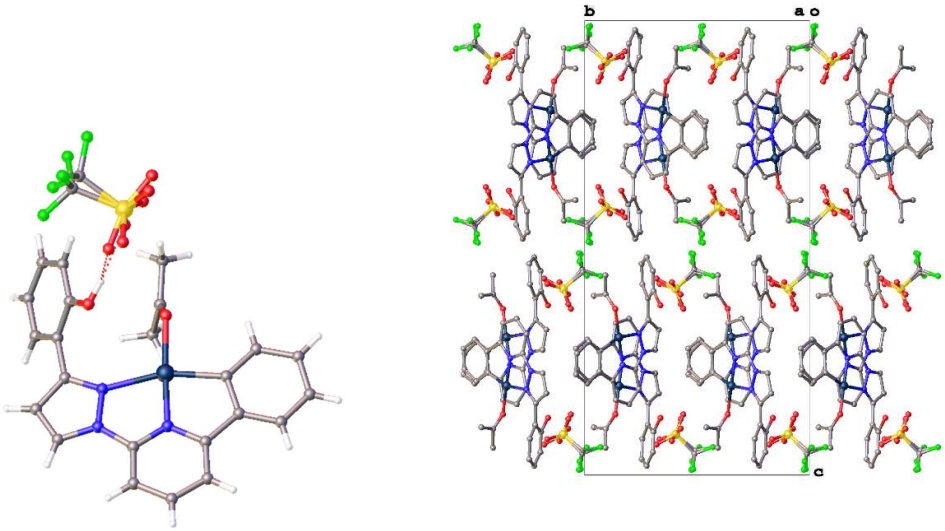

Figure 3.38: Crystal structure and packing of [PtL[29]]OTf. T = 120 K.

Table 3.7: Selected bond lengths, bond angles and distances for [PtL[29]]OTf

Bond Lengths (Å)		*Bond Angles (°)*		*Distances (Å)*	
$Pt\text{-}N_{(py)}$	1.942(7)	$C\text{-}Pt\text{-}N_{(pyrazole)}$	161.3(3)	$Pt\cdots Pt$	6.155
$Pt\text{-}N_{(pyrazole)}$	2.109(6)	$N_{(py)}\text{-}N\text{-}O_{(acetone)}$	175.4(3)		
Pt-C	1.995(8)	$C\text{-}Pt\text{-}N_{(py)}$	82.6(3)		
$Pt\text{-}O_{(acetone)}$	2.055(5)	N-Pt-N	78.7(3)		

The increase in chelate ring size for the Pt(II) complex of L^{34} was intended to decrease the strain from complexation on the ligand and allow binding to the O-H moiety Figure 3.39).

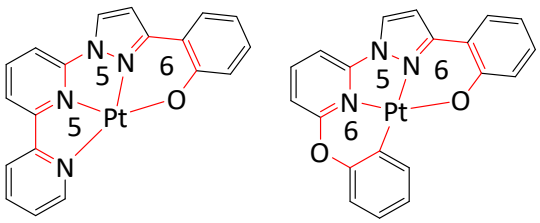

Figure 3.39: Comparison of the chelate ring sizes of PtL[29] and PtL[32]

Analysis of the ^{1}H NMR spectrum once again shows the O-H proton is present and remains unbound (Figure 3.40).

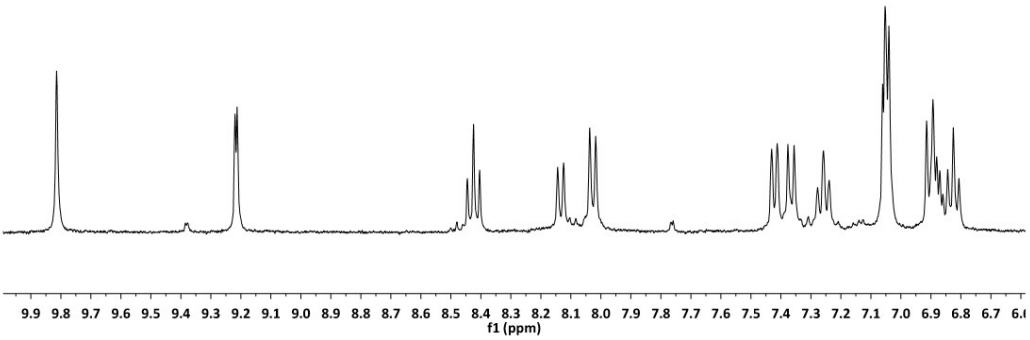

Figure 3.40: 400 MHz 298 K ^{1}H NMR spectrum of PtL^{32}Cl in DMSO-d_6.

3.6 Synthesis of Tridentate coordinated Ir(III) complexes

3.6.1 Synthesis of N^N^O complexes

Hydrazone-based Ligands

The Ir(III) complexes of ligands L^{15}-L^{18} (Figure 3.41) were all prepared by reaction of the corresponding proligands with an intermediate iridium dimer [Ir(dpyx)Cl(μ-Cl)$_2$]$_2$.

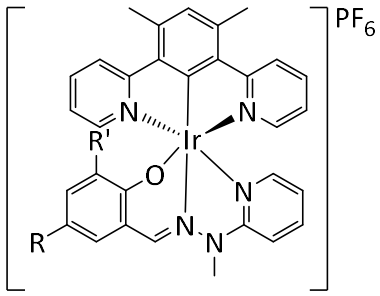

[Ir(dpyx)L^{14}]PF_6 R, R' = H
[Ir(dpyx)L^{15}]PF_6 R = OMe, R' = H
[Ir(dpyx)L^{16}]PF_6 R = OCF_3, R' = H
[Ir(dpyx)L^{17}]PF_6 R, R' = Cl

Figure 3.41: Chemical Structure of Ir(III) complexes of L^{14} – L^{17}. dpyx = 1,3-Di(2-pyridyl)-4,6-dimethylbenzene (dpyx).

The synthetic route is displayed in Scheme 3.15. The tridentate proligand dpyxH is known to react with $IrCl_3.3H_2O$ in ethoxyethanol/water to give a dichloro-bridged dimer [Ir(dpyx)Cl(μ-Cl)$_2$]$_2$.[98] Reaction of the di-chloro bridged iridium dimer with proligands HL^{14} – HL^{17} was carried out in ethylene glycol at 195°C for 90 minutes, leading to the corresponding complexes. The chloride counter anion was exchanged for PF_6 by precipitation in aq. sat. KPF_6. The complexes were purified by recrystallization in acetonitrile/ether.

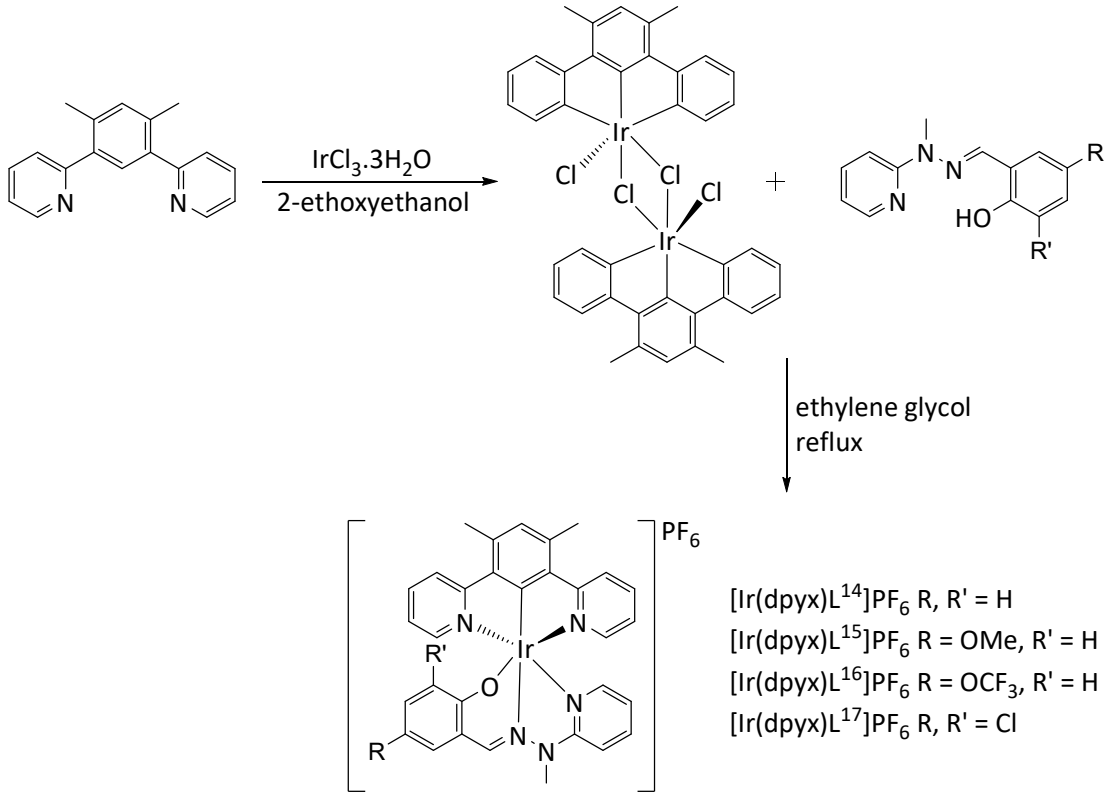

Scheme 3.15: Synthetic route to complexes [Ir(dpyx)L[14]]PF$_6$ - [Ir(dpyx)L[17]]PF$_6$.

The identity of the complexes was confirmed by ^{1}H NMR and ^{13}C NMR spectroscopy and electrospray ionisation (ESI) mass spectrometry. Successful complexation of the ligand showed the absence of the OH proton in the ^{1}H NMR spectrum and high resolution mass spectrometry also confirmed the identity of the species.

Small crystals, suitable for X-ray diffraction, were obtained of [Ir(dpyx)L^{15}]PF$_6$ by slow evaporation of a MeCN solution. There is one molecule of MeCN per [Ir(dpyx)L^{15}]PF$_6$. The crystal structure and packing can be seen in Figure 3.42 and a summary of important bond lengths and angles in Table 3.8. The desired (N^C^N)(N^N^O) coordination is evident. The iridium(III) centre exhibits a distorted octahedral geometry due to the geometric constraints of the tridentate binding of dpyx. The Ir-C bond (1.9483(16) Å) is shortened with respect to analogous bonds in [Ir(dpyx)(DMSO)Cl$_2$] (1.975(4) Å).[150] The Pt-N distances of the flanking pyridine rings (2.0352(14) and 2.0527(14) Å) are also shortened with respect to those in [Ir(dpyx)(DMSO)Cl$_2$] (2.067(3) and 2.087(3) Å).

The molecules take a head-to-tail orientation and there is evidence of π-π interactions with an interplanar distance of 3.729 Å.

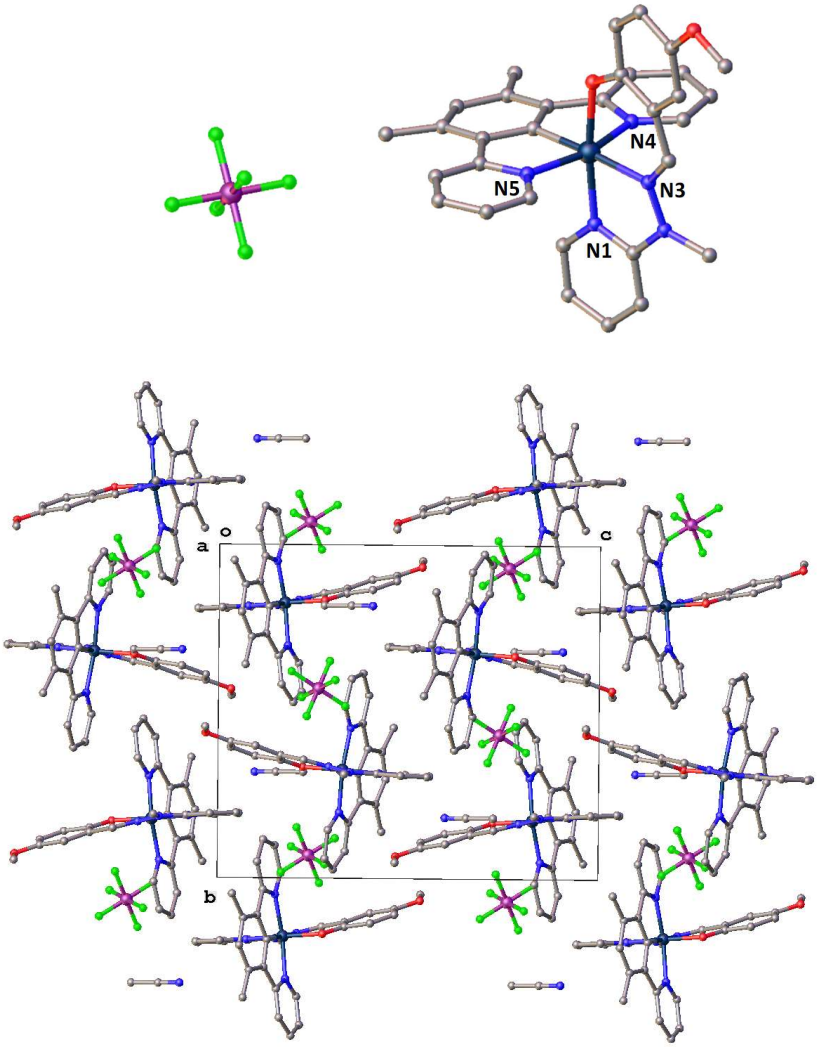

Figure 3.42: Crystal structure and packing of [Ir(dpyx)L[15]]PF_6. T = 120 K.

Table 3.8: Selected bond lengths, bond angles and distances for [Ir(dpyx)L[15]]PF_6

Bond Lengths (Å)		*Bond Angles (°)*		*Distances (Å)*	
Ir-C	1.9483(16)	N5-Ir-N4	161.42(6)	Ir···Ir	8.804
Ir-N4	2.0352(14)	C-Ir-N3	175.57(6)		
Ir-N5	2.0527(14)	O-Ir-N1	171.70(5)		
Ir-N1	2.0190(14)	C-Ir-N4	80.80(6)		
Ir-N3	2.0782(13)	N1-Ir-N3	78.79(5)		
Ir-O	2.0334(12)	O-Ir-N3	93.03(5)		

4 Photophysical Characterisation

4.1 Tridentate Pt(II) Complexes

4.1.1 Imine-based complexes

Electronic Absorption Spectra

The absorption spectra of complexes $PtL^{1-4}Cl$ (Figure 4.1) and $Pt(L^1)C{\equiv}C\text{-}Ar$ (Figure 4.2) were recorded in DCM at room temperature. The complexes show bands with high extinction coefficients in the far UV, moderately intense bands at ~400 nm and less intense bands at 500-600 nm.

The electronic spectra resemble those of the dioxovanadium(v) schiff-base complexes reported by Asgedom *et al*. using ligand HL^1 and a series of derivatives.[151] The very intense bands at wavelengths below 300 nm are assigned to $^1\pi\text{-}\pi^*$ transitions as they also appear in the ligand spectra.[151] We assign the multiple absorption bands centred around ~400 nm and 500/550 nm as charge-transfer transitions which involve the metal, and/or the chloride ligand and/or the imine ligand in line with the assignments of Asgedom *et al.* and Williams *et al.*[79]

The absorption wavelengths are very similar in each of the complexes but there is a significant red shift of the lowest energy band for PtL^2Cl; the lowest energy band has a λ_{max} of 550 nm, compared to 511nm for PtL^1Cl. The –OMe substituent on PtL^2Cl is strongly electron-donating; the red shift suggests the substituent is affecting the HOMO. This behaviour is indicative of transitions with an appreciable degree of charge-transfer character.[55]

Although the exchange of the chloride ligand for the phenylacetylide ligand does not change the spectral profile substantially, we do observe a significant increase in extinction coefficients for the higher energy absorption bands of $Pt(L^1)C_2Ar$. This is due to transitions within the Ar-C≡C unit and possibly also the introduction of additional charge-transfer transitions involving the acetylide.

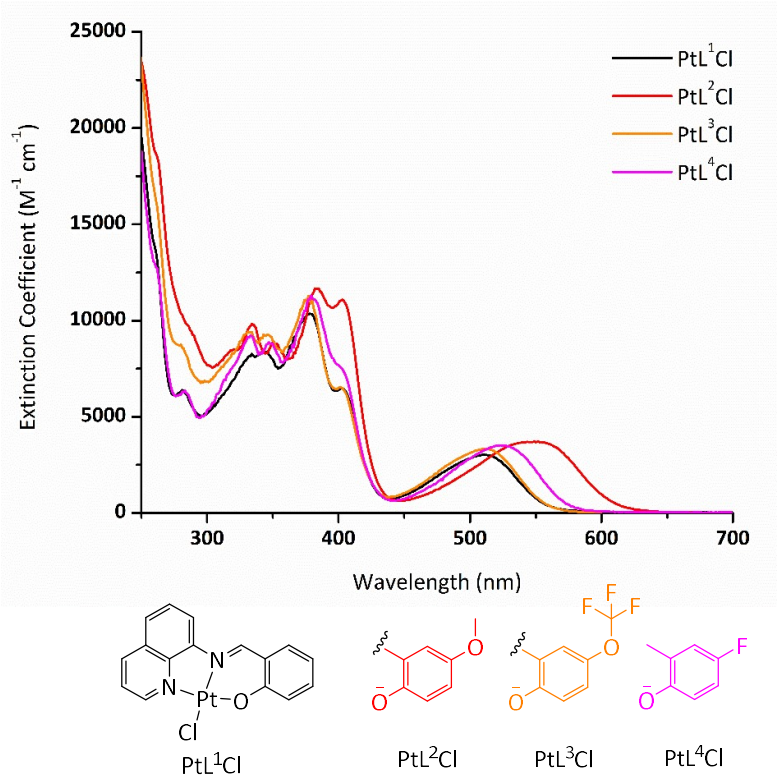

Figure 4.1: UV-Vis electronic absorption spectra of $PtL^{1-4}Cl$ in DCM at 298 K.

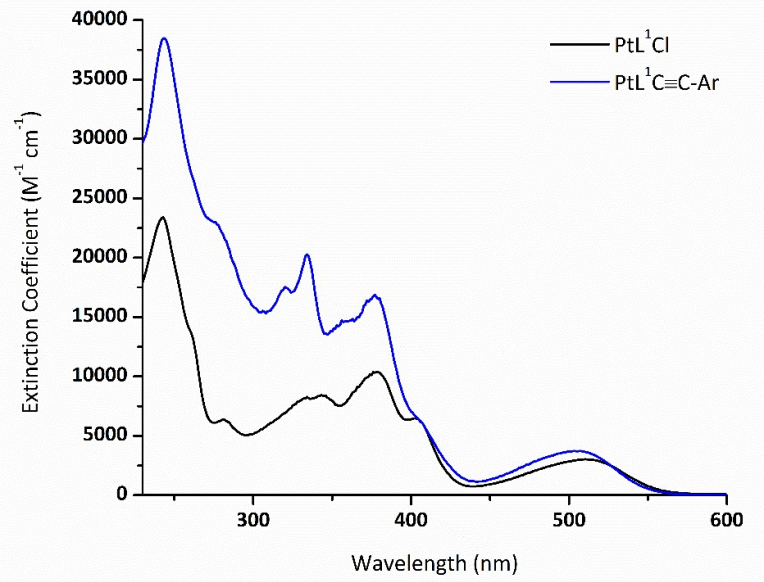

Figure 4.2: UV-Vis electronic absorption spectra of $PtL^{1}Cl$ and $PtL^{1}C{\equiv}C\text{-}Ar$ in DCM at 298 K.

Emission

The emission spectra of the complexes $PtL^{1-4}Cl$ and $PtL^{1}C{\equiv}C\text{-}Ar$ were recorded in degassed DCM at room temperature. Complexes $PtL^{1}Cl$, $PtL^{3}Cl$ and $PtL^{4}Cl$ displayed highly structured emission bands in the range 635 – 720 nm. The component band of highest

intensity is the 0-0 transition, suggesting little difference in geometry between the ground states and the emissive excited electronic states.[55] In contrast, weaker, structureless emission is displayed by complex PtL^2Cl in the far-red region (Figure 4.3). The parent complex PtL^1Cl emits light with a PLQY of 4%, whereas PtL^3Cl has a PLQY of 2.2%, PtL^4Cl has a PLQY of 2.9% and PtL^2Cl has a PLQY of 0.5%.

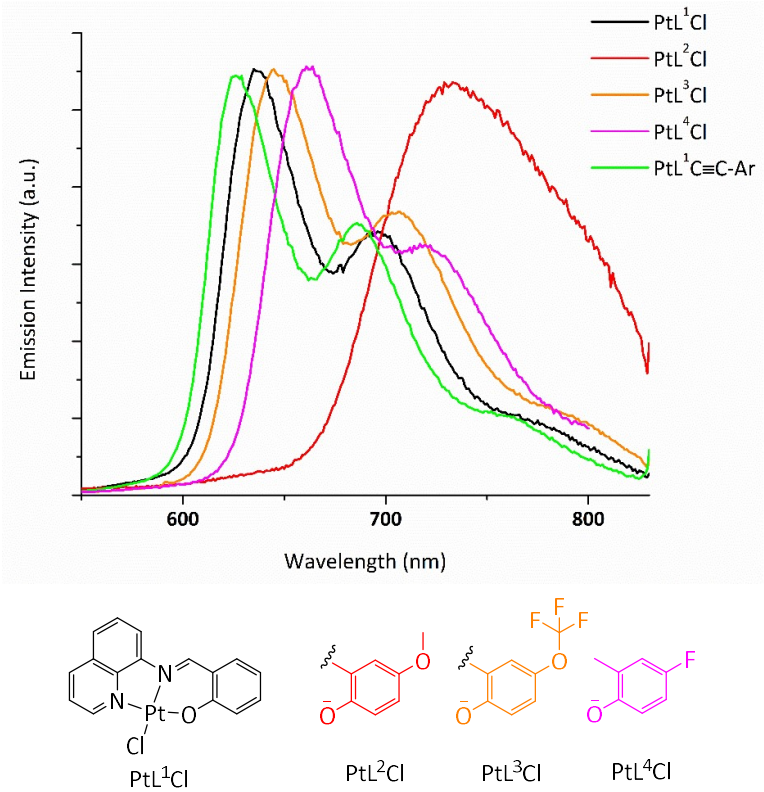

Figure 4.3: Normalised emission spectra of $PtL^{1-4}Cl$ and $PtL^1C{\equiv}C$-Ar in deoxygenated dichloromethane at 298 K.

The emission lifetime (τ) of the complexes are reported in Table 4.1, all complexes show susceptibility to quenching by dioxygen confirming that emission originates from a triplet state. The emission bimolecular rate constants for quenching by O_2 (k_q) of $PtL^{1-4}Cl$ and $PtL^1C{\equiv}C$-Ar are similar to the k_q values (~10^8 to 10^9 mol^{-1} dm^3 s^{-1}) of luminescent Pt(II) complexes reported in the literature.[89] The radiative (k_r) and nonradiative (k_{nr}) constants were estimated from the PLQYs (ϕ) and lifetimes (τ) of the phosphorescent complexes according to eq. 4.1 and 4.2, respectively. The non-radiative rate constants are significantly higher than the radiative rate constants for all of the complexes.

Table 4.1: Photophysical data for Complexes Pt(L^{1-4})Cl and Pt(L^1)C_2Ar

Complex	298 K							77 K	
	$\lambda_{(abs)}$ (nm)	$\lambda_{(em)}$ (nm)	τ^* (μs)[a]	ϕ[b] (%)	k_r (10^3 s^{-1})	k_{nr} (10^5 s^{-1})	k_q[d] (mol^{-1} dm^3 s^{-1})	$\lambda_{(em)}$ (nm)	τ (μs)
PtL^1Cl	281, 334, 346, 376, 402, 511	635, 700	6.8 (0.6)	4[b]	5.9	1.4	6.8×10^8	615, 677, 755	14
PtL^2Cl	318, 334, 353, 385, 403, 550	735	1.8 (0.3)	0.5[c]	2.8	5.5	1.3×10^9	677, 737	13
PtL^3Cl	280, 334, 346, 377, 401, 512	645, 710	4.5 (0.4)	2.2[b]	4.9	2.2	1.0×10^9	619, 686, 762	11
PtL^4Cl	284, 334, 348, 379, 403, 524	660, 720	4.8 (0.4)	2.9[b]	6.0	2.0	1.0×10^9	626, 689, 768	13
$PtL^1C{\equiv}C$-Ar	279, 320, 334, 378, 406, 505	629, 686	11 (0.4)	4.6[b]	4.3	0.9	1.1×10^9	607, 667, 741	20

[a] Luminescence lifetime in degassed DCM solution; corresponding values in air-equilibrated solution are given in parentheses. [b] ±10%. [c] ±20%
*[d] Bimolecular rate constant for quenching by O_2. *X^2 values are located in appendix 7.3*

$$k_r = \phi\tau^{-1} \quad (4.1)$$

$$k_{nr} = k_r(\phi^{-1} - 1) \quad (4.2)$$

The weaker emission of PtL^2Cl may be explained by considering the general trend in k_{nr} for this series; as the energy of emission decreases the nonradiative rate increases. Exchanging the chloride for the more strongly donating acetylide ligand only causes a small increase in PLQY (to 4.6%), which is attributed to the decrease in k_{nr} rather than any beneficial effect of the acetylide on k_r.

All complexes show increased emission at 77K in frozen EPA glass (EPA = diethyl ether, isopentane and ethanol 2/2/1 by volume) and the estimated lifetimes of the emissions remain in the range of microseconds, indicating phosphorescent emission. All of the complexes displayed highly structured spectra, with an approximate 500 cm^{-1} blue shift of the 0,0 band from the room temperature emission (Figure 4.4). PtL^2Cl appears to be shifted more significantly towards the blue by 1166 cm^{-1} however it is difficult to identify the 0,0 band in the room temperature spectra. The component band of highest intensity appears to be the 0,0 band in each of the spectra, indicating a small degree of distortion of the excited state.

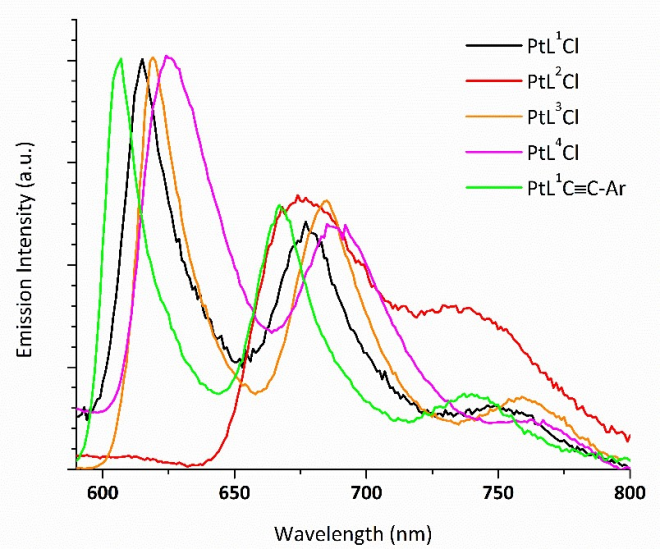

Figure 4.4: Normalised emission spectra of imine based complexes in EPA rigid glass at77 K.

DFT calculations

In order to further understand the molecular orbitals and the nature of excited states, density functional theory (DFT) calculations and time-dependent DFT (TDDFT) were performed using the B3LYP[152–154] method and LANL2DZ basis set for all atoms, with the Gaussian09 program. The orbital densities for the HOMO and LUMO are depicted in Figure 4.5. The HOMOs are spread over the phenol ring, the platinum, the chloride and the imine unit, with very little contribution from the quinoline unit. However, the LUMO is spread over the whole ligand with relatively little contribution from the Pt and the chloride.

It is important to note that the 4-position on the phenol ring appears to make a significant contribution to the HOMO and very little contribution to the LUMO, giving an insight into the substituent effects seen on the photophysical properties of the complexes. This spacial separation of the HOMO and the LUMO allows us to tune the HOMO-LUMO gap by using different substituents in the 4-position which can exert inductive or mesomeric effects that result in an electron donating or withdrawing character.[155] The electronic character of substituents can be quantified according to Hammett values (σ_{meta} or σ_{para}); more negative (positive) values are associated with more electron-donating (withdrawing) groups.[156] Complex PtL^2Cl displays a red shift in both its UV-Vis absorption and emission spectra. This reflects the electron-donating effect of the 4-OMe group (σ_p = -0.27), which destabilises the HOMO, decreasing the HOMO-LUMO gap.

Exchanging the 4-position substituent for 4-OCF_3 and 4-F in PtL^3Cl and PtL^4Cl, respectively, has a less pronounced effect. TDDFT calculations reveal that both the HOMO and LUMO are lowered by approximately the same extent in complexes PtL^3Cl and PtL^4Cl, resulting in very little deviation in ΔE from the parent complex PtL^1Cl. Although there appears to be a node in the LUMO at the 4-position on the phenyl ring, an inductive effect on the LUMO may be anticipated through the meta position of the phenyl ring (4-OCF_3 and 4-F σ_m = 0.38 and 0.34, respectively). Similarly, exchanging the chloride ligand for the acetylide (1-Ethynyl-3,5-bis(trifluoromethyl)benzene) causes a blue shift in the emission wavelength (λ_{em}) due to stabilisation of the HOMO, presumably also through an inductive effect from the CF_3 groups.

TDDFT calculations gave emission wavelengths in good agreement with the experimental data and revealed in all complexes the emission is mainly from HOMO → LUMO (70%) transitions. For all the complexes, the lowest energy absorption (S_0 → S_1) is

derived primarily (by 70% contribution) from the HOMO → LUMO transition. Interestingly, the S_0 → S_1 transition is not observed in the absorption spectra of any of the complexes, however the calculated S_2 state and subsequent transitions match well with the experimentally observed absorption spectra.

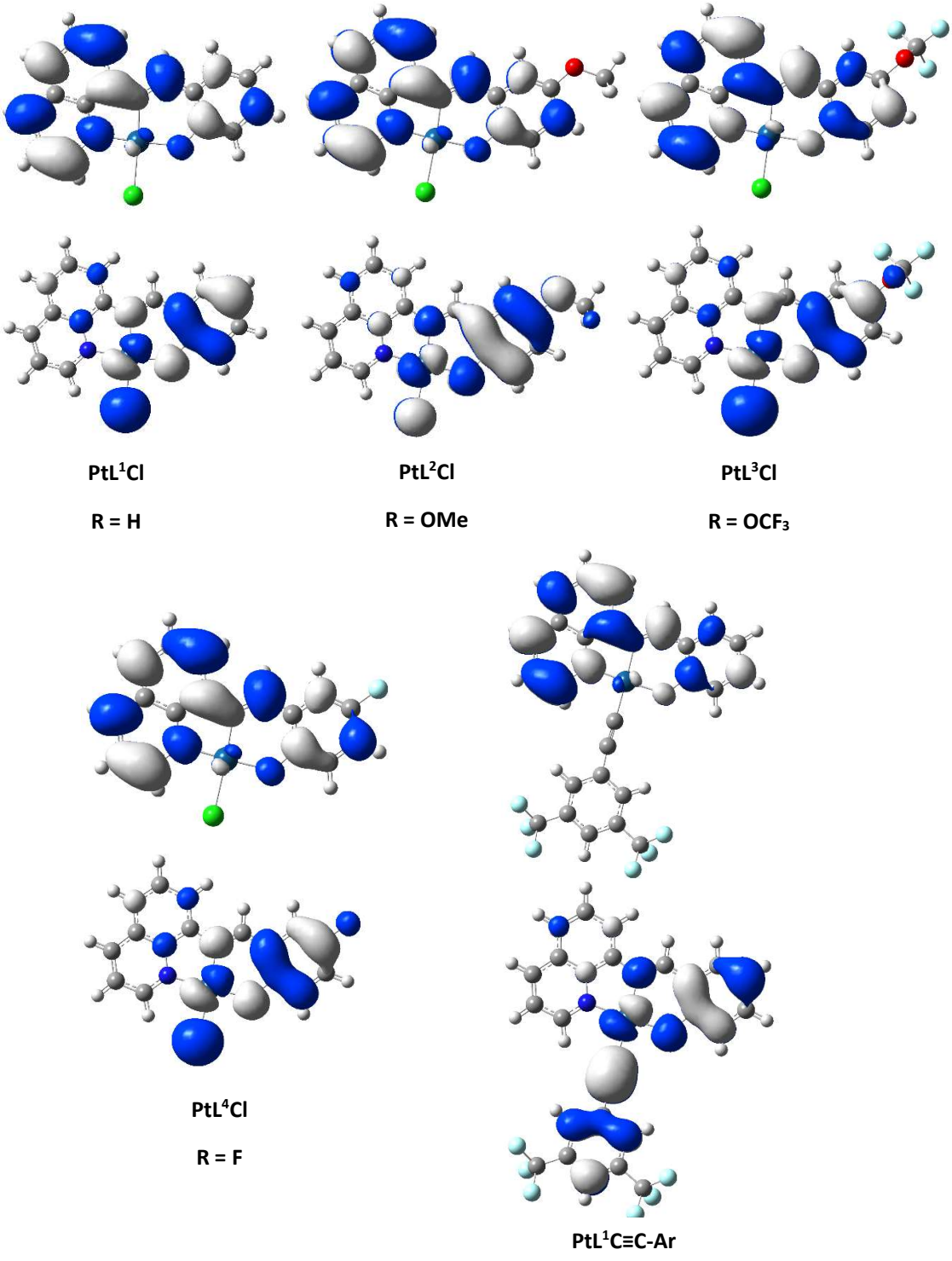

Figure 4.5: Calculated orbital density for the LUMO (top) and HOMO (bottom) of $PtL^{1-4}Cl$ and $PtL^{1}C{\equiv}C\text{-}Ar$ at their optimised S_0 geometries.

4.1.2 Hydrazone based complexes

Electronic Absorption Spectra of N-H complexes

The absorption spectra of $PtL^{5-13}Cl$ were recorded in MeCN at room temperature. We noted difficulties in obtaining consistent extinction coefficient values for each of the complexes; we observed a change in the ratio of various absorption bands upon dilution and the appearance and absence of other absorption bands.

We postulated that we may have a mixture of protonated and deprotonated complex causing the spectral changes we observed (Scheme 4.1). It is well documented that deprotonation of uncoordinated hydrazones occurs only in highly basic conditions but coordination to a metal ion causes a significant enhancement in acidity of the N-H proton.[157] The complexes of substituted hydrazones $R^1HNN=CHR^2$ are known as colorimetric reagents and their acid-base behaviour is accompanied by remarkable colour changes.[158] It was reported by Bacchi *et al.* that the palladium complex of 2-(diphenylphosphino)benzaldehyde 2-pyridylhydrazone (Hpbph) coexisted in both the protonated and deprotonated forms in the crystal.[159]

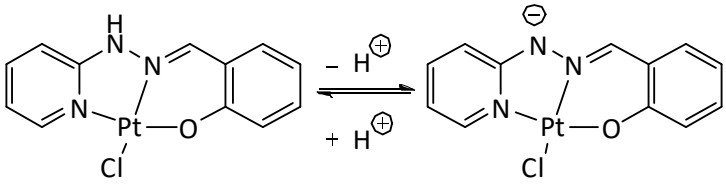

Scheme 4.1: Deprotonation of PtL^5Cl.

To investigate this phenomenon in our Pt-N^N^O^- complexes we measured the electronic absorption spectra of PtL^9Cl in the presence of various concentrations of acid or base in MeCN (Figure 4.6). The protonated complex shows moderately intense charge-transfer absorption bands at 349 and 430 nm. Addition of NEt_3 causes a loss of the 349 nm band and the appearance of two new absorption bands at 358 and 377 nm. We also observe that the absorption band at 430 nm increases in intensity and a new, more intense absorption band emerges at 448 nm. This red shift in absorption is likely due to the extension of π-conjugation in the deprotonated form. We see a colour change from pale yellow in the protonated form to bright yellow in the deprotonated form. The isosbestic points were maintained at 355, 306 and 297nm, indicating that the deprotonation reaction proceeds without any decomposition in this system. The original spectrum can be

recovered completely by addition of an acid such as acetic acid. We repeated this investigation with PtL^8Cl and observed the same acid-base response (Figure 4.7).

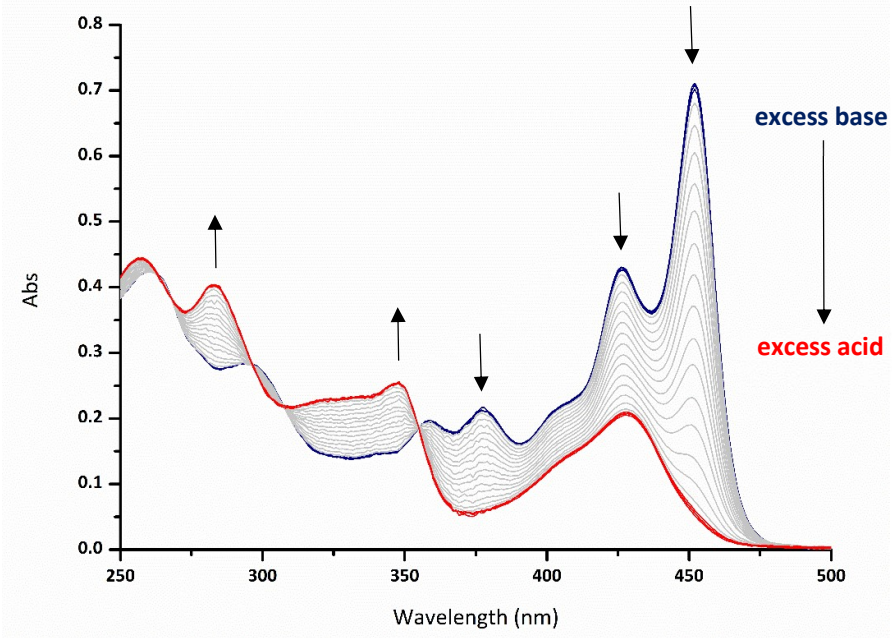

Figure 4.6: UV-Vis electronic absorption of PtL^9Cl at various concentrations of acid and base in MeCN

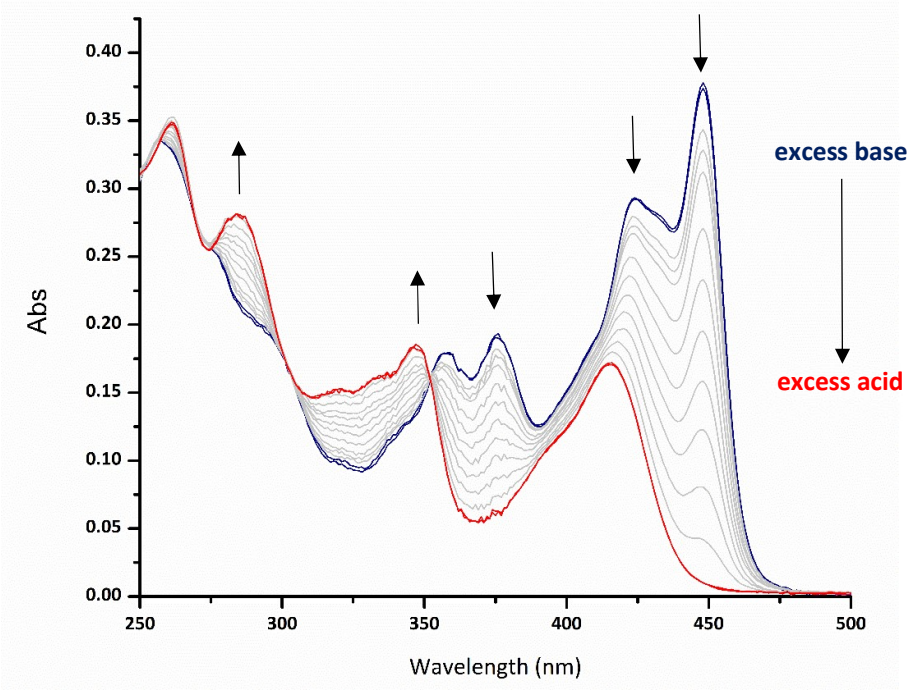

Figure 4.7: UV-Vis electronic absorption of PtL^6Cl at various concentrations of acid and base in MeCN

The extinction coefficients of complexes $PtL^{5-13}Cl$ in the protonated and deprotonated form are listed in Table 4.2. We assign the intense transitions <300 nm as $^1\pi$-π^*, due to the presence of these bands in the ligand spectra. The transitions between the regions of 325 to 360 nm are assigned as metal-to-ligand charge transfer, in line with the original assignment by Mohan *et al* for PtL^1Cl, PtL^6Cl, PtL^8Cl and $PtL^{10}Cl$.[141] The lowest energy transitions in the region of 400 - 500 nm are somewhat influenced by the R group on the phenyl ring, although no clear trend emerges with respect to electron-donating/withdrawing ability.

During the course of our investigation we observed some sensitivity of the complexes to light exposure when in solution. We recorded the spectral changes in a solution of PtL^9Cl when exposed to sunlight over a period of 6 hours (Figure 4.8). A gradual loss of absorption across the whole of the spectrum was observed and a rise in the baseline suggesting the precipitation of an insoluble degradation product.

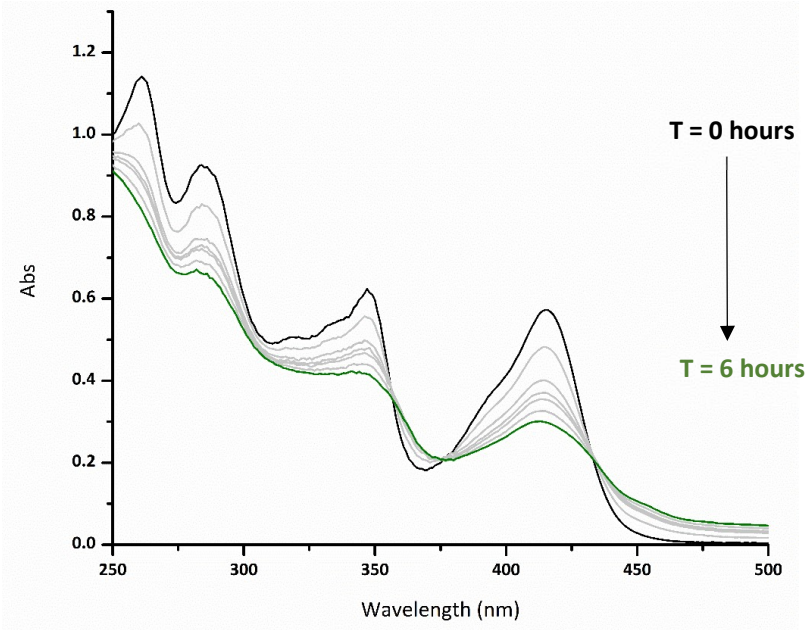

Figure 4.8: UV-Vis electronic absorption of PtL^9Cl in MeCN on exposure to sunlight, measurements taken at hourly intervals.

Table 4.2: Extinction coefficients for complexes $PtL^{5\text{-}13}Cl$ under acidic and basic conditions.

Complex	Absorption λ_{max} / nm [(a)] (ε/ M^{-1} cm^{-1}) excess acid	Absorption λ_{max} / nm [(a)] (ε/ M^{-1} cm^{-1}) excess base
PtL^5Cl	268 (28831), 280 (20472), 346 (9883), 417 (6747)	297 (14434), 358 (9395), 375 (10164), 423 (16350), 447 (22866)
PtL^6Cl	262 (24728), 285 (19663), 349 (12858), 417 (12641)	298 (13303), 358 (12008), 377 (12856), 425 (19787), 448 (25635)
PtL^7Cl	257 (25908), 285 (17955), 351 (11842), 429 (9712)	297 (14429), 359 (7735), 377 (8111), 428 (18810), 454 (33917)
PtL^8Cl	279 (21100), 338 (18715), 410 (15047), 448 (7632)	287 (11893), 351 (22078), 369 (25715), 426 (16881), 449 (23762)
PtL^9Cl	259 (18763), 284 (16792), 349 (10985), 430 (10234)	295 (12653), 361 (8499), 379 (9448), 427 (19159), 453 (31693)
$PtL^{10}Cl$	261 (26190), 284 (19986), 348 (12558), 426 (9282)	297 (14641), 358 (9146), 377 (9625), 426 (19480), 452 (32111)
$PtL^{11}Cl$	264 (21486), 289 (15741), 351 (10975), 409 (14474)	291 (15428), 357 (13589), 376 (13904), 430 (18819), 449 (18077)
$PtL^{12}Cl$	270 (20397), 287 (18363), 349 (13115), 442 (8185)	302 (14179), 365 (8861), 384 (10041), 433 (16646), 458 (26468)
$PtL^{13}Cl$	269 (33055), 334 (12388), 353 (11961), 441 (14829)	297 (22967), 378 (7842), 399 (8498), 441 (21893), 470 (32967)

[(a)] Absorption maxima >250nm

Electronic Absorption Spectra of N-Me Complexes

The absorption spectra of complexes $PtL^{14-20}Cl$ (Figure 4.9) and $PtL^{14}C{\equiv}C$-Ar (Figure 4.10) were recorded in DCM at room temperature. The complexes show bands with high extinction coefficients in the far UV and moderately intense bands at ~350 nm and 400-500 nm. We note the similarity of the spectra to the protonated N-H hydrazone bridged complexes and assign the transitions in the same manner (Figure 4.11). The lowest energy transitions in the region of 475 - 525 nm are again somewhat influenced by the R group on the phenyl ring, although no clear trend emerges with respect to electron-donating/withdrawing ability.

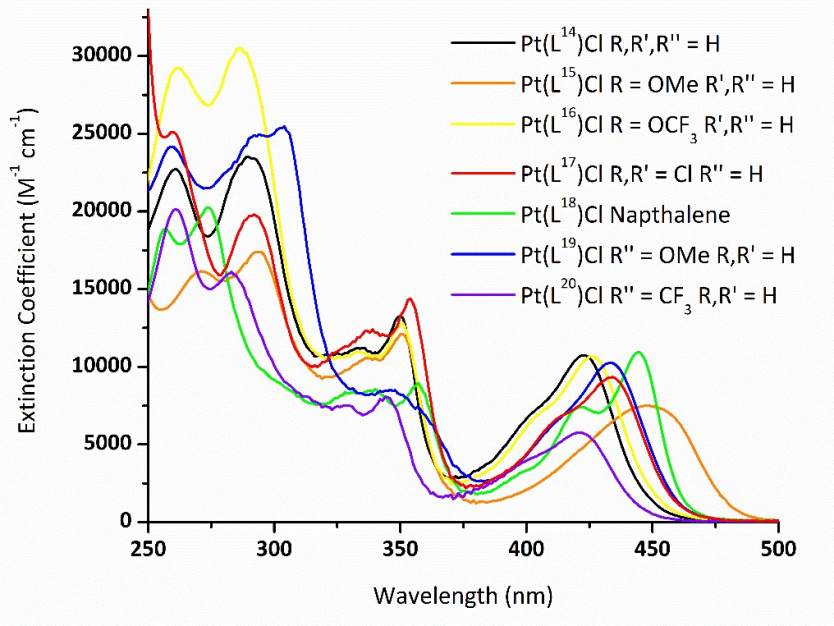

Figure 4.9: UV-Vis electronic absorption spectra of $PtL^{14-20}Cl$.

Although the substitution of the chloride ligand in $PtL^{14}Cl$ by the phenylacetylide ligand in $PtL^{14}C{\equiv}C$-Ar does not change the spectral profile substantially, there is a general red shift of the lower energy absorption bands (Figure 4.10). The strong σ-donation from the phenylacetylide ligand is expected to render the platinum centre more electron-rich and hence raise the dπ(Pt) orbital energy, leading to a lower energy MLCT absorption.[160]

We investigated the effect of both acid and base on the absorption profile of the N-Me complexes and observed no spectral changes. This verifies the origin of the spectral changes observed in the complexes $PtL^{5-13}Cl$ as being due to deprotonation of the N-H. The N-Me complexes did not show any evidence of decomposition, even when solutions were exposed to sunlight during the daylight hours for a period of one week.

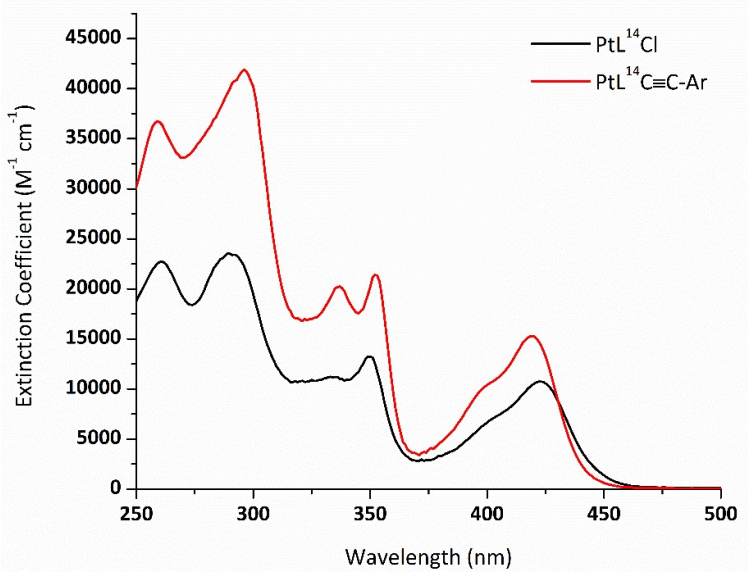

Figure 4.10: UV-Vis electronic absorption spectra of $PtL^{14}Cl$ and $PtL^{14}C{\equiv}C\text{-}Ar$.

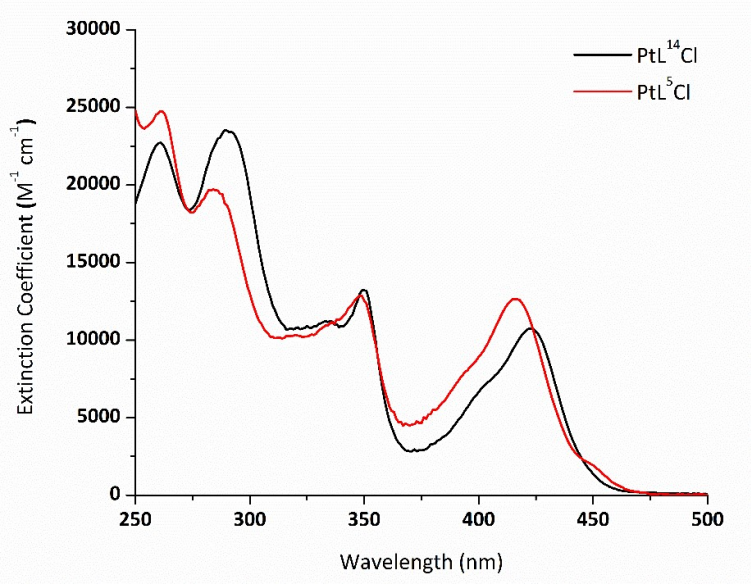

Figure 4.11: UV-Vis electronic absorption spectra of $PtL^{14}Cl$ and $PtL^{5}Cl$.

Emission of Hydrazone Based Pt(II) Complexes

The emission spectra of the hydrazone based Pt(II) complexes were recorded in degassed MeCN $PtL^{5-13}Cl$ or degassed DCM $PtL^{14-20}Cl$ at room temperature.

For all of the N-Me hydrazone based Pt(II) complexes $PtL^{14-20}Cl$ we observed weak luminescence in solution at room temperature; the PLQYs in a degassed solution are of the order of 0.4 — 2.1%. This is in contrast to the related complex $[Pt(tpy)Cl]^+$ which is essentially non emissive under these conditions. The lack of emission from $[Pt(tpy)Cl]^+$ is attributed to the presence of low-lying d-d excited states that provide a thermally activated non-radiative decay pathway for the MLCT state.[51] The introduction of the pseudo-cyclometallating O^- atom probably increases the ligand-field strength and hence the energy of the d-d state, reducing the accessibility of this pathway.

The emission spectra of the N-Me complexes are poorly structured and broad, typical of luminescence from states with a high degree of charge-transfer character (Figure 4.12). The emission maxima are affected by substituents on the phenyl ring, although no clear trend emerges with respect to electron-donating/withdrawing ability. The 'parent' complex $PtL^{14}Cl$ emits light with a PLQY of 1.7% and substitution of the R group causes very little variation in the PLQY (1.5-1.2%). Substitutions on the pyridine have a much less pronounced effect on the wavelength of emission (Figure 4.13) and again the PLQY shows little variation (1.7 – 2.1%).

The component band of highest intensity appears to be the 0—1 transition, with the 0 – 0 transition appearing as a shoulder, indicating a more significant difference in geometry between the ground and excited electronic state compared to the earlier series of complexes.[55] This geometrical distortion of the molecule in the excited state can lead to efficient pathways to non-radiative decay.

Exchanging the chloride in $PtL^{14}Cl$ for the more strongly donating acetylide ligand results in a significant increase in the PLQY of $PtL^{14}C{\equiv}C\text{-}Ar$ to 11% from 1.7%. The emission spectrum is quite similar to that of the parent complex (Figure 4.14), although the vibrational structure is better defined and the emission is marginally blue shifted (approx. 20 nm). Changing the co-ligand to an acetylide also causes an increase in the luminescence lifetime, which is raised to 9.3 vs. 2.1 in the parent complex $PtL^{14}Cl$. The PLQY and lifetime are both increased by a comparable factor suggesting that the increase in PLQY in the acetylide complex is indeed due to a reduction in nonradiative decay pathways.

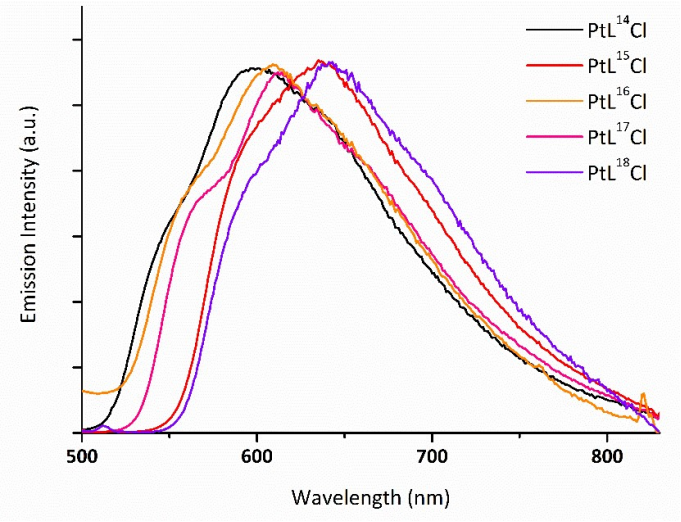

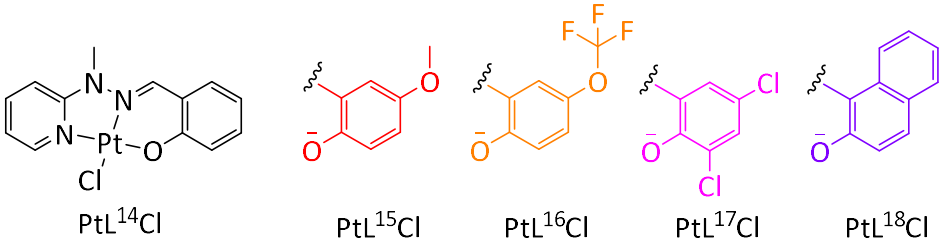

Figure 4.12: Normalised emission spectra of PtL[14-18]Cl in degassed DCM at 298 K.

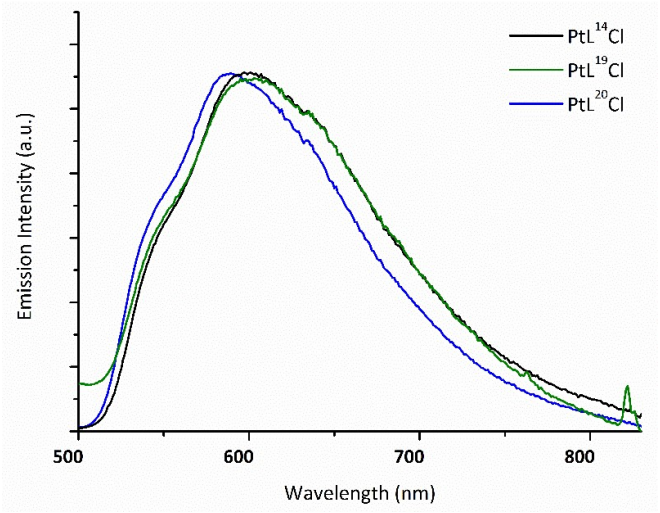

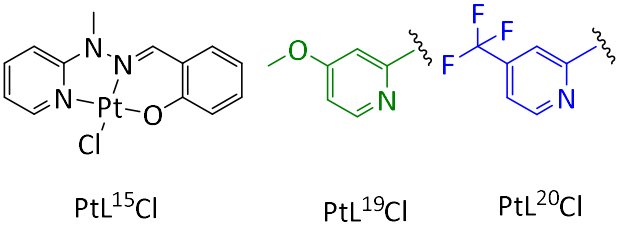

Figure 4.13: Normalised emission spectra of PtL[14]Cl and PtL[19-20]Cl in degassed DCM at 298 K.

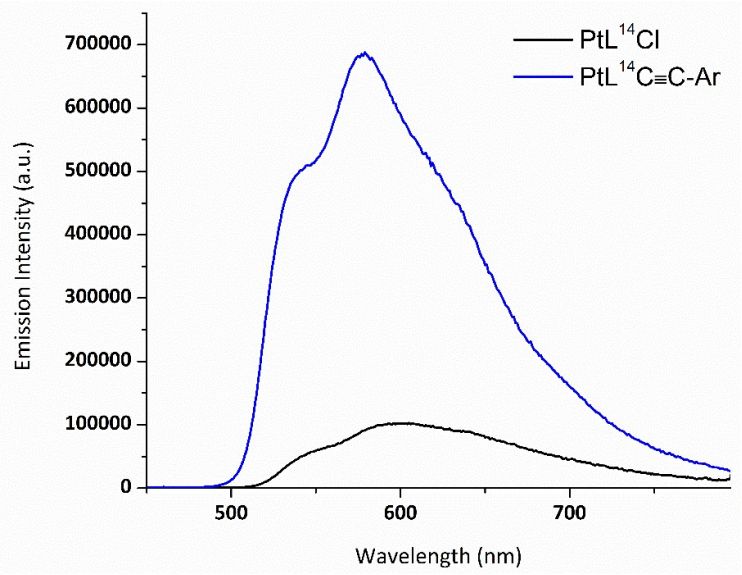

Figure 4.14: Relative emission spectra of PtL[14]Cl vs. PtL[14]C≡C-Ar in degassed DCM at 298 K.

The emission lifetime (τ) of the complexes are reported in Table 4.3, all complexes show susceptibility to quenching by dioxygen confirming that emission originates from a triplet state. The emission bimolecular rate constants for quenching by O_2 (k_q) of PtL$^{14\text{-}20}$Cl and PtL^{14}C≡C-Ar are similar to the k_q values (~10^8 to 10^9 mol^{-1} dm^3 s^{-1}) of luminescent Pt(II) complexes reported in the literature.[89] The radiative (k_r) and nonradiative (k_{nr}) constants were estimated from the PLQY (ϕ) and lifetime (τ) of the phosphorescent complexes according to eq. 4.1 and 4.2, respectively. The non-radiative rate constants are significantly higher than the radiative rate constants for all of the complexes. It is interesting to note that the radiative rate constant for the hydrazone based NMe 'parent' complex, PtL^{14}Cl (8.1 x 10^3 s^{-1}) is higher than the earlier discussed imine based parent complex, PtL^{1}Cl (5.9 x 10^3 s^{-1}), as might be expected if the excited state has more MLCT character. However, the non-radiative rate constant is significantly higher in the hydrazone based complex (4.7 vs 1.4 x 10^5 s^{-1}) resulting in a lower PLQY (1.7 vs 4%). Inspection of the crystal structures of the imine and hydrazone based complexes reveals an insight into this difference, the bite angle in the imine based complex is closer to 180° which gives a stronger ligand field and promotes the d-d energy, reducing k_{nr}. Exchanging the chloride co-ligand for an acetylide ligand increases the radiative rate constant by a small degree but significantly reduces the non radiative decay, resulting in the increased luminescence life time and PLQY. Replacement of the phenol with a naphthol unit causes a significant reduction in PLQY (PtL^{18}Cl, 0.4%), due to a reduction in the radiative decay accompanied by an increase in the non-radiative decay.

Table 4.3: Photophysical data for Complexes $PtL^{14-20}Cl$ and $PtL^{14}C{\equiv}C\text{-}Ar$

Complex	298 K							77 K	
	$\lambda_{(abs)}$ (nm)	$\lambda_{(em)}$ (nm)	τ* (μs)[a]	Φ (%)	k_r (10^3 s^{-1})	k_{nr} (10^5 s^{-1})	k_q[e] (mol^{-1} dm^3 s^{-1})	$\lambda_{(em)}$ (nm)	τ (μs)
$PtL^{14}Cl$	261, 292, 333, 350, 399 (sh), 423	597	2.1 (0.4)	1.7[b]	8.1	4.7	9.2×10^8	529, 575, 628	36
$PtL^{15}Cl$	274, 294, 339, 351, 448	637	3.4 (0.2)	1.5[b]	4.4	2.9	2.1×10^9	564, 614, 674	39
$PtL^{16}Cl$	261, 286, 335, 351, 403 (sh), 427	609	2.3 (0.4)	1.4[b]	6.1	4.3	9.4×10^8	540, 589, 645	40
$PtL^{17}Cl$	261, 293, 338, 354, 412 (sh), 434	614	2.3 (0.3)	1.2[b]	5.2	4.3	1.2×10^9	545, 594, 653	36
$PtL^{18}Cl$	257, 274, 330, 340, 357, 422, 444	641	1.5 (0.4)	0.4[c]	2.7	6.6	8.3×10^8	575, 628, 689	23
$PtL^{19}Cl$	259, 294, 304, 349, 410 (sh), 435	598	1.8 (0.3)	1.7[b]	9.4	5.4	1.3×10^9	528, 573, 627	41
$PtL^{20}Cl$	261, 283, 331, 346, 398 (sh), 422	589	2.0 (0.3)	2.1[d]	11	4.9	1.3×10^9	529, 576, 629	49
$PtL^{14}C{\equiv}C\text{-}Ar$	260, 297, 338, 353, 399 (sh), 420	540 (sh), 578	9.3 (0.4)	11[d]	12	0.9	1.1×10^9	523, 568, 620	55

[a] Luminescence lifetime in degassed DCM solution; corresponding values in air-equilibrated solution are given in parentheses. [b] ±20%.[c] ±30% [d] ±10%

*[e] Bimolecular rate constant for quenching by O_2. *X^2 values are located in appendix 7.3*

All complexes show more intense emission at 77K in frozen EPA glass (EPA = diethyl ether, isopentane and ethanol 2/2/1 by volume) and the estimated lifetimes of the emissions remain in the range of microseconds, indicating phosphorescent emission. All of the complexes displayed highly structured emission, with an approximate 500 cm^{-1} blue shift from the room temperature emission (Figure 4.15). The component band of highest intensity is the 0 – 1 transition in all of the complexes, indicating a larger degree of distortion in the excited state in comparison to the earlier discussed imine based complexes.

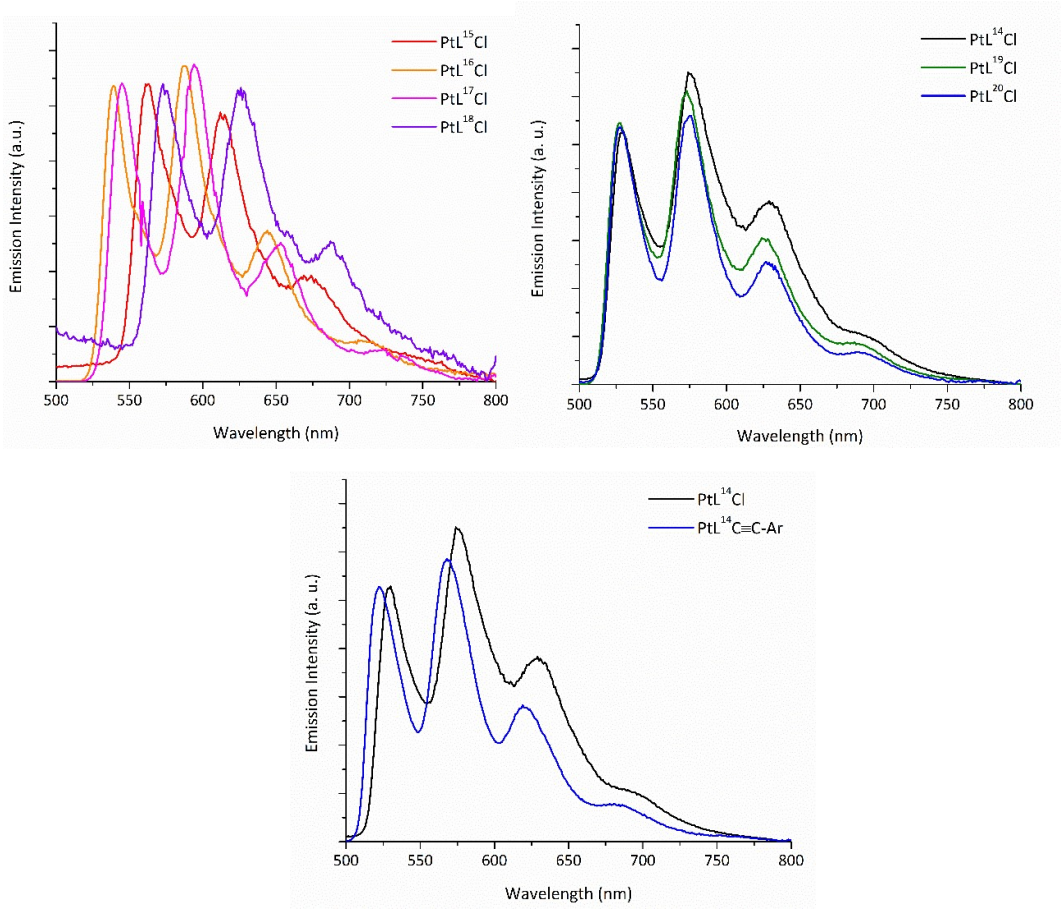

Figure 4.15: Normalised emission spectra of hydrazone (NMe) based complexes in EPA rigid glass at 77 K. Top left: $PtL^{15}Cl$ – $PtL^{18}Cl$; top right: $PtL^{14}Cl$ and $PtL^{19}Cl$ – $PtL^{20}Cl$; bottom: $PtL^{14}Cl$ and $PtL^{14}C{\equiv}C\text{-}Ar$.

Due to the sensitivity to light of the N-H hydrazone bridged complexes the series was deemed unsuitable for detailed luminescence studies. $PtL^{6}Cl$ was chosen as a representative complex for limited emission studies. The emission spectra of $PtL^{6}Cl$ (R = 5-Me) was recorded under acidic and basic conditions in degassed acetonitrile at room temperature (Figure 4.16). Regardless of the pH, the complex was only weakly luminescent in solution at room temperature.

The protonated form of the complex showed broad (half-height width of 145 nm), orange emission (λ_{max} = 597 nm) with a PLQY of 0.003. Close inspection of the emission profile reveals the presence of poorly resolved vibronic structure; the component band of highest intensity appears to be the 0—1 transition, with the 0 – 0 transition appearing as a shoulder, suggesting a reasonably significant difference in geometry between the ground and excited electronic states.[55]

The deprotonated form of the complex showed more structured emission with better resolved vibronic coupling. The emission is red shifted with lowest energy emission band 0—0 and the 0—1 band approximately equal in intensity. The PLQY is reduced to 0.001.

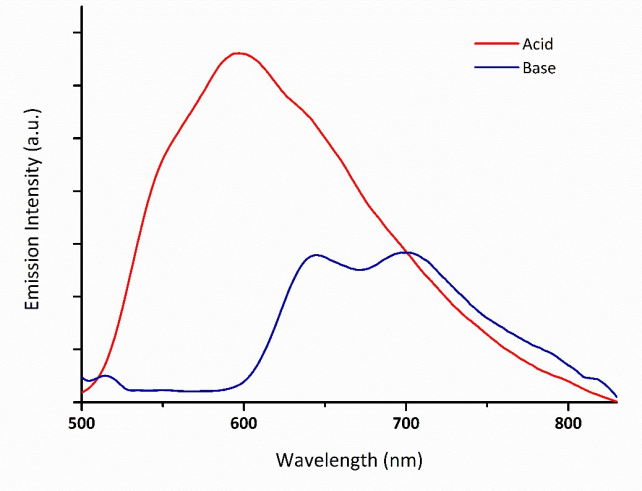

Figure 4.16: Normalised emission spectra of PtL^{6}Cl in degassed MeCN at 298 K with the addition of acetic acid (red) and NEt$_3$ (blue)

DFT calculations

In order to further understand the molecular orbitals and the nature of excited states, density functional theory (DFT) calculations and time-dependent DFT (TDDFT) were performed using the B3LYP[152–154] method and LANL2DZ basis set for all atoms, with the Gaussian09 program. The orbital densities for the HOMO and LUMO of complex PtL^{14}Cl are depicted in Figure 4.17. The HOMO and LUMO are both spread over the whole ligand and the platinum however only the HOMO has contribution from the chloride atom. The lack of spatial separation of the HOMO and LUMO gives an insight into the unpredictable substituent effects seen on the photophysical properties of the complexes.

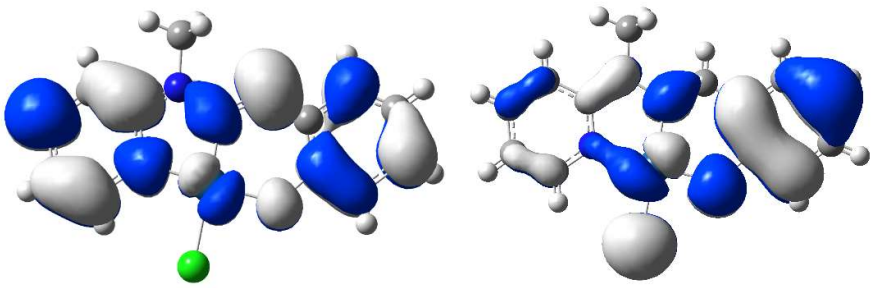

Figure 4.17: Calculated orbital density for the LUMO (left) and the HOMO (right) of PtL[14]Cl at its optimised S_0 geometry.

4.1.3 Pyrazole based complex

Photophysical Properties

The absorption spectrum of PtL[21]Cl was recorded in DCM at room temperature, it shows strong absorption in the high-energy region and slightly weaker absorption in the low-energy region (Figure 4.18). The high energy, intense absorptions can be assigned as ligand based $^1\pi - \pi^*$ transitions. There is a broad low energy band at 429 nm with a shoulder at 410 nm, attributed to charge transfer bands due to the similarity of the spectra to previously discussed complexes. There is no observable emission at ambient temperature in solution or in the solid state.

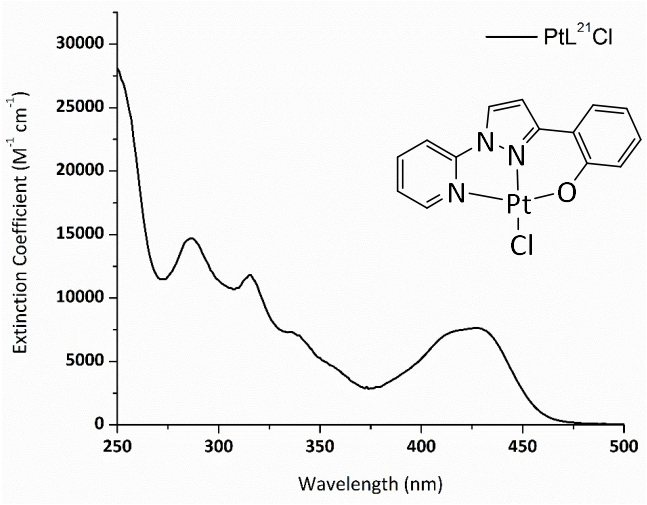

Figure 4.18: UV-Vis electronic absorption spectra of PtL[21]Cl in DCM at 298K.

4.1.4 Hydrazide based complexes

Electronic Absorption Spectra

The absorption spectra of a-PtL^{22}Cl and b-PtL^{22}Cl$_2$ were recorded in DCM at room temperature (Figure 4.19). The transitions below 400 nm are assigned as ligand-centred due to the presence of these bands in the ligand spectra.[131] The absorption bands centred at 470 nm confirm the presence of the N(amidate) atom of the hydrazone ligand (Scheme 4.2). Kitamura *et al.* carried out an in-depth study of the coordination of ligand HL^{22} to Pd(II) – the study found that across 8 complexes, only those with an N(amidate) atom showed an absorption band in this region.[161] The absorption band in the visible region is mainly attributed to the intraligand π – π* transition of the hydrazone ligand. The related Pd(II), Pt(II), Cu(II) and Ni(II) complexes containing N(amidate) atoms also showed a characteristic absorption band in this region, attributed to the intraligand transition.[157,158,161]

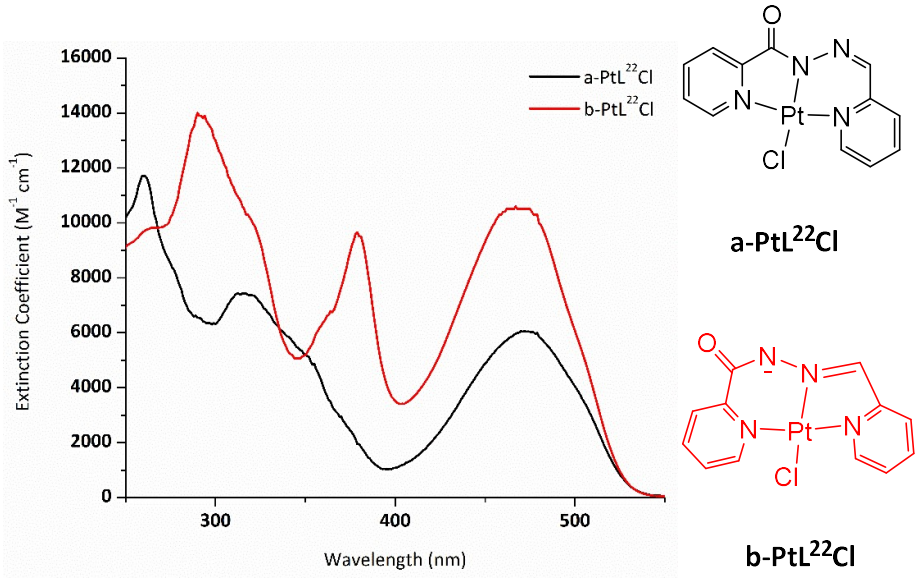

Figure 4.19: UV-Vis electronic absorption spectra of a-PtL^{22}Cl and b-PtL^{22}Cl in DCM at 298K.

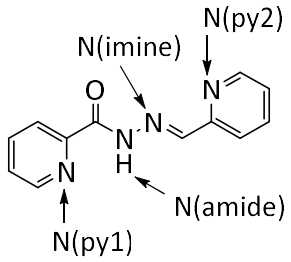

Scheme 4.2: Coordination sites in the hydrazide ligand L^{22}.

Emission

The emission spectra of the hydrazide based complexes were recorded in degassed DCM at room temperature (Figure 4.20). Complex a-PtL^{22}Cl displays highly structured emission bands in the range 625 – 756 nm. The component band of highest intensity is the 0-0 transition, suggesting little difference in geometry between the ground state and the emissive excited electron state. In contrast, weaker, less structured emission is displayed by b-PtL^{22}Cl in the region 531 – 612 nm. The component band of highest intensity appears to be the 0—1 transition, with the 0 – 0 transition appearing as a shoulder, indicating a more significant difference in geometry between the ground and excited electronic state compared to a-PtL^{22}Cl.[55] This geometrical distortion of the molecule in the excited state can lead to efficient pathways to non-radiative decay.

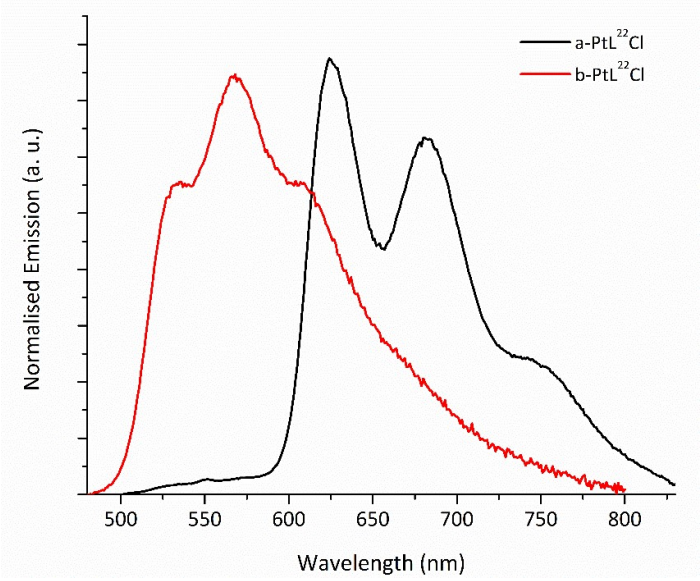

Figure 4.20: Normalised emission spectra of a-PtL^{22}Cl and b-PtL^{22}Cl in degassed DCM at 298 K.

The emission lifetimes (τ) of the complexes are reported in Table 4.4. It is interesting to note that complex a-PtL^{22}Cl shows susceptibility to quenching by dioxygen confirming that emission originates from a triplet state. The emission bimolecular rate constant for quenching by O_2 (k_q) of a-PtL^{22}Cl is similar to the k_q values (~10^8 to 10^9 mol^{-1} dm^3 s^{-1}) of luminescent Pt(II) complexes reported in the literature.[89] Complex b-PtL^{22}Cl however does not show susceptbility to quenching by dioxygen. The PLQY of a-PtL^{22}Cl is 0.5%, whereas b-PtL^{22}Cl has a PLQY of 0.1%. The non-radiative rate constants are significantly higher than the radiative rate constants for both of the complexes. The radiative and non-radiative rate constant is lower in b-PtL^{22}Cl than a-PtL^{22}Cl.

Both the complexes show increased emission at 77K in butyronitrile (Figure 4.21). The complexes display highly structured emission, the emission λ_{max} of complex a-PtL^{22}Cl remains relatively unchanged. It is interesting to note this complex does not display the rigidochromic effect, MLCT states are very sensitive to the medium rigidity while the energy of ligand-centered excited states remain unchanged.[162] A ligand-centered assignment is further supported by the highly structured vibrational profile of a-PtL^{22}Cl. In contrast, we observe an approximate 1000 cm^{-1} blue shift from the room temperature emission λ_{max} of b-PtL^{22}Cl. This shift is the largest of the complexes discussed so far and is indicative of a larger degree of distortion in solution at room temperature. The component band of highest intensity in b-PtL^{22}Cl is the 0 – 1 transition, further indicating a significant degree of distortion in the excited state.

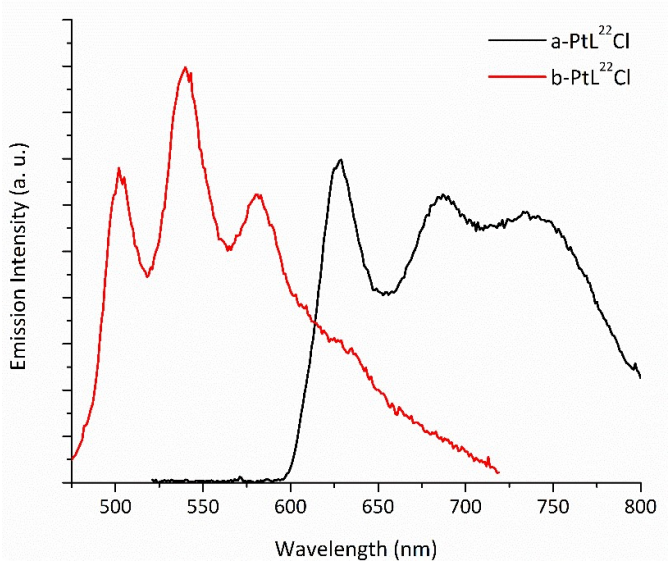

Figure 4.21: Normalised emission spectra of a-PtL^{22}Cl and b-PtL^{22}Cl in butyronitrile rigid glass at 77 K.

Table 4.4: Photophysical data for Complexes a-PtL^{22}Cl and b-PtL^{22}Cl

Complex	298 K							77 K	
	$\lambda_{(abs)}$ (nm)	$\lambda_{(em)}$ (nm)	τ^{*} (μs)[a]	Φ (%)	k_r (10^3 s^{-1})	k_{nr} (10^5 s^{-1})	k_q[d] (mol^{-1} dm^3 s^{-1})	$\lambda_{(em)}$ (nm)	τ (μs)
a-PtL^{22}Cl	261, 317, 356(sh) , 478	625, 683, 756	0.4 (0.2)	0.5[b]	1.3	25	1.1 x 10^9	629, 688, 742	0.9
b-PtL^{22}Cl	293, 323(sh), 381, 471	531, 569, 612	1.5 (1.5)	0.1[c]	0.6	6.6	0	502, 541, 582	0.7

*[a] Luminescence lifetime in degassed DCM solution; corresponding values in air-equilibrated solution are given in parentheses. [b] ±20% [c] ±30% [d] Bimolecular rate constant for quenching by O_2. *X^2 values are located in appendix 7.3*

Table 4.5: Photophysical data for Complexes PtL^{25}Cl

Complex	298 K							77 K		solid state at 298 K		
	$\lambda_{(abs)}$ (nm)	$\lambda_{(em)}$ (nm)	τ^{*} (ns)[a]	Φ[b] (%)	k_r (10^4 s^{-1})	k_{nr} (10^6 s^{-1})	k_q[c] (mol^{-1} dm^3 s^{-1})	$\lambda_{(em)}$ (nm)	τ (μs)	$\lambda_{(em)}$ (nm)	τ (ns)	Φ[d] (%)
PtL^{23}Cl	265, 331, 405	-	-	-	-	-	-	475, 508, 546	8.3	523	770	1.6
PtL^{24}Cl	274, 341, 402	-	-	-	-	-	-	491, 523, 564	5.3	575	1000	1.4
PtL^{25}Cl	268, 326, 416	627	48 (39)	0.1	2.1	2.1	1.6 x 10^9	560, 602, 654	0.1	-	100	---[e]

*[a] Luminescence lifetime in degassed DCM solution; corresponding values in air-equilibrated solution are given in parentheses. [b] ±30%.[c] Bimolecular rate constant for quenching by O_2 [c] ±20% [d] too weak to measure PLQY. *X^2 values are located in appendix 7.3*

4.1.5 Imide and Amide-based complexes

Electronic Absorption Spectra

The imide-based complexes $PtL^{23\text{-}25}Cl$ are very poorly soluble in all common organic solvents. The absorption spectra of imide based complexes $PtL^{23\text{-}25}Cl$ were recorded in dilute (1.2×10^{-5} mol/dm^3) DCM solution at room temperature (Figure 4.22). The complexes show strong absorption in the far UV and less intense bands at ~325 and ~400 nm. The absorption at approx. 270 nm is assigned to ligand based $^1\pi - \pi^*$ transitions due to the presence of this band in the ligand spectra.[121] The absorptions in the low-energy region are assigned to bands of charge transfer character.

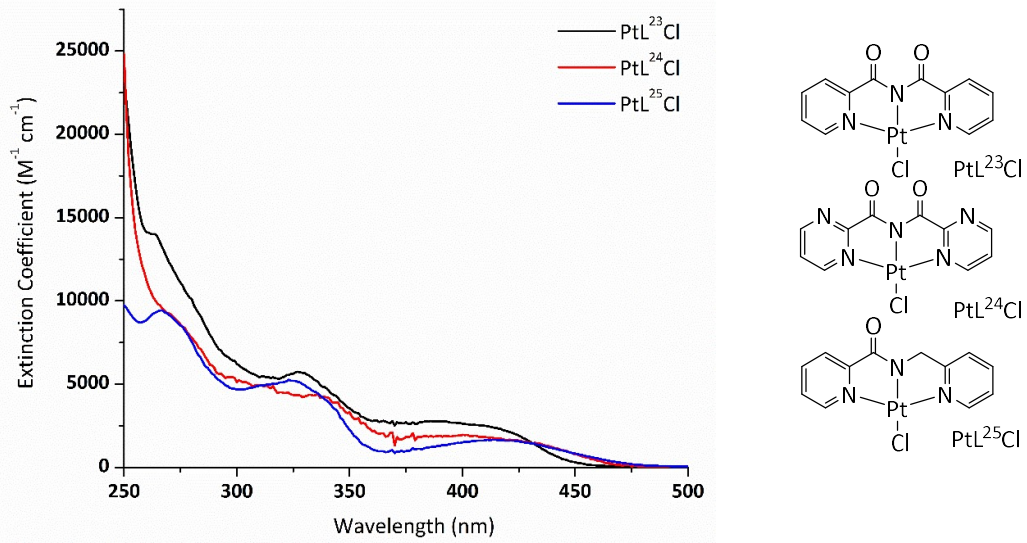

Figure 4.22: UV-Vis electronic absorption spectra of $PtL^{23\text{-}25}Cl$ in DCM at 298K.

Emission

The emission spectra of the complexes $PtL^{23}Cl$ – $PtL^{25}Cl$ were recorded in degassed DCM at room temperature. The imide-based complexes $PtL^{23}Cl$ and $PtL^{24}Cl$ are essentially non-emissive in fluid solution at room temperature. For the amide-based complex $PtL^{25}Cl$ we observe weak luminescence in solution at room temperature (ϕ = 0.1%). The emission spectra are poorly structured and broad, typical of luminescence from states with a high degree of charge-transfer character (Figure 4.23).

The emission lifetime (τ) is reported in Table 4.5. It is interesting to note that despite the relatively short lifetime of complex $PtL^{25}Cl$, we observe susceptibility to quenching by dioxygen confirming that emission originates from a triplet state. The emission bimolecular rate constant for quenching by O_2 (k_q) of $PtL^{25}Cl$ is similar to the k_q values (~10^8 to 10^9 mol^{-1} dm^3 s^{-1}) of luminescent Pt(II) complexes reported in the literature.[89] The non-radiative

rate constant is significantly higher than the radiative rate constant, resulting in weak emission.

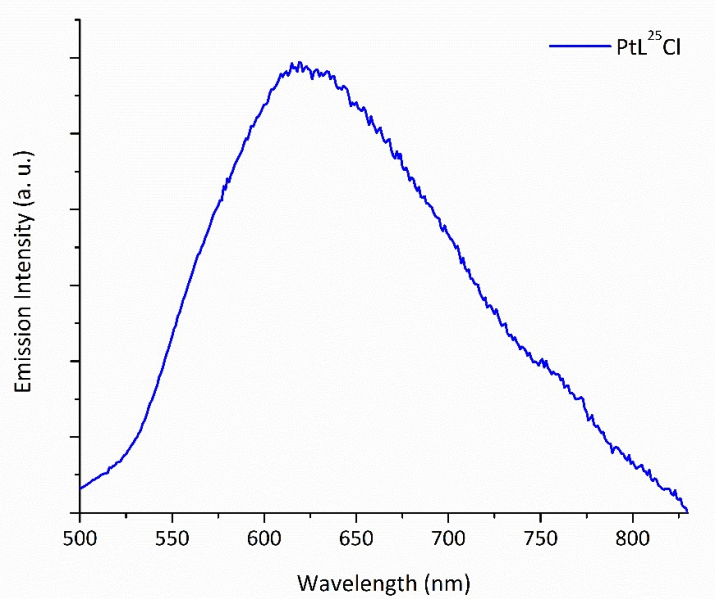

Figure 4.23: Emission spectra of PtL[25]Cl in degassed DCM at 298 K.

In dilute glassy solution at 77 K, all three of the complexes are weakly emissive, displaying more structured emission (Figure 4.24). The emission of PtL[25]Cl is blue shifted from the room temperature emission, although is is difficult to say to what extent as the 0,0 band cannot be identified in the room temperature spectra. The component band of highest intensity appears to be the 0 – 1 transition for each of the complexes, indicating a significant degree of excited state distortion.

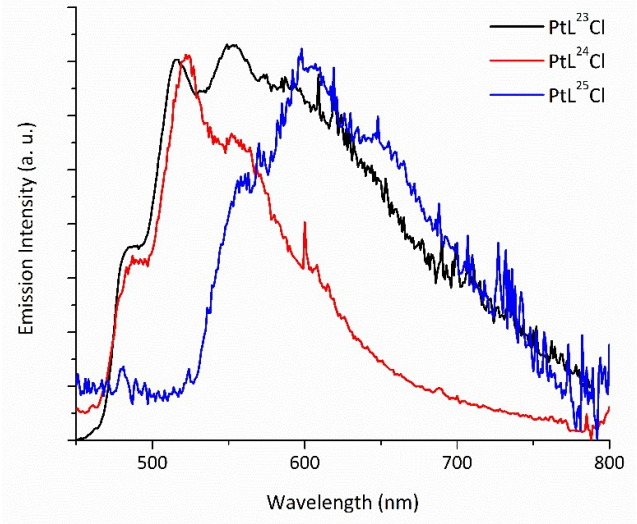

Figure 4.24: Normalised emission spectra of PtL[23]Cl – PtL[25]Cl in EPA rigid glass at 77 K.

The emission spectra of $PtL^{23}Cl$ – $PtL^{25}Cl$ were recorded in the solid state and all three of the complexes are weakly emissive. The imide-based complexes $PtL^{23}Cl$ and $PtL^{24}Cl$ display increased emission compared to the amide-based complex $PtL^{25}Cl$, which was too weak to record a PLQY. Complex $PtL^{23}Cl$ displays broad, poorly structured emission, typical of luminescence from states with a high degree of charge-transfer character (Figure 4.25). The component band of highest intensity appears to be the 0—1 transition, with the 0 – 0 transition appearing as a shoulder, suggesting a reasonable degree of difference in geometry between the ground and excited electronic state.[55] $PtL^{24}Cl$ displays broad, structureless emission with a slightly reduced PLQY (1.4% vs. 1.6% for $PtL^{23}Cl$). It is interesting to note the change in emission profile from the frozen solution spectrum of $PtL^{24}Cl$; the emission has shifted from a highly structured profile to a broad structureless emission indicating there may be a change in the origin of emission. It is possible that the solid-state emission originates from aggregation effects, involving Pt-Pt interactions that give rise to low energy emitting states.

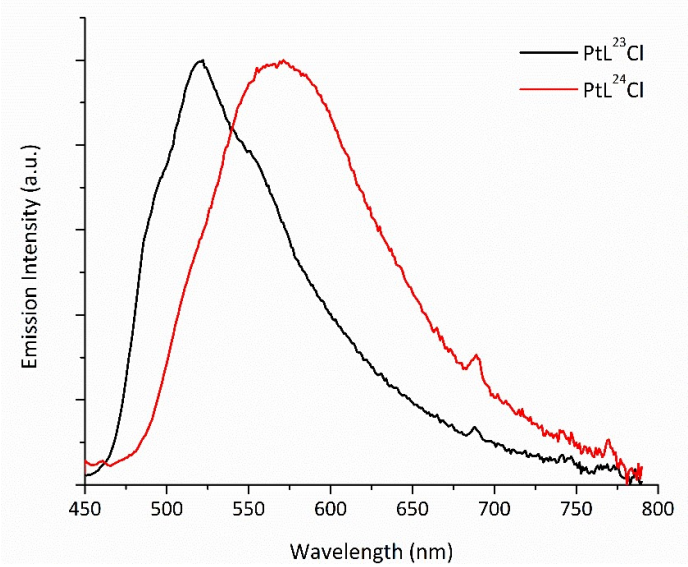

Figure 4.25: Normalised emission spectra of $PtL^{23}Cl$ and $PtL^{24}Cl$ in the solid state at 298 K.

4.2 Tetradentate Pt(II) Complexes

4.2.1 Hydrazone based complex

Electronic Absorption Spectra

The absorption spectrum of PtL^{27} was recorded in DCM at room temperature (Figure 4.26). The complex shows bands with high extinction coefficients in the far UV and less intense bands at ~420 nm. The absorption bands centred at ~420nm and 330 nm closely resemble the charge transfer bands of the parent tridentate complex $PtL^{14}Cl$. The absorption bands below 300 nm are assigned to $^1\pi - \pi^*$ transitions localised on the ligand.

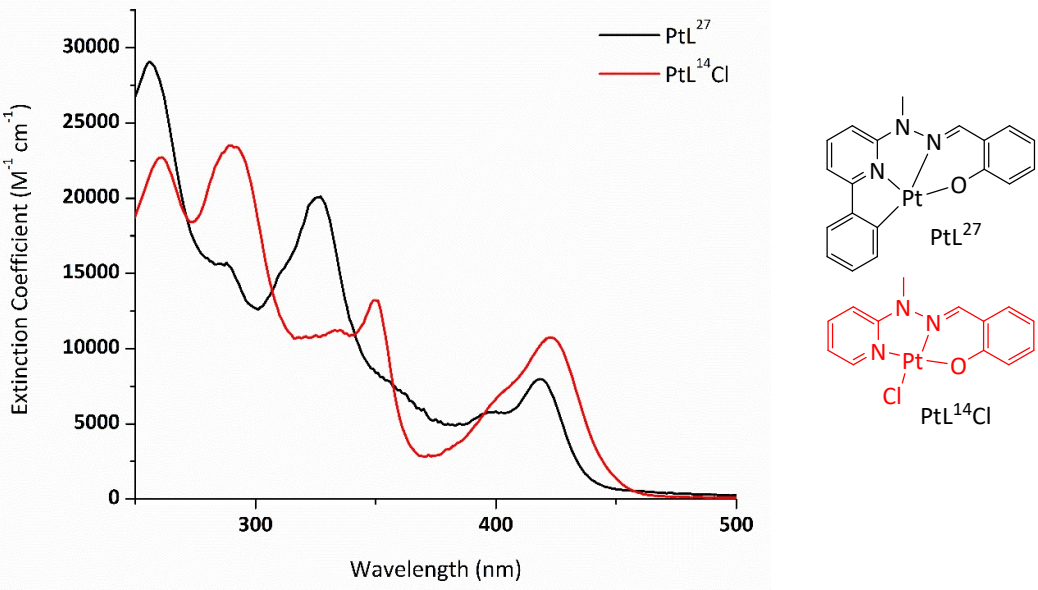

Figure 4.26: UV-Vis electronic absorption spectra of PtL^{27} and $PtL^{14}Cl$ in DCM at 298K.

Emission

The room-temperature and low-temperature (77 K) solution emission spectra were recorded for PtL^{27} and are shown in Figure 4.27. In contrast to the poorly structured emission profile of $PtL^{14}Cl$, the room temperature emission of PtL^{27} is highly structured suggesting a greater ligand character of the lowest-energy triplet state. The component band of the highest intensity is the 0—1 transition, with the 0 – 0 transition appearing as a shoulder, suggesting a reasonable degree of difference in geometry between the ground and excited electronic state.[55]

The PLQY in solution is 0.11 (degassed DCM, 298 K), a significant increase to that of the analogous tridentate $PtL^{14}Cl$ (0.017). The luminescence lifetime (τ = 11 µs) is also increased by a comparable order of magnitude from that of $PtL^{14}Cl$ (τ = 2.1 µs). This increase suggests that the improvement in PLQY is indeed due to a reduction in non-radiative decay

pathways. The PLQY (0.11) luminescence lifetime (11 µs), k_r (10 x 10^3 s^{-1}) and k_{nr} (0.8 x 10^5 s^{-1}) of PtL[27] are all comparable with PtL[14]C≡C-Ar (0.11, 9.3 µs, 12 x 10^3 s^{-1}, 0.9 x 10^5 s^{-1}, respectively).

Complex PtL[27] shows more intense emission at 77 K in frozen EPA glass and the estimated lifetime of emission remains in the range of microseconds, indicating phosphorescent emission. The emission is highly structured, with an approximate ~500 cm^{-1} blue shift from the room temperature emission. The component band of highest intensity is the 0 – 0 transition, indicating a relatively small degree of excited state distortion.

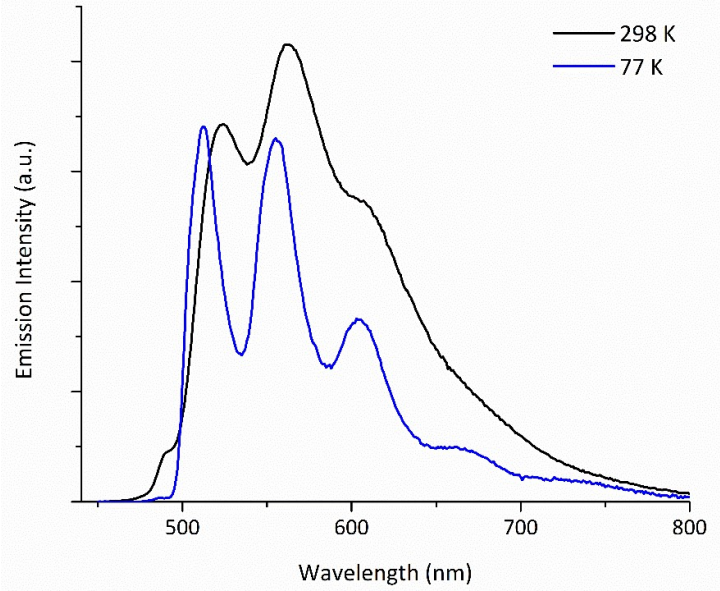

Figure 4.27: Normalised emission spectra of PtL[27] at 298 K (in degassed DCM) and 77 K (in EPA rigid glass).

Table 4.6: Photophysical data of complex PtL[27].

Complex	$\lambda_{(abs)}$ (nm)	298K						77K	
		$\lambda_{(em)}$ (nm)	τ * (µs)[a]	Φ[b] (%)	k_r (10^3 s^{-1})	k_{nr} (10^5 s^{-1})	k_q[c] (mol^{-1} dm^3 s^{-1})	$\lambda_{(em)}$ (nm)	τ (µs)
PtL[27]	257, 327, 399(sh), 419	526, 565, 609	11(0.3)	11	10	0.8	1.5 x 10^9	513, 558, 607, 673	51

*[a] Luminescence lifetime in degassed DCM solution; corresponding values in air-equilibrated solution are given in parentheses. [b] ±10%.[c] Bimolecular rate constant for quenching by O_2. *X^2 values are located in appendix 7.3*

4.2.2 Pyrazole based complexes

Electronic Absorption Spectra

The absorption spectra of pyrazole based complexes $PtL^{29\text{-}31}Cl$ were measured in DCM at room temperature (Figure 4.28).[10] The high energy, intense absorptions (250 – 360 nm) can be assigned as ligand based $^1\pi - \pi^*$ transitions. It is interesting to note that the charge transfer transition at ~400 nm is significantly weaker than the corresponding tridentate complex $PtL^{21}Cl$, suggesting this transition is associated with the phenolate-Pt unit.

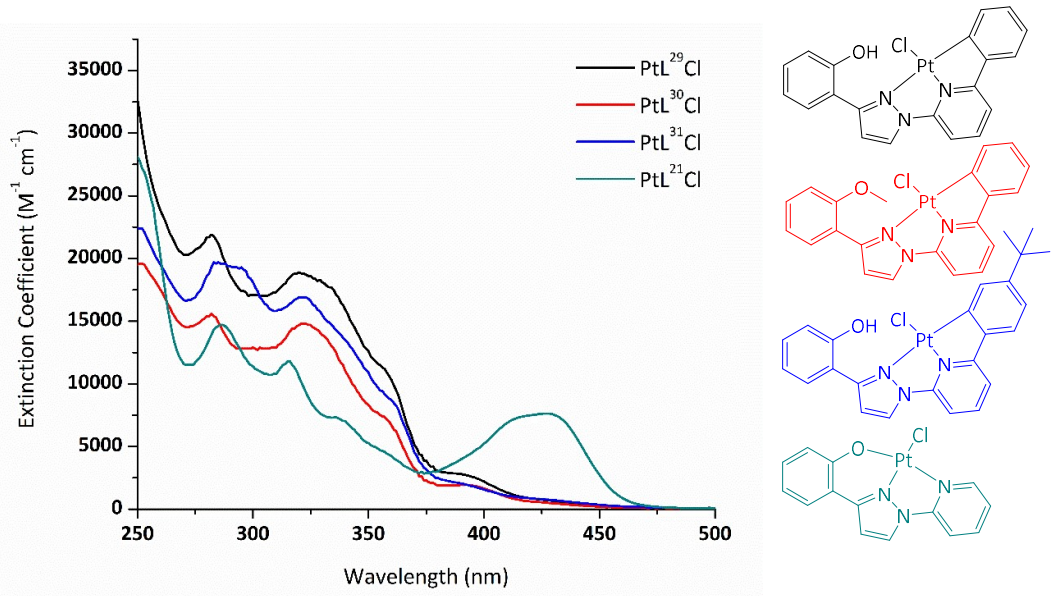

Figure 4.28: UV-Vis electronic absorption spectra of $PtL^{29\text{-}31}Cl$ and $PtL^{21}Cl$ in DCM at 298K.

Emission

The emission spectra of $PtL^{29}Cl$ and $PtL^{30}Cl$ – $PtL^{31}Cl$ were recorded in degassed DMF and DCM at room temperature, respectively. The complexes display highly structured emission bands in the range 502 – 592 nm (Figure 4.29), suggesting emission from a ligand-centred state. The component band of highest intensity is the 0 – 0 transition, indicating little difference in geometry between the ground states and the emissive excited electronic states.

The emission lifetime (τ) of the complexes are reported in Table 4.7, it is interesting to note the complexes do not show susceptibility to quenching by dioxygen. The complexes display weak emission in solution at room temperature, the PLQY of $PtL^{29}Cl$ was too weak to measure. The non-radiative rate constants are significantly higher than the

[10] *Complex $PtL^{32}Cl$ was unsuitable for photophysical studies due to difficulties in purification of the complex.*

radiative rate constants for both of the complexes. It is interesting to note the rates of non-radiative decay in complexes PtL^{30}Cl and PtL^{31}Cl (~10^8 s^{-1}) are significantly higher than all of the previously discussed complexes which are on the order of 10^5 – 10^6 s^{-1}. This may be attributed to the freely rotating phenol ring providing an efficient route to non-radiative decay.

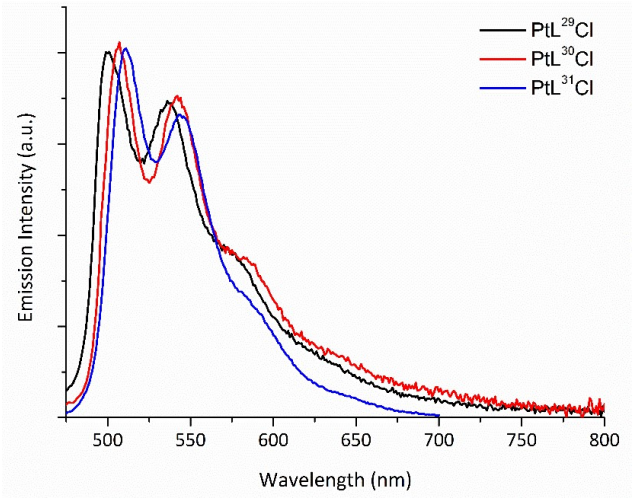

Figure 4.29: Normalised emission spectra of PtL^{29}Cl in degassed DMF and PtL^{30}Cl – PtL^{31}Cl in degassed DCM at 298 K.

The emission spectra of PtL^{29}Cl – PtL^{31}Cl were recorded in the solid state and all three of the complexes are weakly emissive (Figure 4.30). The complexes PtL^{29}Cl and PtL^{30}Cl display increased emission compared to PtL^{31}Cl, which was too weak to record a PLQY. The emission profile remains highly structured suggesting that the solid-state emission originates from the same state as the solution state emission.

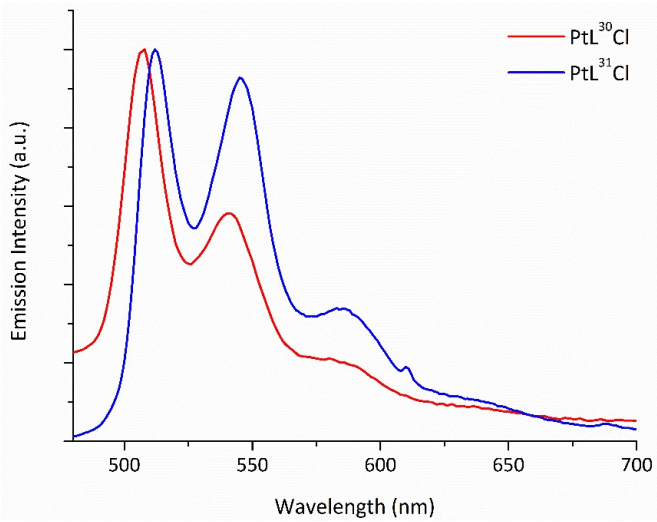

Figure 4.30: Normalised emission spectra of PtL^{30}Cl and PtL^{31}Cl in the solid state at 298 K.

Table 4.7: Photophysical data for complexes $PtL^{29}Cl$ – $PtL^{31}Cl$.

Complex	298 K						solid state at 298 K		
	$\lambda_{(abs)}$ (nm)	$\lambda_{(em)}$ (nm)	τ^{*} (ns)[a]	Φ^{b} (%)	k_r (10^4 s^{-1})	k_{nr} (10^7 s^{-1})	$\lambda_{(em)}$ (nm)	τ (ns)	Φ (%)
$PtL^{29}Cl$	283, 321, 336(sh), 360, 397, 432	502, 539, 583	26+11(55/45)(22+11(50/50))[e]	---[d]	-	-	513, 546, 589	1300	3.2
$PtL^{30}Cl$	284, 324, 359(sh), 396, 431	507, 544, 590	17(17)	0.3	18	59	509, 543, 589	410+130(75/25)[e]	0.23
$PtL^{31}Cl$	286, 297(sh), 323, 363(sh), 397, 431	512, 545, 592	40(40)	0.5	13	25	-	460+130 (75/25)[e]	---[d]

*[a] Luminescence lifetime in degassed DCM solution; corresponding values in air-equilibrated solution are given in parentheses. [b] ±30%.[c] Bimolecular rate constant for quenching by O_2. [d] too weak to measure PLQY. [e]biexponential; relative weightings of components in parenthesis. *X^2 values are located in appendix 7.3*

4.3 Tridentate Ir(III) Complexes

4.3.1 Hydrazone based complexes

Electronic Absorption Spectra

The absorption spectra of tridentate Ir(III) complexes ([Ir(dpyx)(L^{14-17})]PF_6, dpyx = 1,3-Di(2-pyridyl)-4,6-dimethylbenzene) were recorded in MeCN at room temperature (Figure 4.31). The absorption spectra show very intense bands in the near-UV region between 240 – 300 nm, which are assigned to $^1\pi$-π^* transitions from comparison to the literature.[163] The weaker transitions extending into the visible region are attributed to transitions with charge transfer character. The MLCT transitions of the 4-OMe substituted complex are red-shifted with respect to the parent complex, which may be rationalised in terms of destabilisation of the HOMO as a result of the electron-donating nature of the substituent.

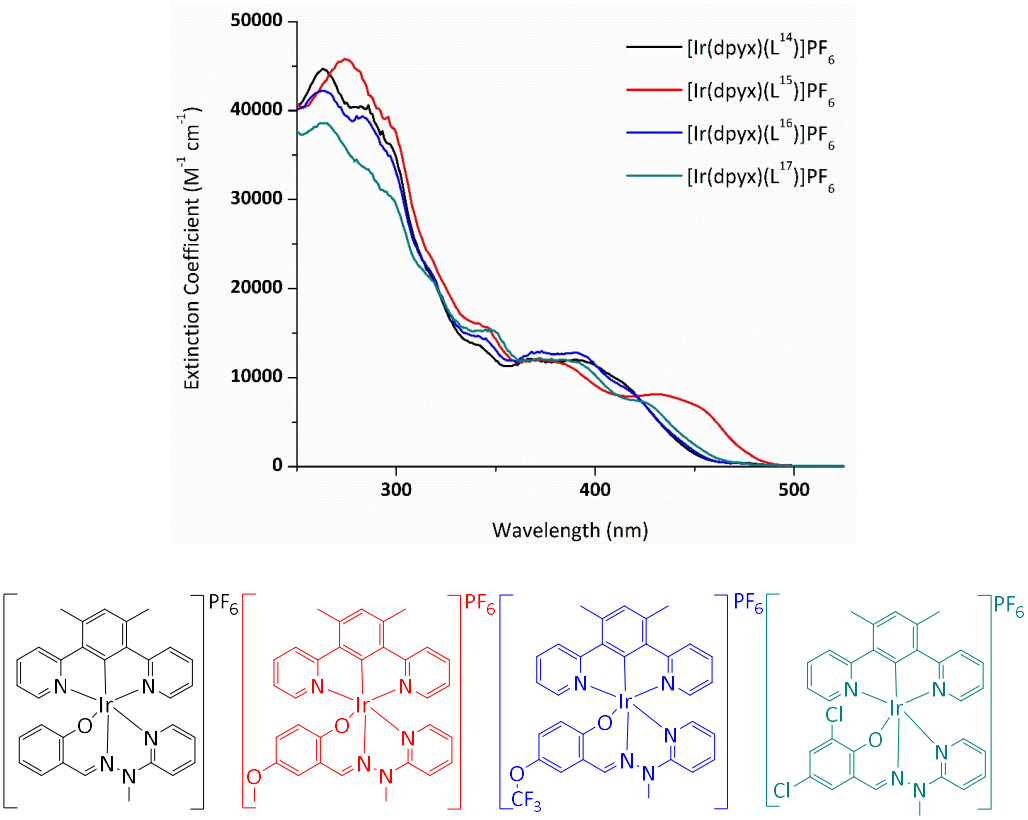

Figure 4.31: UV-Vis electronic absorption spectra of [Ir(dpyx)(L^{14-17})]PF_6 in MeCN at 298K.

Emission

The emission spectra of the hydrazone based Ir(III) complexes were recorded in degassed DCM at room temperature (Figure 4.32). All of the complexes are luminescent in

solution at room temperature, with very little variation in the λ_{max} (~600 nm). Complex [Ir(dpyx)(L^{15})]PF_6 is shifted furthest into the red, mirroring the trend seen in the absorption. The emission spectra display poorly defined vibronic progression; the 0 – 1 band appears to be dominant with the exception of [Ir(dpyx)(HL^{15})]PF_6 where the 0 – 0 and 0 – 1 are equal.

The PLQYs in degassed solution are in the range 0.05 – 0.09 (Table 4.8), the highest value is observed for the parent complex (Φ_{lum} = 0.09) which is the highest energy emitter. Complex [Ir(dpyx)(L^{17})]PF_6 has the lowest PLQY of 5% and also the shortest lifetime (3.0 µs). Some insight into this may be obtained by considering the rate constants for radiative (k_r) and nonradiative (k_{nr}) decay. The values in Table 4.8 indicate that the reduced PLQY and shorter lifetime of this complex are largely due to increased nonradiative decay. The radiative rate constants are similar for all four complexes. The PLQYs of these complexes are higher than that reported for the related [Ir(dpyx)(phbpy)]$^+$, which has a PLQY of 2.3%.[164] Although the radiative rate constants of complexes [Ir(dpyx)($L^{14\text{-}17}$)]PF_6 are a factor of ~10 smaller than for [Ir(dpyx)(phbpy)]$^+$, this increase in PLQY can be attributed to a ~40-fold decrease in the rates of non-radiative decay. This may be due to the increase in chelate ring size in complexes [Ir(dpyx)($L^{14\text{-}17}$)]PF_6 from a 5,5 system in phbpy to a 5,6 system in $L^{14\text{-}17}$ relieving ring strain in the system. The emission life time (τ) of all the complexes show susceptibility to quenching by dioxygen confirming that emission originates from a triplet state.

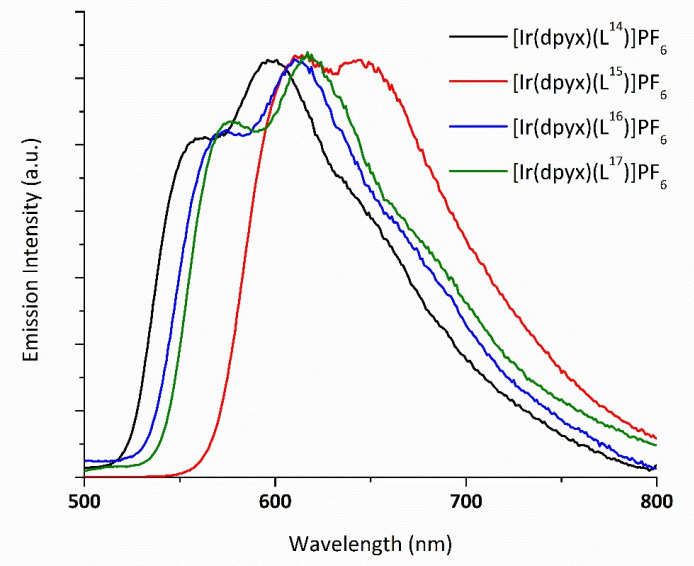

Figure 4.32: Emission spectra of complexes [Ir(dpyx)($L^{14\text{-}17}$)]PF_6 in degassed DCM at 298K.

Table 4.8: Photophysical data for complexes [Ir(dpyx)(L^{14-17})]PF_6

Complex	298K						
	$\lambda_{(abs)}$ (nm)	$\lambda_{(em)}$ (nm)	τ^{*} (μs)[a]	Φ[b] (%)	k_r (10^3 s^{-1})	k_{nr} (10^5 s^{-1})	k_q[c] (mol^{-1} dm^3 s^{-1})
[Ir(dpyx)(L^{14})]PF_6	228 (sh), 248 (sh), 265, 285 (sh), 343 (sh), 370 (sh), 393, 416 (sh)	560, 600	5.4 (0.3)	9	16.7	1.7	1.4×10^9
[Ir(dpyx)(L^{15})]PF_6	229 (sh), 248, 277, 300 (sh), 346 (sh), 380, 434, 457 (sh)	615, 645	6.2 (0.2)	8	12.9	1.5	2.2×10^9
[Ir(dpyx)(L^{16})]PF_6	228 (sh), 246 (sh), 264, 285, 320 (sh), 346, 372, 395, 421 (sh)	575, 615	4.2 (0.3)	8	19.0	2.2	1.4×10^9
[Ir(dpyx)(L^{17})]PF_6	229 (sh), 245, 265, 299 (sh), 320 (sh), 350, 393, 429 (sh)	578, 620	3.0 (0.4)	5	16.7	3.2	9.8×10^8

*[a] Luminescence lifetime in degassed DCM solution; corresponding values in air-equilibrated solution are given in parentheses. [b] ±10%.[c] Bimolecular rate constant for quenching by O_2. *X^2 values are located in appendix 7.3*

Concluding Remarks

We have successfully synthesised and fully characterised a range of new tridentate Pt(II) complexes. We have explored the effect of pseudo-cyclometallating ligands of N^N^O$^-$ or N^N$^-$^N – coordination. The proligands and corresponding complexes are all prepared using relatively mild conditions. The photophysical properties of the complexes have been discussed.

With the exception of the pyrazole-based complex, PtL^{21}Cl, all of the tridentate complexes are weakly emissive in solution at room temperature. The PLQYs are in the range 0.1 – 4%, a noteworthy improvement on the platinum terpyridiyl complex [Pt(tpy)Cl]$^+$ which is essentially non-emissive in solution at room temperature. The Pt(II) complexes with N^N^O$^-$ ligands investigated in this work have higher PLQYs than those with N^N$^-$^N ligands, suggesting the pseudo cyclometallating O$^-$ provides a stronger field than the N$^-$.

Replacement of the chloride ligand in the imine-based PtL^{1}Cl by a strong field acetylide was anticipated to raise the energy of deactivating d-d states, promoting luminescence over non-radiative decay. The exchange causes a small increase in PLQY (4.6% vs 4%), attributed to a reduction in k_{nr} rather than any beneficial effect on k_r. Replacement of the chloride ligand in the hydrazone-based NMe PtL^{14}Cl by an acetylide was more successful, raising the PLQY from 1.7% to 11% in PtL^{14}C≡C-Ar.

We have investigated the design of a more rigid structure based on the N^N^O$^-$ NMe hydrazone based proligands, extending them into tetradentate proligands with a C^N^N^O$^-$ coordination mode. The hydrazone-based NMe complex PtL^{27} has a PLQY of 11%, with an emission lifetime, k_r and k_{nr} of the same order as PtL^{14}C≡C-Ar. The increase in PLQY can be attributed to a decrease in k_{nr} caused by the rigidification of the ligand in comparison to the parent complex PtL^{14}Cl.

Extension of the pyrazole-based tridentate proligand was less successful. We successfully synthesised a series of tetradentate proligands offering a C^N^N^O$^-$ coordination mode, however complexation was only achieved in a tridentate C^N^N manner. The resulting complexes were only very weakly emission in solution at room temperature, due to high non-radiative decay constants likely caused by the free rotation of the phenol in solution providing efficient non-radiative decay pathways.

We have also investigated a series of Ir(III) complexes containing N^C^N and N^N^O^- tridentate ligands. The photophysical properties of the complexes have been discussed. The PLQYs (5 – 9%) are higher than that reported for the related $[Ir(dpyx)(phbpy)]^+$, which has a PLQY of 2.3%.

5 Multimetallic Complexes of Pt(II) and Ir(III)

5.1 Introduction

Although the vast majority of complexes studied for photonic applications focus on monometallic species, in the past two decades there has been a growing interest in compounds incorporating more than one metal centre. There was an initially established view that multinuclear metal complexes give poor device performance due to the PLQYs of early examples of such complexes being considerably lower than for mononuclear analogues.[165–167] However, more recent examples challenge this accepted view and establish that multinuclear complexes are not only viable for incorporation in OLEDs but may offer some intriguing benefits.[167]

Phosphorescent red and near-infrared emitters are required for full colour displays, however currently available red-emitting compounds are not able to match their high performing green counterparts.[168] Many Ru(II) complexes have been studied for this purpose and more recently those of third-row metals such as Pt(II) and Ir(III).[169] Examples of multinuclear systems have begun to emerge as an alternative approach to achieve red-shifted emission. Pt(II) studies have utilised flexible or rigid linkers to bring together two square-planar units to promote d^8—d^8 interactions between the platinum centres or ligand—ligand (π-π) interactions. This typically results in an emission which is red-shifted from the ^{3}MLCT emission of the mononuclear complex.[170] In the case of Ir(III), many examples are individual mononuclear metal complexes linked through an ancillary or bridging ligand. This often results in compounds where the original properties of the mononuclear complex are retained.[171]

This chapter is by no means a comprehensive overview of the literature, but rather it is intended to give a flavour of the diversity of the field and highlight some interesting examples in recent literature.

5.1.1 Pt(II) Complexes

Multinuclear Pt(II) complexes coordinated through multidentate nitrogen-donor ligands have been explored by a number of research groups. The use of pyrazolate bridges to introduce two or more metal centres in a face-to-face manner is of much interest. An early example of such complexes was provided by Gray and co-workers in 1993 who investigated the photophysics of binuclear complexes containing terpyridine ligands and

bridged by a variety of anionic N-N ligands; pyrazole, 7-azaindole, diphenylformamidine and arginine (Figure 5.1).[172] Similar to the monometallic parent complex ($[Pt(tpy)Cl]^+$), the new complexes failed to show emission in solution at room temperature although it was noted that in the solid state and 77K the emission maxima moved to lower energy with decreasing Pt—Pt separation.

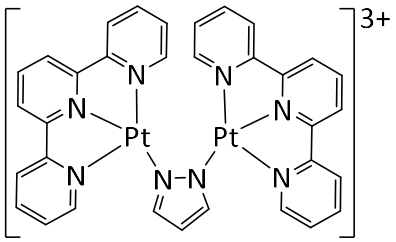

1

Figure 5.1: Binuclear Pt-terpyridine complex reported by by Gray and co-workers.

Che and co-workers, noting the extensive use of multidentate nitrogen-donor ligands in the assembly of cyclic supermolecules, reported the synthesis and photophysical study of a related set of Pt(II) complexes.[173] The platinum-containing macrocycles utilised cyclometallated Pt(II) complexes bearing substituted pyridyl and 2,2'-bipyridyl ligands with various bidentate N-donor linkers; pyrazole, 7-azaindole and benzimidazole (Figure 5.2). Structured emissions were observed for complexes **2 – 5a** in solution at room temperature although the multinuclear complexes have slightly lower PLQYs (**3a** = 0.18, **4a** = 0.12, **5a** = 0.16) than the parent monometallic complex (**2a** = 0.19). In contrast to this, the remaining mono- and multinuclear complexes were either non or very weakly emissive.

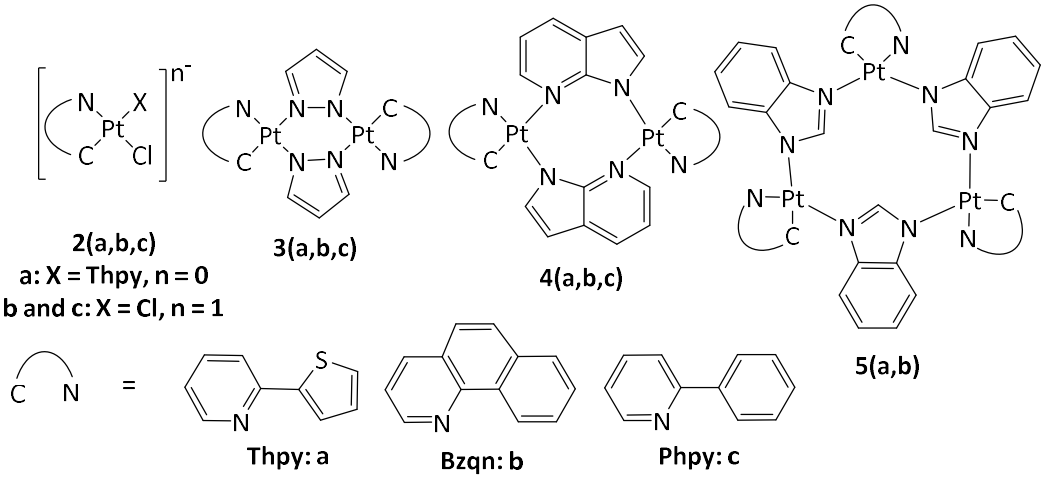

Figure 5.2: Multidentate nitrogen donor bridged Pt(II) complexes reported by Che and co-workers.

Building upon these results, Thomspon and co-workers explored colour tuning in pyrazolate bridged Pt(II) binuclear complexes.[174,175] The steric bulk of the bridging pyrazolate controls the degree of metal—metal interaction, giving compounds **6-8** which emit blue, green and red light, respectively (Figure 5.3). Efficient blue, green and red OLEDs were fabricated with these complexes and in combination allowed the fabrication of WOLEDs which showed high brightness and quantum efficiencies.

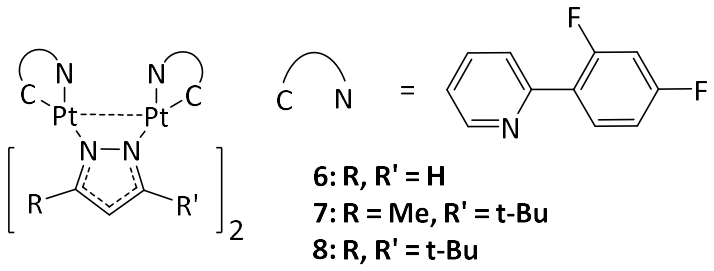

Figure 5.3: Structure of the binuclear complexes used as phosphorescent dopants.

A number of other bridging ligands have been explored in order to bring two Pt(II) centres together in a face-to-face manner. Although a red shift in emission is consistently achieved, PLQYs are also consistently lower than their monometallic counterparts. In 2002, Che and co-workers utilised an isocyanide bridge to increase Pt—Pt interactions in complex **9** (Figure 5.4) and reported a 100 nm red shift accompanied by a significant decrease in PLQY.[176] This was attributed to a change in the nature of emission, from ^{3}MLCT in the monometallic complex to an excimeric intraligand (^{3}IL) excited state. In 2008, Williams and co-workers reported similar findings for N^C^N-coordinated Pt(II) complexes linked through a xanthene core (Figure 5.4).[177]

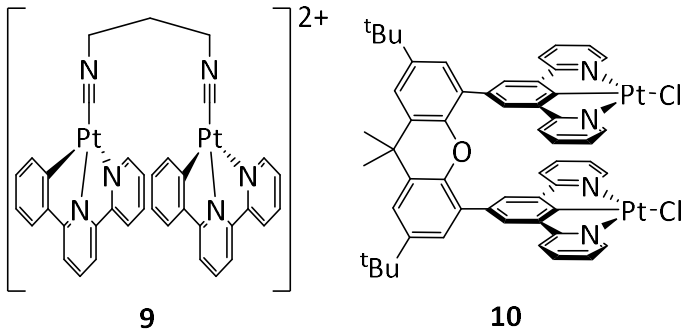

Figure 5.4: Binuclear Pt(II) complexes reported by Che and co-workers (9) and Williams and co-workers (10).

An alternative strategy has been utilised by Kozhevnikov and co-workers, who synthesised a series of five dinuclear Pt(II) complexes based on diphenylpyrazine-based

bridging ligands (Figure 5.5).[168] Rather than promoting Pt—Pt interactions or the formation of excimers, this approach is based on the general observation that the introduction of a second cyclometallated metal centre is accompanied by a red shift, due to the stabilisation of the LUMO.[171] The study reveals that for all six ligands investigated, introduction of a second metal centre leads to significant stabilisation of the LUMO, while the HOMO remains relatively unaffected. Interestingly, for all of the systems, introducing a second metal ion increases the radiative rate constant k_r, despite the red shift. This effect was attributed to the higher degree of spin-orbit coupling expected from the presence of a second Pt(II).

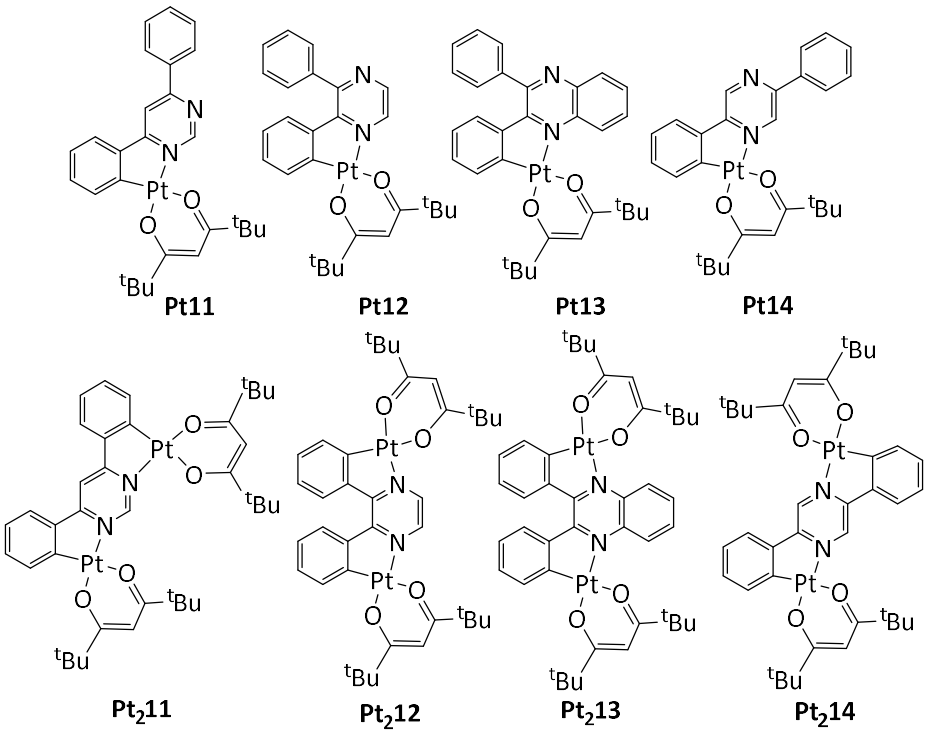

Figure 5.5: Structure of the mononuclear and dinuclear Pt(II) complexes.

Matsumura and co-workers recently reported the near-infrared luminescence of a bis(Pt-salen) complex.[178] The photophysical properties of a fused Pt-salen complex (**$Pt_2$15**) were reported alongside two analogous mononuclear complexes **16** and **17** (Figure 5.6). The luminescence spectra showed the highest-energy maxima of **$Pt_2$15**, **16** and **17** were 636, 558 and 574 nm, respectively, assigned to ^{3}MLCT or $^3\pi\pi^*$ emission (or possibly a mixture of the two).

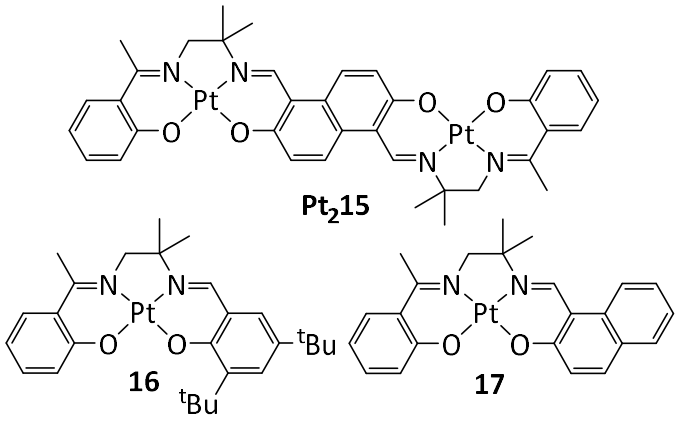

Figure 5.6: Dinuclear complex $Pt_2$15 and structure of the mononuclear analogues 16 and 17.

5.1.2 Ir(III) Complexes

In recent years, interest in multi-nuclear Ir(III) complexes has emerged from the intense and widely successful research into the application of iridium complexes as phosphors for light-emitting devices. In 2006, Monkman and co-workers reported the first incorporation of bridged diiridium complexes into electrophosphorescent OLEDs.[167] The bis(μ-chloro)diiridium(III) complexes typically utilised to access cyclometallated mononuclear Ir(III) complexes are only weakly emissive at room temperature and unsuitable for OLEDs. However, their relative ease of synthesis is attractive for commercialisation purposes; Monkman and co-workers aimed to investigate the use of organic bridging ligands to produce dinuclear iridium complexes as phosphorescent dopants for OLEDs. They found that the traditional μ-chloro bridged dimers could be readily converted to diisocyanato-bridged species on reaction with tetrabutylammonium cyanate (Figure 5.7). Interestingly, despite emitting at the same energy (λ_{max} = ~550 nm) the PLQY is increased considerably from 0.004 to 0.02, with a similar increase in lifetime τ. This increase in ϕ is attributed to a decrease in k_{nr} due to the stronger ligand field of the cyanate ligands increasing the energy gap between the emissive state and the deactivating d-d state. Complex **19** afforded OLEDs with EQE values of 0.8%, which although modest, began to challenge the perception that dinuclear species were not viable as dopants for electrophosphorescent OLEDs.

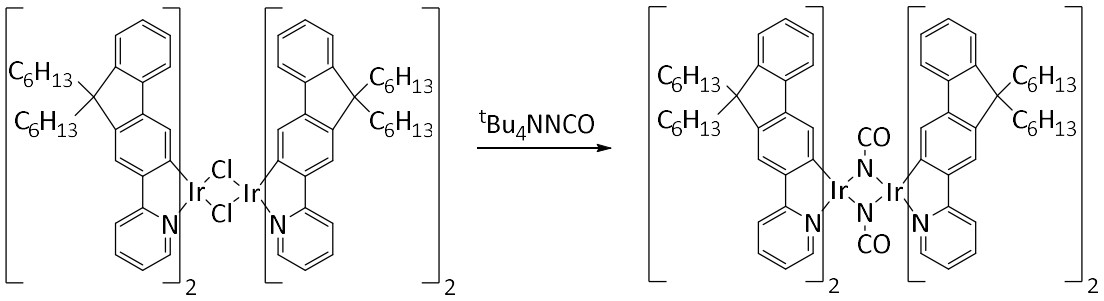

18 **19**

Figure 5.7: The conversion of chloro-bridged dimers to bis-μ-isocyanate-bridged dimers.

Similar to the success seen for Pt(II) complexes, pyrazole ligands have been employed to produce bridged dinuclear iridium complexes. In 2012, Chandrasekhar and co-workers explored the use of different types of pyrazole ligands whose steric bulk was modulated by varying the number and nature of substituents on the 3 and 5 positions.[179] The treatment of a dichloro-bridged iridium dimer with sodium methoxide and a pyrazole (3,5-diphenylpyrazole (Ph_2PzH) or 3(5)-methyl-5(3)-phenylpyrazole (PhMePzH)) resulted in the synthesis of binuclear iridium complexes bridged by one pyrazole ligand and one OH group (Figure 5.8). The phosphorescent emission for each of the bimetallic complexes is red shifted by approximately 50 nm compared to their monometallic counterparts. This is attributed to the π-donating nature of the bridging ligands, which pushes the electron density toward to Ir(III) centre. This raises the energy level of the HOMO, while leaving the LUMO (which is localised on the pyridyl rings of the ppy ligands) relatively unaffected.

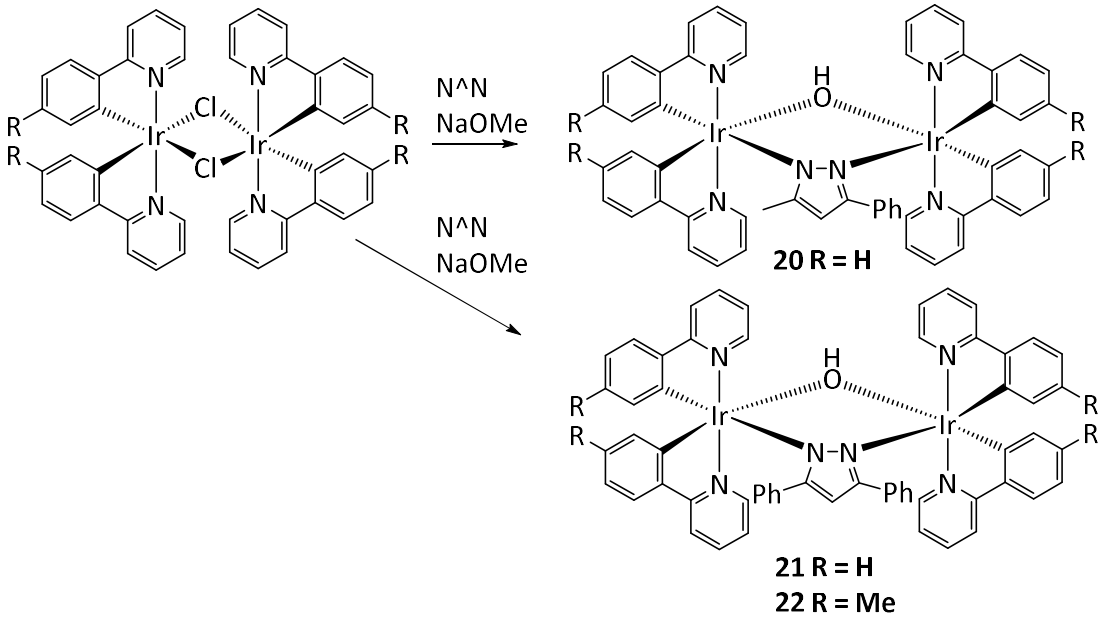

Figure 5.8: Conversion of chloro-bridged iridium dimers to pyrazole bridged dimers; water leads to the bridging OH groups.

In the same year, Chandrasekhar and co-workers also reported the preparation of a series of dinuclear Ir(III) complexes utilising pyridine based linkers (Figure 5.9).[180] The choice of ligands allowed for the variation of the spacer length to modulate the intermetallic distances and for variation in the extent of bridging ligand conjugation to modulate the degree of metal-metal interaction. The diiridium complexes all contain $Ir(ppy)_2$ units bridged by the bis-pyridyl linkers; 1,2-bis(4-pyridyl)-ethane (bpa), 1,3-bis(4-pyridyl)propane (bpp) and trans-1,2-bis(4-pyridyl)ethylene (bpe) afforded metallamacrocycles with two bridging linkers (complexes 23 – 25) whereas the use of N,N'-bis(2-pyridyl)methylene-hydrazine (abp) and N,N'-(bis(2-pyridyl)formylidene)ethane-1,2-diamine resulted in discrete dimers with only one bridging linker (complexes **26** and **27**). For clarity, the ORTEP diagram of **23** and **26** can be seen in Figure 5.10.

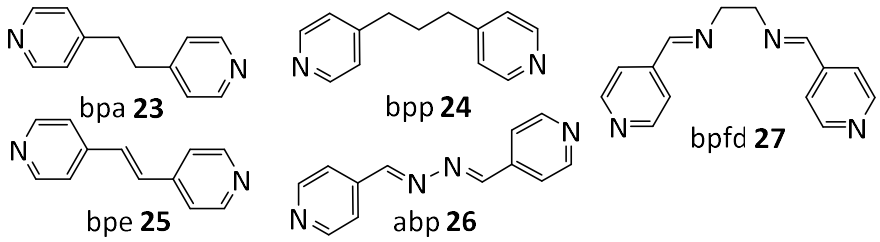

Figure 5.9: Bis-pyridyl linkers employed by Chandrasekhar and co-workers.

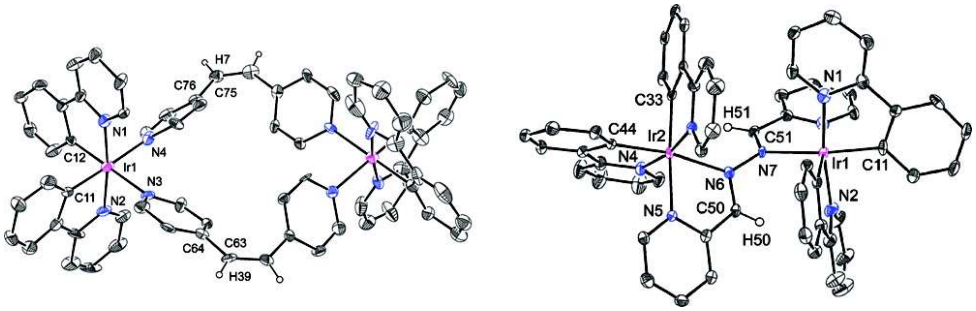

Figure 5.10: ORTEP diagram (40 probability thermal ellipsoids) of the dicationic unit [{Ir(ppy)$_2$}$_2$(μ-bpa)$_2$] in 23 (left) and the dicationic unit [{Ir(ppy)$_2$}$_2$(μ-abp)] in 26.

The emission properties of the complexes were investigated and all were found to be luminescent at room temperature. Complex **23** and **24** are very similar, both show blue emission (480 nm) with a PLQY of 0.45 and 0.48 respectively. The emissive state is attributed to one of ^{3}LC character. The introduction of conjugation into the spacer in complex **25** causes a significant red shift in the emission (~60 nm) with the PLQY remaining relatively high (0.41). Compound **26** and **27** also show a similar red shift in emission; interestingly the PLQY of **26** is impressively high (0.51) whereas in complex **27** is it reduced to 0.12. This reduction in PLQY is thought to originate from an increase in k_{nr}; it is proposed that in solution the C-C bond in the bpfd linker can rotate to alternate between an *anti-*

and *syn*- configuration. The emission in complex **25** – **27** is attributed to states of predominantly ^{3}MLCT character.

Congrave *et al*. recently reported the study of diarylhydrazide bridging ligands to produce dinuclear iridium complexes (**28** – **31**), providing a short conjugative pathway between the two iridium centres (Figure 5.11).[181] The diiridium complexes were synthesised via cleaving of the traditional bis(μ-chloro)-bridged intermediate with the hydrazide ligand in the presence of K_2CO_3. The resulting mixtures of *meso* (ΛΔ, a) and *rac* (ΔΔ/ΛΛ, b) diastereomers were separated and characterised separately. The phenylpyrazole complexes **28** and **29** were non emissive in solution at room temperature due to weaker crystal field strength of the ligands, a case commonly seen for non emissive homoleptic phenylpyrazole complexes.[181] Complexes **30** and **31** were found to be weakly emissive in solution at room temperature (ϕ_{PL} < 1%), emitting in the turquoise and green regions, respectively. This weakness of the emission was attributed to unusually high k_{nr}. In line with the findings of Chandrasekhar and co-workers for complex **27**, the highly flexible bridges are thought to facilitate nonradiative decay via intramolecular motion. Interestingly, when complexes **30** and **31** are doped into poly(methylmethacrylate) (PMMA) the k_{nr} rates decrease by 2-3 orders of magnitude due to suppression of the intramolecular motion, causing the PLQYs to also increase by 2-3 orders of magnitude.

Noting the high values of nonradiative decay in flexible bridged diiridium complexes, Zhou and co-workers have investigated the properties of a series of diiridium complexes with a rigid pyrimidine bridge (Figure 5.12).[182] The electron-deficient character of the pyrimidine ring is also thought to make a good electron acceptor to facilitate the MLCT processes. One mononuclear and two dinuclear Ir(III) complexes can be prepared in a one-pot reaction using 2-phenylpyrimidine-type ligands. The diiridium complexes possess higher HOMO and lower LUMO levels when compared with their mono-iridium counterparts, resulting in an approximate 80 nm red shift in emission. The emission in all cases mainly originates from the ^{3}MLCT transitions and there is very little difference in λ_{max} of diiridium complexes **34** – **37** despite the presence of electron-withdrawing fluorine. This is attributed to neither the HOMO nor the LUMO being localised on the phenyl ring of the phenylpyrimidine unit. The PLQY is close to unity for the mononuclear complexes whereas the diiridium complexes have lower PLQY in the range of 0.36 – 0.68. It is interesting to note that complexes **36** and **37** have the higher ϕ_{PL} of 0.68 which is amongst the highest

PLQYs for dinuclear Ir(III) complexes. The solution-processed device based on complex **35** exhibited an outstanding EQE of 17.9%.

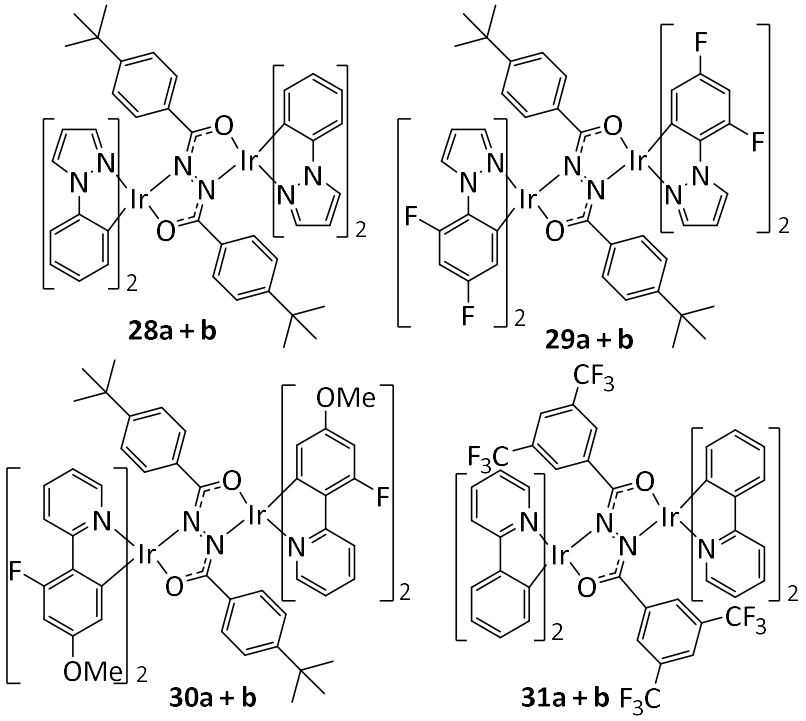

Figure 5.11: Structures of the diiridium complexes (a = ΛΔ meso diastereomers; b = ΔΔ/ΛΛ rac diastereomers) studied by Congrave et al.

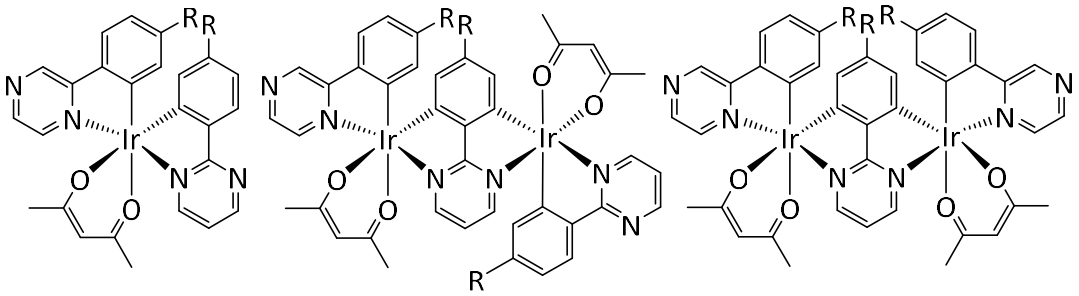

Figure 5.12: Mono- and di-nuclear complexes studied by Zhou and co-workers.

5.1.3 Mixed Heavy Metal Complexes

Although there has been an increased interest in recent years in multinuclear complexes for OLED applications, the vast majority of research has been carried out on systems which compromise more than one atom of the same metal. Noting the absence of mixed-metal polymetallic, cyclometalated complexes having both Pt(II) and Ir(III) present in one luminophore, Williams and co-workers reported an early example of a rigid polynuclear cyclometalated complex incorporating one Ir(III) and two Pt(II) centres using a

pyrimidine based ligand.[171] The related monometallic and dinuclear Pt(II) complexes were also prepared for comparison (Figure 5.13). All four of the complexes were found to be highly luminescent, both in the solid state and in solution at room temperature. Incorporation of a second Pt(II) centre in complex **39** caused a red shift in the λ_{max} of emission (513 to 550 nm) and changed the spectral profile substantially, indeed there are no detectable emission bands corresponding to the mononuclear unit. The monometallic Ir(III) complex **40** is red shifted once again (λ_{max} = 585 nm) and incorporation of two Pt(II) centres to produce complex **41** causes the most significant red shift (λ_{max} = 626 nm). Again there are no detectable emission bands corresponding to the mononuclear unit. The PLQYs are high for each of the complexes (0.31 – 0.54), it is particularly notable that unlike the systems discussed so far the PLQY does not fall off even for the most red-shifted complex **41**. Introduction of subsequent metal centres can be seen to increase the radiative rate constant despite the emission energy decreasing; the k_r roughly doubles going from **38** to **39** and likewise from **40** to **41**.

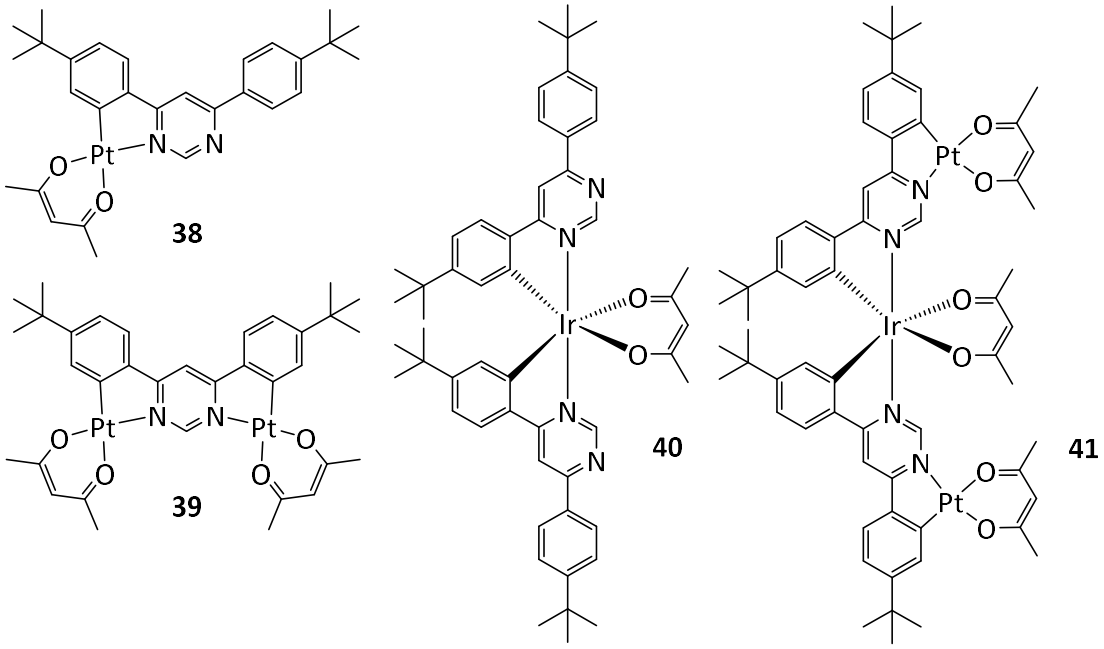

Figure 5.13: Mononuclear, dinuclear and trinuclear complexes studied by Williams and co-workers.

Kozhevnikov and co-workers have built upon the success of this system to incorporate a third Pt(II) metal centre and in 2017 published an unprecedented heterometallic tetranuclear complex, **42** (Figure 5.14).[183] The iridium centre is incorporated first by reaction of 4,6-bis-(4-*t*-butylphenyl)-pyrimidine ($bppymH_2$) with $Ir(acac)_3$ in the presence of *o*-phosphoric acid. The resulting mononuclear complex is then reacted with

K_2PtCl_4 in a mixture of acetic acid and acetonitrile at reflux, followed by treatment with an excess sodium acetylacetonate in acetone to give the target complex **42**.

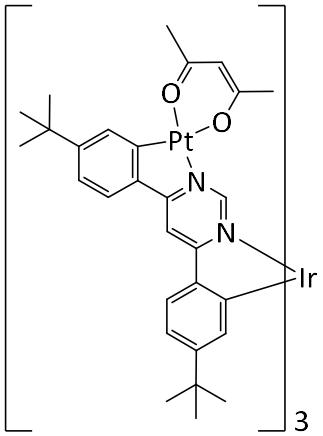

42

Figure 5.14: Heterometallic tetranuclear complex.

The photophysical study of complex **42** revealed intense red emission (λ_{max} = 611 nm) in solution at room temperature. The impressive PLQY of 0.76 renders it one of the brightest red-emitting complexes reported to date. The luminescence lifetime of complex **42** is unusually short at 720 ns (e.g. *fac*-Ir(ppy)$_3$, τ = 1.9 µs), indicating very fast radiative decay. This augmentation of k_r is consistent with the effect of additional metal ions in the previously reported system by Williams and co-workers.[171]

A number of alternative approaches to mixed multinuclear complexes have also seen success in recent years. Acknowledging the success of Ma *et al*. in the use of 1,1,2,2-tetraacetylethane (tae) to assemble emissive Pt(II) dyads[184], Bruce and co-workers reported a heteronuclear Pt–Ir dyad linked by the tae ligand.[185] Complex **43** (Figure 5.15) exhibits intense emission (λ_{max} = 588 nm, ϕ = 0.46, τ = 4.9 µs in CH_2Cl_2 at 298 K), similar to the homometallic Ir dimer **44** (λ_{max} = 586 nm, ϕ = 0.55). There is no evidence of emission from the Pt(II) unit at room temperature but at 77 K the main iridium based band is accompanied by an additional set of weak bands that emerge at higher energy, consistent with emission from the Pt(II) unit. Presumably, at room temperature, energy transfer from the higher-energy Pt unit to the lower-energy Ir moiety must be substantially faster than radiative decay of the Pt(ppy) unit.

Zysman-Colman and co-workers reported hetero-bi- and trimetallic Pt(II) and Ir(III) species linked by a conjugated rigid spacer.[186] The complexes **45** and **46** exhibit red-shifted low energy bands, similar to the Ir-monometallic species with higher absorptivities

associated with the presence of the Pt-monometallic species (Figure 5.16). Complex **45** PLQY is quasi identical to that of the Pt(II) monometallic complex at 8.3% whereas addition of the second Ir(III) centre in complex **46** causes a large increase in PLQY to 31.9%. Interestingly, this is attributed to a large decrease in k_{nr} rather than an increase in k_r.

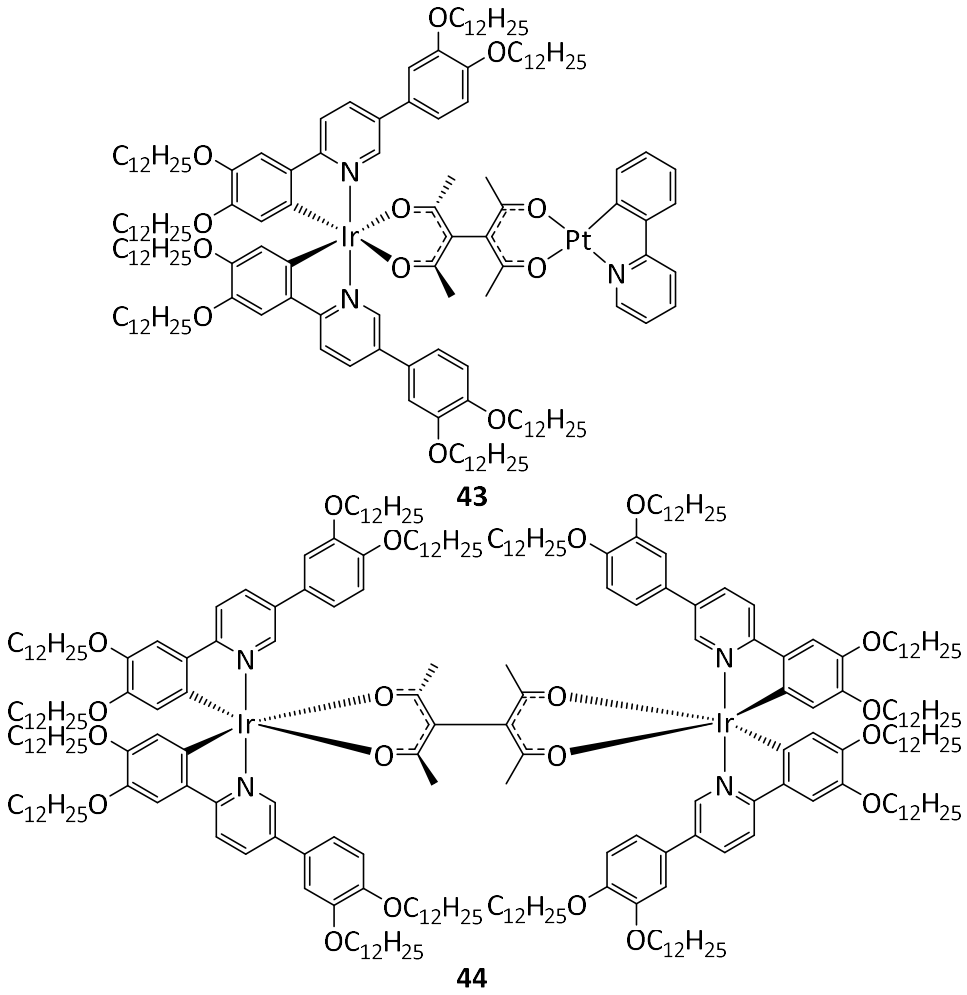

Figure 5.15: Heteronuclear Pt–Ir dyad reported by Bruce and co-workers.

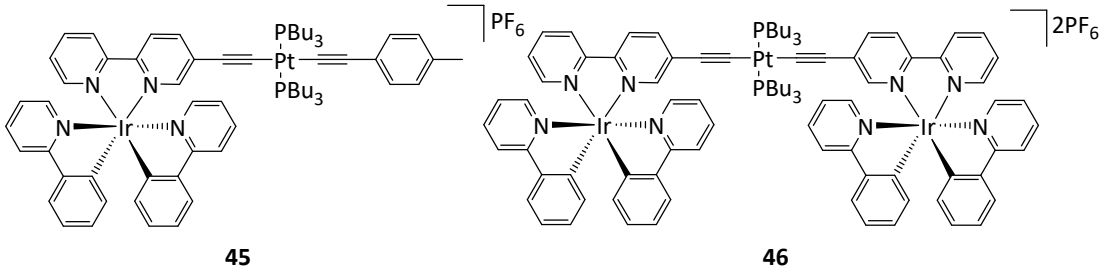

Figure 5.16: Structures of the bi- and trimetallic species reported by Zysman-Colman and co-workers.

From the small number of systems reviewed here it is clear to see that there is a large number of structural variations possible when introducing more than one metal into

a luminophore. Very different properties emerge depending on the bridging ligand and recent literature successfully dispels the myth that multinuclear metal complexes give poor device performance or that they necessarily have inferior PLQYs compared to their mononuclear analogues.

5.2 Synthesis of Bimetallic Complexes

Due to recent reports in the literature debunking the myth that multinuclear systems are unsuitable for application in OLED devices, some of the tridentate ligand systems developed in chapter 3 were chosen for exploration into this emerging field. In particular the work by Kozhevnikov[168,171,183,187] was persuasive and our intention was to build upon the reported success of rigidly linking two or more metals together using the easily accessed pseudo-cyclometallating systems discussed in chapter 3.

5.2.1 Hydrazide Bridged Complexes

Nakajima and co-workers reported the formation of hydrazonato-bridged heterodimetallic Ru(III)-M(II) (M = Mn, Fe, Co, Ni, Cu, Zn and Pd) complexes which attracted our attention due to the mild conditions used to access the complexes.[142,188] The reported palladium(II)-ruthenium(II) complex 47 (Figure 5.17) was synthesised from the monometallic Pd(II) complex and an equimolar amount of $[RuCl_2(PPh_3)_3]$ in DCM at room temperature.

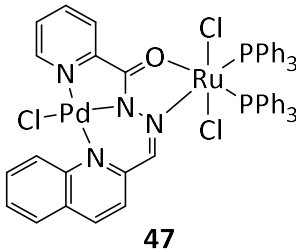

47

Figure 5.17: Pd(II)-Ru(II) complex reported by Nakajima and co-workers.

We found the tridentate Pt(II) complex a-PtL[22]Cl is a similarly good precursor to form a mixed metallic complex using mild conditions. a-PtL[22]Cl was reacted with one equivalent of $[RuCl_2(PPh_3)_3]$ in DCM at room temperature, the resulting solution was concentrated and hexane added to cause precipitation of a dark green solid in an 81% yield (Scheme 5.1).

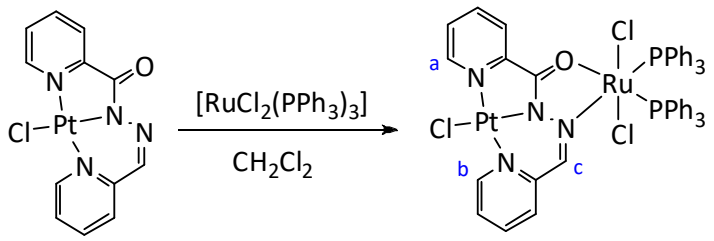

Scheme 5.1: Synthetic procedure to form a-PtCl(μ-L[22])RuCl$_2$(PPh$_3$)$_2$.

The identity of the complex was confirmed by ^{1}H and ^{13}C NMR spectroscopy, electrospray ionisation (ESI) mass spectrometry and elemental analysis. The ^{1}H NMR spectrum of a-PtCl(μ-L[22])RuCl$_2$(PPh$_3$)$_2$ in CDCl$_3$ showed a small upfield shift (0.2 ppm) of proton a + b upon complexation of the second metal centre and proton c is significantly shifted upfield from 7.58 to 6.15 ppm. These observations coincide with those reported by Nakajima and co-workers upon synthesis of complex **47**.

The tridentate Pt(II) complex a-PtL[22]Cl also proved to be a successful precursor to form a mixed Pt(II)-Ir(III) complex. a-PtL[22]Cl was reacted with 0.5 equivalents of [Ir(ppy)$_2$Cl]$_2$ in a mixture of MeOH:DCM at 65°C for 1.5 hours. The resulting solution was evaporated to dryness, dissolved in the minimum amount of MeCN/H$_2$O and pipetted into KPF$_6$ (sat. aq.) to isolate a dark green solid (Scheme 5.2).

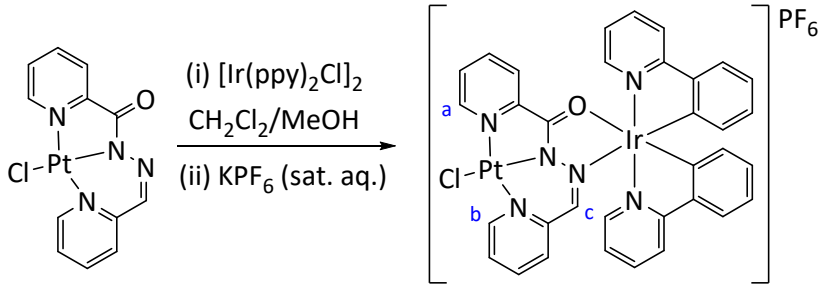

Scheme 5.2: Synthetic procedure to form [a-PtCl(μ-L[22])Ir(ppy)$_2$]PF$_6$.

The identity of the complex was confirmed by ^{1}H and ^{13}C NMR spectroscopy and by electrospray ionisation (ESI) mass spectrometry.

5.2.2 Imide Bridged Complex

Building upon our success with hydrazide bridged complexes, the imide based Pt(II) complex PtL[23]Cl was investigated as a precursor to form a mixed Pt(II)-Ir(III) complex. PtL[23]Cl was reacted with 0.5 equivalents of [Ir(ppy)$_2$Cl]$_2$ in a mixture of MeOH:DCM at 65°C for 2 hours. The resulting solution was evaporated to dryness, dissolved in the minimum amount of DMSO and pipetted into KPF$_6$ to isolate a bright yellow

solid in a 21% yield (Scheme 5.3). The resulting complex $[PtCl(\mu\text{-}L^{23})Ir(ppy)_2]PF_6$ was very poorly soluble in common solvents, although a weak ^1H NMR in deuterated DMSO did support formation of the desired product. The identity of the complex was confirmed by atmospheric pressure solids analysis probe ionisation (ASAP) and accurate mass spectrometry; the measured mass 954.0870 m/z is consistent with the empirical formula $C_{34}H_{24}N_5O_2ClIrPt$ with an accuracy of 2.0 ppm. We interpret this as the molecular ion $[C_{34}H_{24}N_5O_2ClIrPt]^+$.

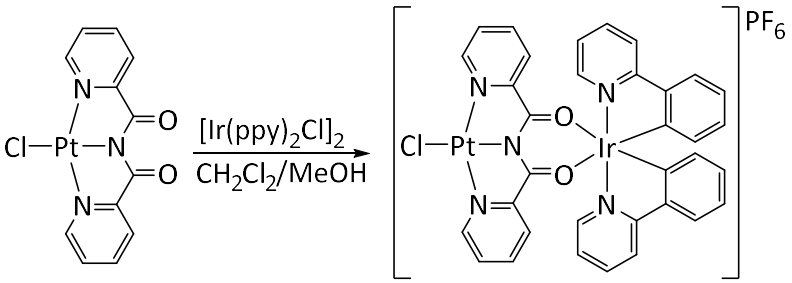

Scheme 5.3: Synthetic procedure to form $[PtCl(\mu\text{-}L^{23})Ir(ppy)_2]PF_6$.

5.2.3 Pyrimidine Bridged Complexes

The N^N^O hydrazone (NMe) based proligand HL^{14} has been extended into a pyrimidine bridged proligand which features potential ditopic N^N^O–N^N^O coordination. A series of such proligands has been synthesised using the synthetic strategy summarised in scheme 5.4.

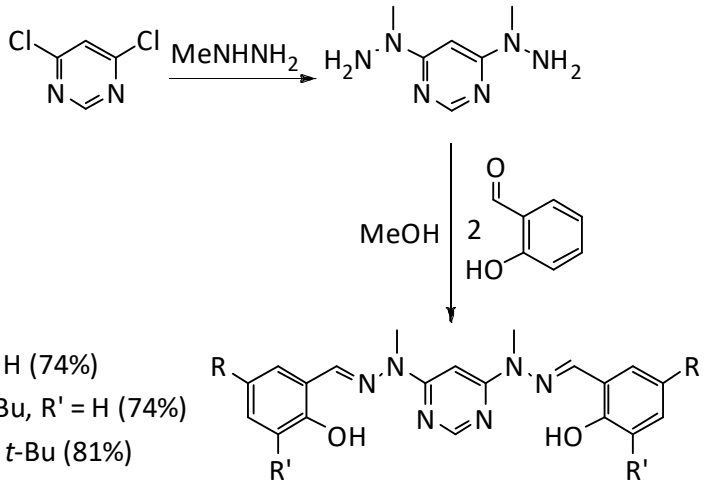

H_2L^{36} R,R' = H (74%)
H_2L^{37} R = *t*-Bu, R' = H (74%)
H_2L^{38} R,R' = *t*-Bu (81%)

Scheme 5.4: Synthetic procedure to form ligands H_2L^{36}-H_2L^{38}.

The key intermediate is 4,6-di(1-methylhydrazino)pyrimidine, from which a variety of bridging bis-terdentate N^N^O-N^N^O proligands can be prepared in one step simply by reaction with an appropriate salicylaldehyde. For example *t*-butyl groups were

incorporated into H_2L^{37} and H_2L^{38} in order to improve the solubility of the final product, since one of the drawbacks of rigid ligands is often poor solubility of products.[187] The reaction invariably produces a fine white powder which can be isolated by filtration in high yields over the two steps.

Condensation of the aldehyde and the hydrazine results in a significant upfield shift of the N=C-H proton in the ^{1}H NMR spectra. For instance, in H_2L^{36} this proton resonates at 8.49 ppm in $CDCl_3$ compared to 9.90 ppm for salicylaldehyde. The aromatic and phenolic protons are largely unaffected, nor is there a significant shift of the N-Me protons.

Crystals of proligands H_2L^{36} and H_2L^{38} were obtained by slow evaporation of chloroform solutions. The structures obtained confirm the identities of the compounds (Figure 5.14). The molecules adopt a spiral configuration, similar to that found in fascinating pyrimidine dihydrazone compounds.[189] The torsional angles between the plane defined by the hydrazone group and the pyrimidine ring is larger in H_2L^{38} (22°) than H_2L^{36} (13°) as is the angle between the phenol rings, 61 and 23°, respectively.

In the first instance, we explored the complexation chemistry of the proligand HL^{36} with Pt(II). Due to our successful complexation of proligands HL^{14} – HL^{20} using K_2PtCl_4, we initially attempted to synthesise a bimetallic Pt(II) complex using the same method. K_2PtCl_4 and the proligand H_2L^{36} in a 2:1 molar ratio were refluxed in a EtOH:H_2O mixture for 2 hours. The resulting mixture was cooled to ambient temperature and filtered to yield the crude product. Initial analysis of the crude reaction material revealed a complex mixture of products in which the predominant product was a monometallic Pt(II) complex in which only one of the N^N^O coordination sites was occupied. Purification of this mixture proved challenging and we were unable to isolate $PtHL^{36}Cl$. In an alternative procedure the mononuclear complex was successfully obtained by refluxing a mixture of the proligand H_2L^{36}, 2.1 equivalents of $Pt(COD)Cl_2$ and an excess of NEt_3 in MeCN (Scheme 5.5). The highly insoluble yellow precipitate was collected by hot filtration to give complex $PtHL^{36}Cl$ in a yield of 52%.

Incorporation of a single Pt(II) ion resulted in a loss of symmetry in the ^{1}H NMR spectrum. Upon complexation there is a downfield shift of the N-Me protons nearest to the metal (a) whereas the resonance of the N-Me protons (a') is less affected (see labelling in Scheme 5.5). For instance, the N-Me protons resonate at 3.61 ppm in DMSO-d_6 in the proligand H_2L^{36} compared to 3.88 and 3.66 ppm in complex $PtHL^6Cl$ for NMe (a) and NMe

(a') respectively. We observe an upfield shift of the remaining phenolic O-H proton, from 10.98 to 10.24 ppm.

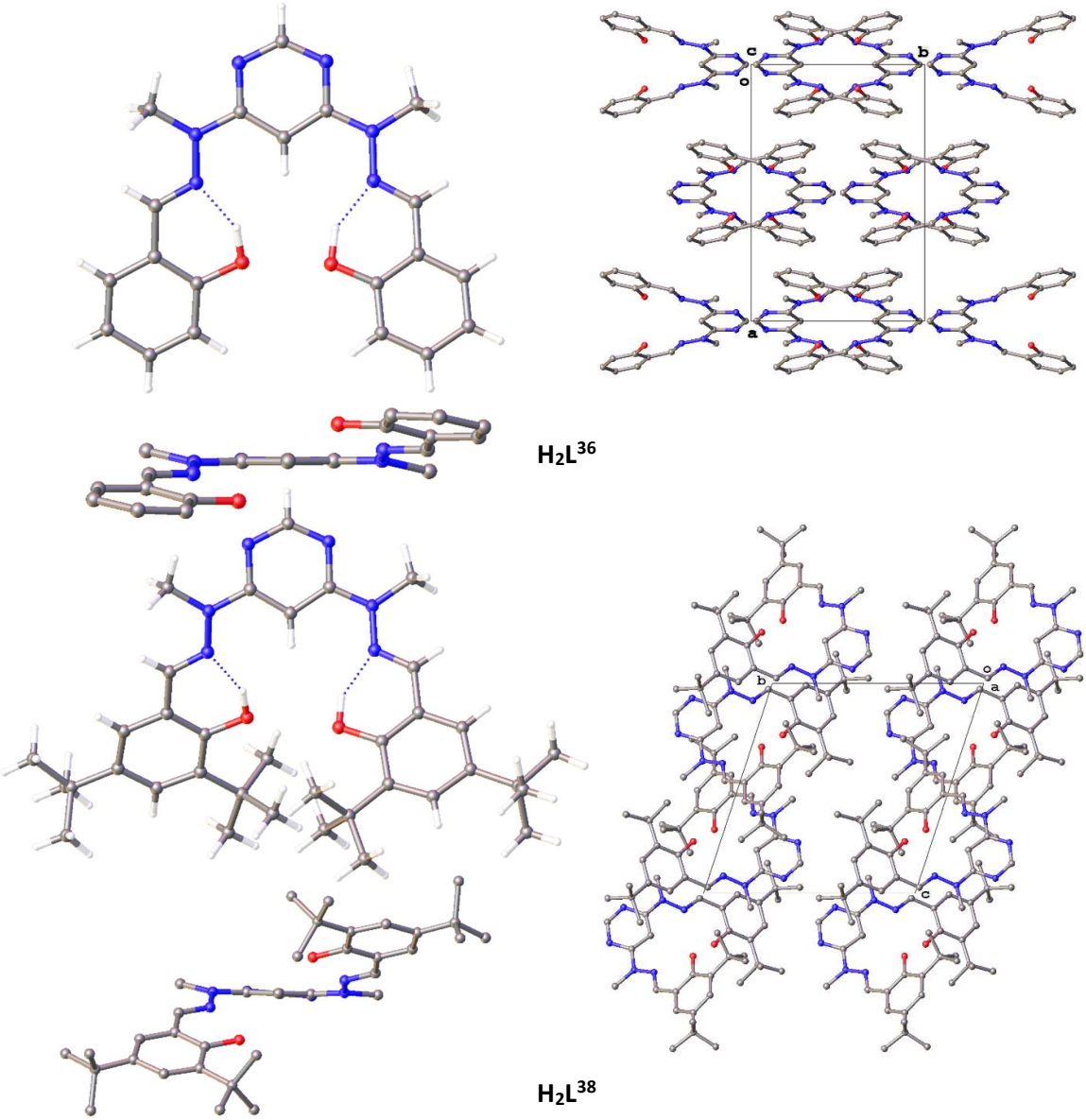

Figure 5.14: Crystal structure and packing of H_2L^{36} (above) and H_2L^{38} (below) ; T = 120 K. Hydrogen atoms are omitted for clarity.

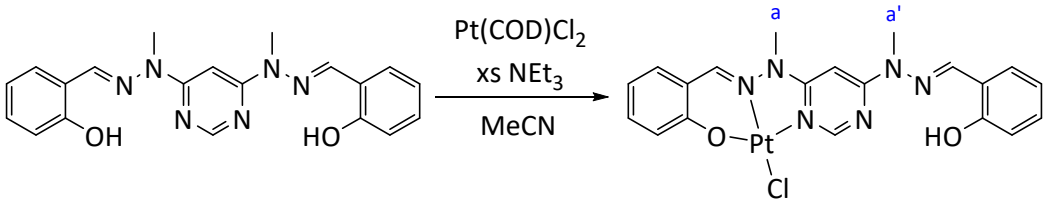

Scheme 5.5: Synthesis of $PtHL^{36}Cl$

A number of unsuccessful attempts were made to synthesise the dinuclear Pt(II) complex of H_2L^{36}, which we attribute to the highly insoluble nature of $PtHL^{36}Cl$ preventing

further reaction. Incorporation of t-butyl groups into H_2L^{37} and H_2L^{38} was anticipated to increase the solubility of the resulting product and facilitate the formation of a dinuclear Pt(II) complex but we found that the solubility of the resulting proligands was decreased in MeCN and we were unable to form even their corresponding mononuclear Pt(II) complexes.

We have also explored the complexation chemistry of the proligands H_2L^{36} – H_2L^{39} with iridium(III), synthesising a series of mono- and dinuclear complexes (Scheme 5.6). The tridentate proligand dpyxH is known to react with $IrCl_3.3H_2O$ in ethoxyethanol/water to give a dichloro-bridged dimer $[Ir(dpyx)Cl(\mu\text{-}Cl)_2]_2$.[98] Reaction of the di-chloro bridged iridium dimer with proligands H_2L^{36} – H_2L^{39} was carried out in ethylene glycol at 195°C for 90 minutes, leading to the corresponding mono or dinuclear complexes depending on the stoichiometry used. The chloride counter anion was exchanged for PF_6 by precipitation in aq. sat. KPF_6. The complexes were purified by column chromatography followed by recrystallization from acetonitrile/ether.

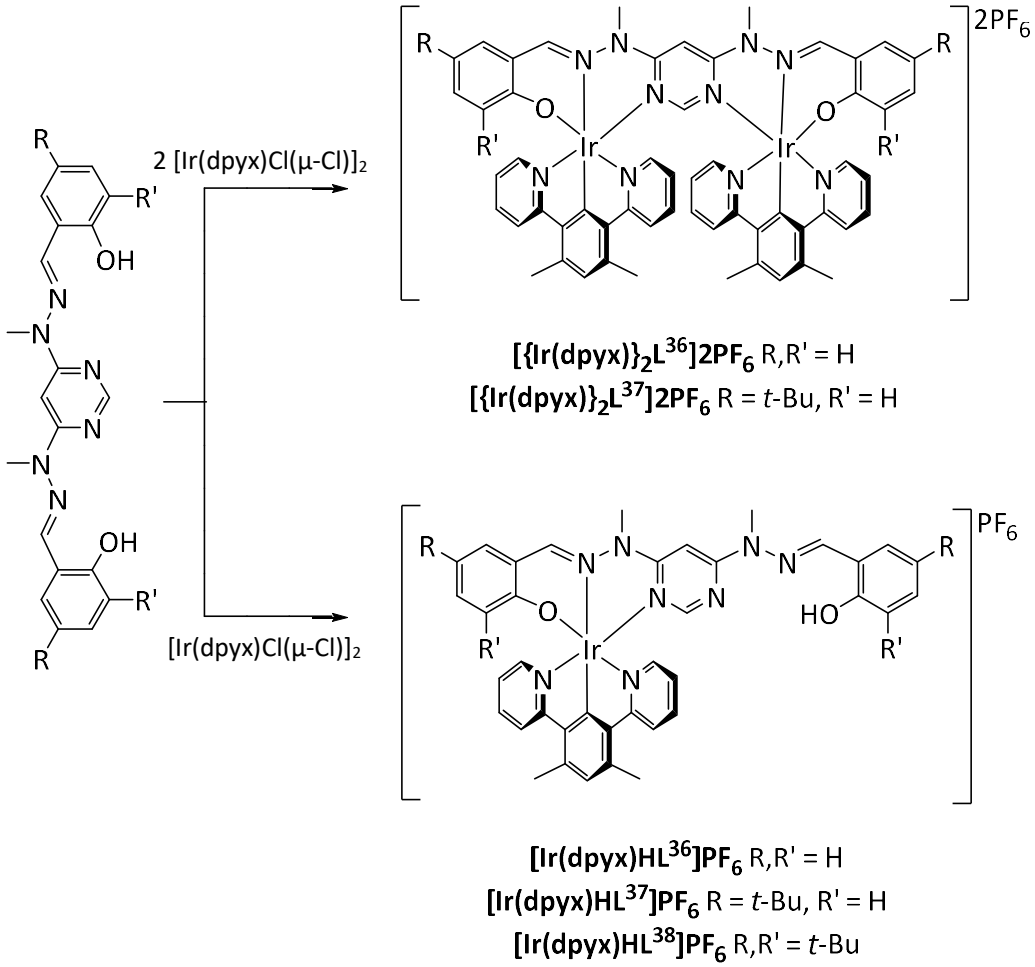

$[\{Ir(dpyx)\}_2L^{36}]2PF_6$ R,R' = H
$[\{Ir(dpyx)\}_2L^{37}]2PF_6$ R = *t*-Bu, R' = H

$[Ir(dpyx)HL^{36}]PF_6$ R,R' = H
$[Ir(dpyx)HL^{37}]PF_6$ R = *t*-Bu, R' = H
$[Ir(dpyx)HL^{38}]PF_6$ R,R' = *t*-Bu

Scheme 5.6: Synthesis of dinuclear and mononuclear Ir(III) complexes.

The identity of the complexes was confirmed by ^{1}H and ^{13}C NMR spectroscopy and by electrospray ionisation (ESI) mass spectrometry. Crystals of $[\{Ir(dpyx)\}_2L^{36}]2PF_6$ and $[\{Ir(dpybx)\}_2L^{37}]2PF_6$ suitable for X-ray diffraction were obtained from a MeCN solution by slow evaporation of the solvent (Figure 5.15 and Figure 5.16, respectively). A summary of important bond lengths and angles are shown in Table 5.1.

Table 5.1: Selected Bond Distances (Å) and Angles (deg) for the Iridium Complexes $[Ir(dpybx)_2L^{36}]2PF_6$ and $[Ir(dpybx)_2L^{37}]2PF_6$

		$[Ir(dpybx)_2L^{36}]2PF_6$	$[Ir(dpybx)_2L^{37}]2PF_6$
Bond Lengths	Ir1-O1	2.013(7)	2.026(4)
	Ir1-N1	2.066(8)	2.079(5)
	Ir1-N3	2.017(7)	2.027(5)
	Ir1-N4	2.049(9)	2.045(5)
	Ir1-N5	2.023(8)	2.051(5)
	Ir1-C19	1.971(10)	1.952(5)
	Ir2-O2	2.036(7)	2.029(4)
	Ir2-N6	2.007(8)	2.029(5)
	Ir2-N8	2.074(7)	2.079(5)
	Ir2-N9	2.051(8)	2.053(5)
	Ir2-N10	2.073(8)	2.055(5)
	Ir2-C45	1.966(9)	1.947(5)
Bond Angles	O1-Ir1-N3	172.1(3)	171.58(17)
	N1-Ir1-C19	177.7(4)	176.0(2)
	N5-Ir1-N4	161.3(4)	160.87(19)
	O2-Ir2-N6	171.5(3)	171.44(17)
	N8-Ir2-C45	176.2(3)	178.2(2)
	N9-Ir2-N10	161.2(3)	160.42(18)
Distances	Ir1-Ir2	5.984	6.021

In both of the structures the iridium atoms are hexacoordinated in a distorted octahedral mode. The intermetallic distance is 5.984 and 6.021 Å in $[\{Ir(dpyx)\}_2L^{36}]2PF_6$ and $[\{Ir(dpyx)\}_2L^{37}]2PF_6$, respectively and the mean values of the Ir-C (1.959 Å) and Ir-N (2.05 Å) bonds in the Ir(dpyx) unit are within the normal ranges expected for such cyclometalated complexes.[163] The mean values of the Ir-N(hydrazone) (2.0745 Å), Ir-N(pyridine) (2.02 Å) and Ir-O (2.026 Å) are similar to those reported for the monometallic complex $[Ir(dpyx)L^{15}]PF_6$ discussed earlier in the text.

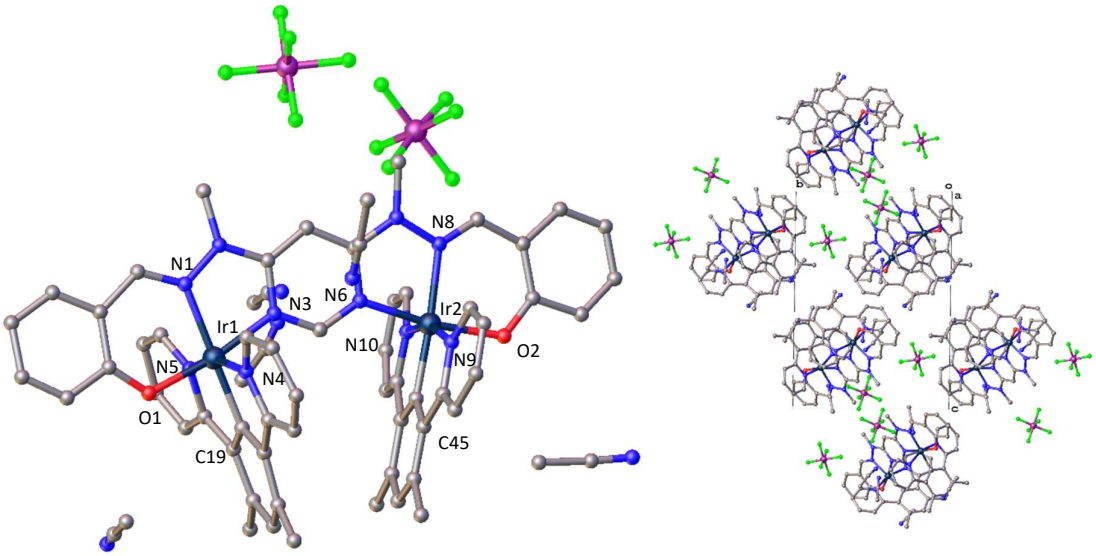

Figure 5.15: Crystal Structure and Packing of Iridium Complex [{Ir(dpyx)}$_2$L^{36}]2PF$_6$; T = 120 K. Hydrogen atoms are omitted for clarity.

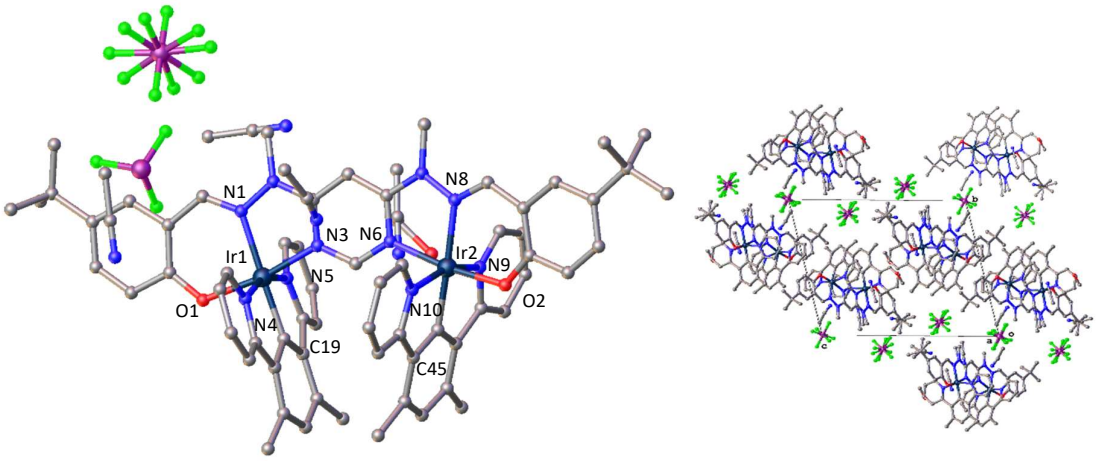

Figure 5.16: Crystal Structure and Packing of Iridium Complex [{Ir(dpyx)}$_2$L^{37}]2PF$_6$; T = 120 K. Hydrogen atoms are omitted for clarity.

The successful formation of both Pt(II) and Ir(III) monometallic complexes with these ditopic ligands led us to explore the formation of a mixed metal binuclear complex. Owing to the harsh conditions required for the preparation of [Ir(dpyx)HL^{36}]PF$_6$ – [Ir(pyxHL^{38}]PF$_6$, we tried incorporating the iridium centre first, to be followed by the introduction of the platinum ions. We made several unsuccessful attempts to introduce a platinum ion before altering our strategy and attempting to incorporate the platinum centre first, to be followed by the introduction of the iridium ion. The monometallic Pt(II) complex, PtHL^{36}Cl, was reacted with the dichloro-bridged dimer [Ir(dpyx)Cl(μ-Cl)$_2$]$_2$ in ethylene glycol at 195 °C. The chloride counter anion was exchanged for PF$_6$ by precipitation

in aq. sat. KPF_6. Initial analysis of the crude reaction material revealed a complex mixture of products in which the predominant product was the desired mixed multinuclear complex $[Ir(dpybx)(L^{36})PtCl]PF_6$ (Figure 5.17). The identity of the complex was confirmed by electrospray ionisation (ESI) mass spectrometry and accurate mass spectrometry; the measured mass of 1053.1658 m/z is consistent with the empirical formula $C_{38}H_{33}N_8O_2ClIrPt$ with an accuracy of 0.9 ppm. We interpret this as the molecular ion $[C_{38}H_{33}N_8O_2ClIrPt]^+$. Purification of this mixture proved challenging and we were unable to isolate the complex in sufficient purity for further studies.

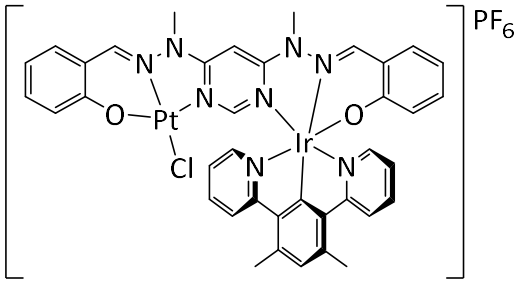

Figure 5.17: Mixed Pt(II)-Ir(III) multinuclear complex $[Ir(dpybx)(L^{36})PtCl]PF_6$.

5.3 Photophysical Properties of Bimetallic Complexes

5.3.1 Hydrazide Bridged Complexes

Electronic Absorption Spectra

The absorption spectra of complexes a-$PtCl(\mu\text{-}L^{22})RuCl_2(PPh_3)_2$ and $[a\text{-}PtCl(\mu\text{-}L^{22})Ir(ppy)_2]PF_6$ were recorded in DCM at room temperature (Figure 5.18).

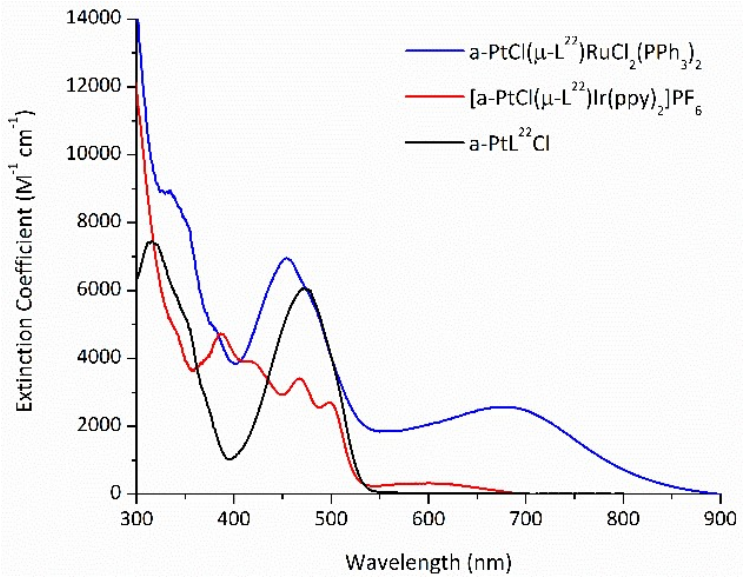

Figure 5.18: UV-Vis electronic absorption spectra of a-$PtCl(\mu\text{-}L^{22})RuCl_2(PPh_3)_2$, $[a\text{-}PtCl(\mu\text{-}L^{22})Ir(ppy)_2]PF_6$ and a-$PtL^{22}Cl$ in DCM at 298 K.

The key transitions in the UV-Vis electronic absorption spectra of a-PtL^{22}Cl are retained in a-PtCl(μ-L^{22})RuCl$_2$(PPh$_3$)$_2$, with the presence of an additional broad transition centred at ~700 nm attributed to a MLCT band related to the RuCl$_2$(PPh$_3$)$_2$ unit.[131] The UV-Vis electronic absorption spectra of [a-PtCl(μ-L^{22})Ir(ppy)$_2$]PF$_6$ is markedly different from that of a-PtL^{22}Cl. The intense bands centred at approximately 400 nm are attributed to ^{1}MLCT transitions and the band centred at ~600 nm is attributed to the ^{3}MLCT transition of the Pt unit.

Emission

Complexes a-PtCl(μ-L^{22})RuCl$_2$(PPh$_3$)$_2$ and [a-PtCl(μ-L^{22})Ir(ppy)$_2$]PF$_6$ display no observable emission at ambient temperature in solution or the solid state. In glassy solution at 77 K, the complexes are weakly emissive, displaying a structurally well resolved luminescence spectrum.

The emission of a-PtCl(μ-L^{22})RuCl$_2$(PPh$_3$)$_2$ is similar to that of a-PtL^{22}Cl (Figure 5.19). The emission of a-PtCl(μ-L^{22})RuCl$_2$(PPh$_3$)$_2$ is therefore thought to originate from states involving the Pt(II) centre suggesting minimal excited-state interactions between the Pt(II) and Ru(II) centres. The estimated lifetime of emission is in the range of microseconds, indicating phosphorescent emission (Table 5.2).

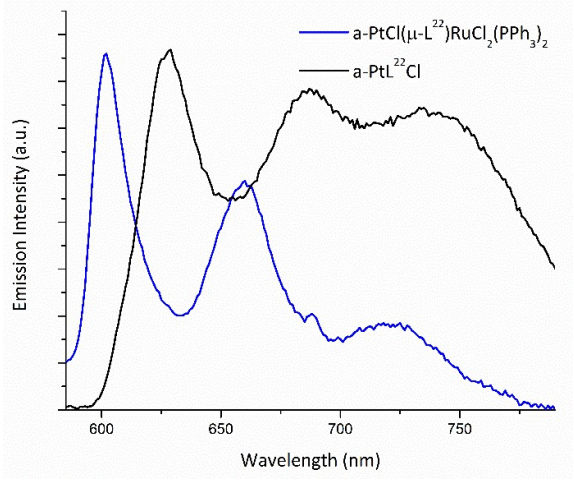

Figure 5.19: Normalised emission spectra of a-PtCl(μ-L^{22})RuCl$_2$(PPh$_3$)$_2$ in butyronitrile rigid glass at 77 K and a-PtL^{22}Cl in EPA rigid glass at 77 K.

The 77 K emission spectra of [a-PtCl(μ-L^{22})Ir(ppy)$_2$]PF$_6$ appears to display dual emission, with bands attributable to the Ir(III) and Pt(II) components appearing simultaneously. The bands around 496 nm are attributed to the Ir(III) component whereas

the bands around 659 nm are attributed to the Pt(II) component. Again, there appears to be minimal excited-state interactions.

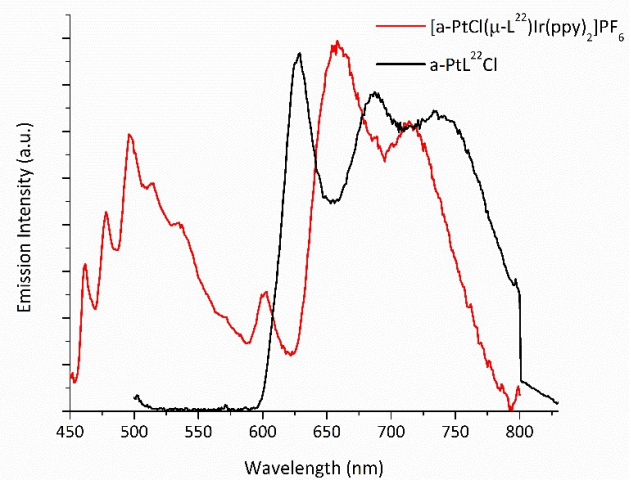

Figure 5.20: Normalised emission spectra of [a-PtCl(μ-L^{22})Ir(ppy)$_2$]PF$_6$ in butyronitrile rigid glass at 77 K and a-PtL^{22}Cl in EPA rigid glass at 77 K.

5.3.2 Imide Bridged Complexes

Photophysical Properties

Complex [PtCl(μ-L^{23})Ir(ppy)$_2$]PF$_6$ is very poorly soluble in all common organic solvents. The absorption spectrum of complex [PtCl(μ-L^{23})Ir(ppy)$_2$]PF$_6$ was recorded DCM at room temperature (Figure 5.21). It can be seen that spectrum is very similar to that of PtL^{23}Cl, although the extinction coefficients are greatly increased, by a factor of around 2, throughout the spectrum. The lowest energy band is slightly blue-shifted in [PtCl(μ-L^{23})Ir(ppy)$_2$]PF$_6$, from 405 nm in PtL^{23}Cl to 396 nm in [PtCl(μ-L^{23})Ir(ppy)$_2$]PF$_6$. There is no observable emission at ambient temperature or 77 K in solution or in the solid state.

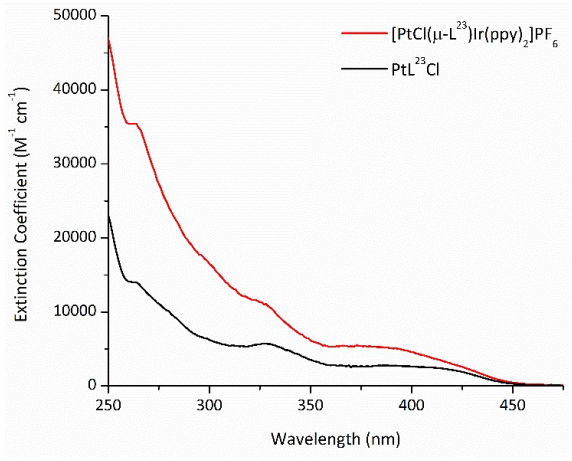

Figure 5.21: UV-Vis electronic absorption spectra of [PtCl(μ-L^{23})Ir(ppy)$_2$]PF$_6$ and PtL^{23}Cl in DCM at 298 K.

Table 5.2: Photophysical data for complexes a-PtL^{22}Cl, a-PtCl(μ-L^{22})RuCl$_2$(PPh$_3$)$_2$ and [a-PtCl(μ-L^{22})Ir(ppy)$_2$]PF$_6$

Complex	298 K							77 K	
	$\lambda_{(abs)}$ (nm)	$\lambda_{(em)}$ (nm)	τ * (μs)[a]	Φ[b] (%)	k_r (10^3 s^{-1})	k_{nr} (10^5 s^{-1})	k_q[c] (mol^{-1} dm^3 s^{-1})	$\lambda_{(em)}$ (nm)	τ (μs)
a-PtL^{22}Cl	261, 317, 356(sh) , 478	625, 683, 756	0.4 (0.2)	0.5	1.3	25	1.1 x 10^9	629, 688, 742	0.9
a-PtCl(μ-L^{22})RuCl$_2$(PPh$_3$)$_2$	290(sh), 348, 455, 692	-	-	-	-	-	-	601, 660, 722	16+4(75/25)[d]
[a-PtCl(μ-L^{22})Ir(ppy)$_2$]PF$_6$	258, 297(sh), 389, 423, 469, 501, 602	-	-	-	-	-	-	462, 479, 496, 515, 537, 602, 659, 715	(λ = 496) 12 (λ = 659) =15+3(80/20)[d]

*[a] Luminescence lifetime in degassed DCM solution; corresponding values in air-equilibrated solution are given in parentheses. [b] ±20%.[c] Bimolecular rate constant for quenching by O_2. [d]biexponential; relative weightings of components in parenthesis. *X^2 values are located in appendix 7.3*

5.3.3 Pyrimidine Bridged Complexes

Pt(II) Complexes

Electronic Absorption Spectra

The absorption spectrum of $PtHL^{36}Cl$ was recorded in DCM at room temperature (Figure 5.22). It can be seen that the absorption of $PtHL^{36}Cl$ is red-shifted compared to $PtL^{14}Cl$, which may be attributed to the increased conjugation in the proligand HL^{36} or the change from a pyridine to a pyrimidine ring. The absorption bands below 300 nm are assigned to $^1\pi - \pi^*$ transitions localised on the ligand. The absorption bands centred at ~430 nm and in the region 300 – 375 nm closely resemble the charge transfer bands of the parent tridentate complex $PtL^{14}Cl$ and thus are assigned similarly.

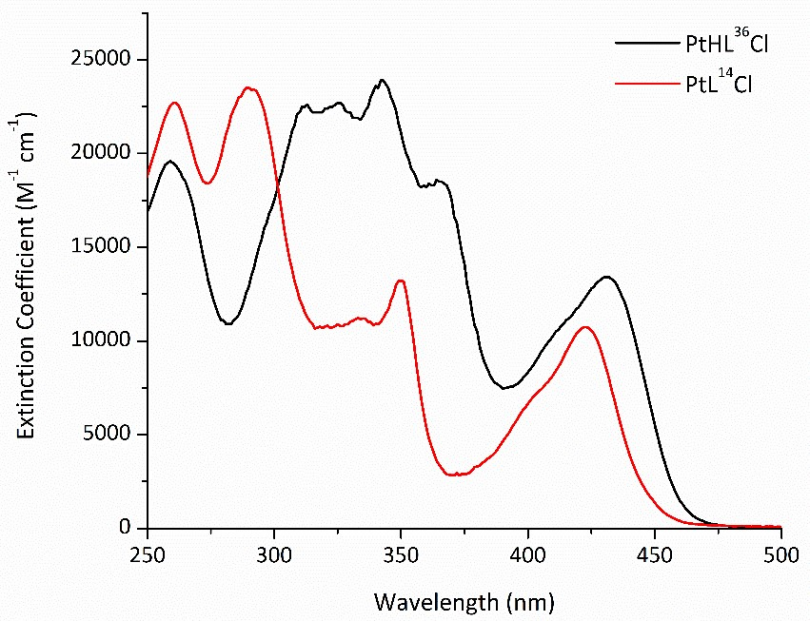

Figure 5.22: UV-Vis electronic absorption spectra of $PtHL^{36}Cl$ and $PtL^{14}Cl$ in DCM at 298 K.

Emission

The complex $PtHL^{36}Cl$ is essentially non-emissive in solution at room temperature, however in dilute glassy solution at 77 K we observe highly structured emission (Figure 5.23). The λ_{max} emission is slightly red-shifted compared to $PtL^{14}Cl$, by approximately 300 cm^{-1}. It is notable that the 0 – 0 vibrational component is higher than the 0 – 1 in $PtHL^{36}Cl$, suggesting less excited-state distortion than for $PtL^{14}Cl$, although the value of 0.91 is still indicative of a large degree of distortion. The luminescence lifetime τ of complex $PtHL^{36}Cl$ is 33 µs, comparable to the of $PtL^{14}Cl$ (36 µs) and indicating phosphorescent emission.

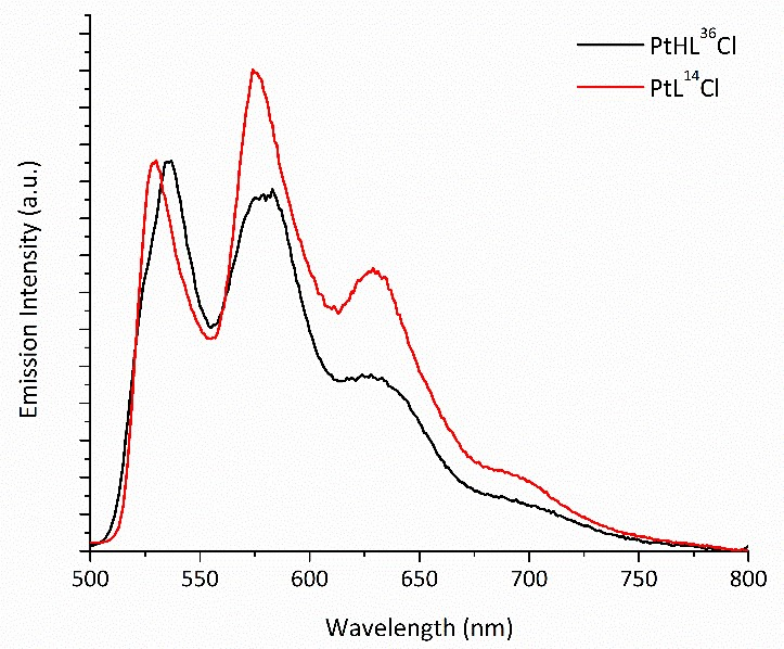

Figure 5.23: Normalised emission spectra of $PtHL^{36}Cl$ in butyronitrile and $PtL^{14}Cl$ in frozen EPA glass at 77 K.

Ir(III) Complexes

Electronic Absorption Spectra

The absorption spectra of the monometallic $[Ir(dpyx)HL^{36}]PF_6$ — $[Ir(dpyx)HL^{38}]PF_6$ were recorded in DCM at room temperature (Figure 5.24). It can be seen that there is very little variation in the absorption of each of the complexes, although there does appear to be a slight red shift of the lowest energy band with the addition of increasing numbers of t-butyl groups. Comparison with the absorption spectrum of $[Ir(dpyx)L^{14}]PF_6$ shows a red shift in the whole spectrum which may be attributed to the increased conjugation in the proligand HL^{36} or the change from a pyridine to a pyrimidine ring. The bands between 300 – 400 nm can thus be attributed to $^1\pi$-π^* transitions and the weaker transition extending to 450 nm are attributed to transitions with charge transfer character.

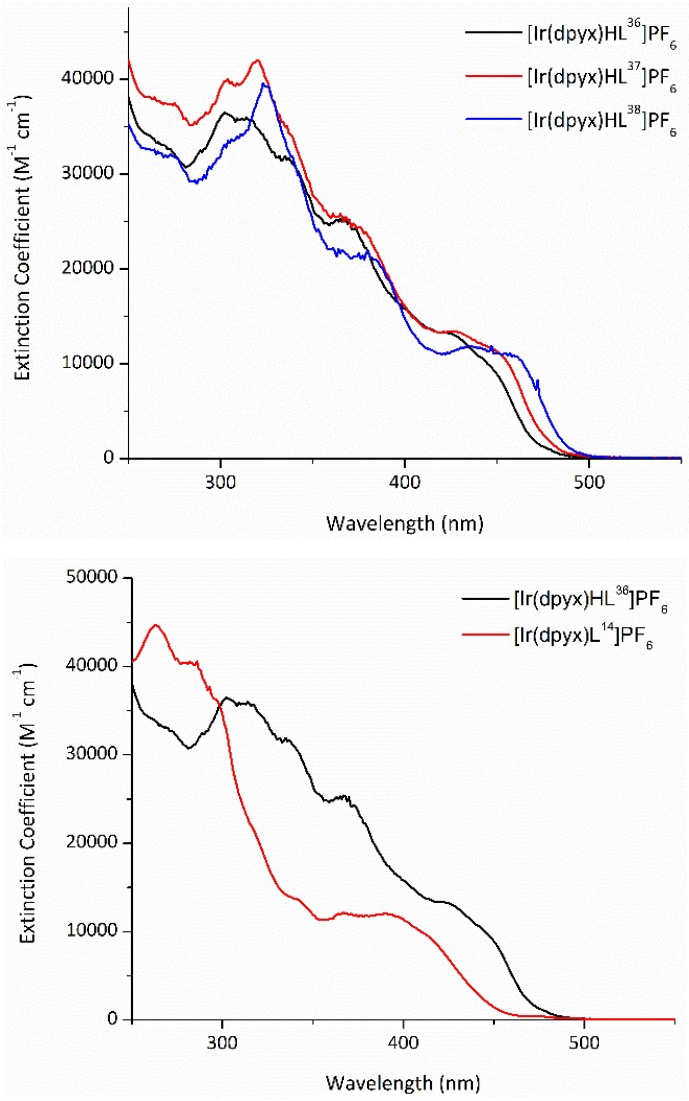

Figure 5.24: UV-Vis electronic absorption spectra of [Ir(dpyx)HL^{36}]PF$_6$ – [Ir(dpyx)HL^{38}]PF$_6$ in DCM at 298 K (top) and [Ir(dpyx)HL^{36}]PF$_6$ and [Ir(dpyx)L^{14}]PF$_6$ (bottom).

The absorption spectra of bimetallic [{Ir(dpyx)}$_2$L^{36}]2PF$_6$ and [{Ir(dpybx)}$_2$L^{37}]2PF$_6$ were recorded in DCM at room temperature (Figure 5.25). It can be seen that once again there is very little variation in the absorption of both of the complexes, although there does appear to be a slight red-shift of the lowest energy band with the addition of the t-butyl groups. It can be seen that the absorption of [{Ir(dpyx)}$_2$L^{36}]2PF$_6$ is strongly red-shifted compared to [Ir(dpyx)HL^{36}]PF$_6$ and the extinction coefficient of the lowest energy band is greatly increased.

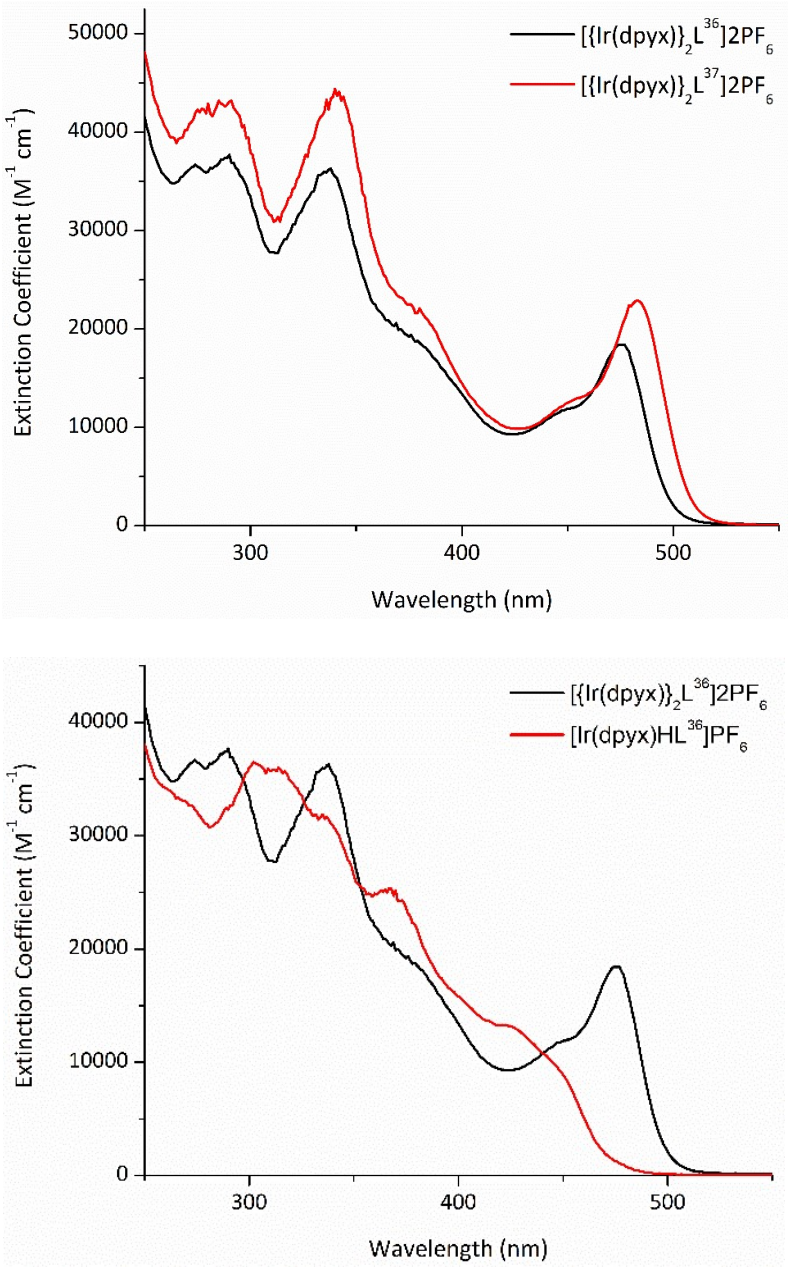

Figure 5.25: UV-Vis electronic absorption spectra of [{Ir(dpyx)}$_2$L^{36}]2PF$_6$ and [{Ir(dpybx)}$_2$L^{37}]2PF$_6$ in DCM at 298 K (top) and [{Ir(dpyx)}$_2$L^{36}]2PF$_6$ and [Ir(dpyx)HL^{36}]PF$_6$ (bottom).

Emission

The emission spectra of the monometallic [Ir(dpyx)HL^{36}]PF$_6$ - [Ir(dpyx)HL^{38}]PF$_6$ were recorded in degassed DCM at room temperature (Figure 5.26). All of the complexes are luminescent in solution at room temperature. There is a ~10 nm red-shift of what appears to be the 0 – 0 band on the addition of increasing numbers of t-butyl groups. The emission spectra display poorly defined vibronic progression. It is noteworthy that the emission (λ_{max}) observed for [Ir(dpyx)HL^{36}]PF$_6$ and the earlier reported monometallic complex [Ir(dpyx)L^{14}]PF$_6$ are identical, both showing emission maxima at 560 and 600 nm.

The PLQYs in degassed solution at 298 K are in the range 0.006 – 0.016 (Table 5.3). Some insight into this may be obtained by considering the rate constants for radiative (k_r) and nonradiative (k_{nr}) decay. The 'parent' complex [Ir(dpyx)HL[36]]PF_6 has a PLQY of 0.6%, which is increased in [Ir(dpyx)HL[37]]PF_6 to 1.6% due to an increase in k_r accompanied by a decrease in k_{nr}. The PLQY of [Ir(dpyx)HL[38]]PF_6 is reduced to 0.2% which can be attributed to a decrease in k_r while k_{nr} appears unaffected from the parent complex. In comparison to the earlier reported monometallic complexes, [Ir(dpyx)L[14]]PF_6 – [Ir(dpyx)L[17]]PF_6, there is a tenfold decrease in the rate of radiative decay. Interestingly, the rates of non-radiative decay are of the same order in both series.

The emission life time (τ) of all the complexes show susceptibility to quenching by dioxygen confirming that emission originates from a triplet state. The emission bimolecular rate constant for quenching by O_2 (k_q) of [Ir(dpyx)HL[36]]PF_6 - [Ir(dpyx)HL[38]]PF_6 are of the same order as the previously dicussed monometallic complexes, [Ir(dpyx)L[14]]PF_6 – [Ir(dpyx)L[17]]PF_6.

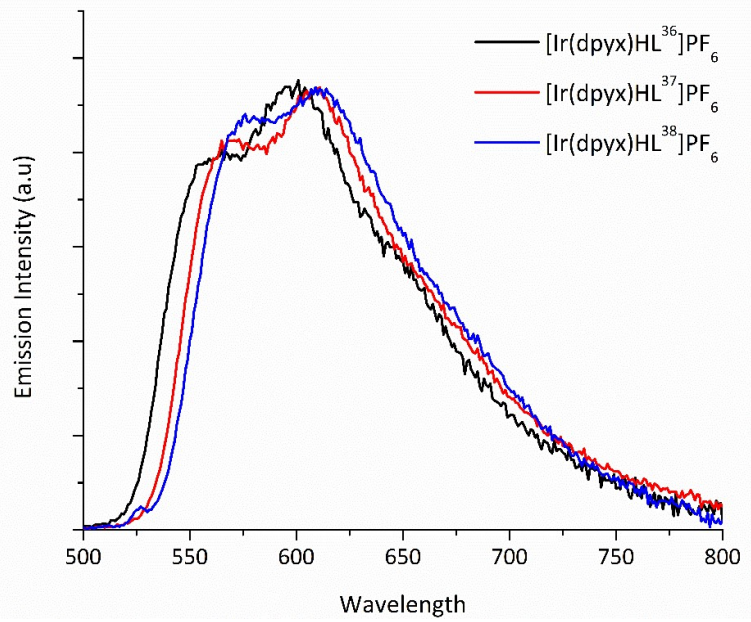

Figure 5.26: Normalised emission spectra of [Ir(dpyx)HL[36]]PF_6 - [Ir(dpyx)HL[38]]PF_6 in degassed DCM at 298 K.

All complexes show increased emission at 77K in frozen butyronitrile and the estimated lifetimes of the emissions remain in the range of microseconds, indicating phosphorescent emission. All of the complexes displayed highly structured spectra, with an approximate 800 cm^{-1} blue-shift of the 0,0 band from the room temperature emission

(Figure 5.27). The 0,0 band is dominant, suggesting a relatively small degree of distortion in the excited state.

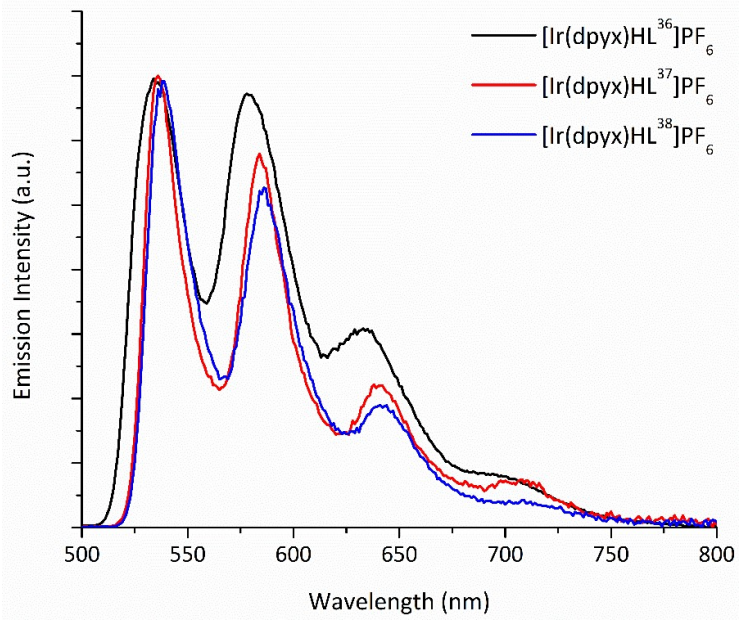

Figure 5.27: Normalised emission spectra of [Ir(dpyx)HL^{36}]PF$_6$ - [Ir(dpyx)HL^{38}]PF$_6$ in butyronitrile glass at 77 K.

The emission spectra of the bimetallic [{Ir(dpyx)}$_2$L^{36}]2PF$_6$ and [{Ir(dpybx)}$_2$L^{37}]2PF$_6$ were recorded in degassed DCM at room temperature (Figure 5.28). Both of the complexes are luminescent in solution at room temperature. There is a small red-shift in emission (~6 nm) compared to [Ir(dpyx)HL^{36}]PF$_6$ and [Ir(dpyx)HL^{37}]PF$_6$ with the addition of a second Ir(III) centre. As we observed for the monometallic complexes [Ir(dpyx)HL^{36}]PF$_6$ - [Ir(dpyx)HL^{38}]PF$_6$, there is a ~10 nm red-shift in the emission from [{Ir(dpyx)}$_2$L^{36}]2PF$_6$ (566 nm) to [{Ir(dpybx)}$_2$L^{37}]2PF$_6$ (576 nm) with the addition of the t-butyl group.

Although there is a relatively small effect on the energy of emission with the addition of the second Ir(III) centre, there is a significant effect on the PLQY of luminescence. There is a 6-fold increase in the PLQY for each of the complexes with the addition of the second Ir(III) centre (Table 5.3). The 'parent' complex [{Ir(dpyx)}$_2$L^{36}]2PF$_6$ has a PLQY of 3.7%, which is increased to 11% in [{Ir(dpybx)}$_2$L^{37}]2PF$_6$, which is attributed to a significant decrease in the non-radiative rate constant of [{Ir(dpybx)}$_2$L^{37}]2PF$_6$.

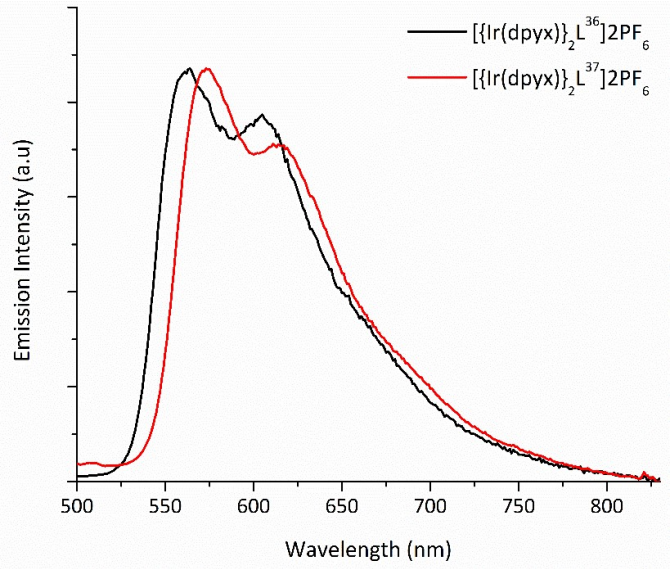

Figure 5.28: Normalised emission spectra of $[\{Ir(dpyx)\}_2L^{36}]2PF_6$ and $[\{Ir(dpybx)\}_2L^{37}]2PF_6$ in degassed DCM at 298 K.

Both complexes show increased emission at 77K in frozen butyronitrile and the estimated lifetimes of the emissions remain in the range of microseconds, indicating phosphorescent emission. Both of the complexes displayed highly structured spectra, with an approximate 800 cm^{-1} blue-shift of the 0,0 band from the room temperature emission (Figure 5.29). The 0,0 band is dominant, suggesting a relatively small degree of distortion in the excited state.

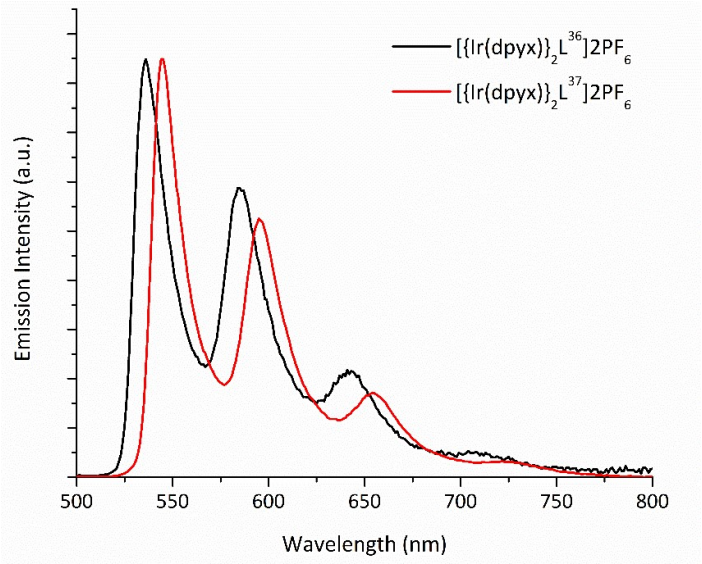

Figure 5.29: Normalised emission spectra of $[\{Ir(dpyx)\}_2L^{36}]2PF_6$ and $[\{Ir(dpybx)\}_2L^{37}]2PF_6$ in butyronitrile at 77 K.

Table 5.3: Photophysical data for complexes [Ir(dpyx)HL[36]]PF_6 - [Ir(dpyx)HL[38]]PF_6 and [{Ir(dpyx)}$_2$L[36]]$2PF_6$ - [{Ir(dpyx)}$_2$L[37]]$2PF_6$.

Complex	298 K							77 K	
	$\lambda_{(abs)}$ (nm)	$\lambda_{(em)}$ (nm)	τ * (μs)[a]	Φ (%)	k_r (10^3 s^{-1})	k_{nr} (10^5 s^{-1})	k_q[e] (mol^{-1} dm^3 s^{-1})	$\lambda_{(em)}$ (nm)	τ (μs)
Monometallic									
[Ir(dpyx)HL[36]]PF_6	303, 318(sh), 340(sh), 370(sh), 428, 450(sh)	560(sh), 599	4.6(0.3)	0.6[b]	1.3	2.2	1.4×10^9	535, 581, 636, 708	18
[Ir(dpyx)HL[37]]PF_6	305(sh), 320, 378(sh), 430, 445(sh)	570(sh), 608	6.4(0.3)	1.6[b]	2.5	1.5	1.5×10^9	537, 584, 643, 709	15
[Ir(dpyx)HL[38]]PF_6	305(sh), 325, 384(sh), 436, 463(sh)	578(sh), 612	5.0(0.3)	0.2[c]	0.4	2.0	1.4×10^9	539, 587, 642, 716	18
Bimetallic									
[{Ir(dpyx)}$_2$L[36]]$2PF_6$	275, 289, 339, 385(sh), 446(sh), 476	566, 606(sh)	0.9(0.2)	3.7[d]	41	11	1.8×10^9	536, 586, 645, 717	15
[{Ir(dpyx)}$_2$L[37]]$2PF_6$	276, 289, 341, 385(sh), 448(sh), 484	576, 618(sh)	4.0(0.2)	11[d]	28	2.2	2.2×10^9	545, 597, 655, 728	18

[a] Luminescence lifetime in degassed DCM solution; corresponding values in air-equilibrated solution are given in parentheses. [b] ±20% [c] ±30% [d] ±10%

*[e] Bimolecular rate constant for quenching by O_2. *X^2 values are located in appendix 7.3*

Concluding Remarks

We have successfully synthesised and characterised a range of novel bimetallic complexes, incorporating a combination of Pt(II), Ir(III) and Ru(II) centres.

We began by exploring the coordination of a second metal centre to two of our previously prepared monometallic complexes. The hydrazide-based complex a-PtL^{22}Cl provided a N^O- donor set of which we explored the coordination to Ru(II) and Ir(III) whilst the imide-based complex PtL^{23}Cl provided a O^O- donor set of which we explored the coordination to Ir(III).

The hydrazide-bridged complexes a-PtCl(μ-L^{22})$RuCl_2(PPh_3)_2$ and [a-PtCl(μ-L^{22})$Ir(ppy)_2$]PF_6 have high extinction coefficients over a wide range of the UV-Visible spectrum, a-PtCl(μ-L^{22})$RuCl_2(PPh_3)_2$ in particular absorbs strongly from 250 to 900 nm. Both complexes are non-emissive at room temperature. Measurements at 77 K reveal structured emission from the Pt(II) unit in both complexes and the Ir(III) unit in [a-PtCl(μ-L^{22})$Ir(ppy)_2$]PF_6. There appears to be minimal ground state interactions between the Pt(II) and Ru(II)/Ir(III) unit in each of the complexes.

The imide-bridged complex [PtCl(μ-L^{23})$Ir(ppy)_2$]PF_6 has a UV-Visible profile very similar to that of the parent monometallic Pt(II) complex and we observed no emission in solution at 298 K or 77 K or in the solid state.

We have extended the hydrazone-based proligand HL^{14} into the proligands H_2L^{36} – H_2L^{38}, offering two N^N^O-coordination sites bridged by a central pyrimidine ring. The coordination chemistry with Pt(II) and Ir(III) has been explored, preparing a monometallic Pt(II) complex alongside monometallic and bimetallic Ir(III) complexes. We were unsuccessful in our attempts to synthesise a bimetallic Pt(II) or a mixed Pt(II)/Ir(III) complex.

The monometallic Pt(II) complex, PtHL^{36}Cl, is non-emissive in solution at room temperature and in the solid state, although at 77 K weak emission is observed. The monometallic Ir(III) complexes are weakly emissive in solution at room temperature (0.2 – 1.6%), notably weaker than the corresponding monometallic [Ir(dpyx)L^{14}]PF_6 (9%). Comparison of the rates of radiative and non-radiative decay reveal this decrease in PLQY is attributable to a ten-fold decrease in k_r.

Coordination of the second Ir(III) centre causes a significant red-shift in the lowest energy absorption and the emission is shifted further into the red region by a small degree. The bimetallic Ir(III) complexes, $[\{Ir(dpyx)\}_2L^{36}]2PF_6$ and $[\{Ir(dpyx)\}_2L^{37}]2PF_6$, both show increased emission in solution at ambient temperature in comparison to their monometallic counterparts, with PLQYs of 3.7 and 11%, respectively. The increase in the PLQY of $[\{Ir(dpyx)\}_2L^{36}]2PF_6$ compared to the monometallic $[Ir(dpyx)HL^{36}]PF_6$ is attributed to a large increase in k_r whilst the increased emission of $[\{Ir(dpyx)\}_2L^{37}]2PF_6$ is attributed to a large decrease in $k_{nr.}$

6 Experimental

6.1 Synthesis: general remarks

Materials.

Reagents were obtained from commercial sources and used without further purification unless stated otherwise. Tetrabutylammonium hexafluorophosphate was recrystallized multiple times using ethanol. All solvents used in preparative work were at least Analar grade and water was purified using the $Purite_{STILL}$ $plus^{TM}$ system. Dry solvents were obtained from HPLC grade solvent that had been passed through a Pure Solv 400 solvent purification system and stored over activated 3 or 4Å molecular sieves. For procedures involving dry solvent, glassware was oven-dried for at least 8 hours prior to use. Dedicated oxygen-free argon cylinders (BOC, UK) were used to provide an inert atmosphere.

Physical Measurements.

NMR spectra were recorded on a Bruker Avance-400 (400 MHz ^{1}H and 100 MHz ^{13}C) spectrometer. Two-dimensional NMR (COSY, NOESY, HSQC and HMBC) were acquired by the solution state NMR service at University of Durham on Varian VNMRS-600 (600 MHz) or VNMRS-700 (700 MHz) instruments. Chemical shifts (δ) are in ppm, referenced to residual protio-solvent resonances, and coupling constants are given in Hertz.

ES-MS data (positive and negative ionisation modes) were obtained on a Waters TQD mass spectrometer interfaced with an Acquity UPLC system with acetonitrile as the carrier solvent. ASAP experiments were performed on Waters Xevo QToF mass spectrometer. MALDI experiments were performed on Autoflex II ToF/ToF mass spectrometer (Bruker Daltonik GmBH) with a trans-2-[3-(4-tert-Butylphenyl)-2-methyl-2-propenylidene]malononitrile (DCTB) matrix.

Thin-layer chromatography (TLC) was carried out using silica plates (MerckArt 5554) which were fluorescent upon irradiation at 254nm and preparative column chromatography was carried out using silica (Merck Silica Gel 60, 230-400 mesh). Analytical and preparative HPLC was performed by the chromatography service at Durham University.

Elemental analysis was performed by either Mr Stephen Boyer (London Metropolitan University elemental analysis service) or Dr. Emily Unsworth using an Exeter CE-440 Elemental Analyser device (University of Durham elemental analysis service).

Electronic spectra were recorded on a PerkinElmer Lambda 900 spectrophotometer or a Biotek Instruments EVIKON XS spectrometer operating with LabPower software. Diffuse-reflectance spectra were obtained by fixed-angle oblique illumination of the sample using an Energetiq LDLS EQ99 broad-band lamp and collection perpendicular to the face of the sample using an Ocean Optics Maya Pro 2000 spectrometer. Data were recorded using the Ocean Optics software, and integration times were adjusted to afford maximum response of the spectrometer without saturation of the detector. NaCl was used as the white standard.

Solution-based emission were acquired on a Jobin Yvon Spex Fluoromax-2 spectrometer. All samples were contained within quartz cuvettes of 1 cm path length. Samples that were to be measured in the absence of air were degassed within the cuvette by three freeze-pump-thaw cycles. Emission was recorded at 90◦ to the excitation source, and appropriate filters were used when required to remove second-order peaks. All emission spectra were corrected after acquisition for dark count and for the spectral response of the detector.

The PLQY were determined relative to a reference an aqueous solution of $[Ru(bpy)_3]Cl_3$. The PLQY of this complex is well established in air-equilibrated H_2O to be 0.028.[190] To measure the PLQY, a sample of the complex was prepared so that the absorbance at the excitation wavelength was below 0.1 and a solution of $[Ru(bpy)_3]Cl_3$ with a similar intensity was prepared. The emission spectra of the complex and reference were measured under identical conditions and the PLQY was determined by equation 6.1.

$$\Phi = \Phi_{st} \times \frac{I}{I_{st}} \times \frac{A_{st}}{A} \times \frac{n^2}{n_{st}^2} \quad (6.1)$$

φ represents the PLQY, I the overall integrated intensity, A the absorbance at the excitation wavelength and n^2 the refractive index of the solvent, the subscript st denotes the standard and all other values the sample.

The potential for error is always present in any measurement and a discussion of the potential sources of error in this method are warranted.

The absorbance of the two solutions must be appropriately dilute (typically A < 0.1) in order to avoid internal filter effects and errors arising from uneven distribution of the excited species in the detected volume.[191] The measurement of the absorption spectrum of a compound has associated errors, such as instrumental noise, accuracy of the wavelength scale and accuracy of the intensity scale. This can result in a variation of absorbance values for a sample. The error is greater when reading off a slope, so a flat portion of the spectrum is always preferred to give a more accurate measurement. The use of equation 6.1 is restricted to comparison of compounds which can be excited at a common wavelength, so on occasion a compromise must be made and the absorbance value cannot always be read from a flat part of the spectrum for both compounds.

For measurements in deoxygenated solutions, particular care must be taken to ensure oxygen is completely removed from the solution. This is achieved via freeze-pump-thaw cycles which, if performed without care while using a volatile solvent, may lead to the loss of solvent and alter the solution concentration. Due to instrument design, we were unable to measure the absorbance after degassing a solution and therefore cannot confirm the concentration was unaffected.

A number of factors affect the quality of the emission spectra, which may influence the spectral shape, position and intensity.[192] Sources of uncertainty include; the wavelength accuracy of the instruments excitation and/or emission channel and the range of linearity of the instruments detection system.[192] The availability of high quality spectrofluorimeters and correction file for the specific fluorimeter and detector reduces the error assocated with the measurement of emission spectra, however the response of the detector may change over time and this is generally more significant in the red region of the spectrum.

The emission of a compound may show a temperature dependence, although the effect of this error is minimised by measuring the emission of the compound and the standard in quick succession. Additionally, although the spectrum is corrected for the baseline, the brightness of a compound will affect the signal to noise ratio and hence reduce the error associated with brighter compounds.

The equation itself makes a number of assumptions. For the compound and the reference it is assumed that; reflection losses are the same, internal reflection effects are equal, reabsorption and reemission are negligible and the integrated luminescence

intensity is proportional to the fraction of light absorbed.[193] Additionally, all of the literature values are assumed to be correct.

A systematic examination of this method of PLQY determination by Resch-Genger and co-workers in 2011 concluded that relative uncertainties of 3 – 5% for absolute quantum yield measurements seem to be accomplishable with well-trained personnel utilising six independent measurements of the sample and the standard.[194] Resch and co-workers later expanded this discussion and moved to recommend the following uncertainties: ±4% for PLQY > 0.4, ±10% for 0.2 > PLQY > 0.02, ±20% for 0.02 > PLQY > 0.005 and ±30% for PLQY < 0.005.[192]

Lifetimes were determined using an Edinburgh Instruments OB 920 fluorimeter. Luminescence lifetimes of the complexes up to approximately 10 µs were measured by time-correlated single-photon counting (TCSPC) method, using an EPL375 pulsed-diode laser as excitation source (374 nm excitation, pulse length of 60 ps). The laser repetition rate was selected so that the pulse period was at least 5-10 times longer than the complex lifetime. The emission was detected at 90◦ to the excitation source, after passage through a monochromator, using a Peltier-cooled R928. Lifetimes in excess of 10 µs were measured by multichannel scaling, and a xenon flash lamp was used as the excitation source (excitation wavelength matched to a suitable absorption band of the complex, pulse length of 2 µs). TCSPC is widely accepted as one of the most accurate methods of lifetime determination due factors such as; shot noise-limited detection, high photon economy, low temporal jitter, higher temperal precision and high dynamic range.[195]

The lifetimes were obtained by least-squares fitting to a mono-exponential decay and goodness-of-fit was assessed from the residuals (X^2). Low temperature (77 K) experiments were performed using a glass vacuum cold finger apparatus built in house. A small amount of sample was dissolved in either a 2:2:1 solvent mix of ether/isopentane/ethanol (EPA) or butyronitrile and placed into a glass tube. The cold finger was filled with liquid nitrogen and the tube containing the sample was inserted.

Electrochemical measurements were carried out using a Palm Emstat2 potentiostat with a three-electrode cell equipped with a platinum auxiliary electrode, a glassy carbon working electrode, and either a Ag/AgNO3 or a platinum reference electrode (CH2Cl2). Potentials are reported with reference to an internal standard ferrocenium/ferrocene (Fc+/0).

Magnetic susceptibility data were recorded using a SQUID magnetometer (MPMS7, Quantum Design) in a 1 T external field. Data were corrected for underlying diamagnetism using tabulated Pascal's constants and fit using julX (Dr. E. Bill). EPR measurements were carried out at the EPSRC National UK EPR Facility and Service in the Photon Science Institute at The University of Manchester. X-Band spectra were collected using a Bruker EMX Micro spectrometer. Simulations were performed using Bruker's Xsophe software package (Dr. S. Sproules).[196]

Melting points were taken on a Gallenkamp melting point apparatus.

Crystallography.

Single-crystal X-ray data was collected on a Bruker D8Venture diffractometer (IμS microfocus sources, focusing mirrors, CMOS Photon100 detector) using λMoKα (λ = 0.71073Å) radiation, equipped with Cryostream (Oxford Cryosystems) open-flow nitrogen cryostates, the temperature on the crystals was maintained at 120.0 K. All structures were solved by direct methods and refined by full-matrix least squares on F^2 for all data using SHELXTL[197] and OLEX2[198] software by Dr. D. S. Yufit (University of Durham).

Density Functional Theory.

DFT geometry optimisations, frequency, stability and TD-DFT excitation calculations were performed using Gaussian 09. The geometry optimizations of the complexes were performed at the B3LYP level of DFT[152–154] and LANL2DZ basis set for all atoms.

6.2 Synthesis: Chapter 1

H(Mabiq) was synthesized as previously described,[36,37] with the following modification; 4,4′-dihydroxy-2,2′-biquinazoline was synthesized by heating oxalylbis(anthranilamide) in a round bottom flask, under vacuum, at ~350 °C, using a heating mantle. The resultant dark brown solid was recrystallized from DMF (61% yield) and the product was confirmed by comparison of the IR to previously reported data.[37]

Co(Mabiq)Cl_2 (1).

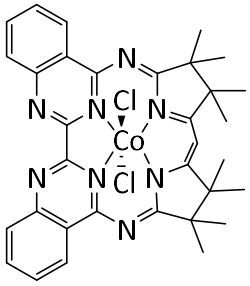

$CoCl_2 \cdot 6H_2O$ (66 mg, 0.28 mmol) was added to an aerated solution of H(Mabiq) (100 mg, 0.18 mmol) and triethylamine (24 µL, 0.19 mmol) in CH_2Cl_2 (10 mL). The solution was left to stir overnight, filtered through celite and the solvent removed in vacuo, leaving a dark brown solid. The product was recrystallized by slow evaporation of a solution of **1** in CH_2Cl_2 (97 mg, 0.14 mmol, 78% yield).

^{1}H NMR (400 MHz, $CDCl_3$): δ= 9.19 (dd, *J* = 8.3, 0.8 Hz, 2H), 8.53 (d, *J* = 8.3 Hz, 2H), 8.10 (ddd, *j* = 8.5, 7.0, 1.5 Hz, 2H), 7.89 (ddd, *j* = 8.2, 7.0, 1.1 Hz, 2H), 6.49 (s, 1H), 1.51 (s, 12H), 1.48 (s, 12H). ^{13}C NMR (101 MHz, $CDCl_3$): δ= 186.8, 177.9, 159.3, 156.7, 151.05, 135.7, 129.5, 129.2, 126.5, 124.2, 94.06, 51.9, 51.7, 24.3, 23.4. ASAP-MS(+) (*m/z*): 670 $[M]^+$, 635 $[M\text{-}Cl]^+$, 600 $[M\text{-}2Cl]^+$. UV-Vis λ_{max} (nm (ε, M^{-1} cm^{-1})) in CH_2Cl_2: 273 (8.0 x 10^4), 322 (3.5 x 10^4), 381 (2.3 x 10^4), 432 (8.0 x 10^3), 484 (1.2 x 10^4), 514 (2.7 x 10^4). IR (cm^{-1}): 2978 w, 2930 vw, 1603 m, 1572 m, 1561 m, 1510 s, 1488 m (sh), 1463 s, 1409 m, 1364 s, 1322 w, 1302 w, 1268 m, 1257 w (sh), 1232 m, 1199 w (sh), 1190 w, 1166 s, 1125 m, 1092 s, 1065 s, 1032 m (sh), 1000 m (sh), 963 m, 910 w, 893 m, 878 w, 866 w, 826 m, 813 w, 778 s, 758 m, 737 m (sh), 728 s, 718 m (sh), 697 m, 687 s, 663 w, 638 w, 628 m, 610 s. Anal. Calcd for $C_{34}H_{35}Cl_4CoN_8$: C, 53.99; H, 4.66; N, 14.81. Found: C, 53.85; H, 4.71; N, 14.74.

Co(Mabiq)Cl (2).

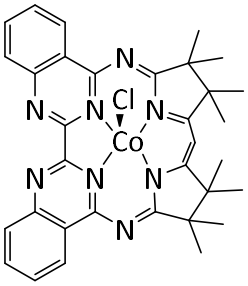

$CoCl_2$ (24 mg, 0.18 mmol) was added to a solution of H(Mabiq) (100 mg, 0.18 mmol) and triethylamine (24 µL, 0.19 mmol) in CH_2Cl_2 (10 mL). The solution was stirred overnight, the resultant green solution was filtered through celite and the solvent removed in vacuo, leaving a dark green solid (107 mg, 94.4% yield). Single crystals were obtained by slow evaporation of a concentrated solution of **2** in CH_2Cl_2.

ASAP-MS(+) (*m/z*): 601 $[M\text{-}Cl]^+$, 543 $[M\text{-}CoCl]^+$. UV-Vis λ_{max} (nm (ε, M^{-1} cm^{-1})) in MeOH: 253 (2.9 x 10^4), 271 (2.2 x 10^4), 318 (1.9 x 10^4), 348 (1.7 x 10^4), 427 (7.0 x 10^3), 442 (7.2 x 10^3), 480 (3.6 x 10^3), 576 (2.1 x 10^3), 618 (2.2 x 10^3), 668 (1.7 x 10^3). IR (cm^{-1}): 2973 w, 1597 m, 1571 s, 1558 m (sh), 1544 w (sh), 1509 s, 1484 m, 1461 s, 1412 m, 1365 m, 1339 w, 1324 w, 1302 w, 1296 w (sh), 1270 m, 1255 w, 1242 m, 1195 w, 1167 m, 1123 s, 1097 vs, 1078 vs, 1031 w, 1017 w, 1006 w, 966 w, 958 w, 893 w, 866 w, 813 w, 811 w, 780 s, 763 m, 736 m, 719 w (sh), 702 w (sh), 668 m, 675 w, 663 w, 646 w, 634 w, 630 w, 611 m. Anal. Calcd for $C_{33}H_{33}CoClN_8$: C, 62.31; H, 5.23; N, 17.62. Found: C, 62.19; H, 5.39; N, 17.52.

Co_2(Mabiq)Cl_3 (3).

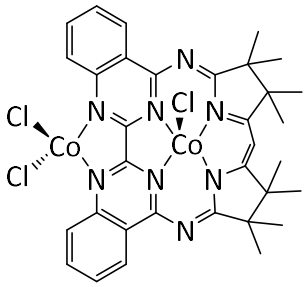

$CoCl_2$ (103 mg, 0.79 mmol) was added to a solution of HMabiq (200 mg, 0.37 mmol) and triethylamine (48 µL, 0.38 mmol) in THF (10 mL). The mixture was stirred overnight, and the resultant green precipitate was filtered and washed with THF and hexane to give the dark green solid **3** (269 mg, 94.6% yield).

ASAP-MS(+) (*m/z*): 601 $[M\text{-}CoCl_3]^+$. UV-Vis λ_{max} (nm (ε, M^{-1} cm^{-1})) in MeOH: 253 (5.1 x 10^4), 271 (4.2 x 10^4), 318 (3.7 x 10^4), 348 (3.0 x 10^4), 427 (1.5 x 10^4), 442 (1.6 x 10^4), 480 (7.4 x

10^3), 576 (4.5 x 10^3), 618 (4.6 x 10^3), 668 (3.5 x 10^3). IR Spectrum (cm^{-1}): 2967 w, 1560 s, 1502 m, 1488 m, 1474 s (sh), 1460 s, 1431 m (sh), 1409 s, 1378 m, 1362 m, 1306 w, 1276 w, 1257 w, 1228 m, 1200 w, 1169 m, 1125 m, 1094 s, 1072 s, 974 w, 956 w, 897 m. Anal. Calcd for $C_{33}H_{33}Co_2Cl_3N_8$: C, 51.75; H, 4.34; N, 14.63. Found: C, 51.75; H, 4.28 N, 14.48.

Co(Mabiq) (4).

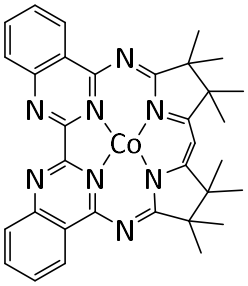

Cp_2Co (8.6 mg, 0.046 mmol) was added to a suspension of **2** (29 mg, 0.046 mmol) in THF (5mL), upon which the mixture immediately turned a deep purple. The reaction was stirred overnight, filtered through celite and the solvent removed in vacuo, yielding a purple solid (22 mg, 79.6% yield). Single crystals were obtained by slow evaporation of a concentrated solution of **4** in THF.

^{1}H NMR (400 MHz, $CDCl_3$): δ= 9.06 (dd, *J* = 8.2, 0.9 Hz, 2H), 8.37 (d, *J* = 8.1 Hz, 2H), 8.19 (td, *j* = 7.6, 2H), 7.64 (td, *j* = 7.6, 2H), 7.54 (s, 1H), 1.55 (s, 12H), 1.39 (s, 12H). ASAP-MS(+) (*m/z*): 600 $[M]^+$. IR (cm^{-1}): 2971 w, 2906 w, 1608 w, 1591 vw (sh), 1564 m, 1548 m, 1506 m, 1480 m, 1463 w, 1446 m, 1414 m, 1388 w, 1374 m, 1364 m (sh), 1354 m, 1325 w, 1280 m, 1253 w, 1222 m, 1187 vw, 1164 m, 1149 m, 1136 s, 1109 m (sh), 1016 w, 967 w, 954 vw, 896 w, 867 m, 819 w (sh), 813 m, 792 vw, 765 vs, 748 s, 696 m, 690 m, 673 m, 632 m, 625 m, 612 m. UV-Vis λ_{max} (nm (ε, M^{-1} cm^{-1})) in THF: 268 (1.4 x 10^4), 324 (3.5 x 10^4), 335 (3.7 x 10^4), 392 (1.9 x 10^4), 403 (2.4 x 10^4), 523 (1.3 x 10^4), 533 (1.4 x 10^4), 913 (2.8 x 10^3), 1048 (2.0 x 10^3), 1210 (2.1 x 10^3). Anal. Calcd for $C_{33}H_{33}CoN_8$: C, 65.99; H, 5.54; N, 18.66. Found: C, 66.16; H, 5.62; N, 18.34.

6.3 Synthesis: Chapter 3

HL[1]

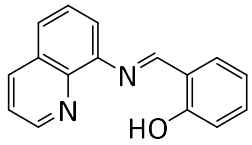

8-aminoquinoline (0.1 g, 0.7 mmol) and salicylaldehyde (85 mg, 0.7 mmol) were placed under vacuum and heated to 65°C with stirring. After 6 hours, an 87% conversion rate was achieved. The resulting orange oil was used in the next step with no purification. The experimental data obtained were in good agreement with that reported in literature.[199]

HL[2]

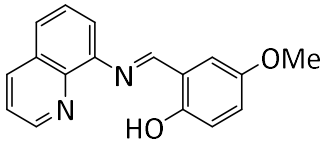

8-aminoquinoline (0.1 g, 0.7 mmol) and 2-hydroxy-5-methoxybenzaldehyde (107 mg, 0.7 mmol) were placed under vacuum and heated to 65°C for 2 hours with stirring. The resulting orange oil was used in the next step with no purification. The experimental data obtained were in good agreement with that reported in literature.[111]

HL[3]

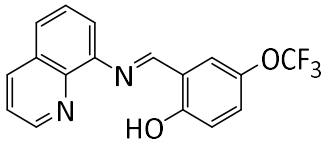

8-aminoquinoline (0.1 g, 0.7 mmol) and 2-hydroxy-5-(trifluoromethoxy)benzaldehyde (144 mg, 0.7 mmol) were placed under vacuum and heated to 65°C for 2 hours with stirring. The resulting orange oil was used in the next step with no purification.

HL[4]

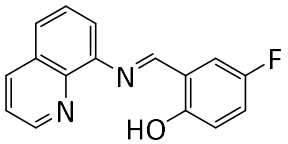

8-aminoquinoline (0.1 g, 0.7 mmol) and 2-hydroxy-5-fluorobenzaldehyde (98 mg, 0.7 mmol) were placed under vacuum and heated to 65°C for 2 hours with stirring. The resulting orange oil was used in the next step with no purification. The experimental data obtained were in good agreement with that reported in literature.[111]

HL[5]

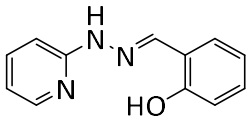

Salicylaldehyde (1 ml, 9 mmol) was added drop wise to a solution of hydrazinopyridine (1 g, 9 mmol) in 30ml of anhydrous methanol. A cream precipitate formed on addition and the resulting lemon suspension was stirred at reflux for 1 hour. The cream powder was isolated and washed with ethanol. The product was dried under high vacuum to give 1.58 g (7.4 mmol, 82% yield).

^{1}H NMR (DMSO-d_6, 400 MHz): 10.89 (1H, s), 10.54 (1H, br s), 8.28 (1H, s), 8.12 (1H, ddd, J = 5, 2 and 1), 7.65 (1H, ddd, J = 8, 7 and 2), 7.57 (1H, dd, J = 8 and 2), 7.19 (1H, ddd, J = 8, 7 and 2), 7.04 (1H, dt, J = 8 and 1), 6.89-6.85 (2H, m), 6.78 (1H, ddd, J = 7, 5 and1). ^{13}C NMR (DMSO-d_6, 101 MHz): 156.4, 155.9, 148.0, 138.6, 138.0, 129.7, 127.2, 120.5, 119.4, 116.0, 115.0, 106.1. MS (ES+): *m/z* 214 $[M+H]^+$.[141,200]

HL[6]

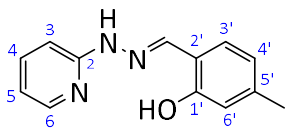

Experimental performed by Jack Fradgley. 2-Hydroxy-4-methylbenzaldehyde (125 mg, 0.92 mmol) was added slowly to a stirred solution of 2-hydrazinopyridine (100 mg, 0.92 mmol)

in MeOH (8 ml) to produce a thick white slurry. The mixture was heated to reflux and stirred for 1 hour. The resulting white slurry was allowed to cool to ambient temperature, filtered and washed with hexane to afford 128 mg of a white solid (61% yield).

^{1}H NMR (DMSO-d_6, 600 MHz): 10.82 (1H, s, H^{NH}), 10.51 (1H, s, H^{OH}), 8.23 (1H, s, H^{imine}), 8.11 (1H, ddd, J = 5, 2, 1, H^{3}), 7.63 (1H, ddd, J = 9, 7, 2, H^{5}), 7.42 (1H, d, J = 8, $H^{3'}$), 6.99 (1H, d, J = 8.5, H^{6}), 6.75 (1H, ddd, J = 7, 5, 1, H^{4}), 6.71 (1H. s. $H^{6'}$), 6.69 (1H, d, J = 8, $H^{4'}$), 2.25 (3H, s, H^{Me}). ^{13}C NMR (DMSO-d_6, 151 MHz): 156.3 (C^{2}), 156.0 ($C^{1'}$), 148.0 (C^{3}), 139.1 ($C^{5'}$), 139.4 (C^{imine}), 138.0 (C^{5}), 127.4 ($C^{3'}$), 120.4 ($C^{4'}$), 117.7 ($C^{2'}$), 116.4 ($C^{6'}$), 114.9 (C^{4}), 106.0 (C^{6}), 21.1 (C^{Me}). MS (ES-): *m/z* 226 $[M-H]^-$.

HL^{7}

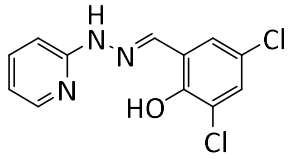

3,5-dichlorosalicylaldehyde (361 mg, 1.89 mmol) was added slowly to a stirred solution of 2-hydrazinopyridine (206 mg, 1.89 mmol) in MeOH (30ml) to produce a thick yellow slurry. The mixture was heated to reflux and stirred for 1 hour. The resulting yellow slurry was allowed to cool to ambient temperature, filtered and washed with hexane. The product was dried under high vacuum to afford 471 mg of a yellow solid (1.67 mmol, 89% yield). The experimental data obtained were in good agreement with that reported in literature.[201]

HL^{8}

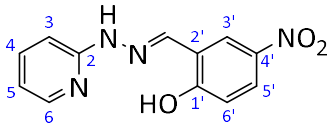

Experimental performed by Jack Fradgley. 2-hydroxy-5-nitrobenzaldehyde (154 mg, 0.93 mmol) was added slowly to a stirred solution of 2-hydrazinopyridine (100 mg, 0.92 mmol) in MeOH (8ml) to produce a thick yellow slurry. The mixture was heated to reflux and stirred for 1 hour. The resulting yellow slurry was allowed to cool to ambient temperature,

filtered and washed with hexane to afford 188 mg of a bright yellow solid (0.73 mmol, 79% yield).

^{1}H NMR (DMSO-d_6, 600 MHz): 11.77 (1H, s, H^{OH}), 11.14 (1H, s, H^{NH}), 8.55 (1H, d, J = 3, $H^{3'}$), 8.31 (1H, s, H^{imine}), 8.14 (1H, d, J = 5, H^{3}), 8.07 (1H, dd, J = 9 and 3, $H^{5'}$), 7.68 (1H, ddd, J = 9, 7 and 2, H^{4}), 7.16 (1H, d, J = 8, H^{6}), 7.06 (1H, d, J = 9, $H^{6'}$), 6.81 (1H, dd, J = 7 and 5, H^{5}). ^{13}C NMR (DMSO-d_6, 151 MHz): 161.2 (C^{OH}), 156.3 (C^{2}), 147.9 (C^{3}), 140.1 ($C^{4'}$), 138.1 (C^{4}), 134.2 (C^{imine}), 125.0 ($C^{5'}$), 122.0 ($C^{2'}$), 121.4 ($C^{3'}$), 116.5 ($C^{6'}$), 115.5 (C^{5}), 106.5 (C^{6}). MS (ES-): *m/z* 257 $[M-H]^{-}$.[200]

HL[9]

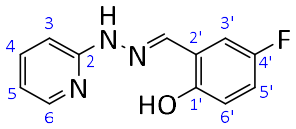

Experimental performed by Jack Fradgley. 5-fluorosalicylaldehyde (133 mg, 0.95 mmol) was added slowly to a stirred solution of 2-hydrazinopyridine (100 mg, 0.92 mmol) in MeOH (8ml) to produce a thick yellow slurry. The mixture was heated to reflux and stirred for 1 hour. The resulting yellow slurry was allowed to cool to ambient temperature, filtered and washed with hexane to afford 109 mg of a bright yellow solid (0.47 mmol, 51% yield).

^{1}H NMR (DMSO-d_6, 700 MHz): 10.97 (1H, s, H^{OH}), 10.22 (1H, s, H^{NH}), 8.24 (1H, s, H^{imine}), 8.12 (1H, dd, J = 5 and 1, H^{3}), 7.64 (1H, ddd, J = 8, 7 and 2, H^{5}), 7.43 (1H, dd, J = 10 and 3, $H^{3'}$), 7.14 (1H, d, J = 8, H^{6}), 7.00 (1H, td, J = 9 and 3, $H^{5'}$), 6.86 (1H, dd. J = 9 and 5, $H^{6'}$), 6.77 (1H, ddd, J = 7, 5 and 1, H^{4}). ^{13}C NMR (DMSO-d_6, 176 MHz): 156.5 (C^{OH}), 155.0 (C^{2}), 151.90 ($C^{2'}$), 147.8 (C^{3}), 138.0 (C^{5}), 136.0 (C^{imine}), 122.1 ($C^{4'}$), 117.1 ($C^{6'}$), 115.9 ($C^{5'}$), 115.2 (C^{5}), 111.5 ($C^{3'}$), 106.4 (C^{6}). MS (ES-): *m/z* 230 $[M-H]^{-}$; HRMS (ES+) m/z = 232.0884 $[M+H]^{+}$; calculated for $[C_{12}H_{11}N_3OF]^{+}$ 232.0886. Mp. = 226-227°C.

HL[10]

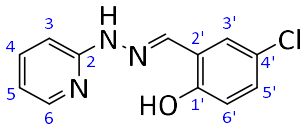

Experimental performed by Jack Fradgley. 5-chlorosalicylaldehyde (151 mg, 0.96 mmol) was added slowly to a stirred solution of 2-hydrazinopyridine (104 mg, 0.95 mmol) in MeOH (8ml) to produce a thick white slurry. The mixture was heated to reflux and stirred for 1 hour. The resulting white slurry was allowed to cool to ambient temperature, filtered and washed with hexane to afford 165 mg of a white solid (0.67 mmol, 70% yield).

^{1}H NMR (DMSO-d_6, 700 MHz): 11.00 (1H, s, H^{OH}), 10.52 (1H, s, H^{NH}), 8.23 (1H, s, H^{imine}), 8.12 (1H, ddd, J = 5, 2 and 1, H^{3}), 7.67 (1H, d, J = 3, H^{5}), 7.64 (1H, ddd, J = 8, 7 and 2, $H^{3'}$), 7.18 (1H, dd, J = 9 and 3, $H^{5'}$), 7.13 (1H, d, J = 8, H^{6}), 6.89 (1H, d, J = 7, $H^{6'}$), 6.78 (1H, ddd, J = 7, 5 and 1, H^{4}). ^{13}C NMR (DMSO-d_6, 176 MHz): 156.4 (C^{OH}), 154.4 (C^{2}), 147.8 (C^{3}), 138.0 ($C^{3'}$), 135.6 (C^{imine}), 128.9 ($C^{5'}$), 125.1 (C^{5}), 123.1 ($C^{4'}$), 122.8 ($C^{2'}$), 117.7 ($C^{6'}$), 115.2 (C^{4}), 106.4 (C^{6}). MS (ES-): *m/z* 246 $[M-H]^{-}$.[200]

HL[11]

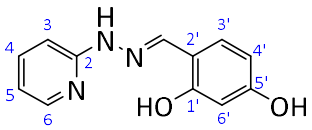

Experimental performed by Jack Fradgley. 2,4-dihydroxybenzaldehyde (134 mg, 0.97 mmol) was added slowly to a stirred solution of 2-hydrazinopyridine (106 mg, 0.97 mmol) in MeOH (8ml) to produce a pale orange slurry. The mixture was heated to reflux and stirred for 1 hour. The resulting orange slurry was allowed to cool to ambient temperature, placed in the fridge overnight, filtered and washed with hexane to afford 97 mg of an orange solid (0.42 mmol, 44% yield).

^{1}H NMR (DMSO-d_6, 700 MHz): 10.66 (2H, s, H^{OH}), 9.69 (1H, s, H^{NH}), 8.16 (1H, s, H^{imine}), 8.10 (1H, ddd, J = 5, 2 and 1, H^{3}), 7.61 (1H, ddd, J = 8, 7 and 2, H^{5}), 7.31 (1H, d, J = 8, $H^{3'}$), 6.92 (1H, d, J = 8, H^{6}), 6.72 (1H, ddd, J = 7, 5 and 1, H^{4}), 6.32 – 6.30 (2H, m, $H^{6'}$ and $H^{4'}$). ^{13}C NMR (DMSO-d_6, 176 MHz): 159.3 ($C^{5'}$), 157.7 ($C^{1'}$), 156.4 (C^{2}), 147.9 (C^{3}), 140.4 (C^{imine}), 137.9 (C^{5}),

129.0 ($C^{3'}$), 114.5 (C^{4}), 111.9 ($C^{2'}$), 107.5 ($C^{6'}$), 105.7 (C^{6}), 102.5 ($C^{4'}$). MS (ES-): *m/z* 228 [M-H]$^{-}$.[202]

HL[13]

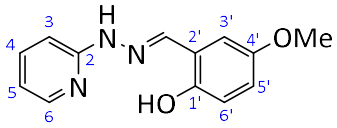

Experimental performed by Jack Fradgley. 2-hydroxy-5-methoxybenzaldehyde (150 mg, 0.98 mmol) was added slowly to a stirred solution of 2-hydrazinopyridine (102 mg, 0.94 mmol) in MeOH (8ml) to produce a white slurry. The mixture was heated to reflux and stirred for 1 hour. The resulting white slurry was allowed to cool to ambient temperature, filtered and washed with hexane to afford 133 mg of a white solid (0.55 mmol, 58% yield).

^{1}H NMR ($CDCl_3$, 700 MHz): 10.25 (1H, br s, H^{OH}), 9.10 (1H, br s, H^{NH}), 8.18 (1H, d, J = 5, H^{3}), 7.91 (1H, s, H^{imine}), 7.66 (1H, t, J = 8, H^{5}), 7.09 (1H, d, J = 8, H^{6}), 6.94 (1H, d, J = 9, $H^{3'}$), 6.87 – 6.84 (2H, m, H^{4} and $H^{5'}$), 6.71 (1H, d, J = 3, $H^{6'}$), 3.79 (3H, s, H^{OMe}). ^{13}C NMR ($CDCl_3$, 176 MHz): 155.6 (C^{2}), 152.8 ($C^{4'}$), 151.5 ($C^{1'}$), 147.5 (C^{3}), 142.9 (C^{imine}), 139.0 (C^{5}), 118.3 ($C^{2'}$), 117.5 ($C^{3'}$), 117.1 ($C^{5'}$), 116.5 (C^{4}), 114.2 ($C^{6'}$), 107.0 (C^{6}). MS (ES+): *m/z* 244 $[M+H]^{+}$.[112]

HL[14]

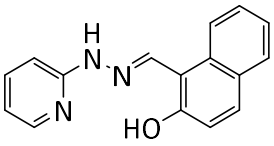

2-Hydroxy-1-napthaldehyde (230 mg, 1.34 mmol) was added to a solution of 2-hydrazinopyridine (146 mg, 1.34 mmol) in MeOH (5ml). The resulting bright yellow slurry was refluxed for 30 mins before allowing to cool to ambient temperature. The mixture was filtered and the solid washed with methanol and hexane. The isolated solid was dried in vacuo to give 301 mg of a bright yellow solid (1.14 mmol, 85% yield). The experimental data obtained was good agreement with that reported in literature.[203]

2-(1-methylhydrazinyl)pyridine

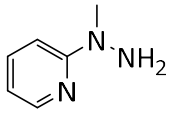

Bromopyridine (3.3 g, 21 mmol) was added under a stream of argon to methyl hydrazine (14.5 g, 315 mmol) to form a pale-yellow solution which was refluxed for 4 hours. The solvent was removed in vacuo to produce a yellow oil, which was washed with 40ml sat. Na_2CO_3 solution and extracted into EtOAc. The organic layer was washed with 2 x 40ml sat. NaCl and dried over magnesium sulphate. The solvent was removed in vacuo to give 1.19 g of a yellow oil (9.66 mmol, 69% yield). The experimental data obtained were in accord with that reported in literature.[204]

HL[14]

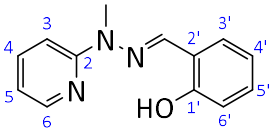

Salicylaldehyde (1.77 g, 14.5 mmol) was added to a solution of 2-(1-methylhydrazinyl)pyridine (1.78 g, 14.5 mmol) in 20ml methanol. The bright yellow solution was refluxed for 1 hour before allowing to cool to ambient temperature. The solvent was slowly removed in vacuo until a precipitate formed and the flask was placed in an ice bath for 30 min. The slurry was filtered and washed with hexane to give 2.63 g of a cream solid (11.57 mmol, 80% yield).

^{1}H NMR (DMSO-d_6, 600 MHz): 10.38 (1H, s, H^{OH}), 8.23 (1H, d, J = 5, H^3), 8.05 (1H, s, H^{imine}), 7.71 (2H, t, J = 8, $H^{3'}$ and H^5), 7.47 (1H, d, J = 9, H^6), 7.19 (1H, t, J = 8, $H^{5'}$), 6.85-6.92 (3H, m, H^4, $H^{4'}$ and $H^{6'}$), 3.61 (3H, s, H^{NMe}). ^{13}C NMR (DMSO-d_6, 151 MHz): 156.8 (C^2), 155.7 (C^{OH}), 147.2 (C^3), 138.1 (C^5), 134.1 (C^{imine}), 129.5 ($C^{5'}$), 127.0 ($C^{3'}$), 121.2 ($C^{2'}$), 119.4 ($C^{6'}$), 116.0 ($C^{4'}$), 115.6 (C^4), 108.5 (C^6), 29.3 (C^{Me}). MS (ES+): *m/z* 228 $[M+H]^+$, 108 $[M - C_7H_6NO+H]^+$; HRMS (ES+): m/z = 228.1130 $[M+H]^+$; calculated for $[C_{12}H_{14}N_3O]^+$ 228.1137. Mp. = 99-101°C. Anal. Cacld for $C_{13}H_{13}N_3O$: C, 68.70; H, 5.77; N, 18.49. Found: C, 68.55; H, 5.76; N, 18.49.

HL[15]

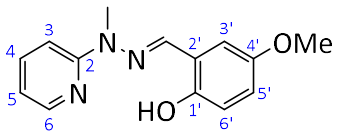

2-hydroxy-5-methoxybenzaldehyde (93 mg, 0.61 mmol) was added to a stirring solution of 2-(1-methylhydrazinyl)pyridine (75 mg, 0.61 mmol) in 3ml methanol to form a yellow solution. The solution was heated to 40°C for a period of 30 minutes and the resulting lemon slurry was allowed to cool to room temperature before filtering and washing with cold methanol to give 104mg of a white solid (0.40 mmol, 66% yield).

^{1}H NMR ($CDCl_3$, 700 MHz): 10.77 (1H, s, H^{OH}), 8.27 (1H, dd, J = 8 and 1, H^{3}), 7.76 (1H, s, H^{imine}), 7.63 (1H, ddd, J = 8.5, 7 and 2, H^{5}), 7.27 (1H, d, J = 8.5, H^{6}), 6.93 (1H, d, J = 9, $H^{3'}$), 6.85-6.83 (2H, m, $H^{5'}$ and H^{4}), 6.80 (1H, d, J = 3, $H^{6'}$), 3.80 (3H, s, H^{OMe}), 3.71 (3H, s, H^{NMe}). ^{13}C NMR ($CDCl_3$, 176 MHz): 156.6 (C^{2}), 152.8 ($C^{4'}$), 151.0 ($C^{1'}$), 147.5 (C^{3}), 138.3 (C^{5}), 138.0 (C^{imine}), 119.3 ($C^{2'}$), 117.3 ($C^{3'}$), 116.4 (C^{4} or $C^{5'}$), 116.3 (C^{4} or $C^{5'}$), 114.5 ($C^{6'}$), 108.8 (C^{6}), 56.1 (C^{OMe}), 29.6 (C^{NMe}). MS (ES+): m/z 258 $[M+H]^{+}$. Mp. = 110-111°C.

HL[16]

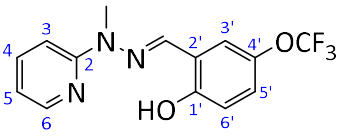

2-Hydroxy-5-(trifluoromethoxy)benzaldehyde (343 mg, 1.66 mmol) was added to a stirring solution of 2-(1-methylhydrazinyl)pyridine (205 mg, 1.66 mmol) in 2ml MeOH to form a yellow solution which was heated to reflux for a period of 30 minutes before being placed in the fridge overnight. The resulting yellow slurry was filtered and washed with cold methanol to isolate 192 mg of a lemon solid (0.62 mmol, 37% yield).

^{1}H NMR ($CDCl_3$, 600 MHz): 11.23 (1H, s, H^{OH}), 8.29 (1H, ddd, J = 5, 2 and 1, H^{3}), 7.74 (1H, s, H^{imine}), 7.65 (1H, ddd, J = 8.5, 7 and 2, H^{5}), 7.25 (1H, d, J = 8.5, H^{6}), 7.14 (1H, d, J = 2.5, $H^{3'}$), 7.09 (1H, dd, J = 9 and 2.5, $H^{5'}$ or $H^{6'}$), 6.98 (1H, d, J = 9, $H^{5'}$ or $H^{6'}$), 6.87 (1H, ddd, J = 7, 5 and 1,H^{4}), 3.71 (3H, s, H^{NMe}). ^{13}C NMR ($CDCl_3$, 151 MHz): 156.4 (C^{2}), 155.4 ($C^{1'}$), 147.7 (C^{3}), 141.8 ($C^{4'}$), 138.4 (C^{5}), 136.6 (C^{imine}), 122.8 ($C^{5'}$ or $C^{6'}$), 122.4 ($C^{3'}$), 121.6 (C^{OCF_3}), 119.8 ($C^{2'}$), 117.7 ($C^{5'}$ or $C^{6'}$), 116.7 (C^{4}), 108.7 (C^{6}), 29.7 (C^{NMe}). MS (ES-): m/z 310 $[M-H]^{-}$; HRMS (ES-): *m/z* 310.0798 $[M-H]^{-}$; calculated for $[C_{14}H_{11}N_3O_2F_3]^{-}$ 310.0803. Mp. = 95-96°C.

HL[17]

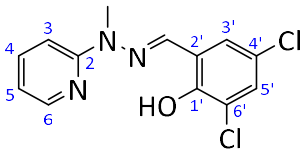

3,5-dichlorosalicylaldehyde (150 mg, 0.79 mmol) was added to a stirring solution of 2-(1-methylhydrazinyl)pyridine (95 mg, 0.77 mmol) in 5ml MeOH to form a yellow solution which precipitated rapidly to form a lemon slurry. The solution was heated to reflux for a period of 30 minutes, before cooling to room temperature. The slurry was filtered and washed with cold methanol to isolate 169 mg of a white solid (0.57 mmol, 74% yield).

^{1}H NMR ($CDCl_3$, 700 MHz): 11.85 (1H, s, H^{OH}), 8.29 (1H, ddd, J = 9.5, 2 and 1, H^{3}). 7.68 (1H, s, H^{imine}), 7.66 (1H, ddd, J = 9, 7 and 2, H^{5}), 7.31 (1H, d, J = 2, $H^{5'}$), 7.28 (1H, d, J = 8.5, H^{6}), 7.18 (1H, d, J = 2.5, $H^{3'}$), 6.90 (1H, ddd, J = 7, 5 and 1, H^{4}), 3.71 (3H, s, H^{NMe}). ^{13}C NMR ($CDCl_3$, 176 MHz): 156.1 (C^{2}), 151.3 ($C^{1'}$), 147.7 (C^{3}), 138.6 (C^{5}), 135.5 (C^{imine}), 129.4 ($C^{5'}$), 127.7 ($C^{3'}$), 124.3 ($C^{2'}$), 122.2 ($C^{6'}$), 121.3 ($C^{4'}$), 117.2 (C^{4}), 108.9 (C^{6}), 29.9 (C^{NMe}). MS (ES+): m/z 296 $[M+H]^+$; HRMS (ES+): *m/z* 296.0362 $[M+H]^+$; calculated for $[C_{13}H_{12}N_3OCl_2]^+$ 296.0357. Mp. = 169-169°C.

HL[18]

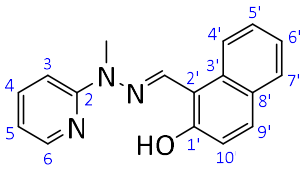

2-Hydroxy-1-napthaldehyde (105 mg, 0.61 mmol) was added to a stirring solution of 2-(1-methylhydrazinyl)pyridine (75 mg, 0.61 mmol) in 3ml MeOH to form a lemon slurry which was heated to reflux for a period of 30 minutes, before cooling to room temperature. The slurry was filtered and washed with cold methanol to isolate 148 mg of a cream solid (0.53 mmol, 87% yield).

^{1}H NMR ($CDCl_3$, 700 MHz): 12.43 (1H, s, H^{OH}), 8.67 (1H, s, H^{imine}), 8.30 (1H, ddd, J = 5, 2 and 1, H^{3}), 8.11 (1H, d, J = 8.5, $H^{4'}$), 7.81 (1H, d, J = 8, $H^{7'}$), 7.76 (1H, d, J = 9, $H^{9'}$), 7.67 (1H, ddd, J = 8.5, 7 and 2, H^{5}), 7.54 (1H, ddd, J = 8.5, 7 and 1, $H^{6'}$), 7.38 (1H, ddd, J = 8, 7 and 1, $H^{5'}$), 7.35 (1H, d, J = 8.5, H^{6}), 7.25 (1H, d, J = 8, $H^{10'}$), 6.86 (1H, dd, J = 7, 5 and 1, H^{4}), 3.83 (3H, s,

H^{NMe}). ^{13}C NMR ($CDCl_3$, 176 MHz): 156.6 (C^2), 156.5 ($C^{1'}$), 147.6 (C^3), 138.4 (C^5), 134.9 (C^{imine}), 132.0 ($C^{8'}$), 131.2 ($C^{9'}$), 129.3 ($C^{7'}$), 128.6 ($C^{3'}$), 127.2 ($C^{6'}$), 123.4 ($C^{5'}$), 120.2 ($C^{4'}$), 119.1 ($C^{10'}$), 116.3 (C^4), 109.8 ($C^{2'}$), 108.6 (C^6). MS (ES-): m/z 276 $[M-H]^-$. Mp. = 148-149°C.

4-methoxy-2-(1-methylhydrazinyl)pyridine

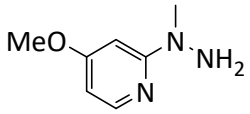

2-Chloro-4-methoxypyridine (126 mg, 0.88 mmol) was stirred under reflux in methyl hydrazine (3ml) for a period of 24 hours. The resulting pale-yellow solution was allowed to cool to room temperature before being diluted with water (10ml) and extracted into Et_2O (3 x 30ml). The organic layers were combined, dried over $MgSO_4$ and the solvent removed in vacuo to yield 130 mg of a pale orange oil (0.85 mmol, 97% yield).

^1H NMR ($CDCl_3$, 400 MHz): 7.98 (1H, d, J = 6), 6.49 (1H, d, J = 6), 6.24 (1H, dd, J = 6 and 2), 4.02 (2H, br s), 3.83 (3H, s), 3.27 (3H, s).

HL[19]

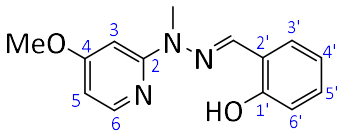

Salicylaldehyde (130 mg, 1.06 mmol) was added to a stirring solution of 4-methoxy-2-(1-methylhydrazinyl)pyridine (120 mg, 0.78 mmol) in MeOH (2.5ml) and the resulting orange solution was stirred for 3 hours at reflux. The solution was allowed to cool to ambient temperature and placed in the fridge overnight. The resulting white crystals were collected by filtration and washed with cold methanol to yield 51 mg of a white solid (0.20 mmol, 19% yield).

^1H NMR ($CDCl_3$, 700 MHz): 11.19 (1H, s, H^{OH}), 8.08 (1H, d, J = 6, H^3), 7.80 (1H, s, H^{imine}), 7.27-7.23 (2H, m, $H^{4'}$ and $H^{5'}$), 7.00 (1H, d, J = 8, $H^{6'}$), 6.93 (1H, td, J = 7.5, $H^{3'}$), 6.75 (1H, d, J = 2, H^6), 6.44 (1H, dd, J = 6, 2), 3.89 (3H, s, H^{OMe}), 3.70 (3H, s, H^{NMe}). ^{13}C NMR ($CDCl_3$, 176 MHz): 167.8 (C^4), 158.6 (C^2), 157.0 ($C^{1'}$), 148.4 (C^3), 138.4 (C^{imine}), 130.2 ($C^{4'}$ or $C^{5'}$), 130.0 ($C^{4'}$ or

$C^{5'}$), 119.7 ($C^{3'}$), 119.4 ($C^{2'}$), 116.7 ($C^{2'}$), 105.2 (C^{5}), 92.6 (C^{6}), 55.3 (C^{OMe}), 29.9 (C^{NMe}). Mp. = 100-101°C.

2-(1-methylhydrazinyl)-4-(trifluoromethyl)-pyridine

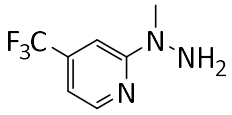

2-Bromo-4-(trifluoromethyl)pyridine (200 mg, 0.88 mmol) was stirred under reflux in methyl hydrazine (3ml) for a period of 24 hours. The resulting pale-yellow solution was allowed to cool to room temperature before being diluted with water (10ml) and extracted into Et_2O (3 x 30ml). The organic layers were combined, dried over $MgSO_4$ and the solvent removed in vacuo to yield 100 mg of a pale-yellow oil (0.48 mmol, 59% yield).

^{1}H NMR ($CDCl_3$, 400 MHz): 8.22 (1H, d, J = 5), 7.30-7.28 (1H, m), 6.72 (1H, dd, J = 5 and 1), 4.00 (2H, br s), 3.32 (3H, s).

HL[20]

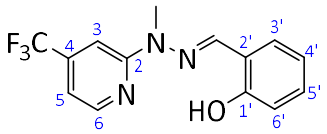

Salicylaldehyde (105 mg, 0.89 mmol) was added to a stirring solution of 2-(1-methylhydrazinyl)-4-(trifluoromethyl)-pyridine (169 mg, 0.86 mmol) in MeOH (2.5ml) and the resulting yellow solution was stirred for 3 hours at reflux. The solution was allowed to cool to ambient temperature and placed in the fridge overnight. The resulting white crystals were collected by filtration and washed with cold methanol to yield 188 mg of a white solid (0.60 mmol, 72% yield).

^{1}H NMR (CDCl3, 700 MHz): 10.83 (1H, br s, H^{OH}), 8.40 (1H, d, J = 5, $H^{?}$), 7.89 (1H, s, H^{3}), 7.43 (1H, s, H^{imine}), 7.28-7.25 (2H, m, $H^{4'}$ and $H^{5'}$), 7.04-7.00 (2H, m, $H^{6'}$ and $H^{3'}$), 6.93 (1H, td, J = 7.5 and 1, H^{5}), 3.73 (3H, d, J = 1, H^{NMe}). ^{13}C NMR ($CDCl_3$, 176 MHz): 156.8, 148.7, 140.4, 130.5, 130.4, 125.2 , 123.6, 122.1, 119.6, 118.7, 116.7, 111.2, 104.4, 29.7. MS (ES+): *m/z* 296 $[M+H]^+$; HRMS (ES+): *m/z* = 296.1011 $[M+H]^+$; calculated for $[C_{14}H_{13}F_3N_3O]^+$ = 296.2672. Mp = 117.5-119.0°C.

3-(dimethylamino)-1-(2-hydroxyphenyl)-prop-2-en-1-one

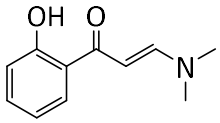

A mixture of 2'-hydroxyacetophenone (0.68 g, 5.0 mmol) and N,N-dimethylformamide dimethyl acetal (2.1 g, 17.5 mmol) was stirred at 75°C in DMF (25ml) for 30 minutes. The mixture was allowed to cool to ambient temperature before being poured into a beaker with brine (100ml) causing a yellow precipitate to form. The mixture was filtered and the solid dried under high vacuum at 50°C to afford 0.92 g of a bright yellow solid (0.48 mmol, 96% yield). The experimental data obtained was good agreement with that reported in literature.[114]

2-(1H-pyrazol-5-yl)phenol

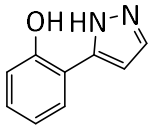

Hydrazine monohydrate (0.63ml, 12.6 mmol) was added to a suspension of 3-(dimethylamino)-1-(2-hydroxyphenyl)-prop-2-en-1-one (0.4 g, 2.1 mmol) in EtOH (10ml) and the mixture was refluxed for 6 hours to afford a white suspension. The suspension was filtered to remove the white solid and the solvent removed in vacuo to afford a beige residue. The residue was washed with H_2O, extracted into EtOAc and the solvent removed in vacuo to afford 0.21 g of a white solid (1.3 mmol, 62% yield). The experimental data obtained were in accord with that reported in literature.[129]

HL[21]

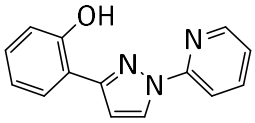

A mixture of 2-(1H-pyrazol-5-yl)phenol (150 mg, 0.94 mmol), 2-bromopyridine (178 mg, 1.12 mmol), trans-1,2-diaminocyclohexane (22 mg, 0.19 mmol), copper iodide (9 mg, 0.05 mmol), K_2CO_3 (273 mg, 1.97 mmol) in dry 1,4-dioxane (2ml) was degassed via freeze-pump-thaw (3 cycles). The mixture was heated at reflux with stirring for 24 hours. After cooling

to ambient temperature, the mixture was diluted with EtOAc (6ml) and filtered through celite and washed through with EtOAc (40ml). The crude product was purified by chromatography with silica gel (hexane/DCM, 50:50) to provide 123 mg of a white solid (0.52 mmol, 55% yield). The experimental data obtained were in good agreement with that reported in literature.[205]

2-(Hydrazinocarbonyl)pyridine

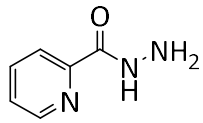

Hydrazine monohydrate (1ml) was added dropwise to a solution of ethyl 2-picolinate (560 mg, 3.7 mmol) in EtOH (3ml). The mixture was heated at reflux overnight before cooling to ambient temperature. The solvent was removed in vacuo to afford 421 mg of a white solid (3.07 mmol, 83% yield). The experimental data obtained were in accord with that reported in literature.[161]

HL[22]

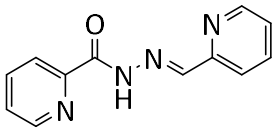

2-Pyridine carboxaldehyde (78 mg, 0.73 mmol) was added dropwise under a steam of argon to a solution of 2-(hydrazinocarbonyl)pyridine (101 mg, 0.73 mmol) in MeOH (2ml). The resulting solution was refluxed for two hours before cooling to ambient temperature. The solvent was removed in vacuo and the resulting brown residue was recrystallized from DCM/hexane to afford 72 mg of a white crystalline solid (0.32 mmol, 44% yield). The experimental data obtained were in good agreement with that reported in literature.[161]

HL[23]

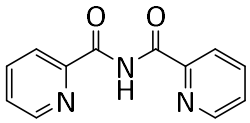

2,4,6-Tris(2-pyridyl)-s-triazine (200 mg, 0.64 mmol) and $Cu(NO_3).3H_2O$ (155 mg, 0.64 mmol) were dissolved in a mixture of deionised water (7ml) and EtOH (5ml). The dark green solution was refluxed for a period of 2 hours and the resulting blue solution was transferred to a petri-dish and heated gently to cause crystallisation. The bright blue crystals were collected by filtration and then dissolved in chloroform (10ml). The resulting blue solution was added to a stirring solution of Ethylenediaminetetraacetic acid disodium salt dihydrate (390 mg, 1.05 mmol) in deionised water (15ml). The resulting biphasic mixture was stirred vigorously for a period of 4 hours. The organic layer was then extracted with chloroform (3 x 30ml), dried over $MgSO_4$ and the solvent removed in vacuo to yield 101 mg of a white solid (0.44 mmol, 69% yield). The experimental data obtained were in accord with that reported in literature.[206]

2,4,6-Tris(2-pyrimidyl)-1,3,5-triazine

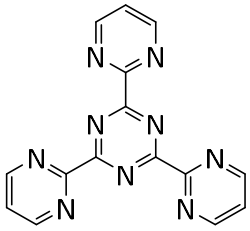

2-Cyanopyrimidine (600 mg, 5.71 mmol) was heated with stirring in a stoppered flask at 150°C for 48h. The solidified product was suspended in Et_2O and filtered to obtain 477 mg of a cream coloured solid (1.51 mmol, 79% yield). The experimental data obtained were in good agreement with that reported in literature.[120]

HL[24]

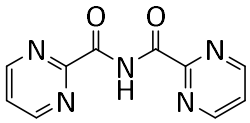

$Cu(NO_3)_2.3H_2O$ (268 mg, 1.11 mmol) in H_2O (10ml) was added to a suspension of 2,4,6-Tris(2-pyrimidyl)-1,3,5-triazine (350 mg, 1.11 mmol) in EtOH (10ml) to form a dark green slurry which was refluxed for a period of 2 hours. The resulting blue solution was poured into a petri dish and allowed to stand for 4 hours. The blue crystals were isolated by filtration and dried *in vacuo*. The blue crystals were then added to a biphasic mixture of aqueous Na_2H_2EDTA (745 mg, 2.00 mmol, 30ml H_2O) in chloroform (20ml) and the stirred at room temperature for a period of 5 hours. The organic layer was extracted with chloroform (3 x 50ml), dried over magnesium sulfate and the solvent removed in vacuo to yield 148 mg of a white solid (0.65 mmol, 58% yield).

HL[25]

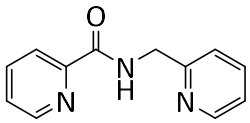

A mixture of ethyl 2-picolinate (302 mg, 2.00 mmol), 2-(methylamino)pyridine (238 mg, 2.20 mmol) and anhydrous 1,4-dioxane (1.4ml) was sealed in a microwave vial and heated at 180°C for 1 hour. The resulting yellow solution was diluted with deionised water (30ml) and extracted into DCM (2 x 30ml). The organic layers were washed with brine, dried over $MgSO_4$ and the solvent removed in vacuo to yield a crude yellow liquid which was purified by column chromatography (5% MeOH in DCM) to yield 96 mg of a fine white powder (0.45 mmol, 23% yield). The experimental data obtained were in accord with that reported in literature.[207]

2-Bromo-6-phenylpyridine

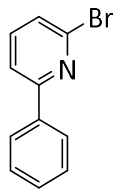

A solution of *n*BuLi (1.6M in hexane, 24ml, 38.4 mmol) was added dropwise at 0°C to a solution of 2-(dimethylamino)ethanol (1.7 g, 19.2 mmol) in 19ml hexane resulting in a pale yellow solution. After 30 min stirring at 0°C, a solution of 2-phenylpyridine (1.0 g, 6.4 mmol) in 6.5ml hexane was added dropwise resulting in an orange solution. The solution was stirred at 0°C for 1 hour and then cooled to -78°C before the addition of CBr_4 (7.4 g, 22.4 mmol) in 22.5ml hexane. The resulting mixture was allowed to stir at -78°C for 1 hour before it was allowed to warm to room temperature overnight. Hydrolysis was then performed at 0°C by the addition of 25ml of H_2O. The organic layer was extracted into EtOAc, dried over $MgSO_4$ and concentrated to give an orange oil. The crude product was purified by chromatography with silica gel (hexane/EtOAc, 95:5) to provide 877 mg of a pale yellow solid (3.75 mmol, 59% yield). The experimental data obtained were in accord with that reported in literature.[208]

2-hydrazino-6-phenyl-pyridine

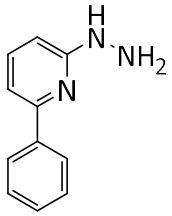

2-Bromo-6-phenylpyridine (260 mg, 1.10 mmol) was refluxed under argon in 20ml hydrazine hydrate for 22 hours before cooling to room temperature. The excess hydrazine hydrate was removed in vacuo, the residue dissolved in chloroform and stirred with K_2CO_3 (300 mg, 2.2 mmol) for 20 minutes. The suspension was filtered through celite and the solvent removed in vacuo to afford 0.184 g of an orange air sensitive oil (0.99 mmol, 90% yield). The resulting orange oil was used in the next step with no formal isolation.

HL[26]

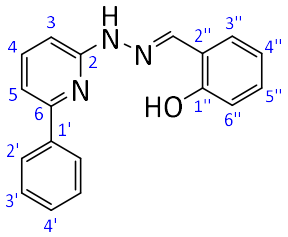

2-hydrazino-6-phenyl-pyridine (87 mg, 0.47 mmol) and salicylaldehyde (143 mg, 1.20 mmol) were refluxed with stirring in MeOH (3ml) under argon for 40 minutes. The resulting yellow slurry was filtered, washed with hexane and purified by chromatography with silica gel (hexane/EtOAc, 90:10) to provide 53 mg of a white solid (0.18 mmol, 39% yield).

^{1}H NMR ($CDCl_3$, 600 MHz): 10.75 (1H, s, H^{OH}), 9.19 (1H, s, H^{NH}), 7.98 (2H, d, J = 8, $H^{2'}$), 7.74 (1H, t, J = 8, H^{4}), 7.59 (1H, s, H^{imine}), 7.46 (2H, t, J = 8, $H^{3'}$), 7.37 (1H, t, J = 7, $H^{4'}$), 7.29 (1H, d, J = 8, H^{5}), 7.24 (1H, t, J = 8, $H^{4''}$), 7.02 (1H, d, J = 8, H^{3}), 7.00 (1H, d, J = 8, $H^{3''}$), 6.98 (1H, d, J = 8, $H^{6''}$), 6.88 (1H, t, J = 8, $H^{5''}$). ^{13}C NMR ($CDCl_3$, 151 MHz): 157.3 (C^{OH}), 156.2 ($C^{1'}$), 155.8 (C^{6}), 142.9 (C^{imine}), 139.5 (C^{4}), 139.2 (C^{2}), 130.5 ($C^{4''}$), 130.0 ($C^{3''}$), 129.3 ($C^{4'}$), 129.0 ($C^{3'}$), 127.1 ($C^{2'}$), 119.6 ($C^{5''}$), 118.4 ($C^{2''}$), 116.7 ($C^{6''}$), 113.3 (C^{5}), 105.2 (C^{3}). MS (ES+): *m/z* 290 $[M+H]^+$; HRMS (ES+): *m/z* 290.1290 $[M+H]^+$; calculated for $[C_{18}H_{16}N_3O]^+$ 290.1293.

2-(1-methylhydrazino)-6-phenyl-pyridine

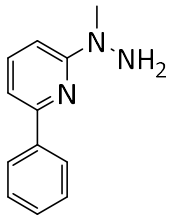

2-Bromo-6-phenylpyridine (100 mg, 0.43 mmol) was refluxed under argon in 6ml methylhydrazine for 2 hours before cooling to room temperature. The mixture was diluted with 10ml water and the product extracted into diethyl ether. The organic layer was dried over $MgSO_4$ and the solvent removed in vacuo to yield 85 mg of a yellow oil (0.43 mmol, 100% yield). The experimental data obtained were in good agreement with that reported in literature.[189]

HL[27]

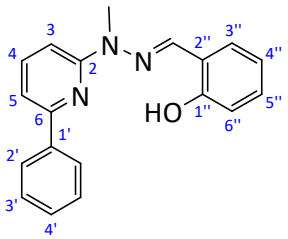

2-(1-methylhydrazino)-6-phenyl-pyridine (88 mg, 0.44 mmol) and salicylaldehyde (54 mg, 0.44 mmol) were refluxed with stirring in MeOH (6ml) under argon for 2 hours. The resulting white slurry was allowed to cool to ambient temperature, filtered and washed with cold methanol to give 98 mg of a white solid (0.32 mmol, 73% yield).

^{1}H NMR ($CDCl_3$, 400 MHz): 11.32 (1H, s, H^{OH}), 8.09 - 8.06 (2H, m, $H^{2'}$), 7.88 (1H, s, H^{imine}), 7.74 (1H, dd, J = 8.5 and 8, H^{4}), 7.53 – 7.42 (3H, m, $H^{3'}$, $H^{4'}$ and H^{5}), 7.36 – 7.24 (3H, m, $H^{4'}$, H^{3} and $H^{3''}$), 7.04 (1H, d, J = 8, $H^{6''}$), 6.97 (1H, td, J = 7.5 and 1, $H^{5''}$), 3.85 (3H, m, H^{NMe}). ^{13}C NMR ($CDCl_3$, 101 MHz): 156.9, 156.2, 155.1, 139.3, 139.1, 138.3, 126.9, 119.7, 119.4, 116.7, 112.7, 107.1, 29.5. MS (ES+): *m/z* 304 $[M+H]^+$.

2-{[2-(3-bromophenyl)hydrazinylidene]methyl}phenol

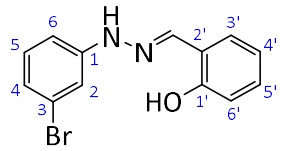

Salicylaldehyde (235 mg, 1.9 mmol) was added to a solution of 3-Bromophenylhydrazine (300 mg, 1.6 mmol) in MeOH (4ml). The resulting yellow solution was refluxed for 2 hours to produce a yellow slurry. The mixture was allowed to cool to ambient temperature and then filtered and washed with hexane to yield 277 mg of a beige solid (0.95 mmol, 60% yield).

^{1}H NMR ($CDCl_3$, 700 MHz): 10.54 (1H, s, H^{NH}), 10.25 (1H, s, H^{OH}), 8.18 (1H, s, H^{imine}), 7.62 (1H, d, J = 8, $H^{6'}$), 7.17 (2H, t, J = 8, H^{5} and $H^{5'}$), 7.14 (1H, t, J = 2, H^{2}), 6.94 (1H, d, J = 8, H^{6}), 6.90 (1H, d, J = 8, H^{4}), 6.89-6.85 (2H, m, $H^{3'}$ and $H^{4'}$). ^{13}C NMR ($CDCl_3$, 176 MHz): 155.6 (C^{OH}), 146.5 (C^{1}), 137.5 (C^{imine}), 131.2 (C^{5} or $C^{5'}$), 129.6 (C^{5} or $C^{5'}$), 126.8 ($C^{6'}$), 122.5 (C^{3}), 121.0 (C^{4}), 120.6 ($C^{2'}$), 119.4 ($C^{3'}$ or $C^{4'}$), 115.9 ($C^{3'}$ or $C^{4'}$), 113.8 (C^{2}), 110.8 (C^{6}). MS (ES+): *m/z* 291 $[M+H]^+$.

HL[28]

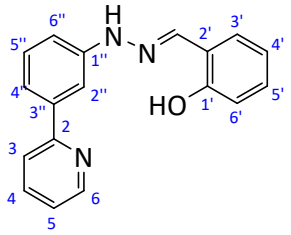

A mixture of 2-{[2-(3-bromophenyl)hydrazinylidene]methyl}phenol (300 mg, 1.57 mmol), Lithium Chloride (348 mg, 8.21 mmol), 2-(tributylstannyl)pyridine (480 mg, 1.30 mmol) and $Pd(PPh_3)_4$ (51 mg, 0.04 mmol) in anhydrous toluene (7ml) was degassed via freeze-pump-thaw (3 cycles). The mixture was heated at reflux with stirring for 48 hours. After cooling to ambient temperature, a solution of saturated aqueous KF (12ml) was added and stirring was continued for 1 hour. The resulting slurry was filtered via celite, washed through with toluene (40ml) and the solvent removed in vacuo to afford a brown oil. The crude oil was washed with 5% aq. $NaHCO_3$ solution (2 x 75ml) and extracted into DCM. The organic layer was dried over potassium carbonate and the solvent removed in vacuo to afford an orange oil. The crude product was purified by chromatography with silica gel (hexane/EtOAc, 70:30) to provide 72 mg of a white solid (0.25 mmol, 19% yield).

^{1}H NMR ($CDCl_3$, 600 MHz): 10.87 (1H, s, H^{OH}), 8.70 (1H, d, J = 5, H^6), 7.86 (1H, s, H^{imine}), 7.73-7.78 (3H, m, H^3, H^5 and H^{NH}), 7.61 (1H, t, J = 2, $H^{2''}$), 7.50 (1H, d, J = 8, $H^{4''}$), 7.40 (1H, t, J = 8, $H^{5''}$), 7.22-7.25 (2H, m, H^4 and $H^{4'}$), 7.14 (1H, dd, J = 8 and 2, $H^{6'}$), 7.08 (1H, dd, J = 8 and 2, $H^{6''}$), 7.00 (1H, d, J = 8, $H^{3'}$), 6.90 (1H, t, J = 8, $H^{5'}$). ^{13}C NMR ($CDCl_3$, 151 MHz): 157.2 (C^{OH} and C^2), 149.7 (C^6), 144.1 ($C^{3''}$), 141.6 (C^{imine}), 140.7 ($C^{1''}$), 137.1 (C^3 or C^5), 130.2 (C^4 or $C^{4'}$), 130.2 ($C^{5''}$), 129.6 ($C^{6'}$), 122.5 (C^4 or $C^{4'}$), 120.9 (C^3 and C^5), 119.6 ($C^{5'}$), 119.6 ($C^{4'}$), 118.6 ($C^{2'}$), 116.7 ($C^{3'}$), 113.3 ($C^{6''}$), 111.4 ($C^{2''}$). MS (ES-): m/z 288 $[M-H]^-$; HRMS (ES+): *m/z* 290.1302 $[M+H]^+$; calculated for $[C_{18}H_{16}N_3O]^+$ 290.1293.

HL[29]

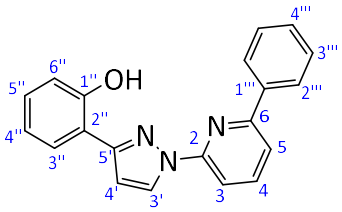

A mixture of 2-(1H-pyrazol-5-yl)phenol (150 mg, 0.94 mmol), 2-Bromo-6-phenylpyridine (263 mg, 1.12 mmol), trans-1,2-diaminocyclohexane (21.5 mg, 0.19 mmol), copper iodide (9 mg, 0.05 mmol), K_2CO_3 (273 mg, 1.97 mmol) in dioxane (2ml) was degassed via freeze-pump-thaw (3 cycles). The mixture was heated at reflux with stirring for 24 hours. After cooling to ambient temperature, the mixture was diluted with EtOAc (6ml) and filtered through celite and washed through with EtOAc (40ml). The crude product was purified by chromatography with silica gel (hexane/DCM, 50:50) to provide 267 mg of a white solid (91% yield).

^{1}H NMR ($CDCl_3$, 600 MHz): 10.76 (1H, s, H^{OH}), 8.82 (1H, d, J = 3, $H^{3'}$), 8.11 - 8.08 (2H, m, $H^{3'''}$), 7.93 (1H, t, J = 8, H^4), 7.82 (1H, dd, J = 8 and 1, H^3), 7.69 – 7.65 (2H, m, H^5 and $H^{6''}$), 7.54 – 7.45 (3H, m, $H^{2'''}$ and $H^{4'''}$), 7.31 - 7.27 (1H, m, $H^{4''}$), 7.09 (1H, dd, J = 8 and 1, $H^{3''}$), 6.97 (1H, td, J = 8 and 1, $H^{5''}$), 6.90 (1H, d, J = 3, $H^{4'}$). ^{13}C NMR ($CDCl_3$, 151 MHz): 104.9 ($C^{4'}$), 110.3 (C^3), 116.3 ($C^{2''}$), 117.3 ($C^{3''}$), 118.1 (C^5), 119.6 ($C^{5''}$), 127.1 ($C^{3'''}$ and $C^{6''}$), 128.3 ($C^{3'}$), 129.0 ($C^{2'''}$), 129.7 ($C^{4'''}$), 130.1 ($C^{4''}$), 138.3 ($C^{1'''}$), 139.9 (C^4), 150.4 (C^6), 154.0 (C^2), 156.3 ($C^{5'}$ and C^{OH}). MS (ES+): *m/z* 314 $[M+H]^+$; HRMS (ES+): *m/z* 314.1294 $[M+H]^+$; calculated for $[C_{20}H_{16}N_3O]^+$ 314.1293. Mp = 137-139°C. Anal. Cacld for $C_{20}H_{15}N_3O$: C, 76.66; H, 4.83; N, 13.41. Found: C, 76.53; H, 4.85; N, 13.38.

3-(dimethylamino)-1-(2-methoxyphenyl)-2-propen-1-one

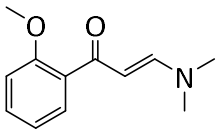

A mixture of 2'-methoxyacetophenone (0.64 g, 5.10 mmol) and N,N-dimethylformamide dimethyl acetal (2.2 g, 18.1 mmol) was refluxed in DMF (24ml) overnight. The mixture was allowed to cool to ambient temperature before being washed with brine (100ml), extracted into EtOAc (3 x 75ml) and dried over $MgSO_4$. The solvent was removed in vacuo to yield

1.03 g of a viscous orange oil (5.0 mmol, 99% yield). The experimental data obtained were in accord with that reported in literature.[209]

3-(2-methoxyphenyl)pyrazole

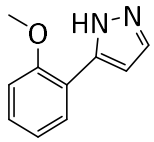

Hydrazine monohydrate (3ml, 61.5 mmol) was added to a suspension of 3-(dimethylamino)-1-(2-methoxyphenyl)-2-propen-1-one (1.032 g, 5.03 mmol) in EtOH (5ml) and the mixture was refluxed for 48 hours to afford a yellow solution. The solvent was removed in vacuo to afford a crude brown oil which was purified by chromatography with silica gel (hexane/EtOAc, 40:60) to provide 562 mg of a yellow solid (3.2 mmol, 64% yield). The experimental data obtained were in accord with that reported in literature.[210]

HL[30]

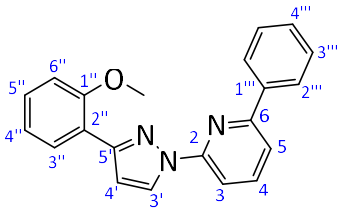

A mixture of 3-(2-methoxyphenyl)pyrazole (100 mg, 0.57 mmol), 2-Bromo-6-phenylpyridine (161 mg, 0.69 mmol), trans-1,2-diaminocyclohexane (13.3 mg, 0.12 mmol), copper iodide (6 mg, 0.03 mmol), K_2CO_3 (167 mg, 1.2 mmol) in dioxane (2ml) was degassed via freeze-pump-thaw (3 cycles). The mixture was heated at reflux with stirring for 24 hours. After cooling to ambient temperature, the mixture was diluted with EtOAc (6ml), filtered through celite and washed through with EtOAc (40ml). The crude product was purified by chromatography with silica gel (hexane/DCM, 50:50) to provide 180 mg of a white solid (0.55 mmol, 96% yield).

^{1}H NMR ($CDCl_3$, 600 MHz): 8.76 (1H, d, J = 3, $H^{3'}$), 8.13 (1H, dd, J = 8 and 2, $H^{6''}$), 8.10 (2H, d, J = 7, $H^{2'''}$), 8.05 (1H, d, J = 8, H^{3}), 7.88 (1H, t, J = 8, H^{4}), 7.63 (1H, d, J = 8, H^{5}), 7.51 (2H, t, J = 8, $H^{3'''}$), 7.45 (1H, tt, J = 7 and J = 1, $H^{4'''}$), 7.35 (1H, ddd, J = 9, 7 and 2, $H^{5''}$), 7.07 (1H, td, J = 8 and 1, $H^{4''}$), 7.04 (1H, d, J = 3, $H^{4'}$), 7.02 (1H, d, J = 8, $H^{3''}$), 3.95 (3H, s, H^{OMe}). ^{13}C NMR

($CDCl_3$, 151 MHz): 157.4 ($C^{1''}$), 155.8 (C^6), 151.8 (C^2), 151.1 ($C^{5'}$), 139.5 (C^4), 138.7 ($C^{1'''}$), 129.5 ($C^{5''}$), 129.4 ($C^{4'''}$), 129.0 ($C^{6''}$), 128.9 ($C^{3'''}$), 127.5 ($C^{3'}$), 127.0 ($C^{2'''}$), 122.2 ($C^{2''}$), 121.0 ($C^{4''}$), 117.5 (C^5), 111.6 ($C^{3''}$), 110.9 (C^3), 109.5 ($C^{4'}$), 55.7 (C^{OMe}). MS (ES+): *m/z* 328 $[M+H]^+$; HRMS (ES+): *m/z* 328.1444 $[M+H]^+$; calculated for $[C_{21}H_{18}N_3O]^+$ 328.1450.

4-tert-butylphenylpyridine

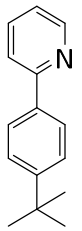

A mixture of 2-bromopyridine (500 mg, 3.16 mmol), 4-tert-butylphenylboronic acid (739 mg, 4.15 mmol), sodium carbonate (3.00 g, 28.3 mmol) in toluene (12ml), distilled water (12ml) and ethanol (2.4ml) was degassed via freeze-pump-thaw (3 cycles). $Pd(PPh_3)_4$ (150 mg, 0.13 mmol) was added and the resulting mixture was heated at reflux with stirring for 24 hours. After cooling to ambient temperature, the mixture was diluted with distilled water (60ml) and extracted with DCM (3 x 75ml). The organic layer was washed with brine (80ml) and dried over magnesium sulphate to give a brown oil. The crude product was purified by chromatography with silica gel (hexane/EtOAc, 95:5) to provide 599 mg of an off-white solid (2.83 mmol, 90% yield). The experimental data obtained were in accord with that reported in literature.[211]

2-bromo-6-(4-tert-butylphenyl)pyridine

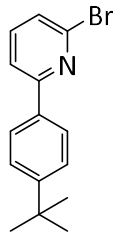

A solution of *n*BuLi (1.6M in hexane, 11ml, 17.6 mmol) was added dropwise at 0°C to a solution of 2-(dimethylamino)ethanol (757 mg, 8.49 mmol) in 8.5ml hexane resulting in a pale yellow solution. After 30 min stirring at 0°C, a solution of 4-tert-butylphenylpyridine (599 mg, 2.83 mmol) in 3ml hexane was added dropwise resulting in an orange solution.

The solution was stirred at 0°C for 1 hour and then cooled to -78°C before the addition of CBr_4 (3.28 g, 9.90 mmol) in 10ml hexane. The resulting mixture was allowed to stir at -78°C for 1 hour before it was allowed to warm to room temperature overnight. Hydrolysis was then performed at 0°C by the addition of 25ml of H_2O. The organic layer was extracted into EtOAc, dried over $MgSO_4$ and concentrated to give an orange oil. The crude product was purified by chromatography with silica gel (hexane/EtOAc, 95:5) followed by a second chromatography with silica gel (hexane/DCM, 80:20) to provide 490 mg of a white solid (1.69 mmol, 60% yield). The experimental data obtained were in accord with that reported in literature.[212]

HL[31]

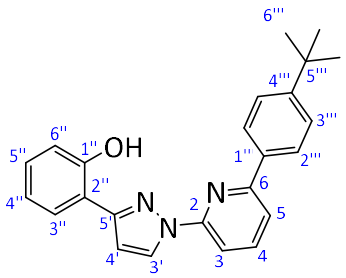

A mixture of 2-(1H-pyrazol-5-yl)phenol (133 mg, 0.83 mmol), 2-bromo-6-(4-tert-butylphenyl)pyridine (200 mg, 0.69 mmol), trans-1,2-diaminocyclohexane (15.8 mg, 0.14 mmol), copper iodide (9 mg, 0.05 mmol), K_2CO_3 (200 mg, 1.50 mmol) in dioxane (2ml) was degassed via freeze-pump-thaw (3 cycles). The mixture was heated at reflux with stirring for 24 hours. After cooling to ambient temperature, the mixture was diluted with EtOAc (6ml) and filtered through celite and washed through with EtOAc (40ml). The crude product was purified by chromatography with silica gel (hexane/DCM, 50:50) to provide 170 mg of a white solid (0.46 mmol, 67% yield).

^{1}H NMR ($CDCl_3$, 600 MHz): 10.77 (1H, s, H^{OH}), 8.81 (1H, d, J = 3, $H^{3'}$), 8.02 (2H, d, J = 8, $H^{3'''}$), 7.90 (1H, t, J = 8, H^4), 7.79 (1H, d, J = 8, H^3), 7.67-7.65 (2H, m, $H^{6''}$ and H^5), 7.54 (2H, d, J = 8, $H^{2'''}$), 7.29 (1H, t, J = 8, $H^{5''}$), 7.09 (1H, d, J = 8, $H^{3''}$), 6.97 (1H, t, J = 7, $H^{4''}$), 6.89 (1H, d, J = 3, $H^{4'}$), 1.39 (9H, s, $H^{6'''}$). ^{13}C NMR ($CDCl_3$, 151 MHz): 156.3 (C^2), 156.2 (C^{OH}), 153.9 ($C^{5'}$), 153.0 ($C^{4'''}$), 150.3 (C^6), 139.7 (C^4), 135.6 ($C^{1'''}$), 130.1 ($C^{5''}$), 128.2 ($C^{3'}$), 127.0 ($C^{6''}$), 126.8 ($C^{3'''}$), 125.9 ($C^{2'''}$), 119.6 ($C^{4''}$), 117.9 (C^5), 117.3 ($C^{3''}$), 116.3 ($C^{2''}$), 109.9 (C^3), 104.8 ($C^{4'}$), 34.9 ($C^{5'''}$),

31.4 ($C^{6'''}$). MS (ES+): *m/z* 370 $[M-H]^+$; HRMS (ES+): *m/z* 370.1912 $[M+H]^+$; calculated for $[C_{24}H_{24}N_3O]^+$ 370.1919.

2-bromo-6-phenoxy-pyridine

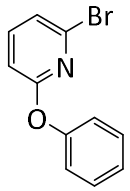

A mixture of phenol (620 mg, 6.6 mmol), NaH (164 mg, 6.8 mmol) and DMF (10ml) was stirred over ice for a period of 10 minutes. A solution of 2,6-dibromopyridine (620 mg, 2.6 mmol) in DMF (6ml) was added slowly and the ice bath was maintained for a further 10 minute period. The solution was then heated to 100°C and stirred overnight under argon. The resulting brown solution was allowed to cool to ambient temperature, quenched with sat. aq. $NaHCO_3$ and extracted into EtOAc. The organic layer was washed with brine, dried over $MgSO_4$ and the solvent removed in vacuo to yield a brown oil. The crude product was purified by chromatography with silica gel (100% hexane to hexane/EtOAc, 95:5) to provide 580 mg of a white solid (2.3 mmol, 89% yield). The experimental data obtained were in accord with that reported in literature.[130]

HL[31]

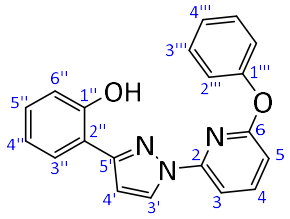

A mixture of 2-(1H-pyrazol-5-yl)phenol (45 mg, 0.28 mmol), 2-bromo-6-phenoxy-pyridine (59 mg, 0.24 mmol), trans-1,2-diaminocyclohexane (9 mg, 0.08 mmol), copper iodide (3 mg, 0.02 mmol), K_2CO_3 (70 mg, 0.5 mmol) in dioxane (1ml) was degassed via freeze-pump-thaw (3 cycles). The mixture was heated at reflux with stirring for 72 hours. After cooling to ambient temperature, the mixture was diluted with EtOAc (6ml) and filtered through celite and washed through with EtOAc (40ml). The crude product was purified by

chromatography with silica gel (100% hexane) to provide 24 mg of a white solid (0.07 mmol, 30% yield).

^{1}H NMR ($CDCl_3$, 700 MHz): 10.66 (1H, s, H^{OH}), 8.27 (1H, d, J = 3, $H^{3'}$), 7.83 (1H, t, J = 8, H^{4}), 7.60 (1H, dd, J = 8 and 1.5, $H^{6''}$), 7.54 (1H, d, J = 8, H^{3} or H^{5}), 7.45 (2H, t, J = 8, $H^{3'''}$), 7.28-7.25 (2H, m, $H^{4''}$ and $H^{4'''}$), 7.21 (2H, d, J = 8, $H^{2'''}$), 7.07 (1H, d, J = 8, $H^{3''}$), 6.95 (1H, t, J = 8, $H^{5''}$), 6.77-6.76 (2H, m, $H^{4'}$ and H^{3} or H^{5}). ^{13}C NMR ($CDCl_3$, 176 MHz): 162.8 (C^{2}), 156.2 ($C^{1''}$), 154.1 ($C^{5'}$), 153.8 ($C^{1'''}$), 148.8 (C^{6}), 142.2 (C^{4}), 130.2 ($C^{4''}$), 129.8 ($C^{3'''}$), 128.4 ($C^{3'}$), 127.1 ($C^{6''}$), 125.2 ($C^{4'''}$), 121.5 ($C^{2'''}$), 119.6 ($C^{5''}$), 117.3 ($C^{3''}$), 116.2 ($C^{2''}$), 108.3 (C^{3} or C^{5}), 105.5 (C^{3} or C^{5}), 104.9 ($C^{4'}$). MS (ES+): *m/z* 330 $[M-H]^{+}$.

Methyl 6-phenylpicolinate

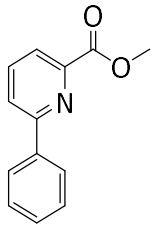

A mixture of methyl-6-bromopicolinate (200 mg, 0.93 mmol), phenylboronic acid (136 mg, 1.12 mmol), 1 M Na_2CO_3 (aq) (4ml) in THF (8ml) was degassed via freeze-pump-thaw (3 cycles). $Pd(PPh_3)_4$ (32 mg, 0.028 mmol) was added and the resulting mixture was heated at reflux with stirring for 24 hours. After cooling to ambient temperature, the mixture was diluted with distilled water (10ml) and extracted with DCM (3 x 40ml). The organic layer was washed with brine (50ml) and dried over magnesium sulphate to give a yellow oil. The crude product was purified by chromatography with silica gel (hexane/EtOAc, 80:20) to provide 186 mg of an off-white solid (0.87 mmol, 94% yield). The experimental data obtained were in accord with that reported in literature.[213]

6-phenyl-pyridine-2-carboxylic acid hydrazide

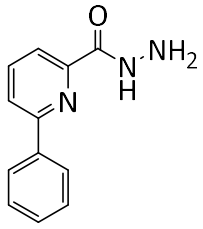

Methyl 6-phenylpicolinate (180 mg, 0.84 mmol) was refluxed under argon in 6ml hydrazine hydrate for 3 hours before cooling to room temperature. The mixture was diluted with 10ml water and the product extracted into diethyl ether. The organic layer was dried over $MgSO_4$ and the solvent removed in vacuo to yield 172 mg of an off-white solid (0.81 mmol). Due to the air-sensitive nature of the material it was used in the next step with no formal isolation.

^{1}H NMR ($CDCl_3$, 400 MHz): 9.17 (1H, br s), 8.13 (1H, dd, J = 7 and 1), 8.02 3 – 8.01 (2H, m), 7.97 – 7.90 (2H, m), 7.55 – 7.45 (3H, m), 7.25 – 7.21 (1H, m).

HL^{33}

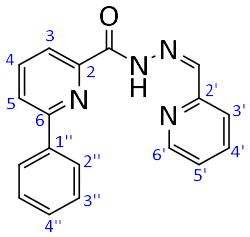

6-phenyl-pyridine-2-carboxylic acid hydrazide (172 mg, 0.81 mmol) and 2-pyridine carboxyaldehyde (89 mg, 0.83 mmol) were refluxed in MeOH (4ml) for a period of 2 hours before allowing to cool to ambient temperature. The solvent was removed in vacuo and successive DCM//hexane recrystallizations afforded 42 mg of a white solid (0.14 mmol, 17% yield).

HL^{33} (Z isomer)

^{1}H NMR ($CDCl_3$, 600 MHz): 11.28 (1H, s, H^{NH}), 8.82 (1H, d, J = 5, $H^{6'}$), 8.30 (1H, dd, J = 7 and 2, H^4), 8.28 – 8.25 (2H, m, $H^{3''}$), 7.97 – 7.94 (2H, m, H^5 and H^3), 7.90 (1H, td, J = 8 and 2, $H^{4'}$), 7.63 (1H, s, H^{imine}), 7.59 – 7.54 (2H, m, $H^{2''}$), 7.54 – 7.51 (2H, m, $H^{3'}$ and $H^{4''}$), 7.38 (1H, ddd, J = 8, 5 and 1, $H^{5'}$). ^{13}C NMR ($CDCl_3$, 151 MHz): 162.9 (C^2), 156.1 (C^6), 152.6 ($C^{2'}$), 149.7 ($C^{C=O}$),

148.7 ($C^{6'}$), 139.6 (C^{imine}), 138.8 ($C^{1''}$), 138.3 (C^{3}), 137.7 ($C^{4'}$), 129.7 ($C^{4''}$), 128.9 ($C^{3''}$), 127.3 ($C^{2''}$), 126.1 ($C^{3'}$), 124.1 ($C^{5'}$), 123.4 (C^{5}), 122.0 (C^{4}). MS (ES-): *m/z* 301 $[M-H]^+$.

PtL^{1}Cl

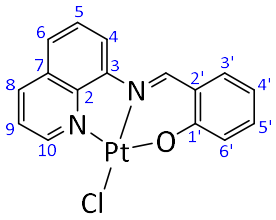

A bright red mixture of HL^1 (50 mg, 0.20 mmol), Pt(1,5-COD)Cl_2 (75 mg, 0.20 mmol) and anhydrous NEt_3 (20 mg, 0.20 mmol) in anhydrous MeCN (1ml) was stirred overnight at reflux under Argon. The mixture was allowed to cool to ambient temperature, filtered and washed with MeCN (2 x 1ml) to yield 78 mg of a red solid (0.16 mmol, 82% yield).

^{1}H NMR (DMSO-d_6, 600 MHz): 9.80 (1H, s, H^{imine}), 9.62 (1H, dd, J = 5.5 and 1, H^{9}), 8.86 (1H, d, J = 8, H^{8}), 8.78 (1H, d, J = 8, H^{4}), 8.06 (1H, d, J = 8, H^{6}), 7.92 (1H, t, J = 8, H^{5}), 7.85 – 7.83 (2H, m, H^{10} and $H^{3'}$), 7.56 (1H, ddd, J = 9, 6 and 2, $H^{5'}$), 6.97 (1H, d, J = 9, $H^{6'}$), 6.76 (1H, t, J = 7, $H^{4'}$). ^{13}C NMR (DMSO-d_6, 151 MHz): 163.7 ($C^{1'}$), 152.6 (C^{9}), 149.9 (C^{imine}), 146.7 (C^{2}), 144.2 (C^{3}), 139.8 (C^{8}), 135.9 ($C^{5'}$), 135.7 (C^{10} or$C^{3'}$), 129.6 (C^{7}), 129.2 (C^{5}), 128.3 (C^{6}), 124.2 (C^{10} or $C^{3'}$), 122.1 ($C^{2'}$), 121.8 ($C^{6'}$), 119.6 (C^{4}), 117.4 ($C^{4'}$). MS (ASAP): *m/z* 478 $[M+H]^+$.

PtL^{2}Cl

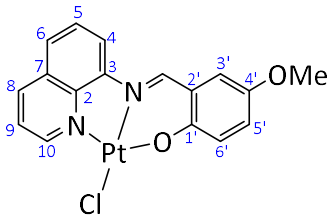

A bright red mixture of HL^2 (31 mg, 0.11 mmol), Pt(1,5-COD)Cl_2 (42 mg, 0.11 mmol) and anhydrous NEt_3 (20 mg, 0.20 mmol) in anhydrous MeCN (1ml) was stirred overnight at reflux under Argon. The mixture was allowed to cool to ambient temperature, filtered and washed with MeCN (2 x 1ml) to yield 43 mg of a purple-red solid (0.08 mmol, 73% yield).

^{1}H NMR (DMSO-d_6, 700 MHz): 9.74 (1H, s, H^{imine}), 9.60 (1H, dd, J = 5 and 1, H^{9}), 8.84 (1H, dd, J = 8 and 1, H^{8}), 8.71 (1H, d, J = 8, H^{4}), 8.03 (1H, d, J = 8, H^{6}), 7.91 (1H, t, J = 8, H^{5}), 7.82 (1H, dd, J = 8 and 5, H^{10}), 7.27 – 7.25 (2H, m, $H^{3'}$ and $H^{5'}$), 6.91 (1H, d, J = 9, $H^{6'}$), 3.76 (3H, s, H^{OMe}). ^{13}C NMR (DMSO-d_6, 176 MHz): 159.2 ($C^{1'}$), 152.1 (C^{9}), 150.0 ($C^{4'}$), 148.4 (C^{imine}), 146.3 (C^{3}), 146.3 (C^{2}), 143.6 (C^{8}), 139.3 (C^{8}), 129.1 (C^{7}), 128.8 (C^{5}), 127.6 (C^{6}), 126.5 ($C^{3'}$), 123.7 (C^{10}), 122.4 ($C^{6'}$), 120.2 ($C^{2'}$), 118.7 (C^{4}), 113.1 ($C^{5'}$). MS (ES-): *m/z* 507 $[M-H]^+$.

PtL^{3}Cl

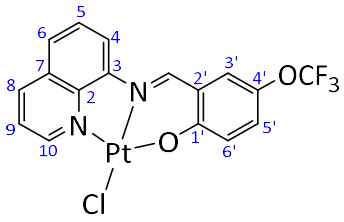

A bright red mixture of HL^3 (37 mg, 0.11 mmol), Pt(1,5-COD)Cl_2 (42 mg, 0.11 mmol) and anhydrous NEt_3 (20 mg, 0.20 mmol) in anhydrous MeCN (1ml) was stirred overnight at reflux under Argon. The mixture was allowed to cool to ambient temperature, filtered and washed with MeCN (2 x 1ml) to yield 35 mg of an orange-red solid (0.06 mmol, 57% yield).

^{1}H NMR (DMSO-d_6, 600 MHz): 9.85 (1H, s, H^{imine}), 9.57 (1H, d, J = 5, H^{9}), 8.84 (1H, d, J = 8, H^{8}), 8.70 (1H, d, J = 8, H^{4}), 8.06 (1H, d, J = 8, H^{6}), 7.91 (1H, t, J = 8, H^{5}), 7.84 – 7.79 (2H, m, H^{10} and $H^{3'}$), 7.53 (1H, dd, J = 9 and 3, $H^{5'}$), 7.00 (1H, d, J = 9, $H^{6'}$). ^{13}C NMR (DMSO-d_6, 151 MHz): 161.6 ($C^{1'}$), 152.2 (C^{9}), 149.1 (C^{imine}), 145.9 (C^{3}), 143.7 (C^{2}), 139.5 (C^{8}), 138.5 ($C^{4'}$), 129.1 (C^{7}), 128.8 (C^{5}), 128.6 ($C^{5'}$), 128.3 (C^{6}), 125.8 (C^{10} or $C^{3'}$), 123.8 (C^{10} or $C^{3'}$), 123.0 ($C^{6'}$), 121.0 ($C^{2'}$), 119.3 (C^{4}). MS (ES+): *m/z* 562 $[M-H]^+$; HRMS (ES+): *m/z* 561.0106 $[M+H]^+$; calculated for $[C_{17}H_{11}N_2O_2F_3ClPt]^+$ 561.0088.

PtL^{4}Cl

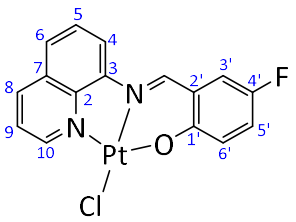

A bright red mixture of HL^4 (29 mg, 0.11 mmol), Pt(1,5-COD)Cl_2 (42 mg, 0.11 mmol) and anhydrous NEt_3 (20 mg, 0.20 mmol) in anhydrous MeCN (1ml) was stirred overnight at

reflux under Argon. The mixture was allowed to cool to ambient temperature, filtered and washed with MeCN (2 x 1ml) to yield 28 mg of an orange-red solid (0.06 mmol, 57% yield).

^{1}H NMR (DMSO-d_6, 600 MHz): 9.74 (1H, s, H^{imine}), 9.54 (1H, dd, J = 5 and 1, H^{9}), 8.81 (1H, dd, J = 8.5 and 1, H^{8}), 8.67 (1H, d, J = 8, H^{4}), 8.02 (1H, d, J = 8.5, H^{6}), 7.88 (1H, t, J = 8, H^{5}), 7.79 (1H, dd, J = 8 and 5.5, H^{10}), 7.54 (1H, dd, J = 9.5 and 3, $H^{3'}$), 7.44 (1H, ddd, J = 9.5, 8 and 3, $H^{4'}$), 6.91 (1H, dd, J = 9 and 5, $H^{6'}$). ^{13}C NMR (DMSO-d_6, 151 MHz): 160.0 ($C^{1'}$), 152.6 ($C^{4'}$), 152.1 (C^{9}), 148.5 (C^{imine}), 145.9 (C^{3}), 143.6 (C^{2}), 139.3 (C^{8}), 129.1 (C^{7}), 128.8 (C^{5}), 128.0 (C^{6}), 123.7 ($C^{5'}$), 122.8 (C^{10}), 120.3 ($C^{6'}$), 119.1 ($C^{2'}$), 117.0 ($C^{3'}$). MS (ES+): *m/z* 496 $[M-H]^+$

PtL^{1}C≡C-Ar

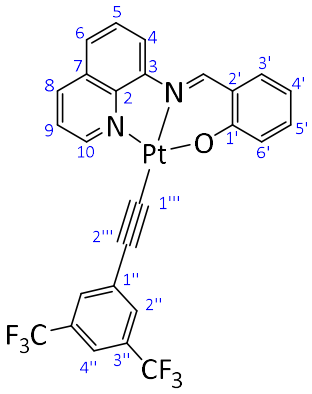

A mixture of PtL^{1}Cl (30 mg, 0.06 mmol), CuI (5 mg, 0.03 mmol), 1-ethynyl-3,5-bis(trifluoromethyl)benzene (23 mg, 0.1 mmol) and anhydrous NEt_3 (0.3ml) in anhydrous DCM (3ml) was refluxed for a period of 48 hours under argon. The solvent was removed in vacuo and the residue purified by column chromatography (gradient from 80 Hex: 20 DCM to 20 Hex: 80 DCM) to yield 21 mg of a red solid (0.03 mmol, 50% yield).

^{1}H NMR (DMSO-d_6, 700 MHz): 9.80 (1H, d, J = 5, H^{10}), 9.15 (1H, s, H^{imine}), 8.49 (1H, d, J = 8, H^{8}), 8.23 (1H, d, J = 7.5, H^{4}), 7.96 (2H, s, $H^{2''}$), 7.79 (1H, d, J = 8, H^{6}), 7.74 (1H, t, J = 8, H^{5}), 7.70 (1H, s, $H^{4''}$), 7.52-7.47 (3H, m, H^{9}, $H^{3'}$ and $H^{5'}$), 7.06 (1H, d, J = 9, $H^{6'}$), 6.67 (1H, t, J = 7, $H^{4'}$). ^{13}C NMR (DMSO-d_6, 176 MHz): 165.5 (C^{3}), 154.9 (C^{10}), 149.7 (C^{imine}), 146.4 ($C^{1'}$), 145.3 (C^{2}), 138.7 (C^{5}), 136.0 ($C^{3'}$ or $C^{5'}$), 135.4 ($C^{3'}$ or $C^{5'}$), 132.4 ($C^{2''}$), 131.5 (C^{CF_3}), 130.2 (C^{8}), 129.0 (C^{5}), 127.6 (C^{6}), 124.8 ($C^{1'''}$), 123.9 (C^{9}), 123.2 ($C^{6'}$ and $C^{2'''}$), 119.1 ($C^{4''}$), 117.7 (C^{2}), 117.5 ($C^{4'}$), 101.3 ($C^{2'}$), 96.5 ($C^{1''}$). MS (ES+): *m/z* 679 $[M+H]^+$; HRMS (ES+): *m/z* 679.0731 $[M+H]^+$; calculated for $[C_{26}H_{15}N_2OF_6Pt]^+$ 679.0715.

PtL^{5}Cl

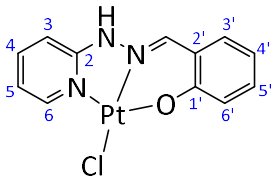

A solution of potassium tetrachloroplatinate (50 mg, 0.12 mmol) in deionised water (1ml) was added to a solution of L^5 (26 mg, 0.12 mmol) in EtOH (2.5ml) and the resulting pale pink solution was refluxed for 4 hours. The resulting mustard yellow slurry was isolated by centrifuge and washed with water (2 x 5ml), EtOH (2 x 5ml) and Et_2O (5ml) to isolate a green solid. The crude product was then extracted into hot MeCN, filtered through celite and the solvent removed in vacuo to produce 32 mg of a yellow solid (0.07 mmol, 60% yield).[141]

^{1}H NMR (DMSO-d_6, 700 MHz): 8.86 (1H, ddd, J = 6, 2 and 1, H^3), 8.70 (1H, s, H^{imine}), 7.97 (1H, ddd, J = 8.5, 7 and 1.5, H^5) 7.70 (1H, dd, J = 8 and 2, $H^{3'}$), 7.45 (1H, ddd, J = 8.5, 6.5 and 2, $H^{4'}$), 7.23 (1H, t, J = 8.5, H^6), 7.09 (1H, d, J = 8.5, $H^{6'}$), 7.01 (1H, ddd, J = 7, 6 and 1, H^4), 6.77 (1H, ddd, J = 8, 7 and 1, $H^{5'}$). ^{13}C NMR (DMSO-d_6, 176 MHz): 159.2 ($C^{1'}$), 153.8 (C^2), 145.2 (C^3), 138.4 (C^5), 138.3 (C^{imine}), 132.8 ($C^{3'}$), 132.3 ($C^{4'}$), 120.7 ($C^{6'}$), 118.6 ($C^{2'}$), 116.0 ($C^{5'}$), 115.2 (C^4), 107.0 (C^6). MS (ES+): *m/z* 442 $[M+H]^+$; HRMS (ES+): *m/z* 442.0206 $[M+H]^+$; calculated for $[C_{12}H_{11}N_3OPtCl]^+$ 442.0217.

PtL^{6}Cl

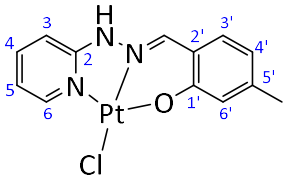

A solution of potassium tetrachloroplatinate (50 mg, 0.12 mmol) in deionised water (1ml) was added to a solution of L^6 (25 mg, 0.12 mmol) in EtOH (2.5ml) and the resulting pale pink solution was refluxed for 4 hours. The resulting orange-brown slurry was isolated by centrifuge and washed with water (2 x 5ml), EtOH (2 x 5ml) and Et_2O (5ml) to isolate 32 mg of a green-brown solid (0.07 mmol, 58% yield).

^{1}H NMR (DMSO-d_6, 700 MHz): 8.83 (1H, ddd, J = 6, 2, and 1, H^3), 8.61 (1H, s, H^{imine}), 7.95 (1H, ddd, J = 9, 7 and 2, H^5), 7.57 (1H, d, J = 8, $H^{3'}$), 7.20 (1H, ddd, J = 9, 2 and 1, H^6), 6.99 (1H, ddd, J = 7, 6 and 1, H^4), 6.91 (1H, s, $H^{6'}$), 6.61 (1H, dd, J = 8 and 2, $H^{4'}$), 2.19 (3H, s, H^{Me}).

^{13}C NMR (DMSO-d_6, 176 MHz): 159.6 ($C^{1'}$), 153.8 (C^{2}), 145.2 (C^{3}), 142.7 ($C^{2'}$), 138.3 (C^{5}), 138.1 (C^{imine}), 132.6 ($C^{3'}$), 120.5 ($C^{6'}$), 118.0 ($C^{4'}$), 116.3 ($C^{5'}$), 115.1 (C^{4}), 106.9 (C^{6}). MS (ES-): *m/z* 456 $[M-H]^-$

PtL^{7}Cl

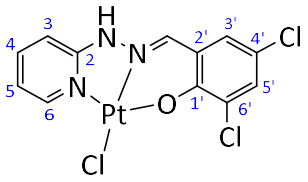

A solution of potassium tetrachloroplatinate (303 mg, 0.73 mmol) in deionised water (5ml) was added to a solution of L^7 (200 mg, 0.71 mmol) in EtOH (15ml) and the resulting pale pink solution was heated at 80°C for 4 hours. The resulting yellow slurry was isolated by centrifuge and washed with water (2 x 5ml), EtOH (2 x 5ml) and Et_2O (5ml) to isolate 300 mg of a mustard yellow solid. The crude material was recrystallized in DMF to isolate 223 mg of a bright yellow solid (0.44 mmol, 61% yield).

^{1}H NMR (DMSO-d_6, 600 MHz): 8.84 (1H, d, J = 6, H^3), 8.72 (1H, s, H^{imine}), 7.99 (1H, ddd, J = 8.5, 7 and 1.5, H^5), 7.88 (1H, d, J = 3, $H^{3'}$), 7.72 (1H, d, J = 3, $H^{5'}$), 7.24 (1H, d, J = 8.5, H^6), 7.03 (1H, t, J = 6.5, H^4). ^{13}C NMR (DMSO-d_6, 151 MHz): 154.3 (C^{OH}), 152.8 (C^{2}), 145.3 (C^{3}), 138.7 (C^{5}), 137.4 (C^{imine}), 130.8 ($C^{5'}$), 130.3 ($C^{3'}$), 125.7 ($C^{4'}$ or $C^{6'}$), 120.5 ($C^{2'}$), 118.2 ($C^{4'}$ or $C^{6'}$), 115.4 (C^{4}), 107.3 (C^{6}). MS (ES-): *m/z* 510 $[M-H]^-$.

PtL^{8}Cl

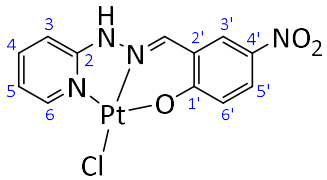

A solution of potassium tetrachloroplatinate (50 mg, 0.12 mmol) in deionised water (1ml) was added to a solution of L^8 (31 mg, 0.12 mmol) in EtOH (2.5ml) and the resulting pale pink solution was refluxed for 4 hours. The resulting orange-yellow slurry was isolated by centrifuge and washed with water (2 x 5ml), EtOH (2 x 5ml) and Et_2O (5ml) to isolate 44 mg of an orange solid (0.09 mmol, 75% yield).[141]

^{1}H NMR (DMSO-d_6, 700 MHz): 8.88 (1H, s, H^{imine} or $H^{3'}$), 8.87 (1H, s, H^{imine} or $H^{3'}$), 8.80 (1H, d, J = 6, H^{3}), 8.22 (1H, dd, J = 9 and 3, $H^{5'}$), 7.98 (1H, ddd, J = 8, 7 and 1, H^{5}), 7.23 (1H, d, J = 8, H^{6}), 7.16 (1H, d, J = 9, $H^{6'}$), 7.01 (1H, t, J = 7, H^{4}). ^{13}C NMR (DMSO-d_6, 176 MHz): 163.7 (C^{OH}), 154.9 (C^{2}), 145.3 (C^{3}), 138.9 (C^{5}), 137.9 (C^{imine}), 137.0 ($C^{4'}$), 130.7 ($C^{3'}$), 125.6 ($C^{5'}$), 121.7 ($C^{6'}$), 118.9 ($C^{2'}$), 115.2 (C^{4}), 107.4 (C^{6}). MS (ES-): *m/z* 486 $[M-H]^-$

PtL^{9}Cl

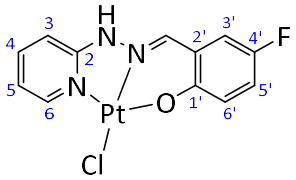

A solution of potassium tetrachloroplatinate (50 mg, 0.12 mmol) in deionised water (1ml) was added to a solution of L^{9} (27 mg, 0.12 mmol) in EtOH (2.5ml) and the resulting pale pink solution was refluxed for 4 hours. The resulting orange slurry was isolated by centrifuge and washed with water (2 x 5ml), EtOH (2 x 5ml) and Et_2O (5ml) to isolate 41 mg of a yellow solid (0.09 mmol, 73% yield).

^{1}H NMR (DMSO-d_6, 700 MHz): 8.86 (1H, ddd, J = 6, 1.5 and 1, H^{3}), 8.68 (1H, s, H^{imine}), 7.98 (1H, ddd, J = 9, 7 and 1.5, H^{5}), 7.61 (1H, dd, J = 10 and 3, $H^{3'}$), 7.34 (1H, ddd, J = 11, 7 and 2, $H^{5'}$), 7.23 (1H, d, J = 8.5, H^{6}), 7.09 (1H, dd, J = 9 and 5, $H^{6'}$), 7.03 (1H, ddd, J = 7, 6 and 1, H^{4}). ^{13}C NMR (DMSO-d_6, 176 MHz): 156.6 ($C^{1'}$), 154.2 (C^{2}), 152.8 ($C^{4'}$), 145.7 (C^{3}), 138.9 (C^{5}), 137.9 (C^{imine}), 122.3 ($C^{6'}$), 120.7 ($C^{5'}$), 118.1 ($C^{2'}$), 116.2 ($C^{3'}$), 115.8 ($C^{4'}$), 107.6 (C^{6}). MS (ES+): *m/z* 460 $[M+H]^+$; HRMS (ES+): *m/z* 460.0113 $[M+H]^+$; calculated for $[C_{12}H_{10}N_3OFPtCl]^+$ 460.0123.

PtL^{10}Cl

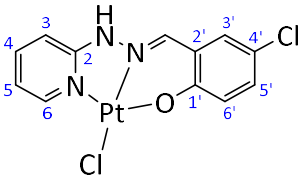

A solution of potassium tetrachloroplatinate (50 mg, 0.12 mmol) in deionised water (1ml) was added to a solution of L^{10} (29 mg, 0.12 mmol) in EtOH (2.5ml) and the resulting pale pink solution was refluxed for 4 hours. The resulting yellow slurry was isolated by centrifuge

and washed with water (2 x 5ml), EtOH (2 x 5ml) and Et_2O (5ml) to isolate 43 mg of a yellow solid (0.09 mmol, 75% yield).

^{1}H NMR (DMSO-d_6, 700 MHz): 8.82 (1H, d, J = 6, H^3), 8.67 (1H, s, H^{imine}), 7.95 (1H, ddd, J = 9, 7 and 1, H^5), 7.84 (1H, d, J = 3, $H^{3'}$), 7.41 (1H, dd, J = 9 and 3, $H^{5'}$), 7.20 (1H, d, J = 9, H^6), 7.07 (1H, d, J = 9, $H^{6'}$), 7.00 (1H, t, J = 7, H^4). ^{13}C NMR (DMSO-d_6, 176 MHz): 158.5 (C^{OH}), 154.5 (C^2), 145.7 (C^3), 138.9 (C^5), 137.8 (C^{imine}), 132.0 ($C^{5'}$), 131.3 ($C^{3'}$), 123.0 ($C^{6'}$), 120.1 ($C^{4'}$ or $C^{2'}$), 119.6 ($C^{4'}$ or $C^{2'}$), 115.7 (C^4), 107.6 (C^6). MS (ES-): *m/z* 476 $[M-H]^-$.

PtL^{11}Cl

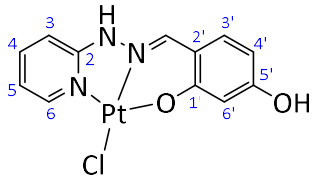

A solution of potassium tetrachloroplatinate (50 mg, 0.12 mmol) in deionised water (1ml) was added to a solution of L^{11} (27 mg, 0.12 mmol) in EtOH (2.5ml) and the resulting pale pink solution was refluxed for 4 hours. The resulting brown slurry was isolated by centrifuge and washed with water (2 x 5ml), EtOH (2 x 5ml) and Et_2O (5ml) to isolate 20 mg of a green solid (0.04 mmol, 36% yield).

^{1}H NMR (DMSO-d_6, 700 MHz): 13.50 (1H, br s, H^{NH}), 9.94 (1H, s, H^{OH}), 8.78 (1H, ddd, J = 6, 2 and 1, H^3), 8.45 (1H, s, H^{imine}), 7.92 (1H, ddd, J = 9, 7 and 2, H^5), 7.48 (1H, d, J = 9, $H^{6'}$), 7.15 (1H, dt, J = 9 and 1, H^6), 6.94 (1H, ddd, J = 7, 6 and 1, H^4), 6.43 (1H, d, J = 3, $H^{4'}$), 6.31 (1H, dd, J = 9 and 2, $H^{3'}$). ^{13}C NMR (DMSO-d_6, 176 MHz): 161.8 ($C^{5'}$), 161.6 ($C^{1'}$), 153.8 (C^2), 145.2 (C^3), 138.20 (C^{imine}), 138.1 (C^5), 134.2 ($C^{6'}$), 114.7 (C^4), 112.0 ($C^{2'}$), 107.6 ($C^{3'}$), 106.7 (C^6), 104.4 ($C^{4'}$). MS (ES-): *m/z* 458 $[M-H]^-$

PtL^{12}Cl

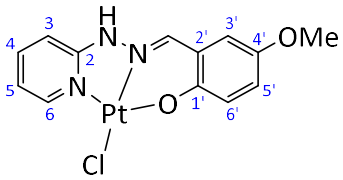

A solution of potassium tetrachloroplatinate (50 mg, 0.12 mmol) in deionised water (1ml) was added to a solution of L^{12} (29 mg, 0.12 mmol) in EtOH (2.5ml) and the resulting pale

pink solution was refluxed for 4 hours. The resulting yellow slurry was isolated by centrifuge and washed with water (2 x 5ml), EtOH (2 x 5ml) and Et_2O (5ml) to isolate 41 mg of a yellow solid (0.09 mmol, 72% yield).

^{1}H NMR (DMSO-d_6, 700 MHz): 8.86 (1H, ddd, J = 6, 2 and 1, H^3), 8.68 (1H, s, H^{imine}), 7.97 (1H, ddd, J = 9, 7 and 2, H^5), 7.23-7.22 (2H, m, H^6 and $H^{3'}$), 7.14 (1H, dd, J = 9 and 3, $H^{5'}$), 7.04 (1H, d, J = 9, $H^{6'}$), 7.01 (1H, ddd, J = 7, 6 and 1, H^4), 3.75 (1H, s, H^{OMe}). ^{13}C NMR (DMSO-d_6, 176 MHz): 154.9 ($C^{1'}$), 153.6 (C^2), 149.6 ($C^{4'}$), 145.2 (C^3), 138.2 (C^5), 137.8 (C^{imine}), 122.4 ($C^{5'}$), 121.5 ($C^{6'}$), 117.3 ($C^{2'}$), 115.1 (C^4), 112.6 ($C^{3'}$), 107.0 (C^6), 55.7 (C^{OMe}). MS (ES-): *m/z* 471 $[M-H]^-$

PtL^{13}Cl

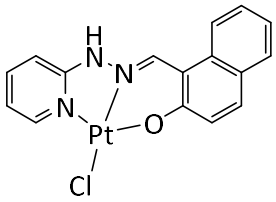

A solution of potassium tetrachloroplatinate (50 mg, 0.12 mmol) in deionised water (1ml) was added to a solution of L^{13} (29 mg, 0.11mmol) in EtOH (2.5ml) and the solution was refluxed for 4 hours. The resulting green slurry was allowed to cool to ambient temperature. The mixture was centrifuged and the collected solid washed with water (5ml), EtOH (5ml) and Et_2O (5ml) before being dried in vacuo to yield 37 mg of a green solid (0.08 mmol, 68% yield).

^{1}H NMR (DMSO-d_6, 400 MHz): 9.65 (1H, s), 8.86 (1H, d, J = 6), 8.08 (1H, d, J = 8.5), 7.99 (1H, ddd, J = 8.5, 7 and 1.5), 7.93 (1H, d, J = 9), 7.89 (1H, d, J = 8), 7.65 (1H, t, J = 8), 7.38 (1H, t, J = 8), 7.33 – 7.30 (2H, m), 7.02 (1H, t, J = 7). The material was not sufficiently soluble to obtain a ^{13}C NMR spectrum.

PtL^{14}Cl

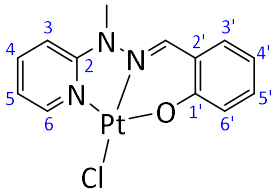

A solution of potassium tetrachloroplatinate (50 mg, 0.12 mmol) in deionised water (1ml) was added to a solution of L^{14} (27 mg, 0.12 mmol) in EtOH (2.5ml) and the resulting pale pink solution was refluxed for 4 hours. The resulting mustard yellow slurry was isolated by centrifuge and washed with water (2 x 5ml), EtOH (2 x 5ml) and Et_2O (5ml) to isolate a green solid. The crude product was then extracted into DCM, filtered through celite and the solvent removed in vacuo to produce 45 mg of a yellow solid (0.10 mmol, 82% yield).

^{1}H NMR (DMSO-d_6, 700 MHz): 9.06 (1H, ddd, J = 6, 2 and 0.5, H^3), 8.94 (1H, s, H^{imine}), 8.07 (1H, ddd, J = 9, 7 and 2, H^5), 7.82 (1H, dd, J = 8 and 2, $H^{3'}$), 7.48 (1H, d, J = 9, H^6), 7.45 (1H, ddd, J = 8.5, 6.5 and 2, $H^{6'}$), 7.09 (2H, m, H^4 and $H^{5'}$), 6.79 (1H, ddd, J = 8, 7 and 1, $H^{4'}$), 3.91 (3H, s, H^{NMe}). ^{13}C NMR (DMSO-d_6, 176 MHz): 159.3 (C^2), 152.9 ($C^{1'}$), 145.9 (C^3), 138.7 (C^5), 137.6 (C^{imine}), 133.7 ($C^{3'}$), 132.5 ($C^{5'}$), 120.5 ($C^{6'}$), 118.8 ($C^{2'}$), 116.1 ($C^{4'}$), 115.8 ($C^{4'}$), 108.7 (C^6), 34.03 (C^{NMe}). MS (ES+): *m/z* 462 $[M\text{-}Cl+MeCN]^+$; HRMS (ES+): *m/z* 461.0865 $[M+H]^+$; calculated for $[C_{15}H_{15}N_4OPt]^+$ 461.0878.

PtL^{15}Cl

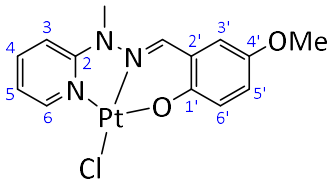

A solution of potassium tetrachloroplatinate (75 mg, 0.18 mmol) in deionised water (1.5ml) was added to a solution of L^{15} (44 mg, 0.17 mmol) in EtOH (4ml) and the resulting pale pink solution was refluxed for 4 hours. The resulting dark green slurry was filtered washed with water (2 x 5ml), EtOH (2 x 5ml) and Et_2O (5ml) to isolate a green solid. The crude product was then recrystallized in hot DMF to produce 36 mg of a yellow solid (0.07 mmol, 43% yield).

^{1}H NMR (DMSO-d_6, 700 MHz): 9.09 (1H, d, J = 6), 8.96 (1H, s), 8.08 (1H, ddd, J = 9, 7 and 2), 7.50 (1H, d, J = 9), 7.37 (1H, d, J = 3), 7.15 (1H, dd, J = 9 and 3), 7.10 (1H, t, J = 7), 7.05 (1H, d, J = 9). The material was not sufficiently soluble to obtain a ^{13}C NMR spectrum. MS (ES+): *m/z* 487 $[M+H]^+$.

PtL^{16}Cl

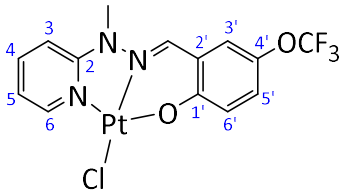

A solution of potassium tetrachloroplatinate (100 mg, 0.24 mmol) in deionised water (2ml) was added to a solution of L^{16} (62 mg, 0.20 mmol) in EtOH (5ml) and the resulting pale pink solution was refluxed for 4 hours. The resulting dark green slurry was filtered washed with water (2 x 5ml), EtOH (2 x 5ml) and Et_2O (5ml) to isolate a green solid. The crude product was then recrystallized in hot DMF to produce 47 mg of a bright yellow solid (0.09 mmol, 43% yield).

^{1}H NMR (DMSO-d_6, 700 MHz): 9.03 (1H, dd, J = 6 and 1, H^3), 9.00 (1H, s, H^{imine}), 8.07 (1H, ddd, J = 9, 7 and 1.5, H^5), 7.88 (1H, d, J = 3, $H^{3'}$), 7.49 (1H, d, J = 9, H^6), 7.43 (1H, dd, J = 9 and 3, $H^{5'}$), 7.13 (1H, d, J = 9, $H^{6'}$), 7.09 (1H, ddd, J = 7, 6 and 1, H^4), 3.91 (3H, s, H^{NMe}). ^{13}C NMR (DMSO-d_6, 176 MHz): 157.8 ($C^{1'}$), 152.9 (C^2), 145.9 (C^3), 138.8 (C^5), 137.9 ($C^{2'}$), 136.9 (C^{imine}), 125.6 ($C^{4'}$), 124.8 ($C^{5'}$), 121.9 ($C^{3'}$), 119.7 (C^{OCF_3}), 118.5 ($C^{6'}$), 116.0 (C^4), 108.8 (C^6). MS (ES+): *m/z* 541 $[M+H]^+$; HRMS (ES+): *m/z* 540.0207 $[M+H]^+$; calculated for $[C_{14}H_{12}N_3O_2F_3PtCl]^+$ 540.0197.

PtL^{17}Cl

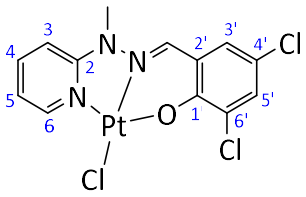

A solution of potassium tetrachloroplatinate (291 mg, 0.7 mmol) in deionised water (5ml) was added to a solution of L^{17} (200 mg, 0.68 mmol) in EtOH (15ml) and the resulting pale

pink solution was refluxed for 4 hours. The resulting dark green slurry was filtered washed with water (2 x 5ml), EtOH (2 x 5ml) and Et_2O (5ml) to isolate a green solid. The crude product was then recrystallized in hot DMF to produce 114 mg of a bright yellow solid (0.22 mmol, 32% yield).

^{1}H NMR (DMSO-d_6, 700 MHz): 9.03 (1H, dd, J = 6 and 1, H^3), 8.98 (1H, s, H^{imine}), 8.09 (1H, ddd, J = 9, 7 and 1.5, H^5), 7.92 (1H, d, J = 3, $H^{3'}$), 7.71 (1H, d, J = 3, $H^{5'}$), 7.79 (1H, d, J = 9, H^6), 7.11 (1H, ddd, J = 7, 6 and 1, H^4), 3.87 (3H, s, H^{NMe}). The material was not sufficiently soluble to obtain a ^{13}C NMR spectrum. MS (ES+): *m/z* 531 $[M\text{-}Cl+MeCN]^+$.

$PtL^{18}Cl$

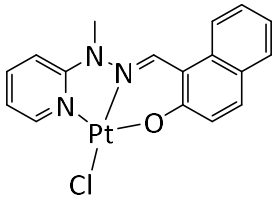

A solution of potassium tetrachloroplatinate (75 mg, 0.18 mmol) in deionised water (1.5ml) was added to a solution of L^{18} (50 mg, 0.17 mmol) in EtOH (4ml) and the resulting pale pink solution was refluxed for 4 hours. The resulting green slurry was filtered washed with water (2 x 5ml), EtOH (2 x 5ml) and Et_2O (5ml) to isolate a green solid. The crude product was then recrystallized in hot DMF to produce 30 mg of a yellow solid (0.06 mmol, 35% yield).

^{1}H NMR (DMSO-d_6, 700 MHz): 9.45 (1H, s), 9.06 (1H, d, J = 7), 8.41 (1H, d, J = 8.5), 8.08 (1H, t, J = 8), 7.92 (1H, d, J = 9), 7.85 (1H, d, J = 8), 7.61 (1H, t, J = 7.5), 7.56 (1H, d, J = 9), 7.36 (1H, t, J = 7), 7.30 (1H, d, J = 9), 7.10 (1H, t, J = 6). The material was not sufficiently soluble to obtain a ^{13}C NMR spectrum. MS (ES+): *m/z* 507 $[M+H]^+$

PtL^{19}Cl

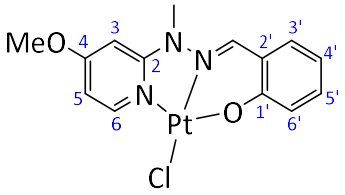

A solution of potassium tetrachloroplatinate (50 mg, 0.12 mmol) in deionised water (1.5ml) was added to a solution of L^{19} (28 mg, 0.11 mmol) in EtOH (4ml) and the resulting pale pink solution was refluxed for 4 hours. The resulting green slurry was filtered washed with water (2 x 5ml), EtOH (2 x 5ml) and Et_2O (5ml) to isolate a green solid. The crude product was then recrystallized in hot DMF to produce 17 mg of a yellow solid (0.03 mmol, 32% yield).

^{1}H NMR (DMSO-d_6, 700 MHz): 8.85 (1H, s, H^{imine}), 8.75 (1H, d, J = 7, H^3), 7.75 (1H, dd, J = 8 and 2, $H^{3'}$), 7.40 (1H, ddd, J = 8.5, 7 and 2, H^5), 7.02 (1H, d, J = 8, $H^{6'}$), 6.88 (1H, d, J = 2.5, H^6), 6.76 – 6.72 (2H, m, H^5 and $H^{4'}$), 3.94 (3H, s, H^{OMe}), 3.86 (3H, s, H^{NMe}). ^{13}C NMR (DMSO-d_6, 176 MHz): 166.8 (C^4), 159.4 ($C^{1'}$), 154.7 (C^2), 146.6 (C^3), 137.3 (C^{imine}), 133.7 ($C^{3'}$), 132.4 ($C^{5'}$), 120.5 ($C^{6'}$), 118.9 ($C^{2'}$), 115.9 ($C^{4'}$), 105.5 (C^5), 91.6 (C^6). MS (ES+): *m/z* 492 $[M+H]^+$; HRMS (ES+): *m/z* 491.0976 $[M+H]^+$; calculated for $[C_{16}H_{17}N_4O_2PtCl]^+$ 491.0978.

PtL^{20}Cl

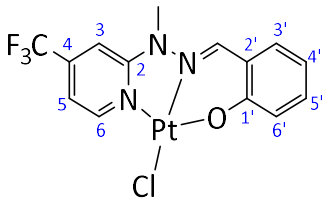

A solution of potassium tetrachloroplatinate (50 mg, 0.12 mmol) in deionised water (1.5ml) was added to a solution of L^{20} (29 mg, 0.11 mmol) in EtOH (4ml) and the resulting pale pink solution was refluxed for 4 hours. The resulting green slurry was filtered washed with water (2 x 5ml), EtOH (2 x 5ml) and Et_2O (5ml) to isolate a green solid. The crude product was then recrystallized in hot DMF to produce 22 mg of a yellow solid (0.04 mmol, 38% yield).

^{1}H NMR (DMSO-d_6, 700 MHz): 9.31 (1H, d, J = 6), 9.07 (1H, s), 7.88 (1H, s), 7.86 (1H, dd, J = 8 and 1.5), 7.48 (1H, ddd, J = 85, 7 and 2), 7.40 (1H, dd, J = 6.5 and 1.5), 7.13 (1H, d, J = 8), 6.82 (1H, t, J = 7). The material was not sufficiently soluble to obtain a ^{13}C NMR spectrum.

MS (ES+): *m/z* 530 $[M+H]^+$; HRMS (ES+): *m/z* 529.0762 $[M]^+$; calculated for $[C_{16}H_{14}N_4OF_3PtCl]^+$ 529.0746.

PtL^{14}C≡C-Ar

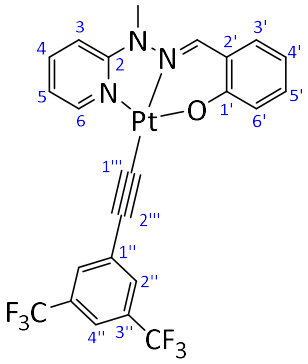

A mixture of PtL^{14}Cl (37 mg, 0.08 mmol), CuI (5 mg, 0.03 mmol), 1-ethynyl-3,5-bis(trifluoromethyl)benzene (30 mg, 0.12 mmol) and anhydrous NEt_3 (0.4ml) in anhydrous DCM (7ml) was refluxed for a period of 48 hours under argon. The resulting slurry was filtered and wash with small volumes of DCM to yield 20 mg of a bright yellow solid (0.03 mmol, 38% yield).

^{1}H NMR (DMSO-d_6, 600 MHz): 9.26 (1H, dd, J = 6 and 1, H^3), 8.91 (1H, s, H^{imine}), 8.10 (1H, ddd, J = 9, 7 and 1.5, H^5), 8.00 (2H, s, H$^{2''}$), 7.88 (1H, s, H$^{4''}$), 7.82 (1H, dd, J = 8 and 2, H$^{3'}$), 7.54 (1H, d, J = 9, H^6), 7.46 (1H, ddd, J = 8.5, 7 and 2, H$^{5'}$), 7.17 (1H, d, J = 8, H$^{6'}$), 7.08 (1H, t, J = 6.5, H^4), 6.81 (1H, t, J = 7, H$^{4'}$), 3.94 (3H, s, H^{NMe}). ^{13}C NMR (DMSO-d_6, 151 MHz): 159.8, 153.0, 149.1, 138.5, 138.4, 134.1, 132.3, 131.7, 130.5, 130.2, 124.2, 122.4, 121.1, 118.8, 116.3, 115.7, 109.1, 104.1, 33.6, 30.7, 7.2. MS (ES+): *m/z* 659 $[M+H]^+$.

PtL^{21}Cl

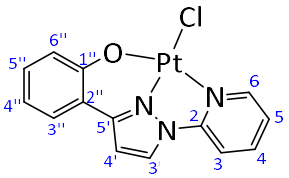

A solution of potassium tetrachloroplatinate (50 mg, 0.12 mmol) in deionised water (1.5ml) was added to a solution of L^{21} (26 mg, 0.11 mmol) in EtOH (4ml) and the resulting pale pink solution was refluxed for 4 hours. The resulting green slurry was filtered washed with water

(2 x 5ml), EtOH (2 x 5ml) and Et_2O (5ml) to isolate a green solid. The crude product was then recrystallized in hot DMF to produce 46 mg of a yellow solid (0.10 mmol, 90% yield).

^{1}H NMR (DMSO-d_6, 700 MHz): 9.42 (1H, d, J = 3, $H^{3'}$), 9.12 (1H, d, J = 6, $H^{6''}$), 8.47 (1H, ddd, J = 8, 7 and 1.5, $H^{4''}$), 8.39 (1H, d, J = 8.5, $H^{3''}$), 8.07 (1H, dd, J = 8 and 2, H^3), 7.82 (1H, d, J = 3, $H^{4'}$), 7.64 (1H, ddd, J = 7, 6 and 1, $H^{5''}$), 7.35 (1H, ddd, J = 8.5, 7 and 2, H^5), 7.18 (1H, dd, J = 8.5 and 1, H^6), 6.85 (1H, ddd, J = 8, 7 and 1, H^4). ^{13}C NMR (DMSO-d_6, 176 MHz): 159.6 (C^2), 148.3 ($C^{6''}$), 147.8 ($C^{1''''}$), 141.2 ($C^{2''}$), 140.6 ($C^{4''}$), 130.9 ($C^{3'}$), 130.6 (C^5), 128.3 (C^3), 122.8 ($C^{5''}$), 121.8 (C^6), 116.0 (C^4), 113.4 ($C^{5'}$), 111.5 ($C^{3''}$), 105.7 ($C^{4'}$). MS (ASAP): *m/z* 467 $[M+H]^+$.

a-PtL^{22}Cl and b-PtL^{22}Cl

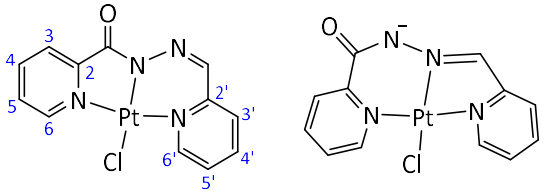

a-PtL^{22}Cl **b-PtL^{22}Cl**

A solution of L^{22} (91 mg, 0.4 mmol), $Pt(COD)Cl_2$ (150 mg, 0.4 mmol) and NEt_3 (41 mg, 0.4 mmol) in MeCN (6ml) was refluxed under argon for a period of 48 hours. The resulting dark red mixture was filtered to yield 143 mg of a purple solid. The crude material was separated by column chromatography (5% MeOH in DCM) to yield 51 mg (0.11 mmol, 28% yield) of a-PtL^{22}Cl and 27 mg (0.06 mmol, 15% yield) of b-PtL^{22}Cl.

a-PtL^{22}Cl: ^{1}H NMR (DMSO-d_6, 600 MHz): 10.0 (1H, d, J = 6, $H^{6'}$), 9.39 (1H, d, J = 6, H^6), 8.29 – 8.26 (2H, m, H^4 and $H^{4'}$), 7.98 (1H, dd, J = 8 and 1, $H^{3'}$), 7.89 (1H, dd, J = 8 and 1, H^3), 7.81 (1H, ddd, J = 7.5, 6 and 1.5, H^5), 7.73 (1H, s, H^{imine}), 7.55 (1H, ddd, J = 7, 6 and 1.5, $H^{5'}$). ^{13}C NMR (DMSO-d_6, 151 MHz): 170.3 ($C^{C=O}$), 151.9 ($C^{6'}$), 149.4 ($C^{2'}$), 149.3 (C^6), 141.7 ($C^{4'}$ or C^4), 140.1 ($C^{4'}$ or C^4), 136.7 (C^2), 136.7 (C^{imine}), 129.6 (C^3), 129.1 (C^5), 126.3 ($C^{3'}$), 124.9 ($C^{5'}$). MS (ES+): *m/z* 457 $[M+H]^+$

b-PtL^{22}Cl: ^{1}H NMR ($CDCl_3$, 400 MHz): 9.97 (1H, dd, J = 6 and 1.5), 9.39 (1H, d, J = 6), 9.04 (1H, dd, J = 8.5 and 2), 8.36 (1H, s), 8.10 (1H, dt, J = 8 and 2), 7.90 (1H, dt, J = 8 and 1.5), 7.50 – 7.44 (2H, m), 7.32 (1H, ddd, J = 8, 6 and 1.5). The material was not sufficiently soluble to obtain a ^{13}C NMR spectrum. MS (ES+): *m/z* 457 $[M+H]^+$

PtL^{23}Cl

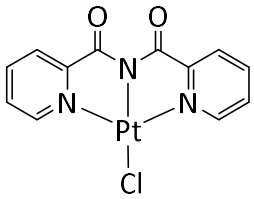

$Pt(COD)Cl_2$ (83 mg, 0.22 mmol) and NEt_3 (22 mg, 0.22 mmol) was added to a stirring solution of L^{23} (50 mg, 0.22 mmol) in MeCN (2ml) and the resulting yellow solution was stirred overnight at 60°C under argon. The resulting yellow slurry was filtered and washed with MeCN to yield 65 mg of a bright yellow solid (0.14 mmol, 64% yield). The experimental data obtained were in accord with that reported in literature.[143]

PtL^{24}Cl

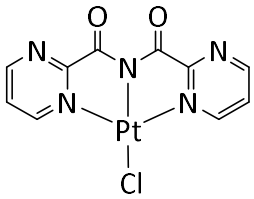

L^{24} (150 mg, 0.65 mmol) and K_2PtCl_4 (272 mg, 0.65 mmol) were stirred in DMF (10ml) at 60°C for a period of 24 hours. The resulting orange slurry was filtered and the filtrates were diluted with H_2O and extracted into DCM. The solvent was removed in vacuo to yield the crude product. The dark orange solid was recrystallized in DMSO to yield 10 mg of a yellow solid (0.02 mmol, 3% yield).

^1H NMR (DMSO-d_6, 700 MHz): 9.32 (2H, m), 7.96 (4H, m). The material was not sufficiently soluble to obtain a ^{13}C NMR spectrum. MS (ES+): *m/z* 459 $[M+H]^+$.

PtL^{25}Cl

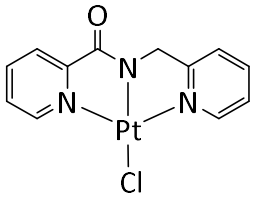

$Pt(COD)Cl_2$ (53 mg, 0.14 mmol) and NEt_3 (14 mg, 0.14 mmol) was added to a stirring solution of L^{25} (30 mg, 0.14 mmol) in MeCN (2ml) and the resulting yellow solution was stirred overnight at 60°C under argon. The resulting yellow slurry was filtered and washed with MeCN to yield 24mg of a bright yellow solid (0.06 mmol, 41% yield).

^{1}H NMR ($CDCl_3$, 700 MHz): 9.13 (1H, d, J = 5.5, $H^{6'}$), 9.02 (1H, d, J = 5.5, H^6), 8.02 (1H, td, J = 8 and 1.5, H^5), 7.94 (1H, td, J = 8 and 1.5, $H^{5'}$), 7.81 (1H, d, J = 8, H^3), 7.48 (1H, ddd, J = 8, 5.5 and 2, H^4), 7.42 (1H, d, J = 8, $H^{3'}$), 7.30 (1H, t, J = 7, $H^{4'}$), 5.07 (2H, s, H^{CH_2}). ^{13}C NMR ($CDCl_3$, 176 MHz): 169.5 ($C^{2'}$), 168.4 ($C^{C=O}$), 157.9 (C^2), 150.0 ($C^{6'}$), 149.5 (C^6), 139.9 (C^5), 138.7 ($C^{5'}$), 127.2 (C^4), 125.7 (C^3), 123.7 ($C^{9'}$), 122.3 ($C^{3'}$), 55.0 (C^{CH_2}). MS (ES+): *m/z* 443 $[M+H]^+$; HRMS (ES+): *m/z* 442.0227 $[M+H]^+$; calculated for $[C_{12}H_{11}N_3OPtCl]^+$ 442.0217.[214]

PtL^{27}

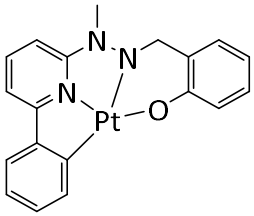

A mixture of L^{27} (30 mg, 0.10 mmol) and K_2PtCl_4 (46 mg, 0.11 mmol) in acetic acid (2ml) was degassed via three freeze-pump-thaw cycles and the resulting mixture was refluxed for 5 days before cooling to ambient temperature. The resulting green-yellow slurry was filtered to yield 15 mg of a green-yellow solid (0.03 mmol, 30% yield).

^{1}H NMR (DMSO-d_6, 700 MHz): 8.94 (1H, s), 8.03 (1H, dd, J = 8.5 and 7.5), 7.79 – 7.76 (2H, m), 7.56 – 7.53 (2H, m), 7.44 (1H, ddd, J = 8.5, 6.5 and 2), 7.31 – 7.26 (3H, m), 7.11 (1H, td, J = 7.5 and 1), 6.77 (1H, ddd, J = 8, 7 and 1), 3.94 (3H, s). The material was not sufficiently soluble to obtain a ^{13}C NMR spectrum. MS (ES+): *m/z* 497 $[M]^+$.

PtL[29]Cl

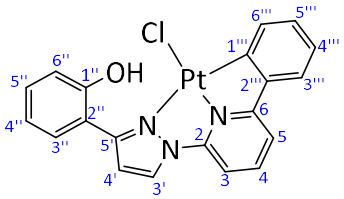

A mixture of L^{29} (137 mg, 0.44 mmol) and K_2PtCl_4 (200 mg, 0.48 mmol) in an acetic acid and water mix (3ml, 9:1) was degassed via 3 freeze-pump-thaw cycles. The resulting slurry was sealed in a microwave vial and heated to 160°C for 3 hours. The product was isolated via centrifuge and washed with H_2O, EtOH and Et_2O to yield 185 mg of a green solid (0.34 mmol, 71% yield).

^{1}H NMR (DMSO-d_6, 700 MHz): 9.98 (1H, s, H^{OH}), 9.08 (1H, d, J = 3, $H^{3'}$), 8.23 (1H, t, J = 8, H^4), 7.95 (1H, d, J = 8, H^3), 7.83 (1H, d, J = 8, H^5), 7.66 (1H, dd, J = 7.5 and 1.5, $H^{6''}$), 7.63 (1H, dd, J = 8 and 1, $H^{3'''}$), 7.60 (1H, dd, J = 7.5 and 1, $H^{6'''}$), 7.25 (1H, ddd, J = 8, 7 and 1.5, $H^{4''}$), 7.14 (1H, d, J = 3, $H^{4'}$), 7.12 (1H, td, J = 7 and 1, $H^{5'''}$), 7.07 (1H, td, J = 7.5 and 1, $H^{4'''}$), 6.92 (1H, dd, J = 8 and 0.5, $H^{3''}$), 6.83 (1H, td, J = 7.5 and 1, $H^{5''}$). ^{13}C NMR (DMSO-d_6, 176 MHz): 163.1 (C^2), 155.6 ($C^{1''}$), 155.5 ($C^{5'}$), 148.1 (C^6), 145.5 ($C^{1'''}$), 140.9 (C^4), 137.2 ($C^{2'''}$), 133.2 ($C^{6'''}$), 132.9 ($C^{6''}$), 132.3 ($C^{3'}$), 131.1 ($C^{4''}$), 129.7 ($C^{5'''}$), 124.7 ($C^{3'''}$), 123.7 ($C^{4'''}$), 118.5 ($C^{5''}$), 115.6 ($C^{2''}$), 115.2 (C^5), 115.1 ($C^{3''}$), 112.5 ($C^{4'}$), 107.6 (C^3). MS (ES+): *m/z* 543 $[M+H]^+$.

PtL[30]Cl

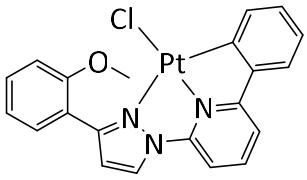

A mixture of L^{30} (36 mg, 0.11 mmol) and K_2PtCl_4 (20 mg, 0.12 mmol) in acetic acid (2ml) was degassed via three freeze-pump-thaw cycles and the resulting mixture was refluxed for 3 days before cooling to ambient temperature. The resulting green-yellow slurry was filtered to yield 17 mg of a green-yellow solid (0.03 mmol, 28% yield).

^{1}H NMR (DMSO-d_6, 400 MHz): 9.13 (1H, d, J = 3), 8.27 (1H, t, J = 8), 7.98 (1H, d, J = 8), 7.87 (1H, d, J = 7.5), 7.66 (1H, dd, J = 7 and 1.5), 7.63 (1H, dd, J = 7.5 and 2), 7.58 (1H, dd, J = 8 and 1), 7.45 (1H, ddd, J = 8, 7.5 and 2), 7.18 – 7.06 (4H, m), 7.02 (1H, td, J = 7.5 and 1), 3.83 (3H, s). ^{13}C NMR (DMSO-d_6, 101 MHz): 163.2, 157.2, 148.2, 145.6, 141.0, 133.3, 132.6,

132.5, 131.4, 129.8, 124.8, 123.8, 119.9, 117.4, 115.4, 112.4, 110.9, 107.8, 55.5. MS (ES+): *m/z* 558 $[M+H]^+$.

PtL^{31}Cl

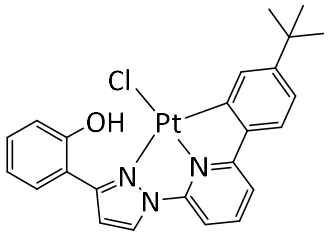

A mixture of L^{31} (55 mg, 0.15 mmol) and K_2PtCl_4 (75 mg, 0.18 mmol) in acetic acid (3ml) was degassed via three freeze-pump-thaw cycles and the resulting mixture was refluxed for 3 days before cooling to ambient temperature. The resulting green-yellow slurry was filtered to yield 8 mg of a yellow solid (0.01 mmol, 9% yield).

^{1}H NMR (DMSO-d_6, 400 MHz): 10.01 (1H, s), 9.10 (1H, d, J = 3), 8.23 (1H, t, J = 8), 7.94, (1H, d, J = 8), 7.80 (1H, d, J = 8), 7.72 – 7.70 (2H, m), 7.56 (1H, d, J = 8), 7.27 (1H, ddd, J = 8, 7.5 and 2), 7.17 (1H, d, J = 3), 7.13 (1H, dd, J = 8 and 2), 6.94 (1H, dd, J = 8 and 1), 6.85 (1H, td, J = 7.5 and 1), 1.27 (9H, s). Insufficient material was produced to obtain a ^{13}C NMR spectrum. ASAP: *m/z* 563 $[M-Cl]^+$.

PtL^{32}Cl

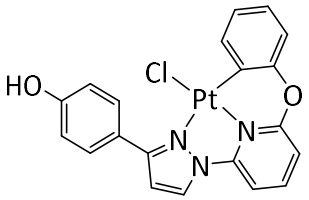

A mixture of L^{32} (28 mg, 0.09 mmol) and K_2PtCl_4 (42 mg, 0.10 mmol) in acetic acid (3ml) was degassed via three freeze-pump-thaw cycles and the resulting mixture was refluxed for 3 days before cooling to ambient temperature. The resulting green slurry was filtered to yield 7 mg of a green-yellow solid (0.01 mmol, 14% yield).

^{1}H NMR (DMSO-d_6, 400 MHz): 9.81 (1H, s), 9.22 (1H, d, J = 3), 8.42 (1H, t, J = 8), 8.13 (1H, d, J = 8), 8.03 (1H, d, J = 8), 7.42 (1H, d, J = 7.5), 7.37 (1H, d, J = 8.5), 7.26 (1H, t, J = 8), 7.06 –

7.04 (3H, m), 6.91 – 6.86 (2H, m), 6.82 (1H, t, J = 7.5). Insufficient material was produced to obtain a ^{13}C NMR spectrum. ASAP: *m/z* 524 $[M\text{-}Cl]^+$.

[Ir(dpyx)L^{14}]PF$_6$

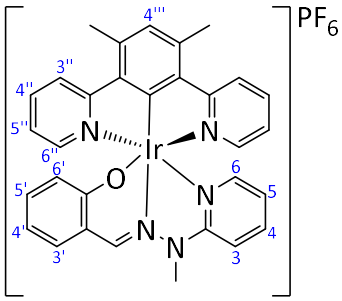

A mixture of L^{14} (24 mg, 0.11 mmol) and $[Ir(dpyx)Cl(\mu\text{-}Cl)_2]_2$ (50 mg, 0.05 mmol) in ethylene glycol (1.5ml) was heated to 195°C for 90 mins under argon. The resulting brown slurry was diluted with H_2O (2ml) and pipetted into sat. aq. KPF_6 to produce a bright yellow solid. The crude product was isolated by centrifuge and washed with H_2O. The crude product was recrystallized in acetone/hexane to yield 31 mg of a bright yellow solid (0.04 mmol, 34% yield).

^1H NMR (DMSO-d_6, 700 MHz): 9.01 (1H, s), 8.21 (2H, d, J = 2.5, $H^{6''}$), 7.87 (2H, t, J = 8, $H^{5''}$), 7.79 – 7.78 (3H, m, $H^{3''}$ or H^3), 7.64 (1H, ddd, J = 9, 7 and 1.5, $H^{4'}$), 7.48 (1H, d, J = 9, $H^{3'}$), 7.15 (1H, s, $H^{4'''}$), 7.11 (2H, t, J = 6.5, $H^{4''}$), 7.00 (1H, ddd, J = 8, 7 and 2, H^5), 6.86 (1H, d, J = 6, $H^{6'}$), 6.62 (1H, t, J = 7, H^4), 6.57 (1H, t, J = 7), 6.43 (1H, d, J = 8.5), 4.20 (3H, s, H^{NMe}), 2.85 (6H, s, H^{Me}). ^{13}C NMR (DMSO-d_6, 176 MHz): 178.7, 168.9, 160.8, 154.5, 150.4, 149.6, 139.8, 139.2, 138.0, 137.9, 137.6, 135.0, 131.5, 131.4, 123.8, 123.2, 121.8, 119.5, 116.6, 115.1, 109.3, 33.7, 21.9. MS (ES+): *m/z* 678 $[M]^+$.

[Ir(dpyx)L^{15}]PF$_6$

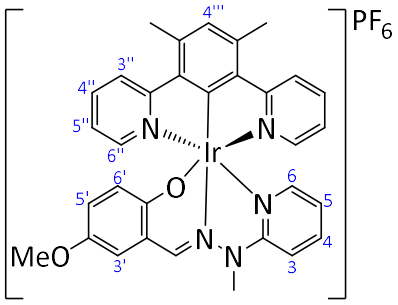

A mixture of L^{15} (25 mg, 0.11 mmol) and [Ir(dpyx)Cl(μ-Cl)$_2$]$_2$ (50 mg, 0.05 mmol) in ethylene glycol (1.5ml) was heated to 195°C for 90 mins under argon. The resulting brown slurry was diluted with H_2O (2ml) and pipetted into sat. aq. KPF_6 to produce a bright yellow solid. The crude product was isolated by centrifuge and washed with H_2O. The crude product was recrystallized in MeCN/Et_2O to yield 55 mg of a bright yellow solid (0.06 mmol, 59% yield). ^{1}H NMR (CD_3CN, 700 MHz): 8.83 (1H, s, H^{imine}), 8.21 (1H, d, J = 2, H$^{6''}$), 7.79 (2H, ddd, J = 9, 7 and 2, H$^{5''}$), 7.68 (2H, ddd, J = 6, 2 and 1, H$^{3''}$), 7.58 – 7.56 (1H, m, H^5), 7.24 (1H, d, J = 3, H$^{3'}$), 7.19 (1H, d, J = 9, H^6), 7.16 (1H, s, H$^{4'''}$), 7.01 (2H, ddd, J = 7.5, 6 and 1, H$^{4''}$), 6.99 (1H, ddd, J = 6, 2 and 1, H^3), 6.77 (1H, dd, J = 9 and 3, H$^{5'}$), 6.47 (1H, ddd, J = 7, 6 and 1, H^4), 6.39 (1H, d, J = 9, H$^{6'}$), 4.11 (3H, s, H^{NMe}), 3.77 (3H, s, H^{OMe}), 2.88 (6H, s, H^{Me}). ^{13}C NMR (CD_3CN, 176 MHz): 179.6, 170.6, 157.3, 156.0, 151.4, 151.3, 150.7, 140.6, 139.7, 139.5, 139.0, 138.7, 125.0, 123.8, 123.4, 122.4, 119.3, 117.5, 116.4, 110.1, 56.5, 34.7, 22.5. MS (ES+): *m/z* 708 [M]$^+$; HRMS (ES+): *m/z* 706.1912 [M]$^+$; calculated for [$C_{32}H_{29}N_5O_2Ir$]$^+$ 706.1927.

[Ir(dpyx)L^{16}]PF$_6$

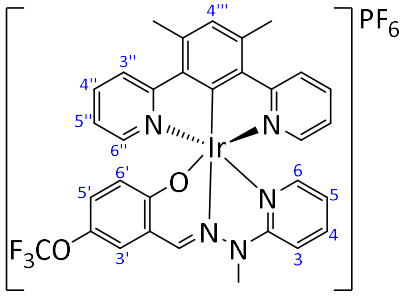

A mixture of L^{16} (30 mg, 0.11 mmol) and [Ir(dpyx)Cl(μ-Cl)$_2$]$_2$ (50 mg, 0.05 mmol) in ethylene glycol (1.5ml) was heated to 195°C for 90 mins under argon. The resulting brown slurry was diluted with H_2O (2ml) and filtered to yield a mustard yellow solid. The crude product was dissolved in hot DMSO and pipetted into sat. aq. KPF_6 to produce a bright yellow solid. The

crude product was isolated by centrifuge and washed with H_2O to yield 47 mg of a bright yellow solid (0.05 mmol, 47% yield).

^{1}H NMR (CD_3CN, 700 MHz): 8.81 (1H, s, H^{imine}), 8.23 (2H, d, J = 8.5, $H^{6''}$), 7.82 (2H, ddd, J = 8, 7.5 and 1.5, $H^{5''}$), 7.70 – 7.68 (3H, m, $H^{3'}$ and $H^{3''}$), 7.80 (1H, ddd, J = 8.5, 7 and 1.5, H^5), 7.22 (1H, d, J = 9, H^6), 7.18 (1H, s, $H^{4'''}$), 7.05 – 7.00 (4H, m, H^3, $H^{5'}$ and $H^{4''}$), 6.50 (1H, ddd, J = 8, 6 and 1, H^4), 6.47 (1H, d, J = 9, $H^{6'}$), 4.11 (3H, s, H^{NMe}), 2.89 (6H, s, H^{Me}). ^{13}C NMR (CD_3CN, 176 MHz): 177.7, 169.5, 159.9, 150.4, 139.8, 138.8, 138.0, 137.9, 137.8, 131.8, 126.1, 125.0, 124.1, 122.9, 119.3, 117.5, 117.3, 109.4, 33.8, 21.5. MS (ES+): *m/z* 762 $[M]^+$; HRMS (ES+): *m/z* 760.1632 $[M]^+$; calculated for $[C_{32}H_{26}N_5O_2F_3Ir]^+$ 760.1645.

[Ir(dpyx)L^{16}]PF$_6$

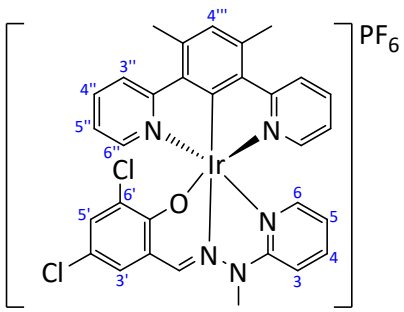

A mixture of L^{17} (12 mg, 0.04 mmol) and $[Ir(dpyx)Cl(\mu\text{-}Cl)_2]_2$ (20 mg, 0.02 mmol) in ethylene glycol (1.5ml) was heated to 195°C for 90 mins under argon. The resulting brown slurry was diluted with H_2O (2ml) and filtered to yield a mustard yellow solid. The crude product was dissolved in hot DMSO and pipetted into sat. aq. KPF_6 to produce a bright yellow solid. The crude product was isolated by centrifuge and washed with H_2O to yield 18 mg of a bright yellow solid (0.02 mmol, 99% yield).

^{1}H NMR (DMSO-d_6, 600 MHz): 9.10 (1H, s, H^{imine}), 8.24 (2H, d, J = 8, $H^{6''}$), 7.98 (1H, d, J = 3, $H^{5'}$), 7.92 (2H, t, J = 8, $H^{5''}$), 7.83 (2H, dd, J = 6 and 1, $H^{3''}$), 7.70 (1H, ddd, J = 9, 7 and 1.5, H^5), 7.55 (1H, d, J = 9, H^6), 7.35 (1H, d, J = 3, $H^{3'}$), 7.18 (1H, s, $H^{4'''}$), 7.15 (1H, ddd, J = 7.5, 6 and 1, $H^{4''}$), 6.85 (1H, dd, J = 6 and 1, H^3), 6.65 (1H, t, J = 7, H^4), 4.21 (3H, s, H^{NMe}), 2.88 (6H, s, H^{Me}). ^{13}C NMR (DMSO-d_6, 151 MHz): 177.7, 168.8, 154.7, 153.9, 150.6, 149.6, 140.1, 138.3, 128.1, 138.0, 137.4, 132.4, 131.8, 130.1, 126.3, 123.8, 123.3, 121.7, 118.1, 117.2, 117.1, 109.6, 34.0, 30.7, 21.9. MS (ES+): *m/z* 746 $[M]^+$; HRMS (ES+): *m/z* 744.1039 $[M]^+$; calculated for $[C_{31}H_{25}N_5O_2Cl_2Ir]^+$ 744.1042.

6.3 Synthesis: Chapter 5

a-PtCl(μ-L^{22})RuCl$_2$(PPh$_3$)$_2$

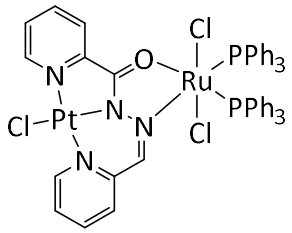

A solution of a-PtL^{22}Cl (20 mg, 0.04 mmol) and $RuCl_2(PPh_3)_3$ (42 mg, 0.04 mmol) in DCM (7ml) was stirred for 4 hours. The solution was reduced to approximately 2.5ml and hexane (9ml) was added to cause precipitation. The slurry was filtered to yield 41 mg of a dark green solid (0.03 mmol, 75%).

^{1}H NMR ($CDCl_3$, 600 MHz): 10.06 (1H, d, J = 6.5), 9.41 (1H, d, J = 6), 7.92 (1H, td, J = 8 and 1), 7.85 (1H, d, J = 3), 7.71 (1H, td, J = 7.5 and 1), 7.67 – 7.64 (6H, m), 7.55 (1H, d, J = 8), 7.49 (1H, ddd, J = 7.5, 5.5 and 1), 7.47 – 7.43 (6H, m), 7.25 – 7.22 (6H, m), 7.20 (1H, ddd, J = 7, 6 and 1.5), 7.16 – 7.13 (6H, m), 7.06 – 7.02 (6H, m), 6.13 (1H, d, J = 8). The material was not sufficiently stable in solution to obtain a ^{13}C spectrum. MS (ES+): *m/z* 1117 $[M(-Cl)+H]^+$; HRMS (ES+): *m/z* 1112.0632 $[M(-Cl)]^+$; calculated for $[C_{48}H_{39}N_4OP_2Cl_2RuPt]^+$ 1112.0662. Anal. Calcd for $C_{48}H_{39}N_4OP_2Cl_3RuPt$: C, 49.21; H, 3.42; N, 5.12. Found: C, 50.03; H, 3.41; N, 4.86.

[a-PtCl(μ-L^{22})Ir(ppy)$_2$]PF$_6$

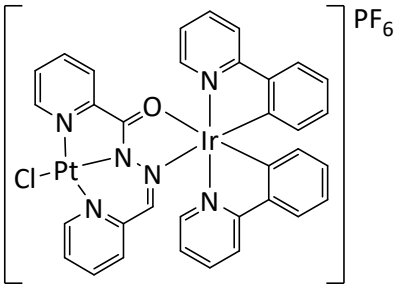

$[Ir(ppy)_2Cl]_2$ (12 mg, 0.011 mmol) and a-PtL^{22}Cl (10 mg, 0.022 mmol) were heated to 65°C in a MeOH:DCM (1.2:1, 2.2ml) mixture for a period of two hours. The solvent was removed in vacuo and the residue dissolved in the minimum amount of MeCN/H_2O mix. The solution was pipetted into sat. aq. H_2O, centrifuged and washed with H_2O to isolate 20 mg of a green solid (0.018, 82% yield).

^{1}H NMR ($(CD_3)_2CO$, 600 MHz): 10.17 (1H, dd, J = 8 and 1.5), 9.54 (1H, ddd, J = 6, 1.5 and 0.5), 8.80 (1H, ddd, J = 6, 1.5 and 1), 8.67 (1H, ddd, J = 6, 1.5 and 1), 8.39 (1H, td, J = 8 and 1.5), 8.29 (1H, td, J = 8 and 1.5), 8.27 – 8.25 (2H, m), 8.22 (1H, dd, J = 8 and 1.5), 8.07 – 8.04 (2H, m), 8.01 (1H, ddd, J = 8, 6 and 1.5), 7.85 (2H, td, J = 8 and 1), 7.73 (1H, ddd, J = 7.5, 6 and 1.5), 7.48 (1H, dd, J = 8 and 1.5), 7.39 (1H, ddd, J = 7, 6 and 1.5), 7.34 (1H, ddd, J = 7.5, 6 and 1.5), 7.30 (1H, s), 7.01 (1H, td, J = 7.5 and 1), 6.97 (1H, td, J = 7.5 and 1), 6.87 (1H, td, J = 7.5 and 1), 6.83 (1H, td, J = 7.5 and 1), 6.32 (1H, dd, J = 8 and 1), 6.18 (1H, dd, J = 7.5 and 1). ^{13}C NMR ($(CD_3)_2CO$, 151 MHz): 167.8, 166.9, 158.3, 153.4, 150.9, 150.2, 149.3, 147.9, 147.6, 144.9, 144.0, 142.3, 140.9, 139.8, 139.2, 139.0, 133.0, 132.4, 131.7, 130.3, 130.1, 129.5, 128.0, 127.8, 124.9, 124.4, 123.5, 122.7, 122.5, 119.9, 119.6. MS (ES+): *m/z* 956 $[M]^+$; HRMS (ES+): *m/z* 955.1071 $[M]^+$; calculated for $[C_{34}H_{25}N_6OClPtIr]^+$ 955.1033

$[PtCl(\mu\text{-}L^{25})Ir(ppy)_2]PF_6$

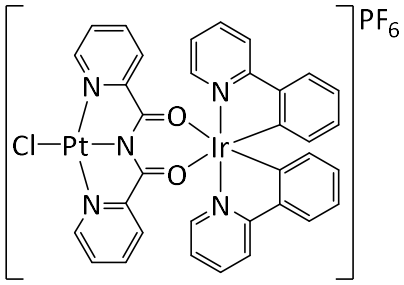

$[Ir(ppy)_2Cl]_2$ (12 mg, 0.011 mmol) and PtL^2Cl (10 mg, 0.022 mmol) were heated to 65°C in a MeOH:DCM (1.2:1, 2.2ml) mixture for a period of two hours. The solvent was removed in vacuo and the residue dissolved in the minimum amount of hot DMSO. The solution was pipetted into sat. aq. H_2O, centrifuged and washed with H_2O to isolate 5 mg of a yellow solid (0.004, 21% yield).

^{1}H NMR (DMSO-d_6, 400 MHz): 9.50, 6.06, 8.45 – 8.40, 8.28, 8.02, 7.94 – 7.89, 7.71, 7.06, 6.92, 5.92. The material was not sufficiently soluble to obtain a ^{13}C NMR spectrum. MS (ES+): *m/z* 956 $[M]^+$; HRMS (ES+): *m/z* 954.0870 $[M]^+$; calculated for $[C_{34}H_{24}N_5O_2ClPtIr]^+$ 954.0851.

4,6-di(1-methylhydrazino)pyrimidine

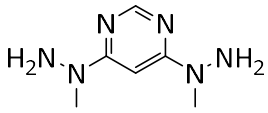

4,6-Dichloropyrimidine (720 mg, 4.83 mmol) was stirred in methylhydrazine (10ml) at reflux under argon for 2 hours. The resulting solution was diluted with 20ml water and the product extracted into DCM. The organic layer was dried over $MgSO_4$ and the solvent removed in vacuo to yield 702 mg of a cream solid (4.17 mmol, 86% yield). The experimental data obtained were in accord with that reported in literature.[189]

H_2L^{36}

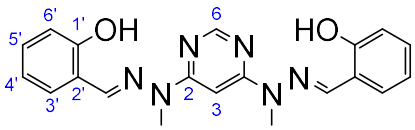

Salicylaldehyde (254 mg, 2.08 mmol) was added slowly to a solution of 4,6-di(1-methylhydrazino)pyrimidine (175 mg, 1.04 mmol) in MeOH (5ml). The yellow solution was stirred under argon at reflux for 1 hour before cooling to ambient temperature. The resulting lemon slurry was filtered and washed with cold methanol to yield 295 mg of a cream powder (0.78 mmol, 75% yield).

^{1}H NMR ($CDCl_3$, 700 MHz): 10.98 (2H, s, H^{OH}), 8.48 (1H, s, H^6), 7.90 (2H, s, H^{imine}), 7.28-7.26 (4H, m, $H^{3'}$ + $H^{4'}$), 7.04 (2H, d, J = 9, $H^{6'}$), 6.91 (2H, td, J = 7.5 and 1, $H^{5'}$), 6.80 (1H, s, H^3), 3.66 (6H, s, H^{NMe}). ^{13}C NMR ($CDCl_3$, 176 MHz): 162.0 (C^6), 157.6 ($C^{1'}$), 157.3 (C^6), 141.6 (C^{imine}), 130.7 ($C^{3'}$ and $C^{4'}$), 119.5 ($C^{5'}$), 118.8 ($C^{2'}$), 117.1 ($C^{6'}$), 85.7 (C^3), 30.0 (C^{NMe}). MS (ES-): *m/z* 375 $[M-H]^-$; HRMS (ES-): *m/z* 375.1583 $[M-H]^-$; calculated for $[C_{20}H_{19}N_6O_2]^+$ 601.4230.

H_2L^{37}

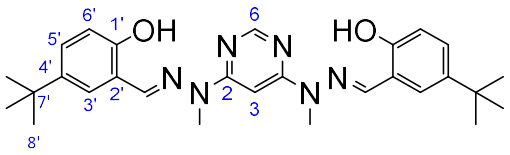

5-tert-Butyl-2-hydroxybenzaldehyde (210 mg, 1.18 mmol) was added slowly to a stirring solution of 4,6-di(1-methylhydrazino)pyrimidine (100 mg, 0.59 mmol) in MeOH (6ml). The yellow solution was stirred under argon at reflux for 1 hour before cooling to ambient temperature. The resulting lemon slurry was filtered and washed with cold methanol to yield 247 mg of a cream powder (0.51 mmol, 86% yield).

^{1}H NMR ($CDCl_3$, 700 MHz): 10.80 (2H, s, H^{OH}), 8.49 (1H, d, J = 7, H^6), 7.96 (2H, s, H^{imine}), 7.31 (2H, dd, J = 8.5 and 2.5, $H^{5'}$), 7.27 (1H, s, $H^{3'}$), 6.98 (2H, d, J = 9, $H^{6'}$), 6.84 (1H, d, J = 1, H^3), 3.70 (6H, s, H^{NMe}), 1.33 (18H, s, $H^{t\text{-}butyl}$). ^{13}C NMR ($CDCl_3$, 176 MHz): 162.1 (C^2), 155.4 (C^6), 142.3 ($C^{1'}$), 142.2 (C^{imine}), 128.2 ($C^{5'}$), 127.3 ($C^{3'}$), 125.3 ($C^{4'}$), 118.0 ($C^{2'}$), 116.7 ($C^{6'}$), 85.79 (C^3), 34.2 ($C^{7'}$), 31.6 ($C^{t\text{-}butyl}$), 30.1 (C^{NMe}). MS (ES+): *m/z* 489 $[M+H]^+$

H_2L^{38}

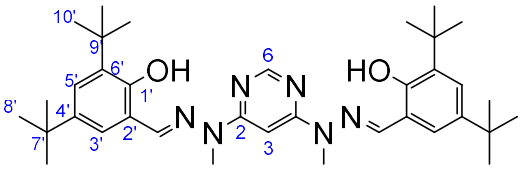

3,5-di-tert-Butyl-2-hydroxybenzaldehyde (84 mg, 0.36 mmol) was added slowly to a stirring solution of 4,6-di(1-methylhydrazino)pyrimidine (30 mg, 0.18 mmol) in MeOH (1ml). The yellow solution was stirred under argon at reflux for 1 hour before cooling to ambient temperature. The resulting lemon slurry was filtered and washed with cold methanol to yield 68mg of a white powder (0.11 mmol, 61% yield).

^{1}H NMR ($CDCl_3$, 700 MHz): 11.50 (2H, s, H^{OH}), 8.54 (1H, s, H^3), 7.99 (2H, s, H^{imine}), 7.33 (2H, d, J = 2.5, $H^{5'}$), 7.11 (2H, d, J = 2.5, $H^{3'}$), 6.78 (1H, s, H^6), 3.67 (6H, s, H^{NMe}), 1.41 (18H, s, $H^{8'}$), 1.33 (18H, s, $H^{10'}$). ^{13}C NMR ($CDCl_3$, 176 MHz): 162.2 (C^2), 157.6 (C^6), 154.5 ($C^{1'}$), 143.6 (C^{imine}), 140.9 ($C^{4'}$), 136.8 ($C^{6'}$), 125.8 ($C^{5'}$), 125.5 ($C^{3'}$), 117.9 ($C^{2'}$), 86.2 (C^3), 35.3 ($C^{9'}$), 34.3

($C^{7'}$), 31.7 ($C^{10'}$), 30.4 (C^{NMe}), 29.8 ($C^{8'}$). MS (ES+): *m/z* 601 $[M+H]^+$; HRMS (ES+): *m/z* 601.4253 $[M+H]^+$; calculated for $[C_{36}H_{53}N_6O_2]^+$ 601.4230.

PtHL^{36}Cl

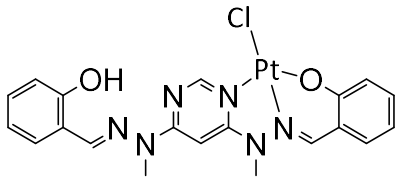

H_2L^{36} (44 mg, 0.12 mmol), $Pt(COD)Cl_2$ (110 mg, 0.29 mmol) and NEt_3 (24 mg, 0.23 mmol) were refluxed in MeCN (4 ml) for a period of 24 hours under argon. The slurry was allowed to cool to ambient temperature before being filtered. The crude material was suspended in MeCN (2ml) at reflux for one hour before hot filtration to yield 17 mg of a yellow-green solid (0.028 mmol, 24% yield).

^{1}H NMR (DMSO-d_6, 700 MHz): 9.03 (1H, s), 8.95 (1H, s), 8.33 (1H, s), 8.04 (1H, d, J = 7), 7.80 (1H, d, J = 8), 7.43 (1H, ddd, J = 9, 7 and 1.5), 7.28 (1H, ddd, J = 8, 7 and 1.5), 7.04 (1H, d, J = 8), 7.00 (1H, s), 6.95 – 6.92 (2H, m), 6.76 (1H, t, J = 7), 3.89 (3H, s), 3.69 (3H, s). The material was not sufficiently soluble to obtain a ^{13}C NMR spectrum. MALDI-TOF: *m/z* 606 $[M+H]^+$.

[Ir(dpyx)HL^{36}]PF$_6$

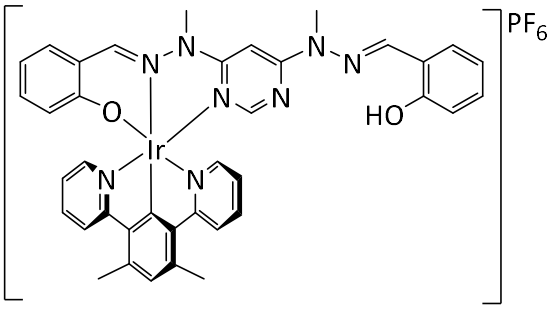

H_2L^{36} (36 mg, 0.096 mmol) and $[Ir(dpyx)Cl(\mu\text{-}Cl]_2$ (50 mg, 0.048 mmol) were heated to 195°C in ethylene glycol (1.5ml) for 90 minutes under argon. The resulting slurry was allowed to cool to ambient temperature before adding 5ml H_2O and filtering to obtain an orange-brown solid. The crude material was dissolved in the minimum volume of hot DMSO,

pippeted into sat. aq. H_2O, centrifuged and washed with H_2O to yield 22 mg of a yellow solid (0.023 mmol, 24% yield).

^{1}H NMR (CD_3CN, 700 MHz): 10.41 (1H, s), 8.90 (1H, s), 8.25 (2H, d, J = 9), 8.16 (1H, s), 7.85 – 7.82 (4H, m), 7.72 (1H, dd, J = 8 and 1.5), 7.51 (1H, d, J = 8), 7.34 (1H, t, J = 8), 7.18 (1H, s), 7.11 – 7.06 (4H, m), 7.00 – 6.98 (2H, m), 6.69 (1H, t, J = 7), 6.62 (1H, s), 6.42 (1H, d, J = 8), 4.10 (3H, s), 3.48 (3H, s), 2.91 (6H, s). ^{13}C NMR (CD_3CN, 176 MHz): 179.7, 178.0, 175.0, 170.7, 162.8, 159.1, 158.1, 151.6, 141.1, 140.6, 139.8, 139.0, 136.2, 133.5, 132.5, 131.9, 125.1, 123.8, 123.0, 120.9, 120.5, 119.8, 118.3, 117.4, 116.8, 85.1, 41.4, 33.9, 30.6, 22.5. MS (ES+): *m/z* 827 $[M+H]^+$.

$[Ir(dpyx)HL^{37}]PF_6$

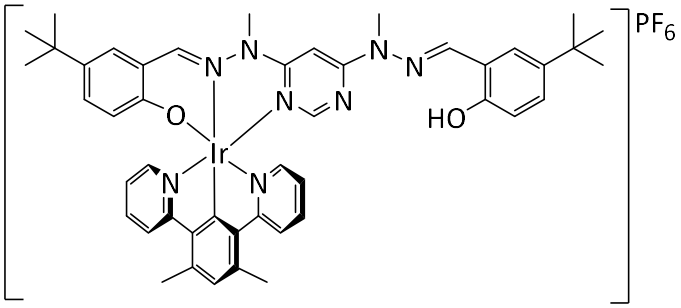

H_2L^{37} (90 mg, 0.184 mmol) and $[Ir(dpyx)Cl(\mu\text{-}Cl]_2$ (87 mg, 0.084 mmol) were heated to 195°C in ethylene glycol (1.5ml) for 90 minutes under argon. The resulting slurry was allowed to cool to ambient temperature before adding 5ml H_2O and filtering to obtain an orange-brown solid. The crude material was dissolved in the minimum volume of hot DMSO, pippeted into sat. aq. H_2O, centrifuged and washed with H_2O to yield 64 mg of a yellow solid (0.059 mmol, 32% yield).

^{1}H NMR (CD_3CN, 700 MHz): 10.29 (1H, s), 8.92 (1H, s), 8.23 (2H, d, J = 8), 8.14 (1H, s), 7.83 – 7.80 (5H, m), 7.71 (1H, d, J = 3), 7.50 (1H, d, J = 2), 7.34 (1H, dd, J = 8.5 and 2), 7.19 (1H, dd, J = 9 and 2.5), 7.15 (1H, s), 7.07 (2H, ddd, J = 7, 6 and 1), 7.03 (1H, d, J = 0.5), 6.89 (1H, d, J = 9), 6.58 (1H, s), 6.36 (1H, d, J = 9), 4.08 (3H, s), 3.45 (3H, s), 2.89 (6H, s), 1.30 (9H, s), 1.29 (9H, s). ^{13}C NMR (CD_3CN, 176 MHz): 178.2, 170.8, 161.0, 159.8, 159.8, 159.0, 158.8, 155.9, 151.5, 143.7, 141.4, 140.6, 139.7, 139.1, 139.0, 132.6, 131.9, 131.7, 129.8, 128.7, 125.1, 123.8, 122.6, 119.3, 119.0, 118.3, 117.0, 85.0, 41.36, 34.7, 34.3, 33.9, 30.6, 22.5. MS (ES+): *m/z* 940 $[M+H]^+$.

[Ir(dpyx)HL^{38}]PF$_6$

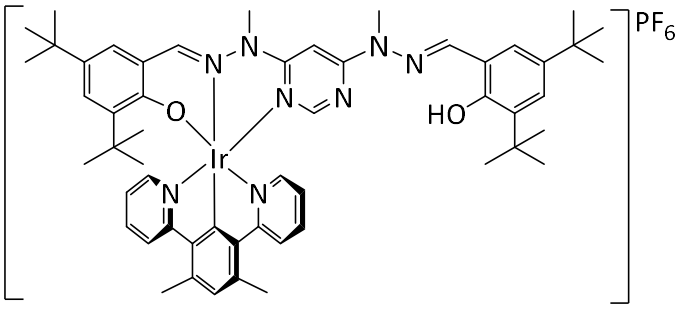

H_2L^{38} (30 mg, 0.05 mmol) and [Ir(dpyx)Cl(μ-Cl)]$_2$ (26 mg, 0.025 mmol) were heated to 195°C in ethylene glycol (1.5ml) for 90 minutes under argon. The resulting slurry was allowed to cool to ambient temperature before adding 5ml H_2O and filtering to obtain an orange-brown solid. The crude material was dissolved in the minimum volume of hot DMSO, pippeted into sat. aq. H_2O, centrifuged and washed with H_2O to yield 29 mg of a yellow solid (0.024 mmol, 48% yield).

^{1}H NMR (CD_3CN, 700 MHz): 11.37 (1H, s), 8.92 (1H, s), 8.20 (2H, d, J = 8), 8.16 (1H, s), 7.82 – 7.78 (4H, m), 7.55 (1H, d, J = 2.5), 7.42 (1H, d, J = 2), 7.32 (1H, d, J = 2), 7.22 (1H, d, J = 3), 7.15 (1H, s), 7.11 (1H, s), 7.04 (2H, ddd, J = 7, 5 and 1), 6.58 (1H, s), 4.10 (3H, s), 3.48 (3H, s), 1.49 (9H, s), 1.30 (18H, s), 0.70 (9H, s). ^{13}C NMR (CD_3CN, 176 MHz): 171.2, 159.9, 159.6, 159.4, 158.9, 155.3, 151.4, 142.6, 141.8, 141.6, 140.4, 139.3, 139.2, 137.6, 137.3, 132.3, 130.1, 128.6, 127.5, 127.3, 124.6, 123.5, 119.3, 118.7, 118.3, 84.77, 35.9, 35.8, 34.9, 34.6, 33.6, 31.7, 31.7, 30.6, 29.8, 29.2, 22.5. MS (ES+): *m/z* 1052 $[M+H]^+$; HRMS (ES+): *m/z* 1049.4940 $[M]^+$; calculated for $[C_{54}H_{66}N_8O_2Ir]^+$ 1049.4915.

[Ir(dpyx)$_2$L^{36}]2PF$_6$

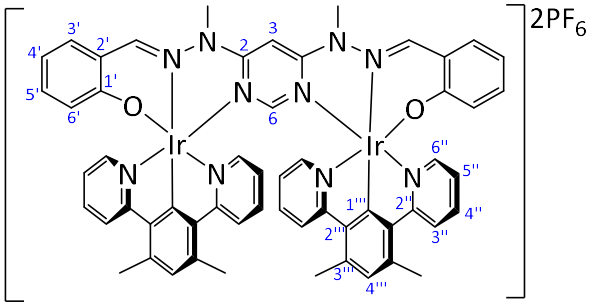

H_2L^{36} (22 mg, 0.058 mmol) and [Ir(dpyx)Cl(μ-Cl)]$_2$ (61 mg, 0.058 mmol) were heated to 195°C in ethylene glycol (1.5ml) for 90 minutes under argon. The resulting slurry was allowed to

cool to ambient temperature before diluting with 2ml H_2O. The filtrates were pippeted into sat. aq. H_2O, centrifuged and washed with H_2O to isolate the crude product. The product was purified by recystallisation in MeCN/Et_2O to yield 4 mg of a yellow solid (0.003 mmol, 5% yield).

^{1}H NMR (CD_3CN, 700 MHz): 8.83 (2H, s, H^{imine}), 8.01 (4H, d, J = 8, $H^{3''}$), 7.70 (4H, ddd, J = 8, 7.5 and 1.5, $H^{4''}$), 7.64 (2H, dd, J = 8 and 2, $H^{3'}$), 7.53 (4H, dd, J = 6 and 1, $H^{6''}$), 7.15 (2H, s, $H^{4'''}$), 7.04 (2H, ddd, J = 9, 7 and 2, $H^{5'}$), 6.87 (4H, ddd, J = 7.5, 5.5 and 1), 6.63 (2H, ddd, J = 8, 7 and 1), 6.46 (1H, s, H^6), 6.28 (2H, d, J = 9, $H^{6'}$), 5.97 (1H, s, H^3), 4.10 (6H, s, H^{NMe}), 2.88 (12H, s, H^{Me}). ^{13}C NMR (CD_3CN, 176 MHz): 175.7 ($C^{1'''}$), 170.0 ($C^{2''}$), 163.0 ($C^{1'}$), 162.1 ($C^{2'''}$), 156.2 (C^2), 151.6 ($C^{6''}$), 142.4 (C^{imine}), 140.6 ($C^{4''}$), 139.0 ($C^{3'''}$), 138.50 ($C^{2'''}$), 136.3 ($C^{3'}$), 134.0 ($C^{5'}$), 133.5 ($C^{4'''}$), 124.5 ($C^{3''}$), 123.5 ($C^{5''}$), 122.9 ($C^{6'}$), 119.9 ($C^{2'}$), 117.1 ($C^{4'}$), 84.65 (C^6), 34.70 (C^{NMe}), 23.0 (C^{Me}). MS (ES+): *m/z* 639 $[M]^{2+}$.

$[Ir(dpyx)_2L^{37}]2PF_6$

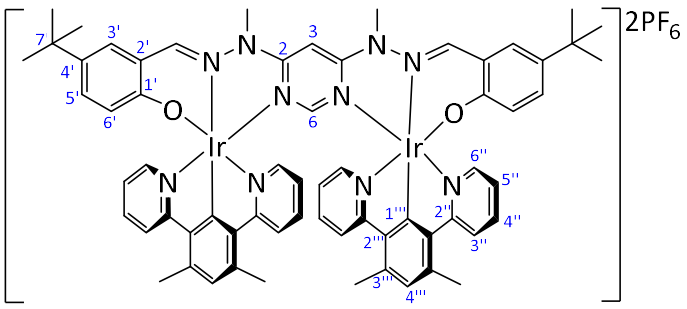

H_2L^{37} (24 mg, 0.048 mmol) and $[Ir(dpyx)Cl(\mu\text{-}Cl]_2$ (50 mg, 0.048 mmol) were heated to 195°C in ethylene glycol (1.5ml) for 90 minutes under argon. The resulting slurry was allowed to cool to ambient temperature before diluting with 2ml H_2O. The filtrates were pippeted into sat. aq. H_2O, centrifuged and washed with H_2O to isolate the crude product. The product was purified by column chromatography (5% MeOH in DCM) to yield 8 mg of a yellow solid (0.006 mmol, 12% yield).

^{1}H NMR (CD_3CN, 700 MHz): 8.87 (2H, s, H^{imine}), 8.02 (4H, d, J = 8, $H^{3''}$), 7.71 (4H, ddd, J = 8, 7.5 and 1.5, $H^{4''}$), 7.64 (2H, d, J = 2.5, $H^{3'}$), 7.53 (4H, ddd, J = 6, 2 and 0.5, $H^{6''}$), 7.16 – 7.14 (4H, m, $H^{5'}$ and $H^{4'''}$), 6.89 (4H, ddd, J = 7, 6 and 1, $H^{5''}$), 6.45 (1H, s, H^6), 6.25 (2H, d, J = 9, $H^{6'}$), 5.97 (1H, s, H^3), 4.12 (6H, s, H^{NMe}), 2.89 (12H, s, H^{Me}), 1.26 (18H, s, H^{butyl}). ^{13}C NMR (CD_3CN, 176 MHz): 175.9 ($C^{1'''}$), 170.0 ($C^{2'''}$), 162.1 (C^3), 161.2 ($C^{1'}$), 156.0 (C^2), 151.5 ($C^{6''}$),

142.7 (C^{imine}), 140.6 ($C^{4''}$), 139.5 ($C^{4'}$), 139.0 ($C^{3'''}$), 138.5 ($C^{2''}$), 133.4 ($C^{5'}$ or $C^{4'''}$), 132.2 ($C^{5'}$ or $C^{4'''}$), 131.9 ($C^{3'}$), 124.5 ($C^{3''}$), 123.5 ($C^{5''}$), 122.4 ($C^{6'}$), 118.9 ($C^{2'}$), 84.5 (C^{6}), 34.7 (C^{NMe}), 34.3 ($C^{7'}$), 31.6 (C^{butyl}), 23.0 (C^{Me}). MS (ES+): *m/z* 695 $[M]^{2+}$; HRMS (ES+): *m/z* 694.2226 $[M]^{2+}$; calculated for $[C_{64}H_{62}N_{10}O_2Ir_2]^+$ 694.2188.

7 Appendix

7.1 Publications arising from work discussed in this thesis

A Series of [Co(Mabiq)Cl_{2-n}] (n = 0, 1, 2) Compounds and Evidence for the Elusive Bimetallic Form

Emma V. Puttock, Priyabrata Banerjee, Manuel Kaspar, Liam Drennen, Dmitry S. Yufit, Eckhard Bill, Stephen Sproules, and Corinna R. Hess

Inorg. Chem., **2015**, *54* (12), pp 5864–5873

7.2 Crystal structure data

Crystal data and structure refinement for Co(Mabiq)Cl_2 (1), 13srv204

Empirical formula	$C_{33}H_{33}Cl_2CoN_8$ x CH_3OH
Formula weight	703.55
Temperature/K	120
Crystal system	triclinic
Space group	P-1
a/Å	9.9013(10)
b/Å	15.0390(14)
c/Å	22.641(2)
α/°	96.477(3)
β/°	99.828(3)
γ/°	102.058(3)
Volume/$Å^3$	3209.9(5)
Z	4
ρ_{calc}mg/mm^3	1.456
m/mm^{-1}	0.744
F(000)	1464.0
Crystal size/mm^3	0.397 × 0.089 × 0.059
2Θ range for data collection	4.28 to 54°
Index ranges	-12 ≤ h ≤ 12, -19 ≤ k ≤ 18, -23 ≤ l ≤ 28
Reflections collected	28168
Independent reflections	13951[R(int) = 0.0849]
Data/restraints/parameters	13951/1/850
Goodness-of-fit on F^2	0.969
Final R indexes [I>=2σ (I)]	R_1 = 0.0642, wR_2 = 0.1045
Final R indexes [all data]	R_1 = 0.1454, wR_2 = 0.1252
Largest diff. peak/hole / e $Å^{-3}$	0.69/-0.62

Crystal data and structure refinement for Co(Mabiq)Cl (2), 13srv319

Empirical formula	$C_{33}H_{33}ClCoN_8$ x 2 CH_2Cl_2
Formula weight	805.91
Temperature/K	120
Crystal system	monoclinic
Space group	$P2_1/c$
a/Å	11.6266(8)
b/Å	21.9485(15)
c/Å	15.0135(10)
α/°	90.00
β/°	108.541(2)
γ/°	90.00
Volume/Å^3	3632.4(4)
Z	4
ρ_{calc}mg/mm^3	1.474
m/mm^{-1}	0.879
F(000)	1660.0
Crystal size/mm^3	0.364 × 0.145 × 0.104
Radiation	MoKα (λ = 0.71073)
2Θ range for data collection	4.3 to 57°
Index ranges	-15 ≤ h ≤ 15, -29 ≤ k ≤ 29, -20 ≤ l ≤ 20
Reflections collected	50205
Independent reflections	9196 [R_{int} = 0.0519, R_{sigma} = 0.0436]
Data/restraints/parameters	9196/0/590
Goodness-of-fit on F^2	1.011
Final R indexes [I>=2σ (I)]	R_1 = 0.0501, wR_2 = 0.1288
Final R indexes [all data]	R_1 = 0.0750, wR_2 = 0.1434
Largest diff. peak/hole / e Å^{-3}	0.85/-1.21

Crystal data and structure refinement for $Co_2(Mabiq)Cl_3$ (3), 13srv319*

Empirical formula	$C_{33}H_{33}Cl_3Co_2N_8O_{0.25}$
Formula weight	769.88
Temperature/K	120
Crystal system	monoclinic
Space group	$P2_1/n$
a/Å	14.387(5)
b/Å	10.175(4)
c/Å	23.559(9)
α/°	90.00
β/°	98.012(4)
γ/°	90.00
Volume/Å^3	3415(2)
Z	4

*limited details are available as data was not of a publishable quality

Crystal data and structure refinement for Co(Mabiq) (4), 13srv326

Empirical formula	$C_{33}H_{33}CoN_8$
Formula weight	600.60
Temperature/K	120
Crystal system	orthorhombic
Space group	Pbca
a/Å	10.199(3)
b/Å	20.351(6)
c/Å	26.781(8)
α/°	90.00
β/°	90.00
γ/°	90.00
Volume/Å^3	5559(3)
Z	8
ρ_{calc}mg/mm^3	1.435
m/mm^{-1}	0.608
F(000)	2512.0
Crystal size/mm^3	0.05 × 0.02 × 0.01
Radiation	synchrotron (λ = 0.68890)
2Θ range for data collection	3.88 to 46°
Index ranges	-11 ≤ h ≤ 11, -23 ≤ k ≤ 23, -29 ≤ l ≤ 30
Reflections collected	36358
Independent reflections	4231 [R_{int} = 0.0984, R_{sigma} = 0.0611]
Data/restraints/parameters	4231/0/511
Goodness-of-fit on F^2	1.054
Final R indexes [I>=2σ (I)]	R_1 = 0.0484, wR_2 = 0.1132
Final R indexes [all data]	R_1 = 0.0743, wR_2 = 0.1267
Largest diff. peak/hole / e Å^{-3}	0.35/-0.53

Crystal data and structure refinement for HL^5, 14srv209

Empirical formula	$C_{12}H_{11}N_3O$
Formula weight	213.24
Temperature/K	120.0
Crystal system	monoclinic
Space group	$P2_1/n$
a/Å	4.617(2)
b/Å	20.615(9)
c/Å	10.849(5)
α/°	90.00
β/°	94.341(12)
γ/°	90.00
Volume/Å^3	1029.7(8)
Z	4
ρ_{calc}g/cm^3	1.376
μ/mm^{-1}	0.092
F(000)	448.0
Crystal size/mm^3	0.41 × 0.04 × 0.03
Radiation	MoKα (λ = 0.71073)
2Θ range for data collection/°	5.46 to 54.98
Index ranges	-5 ≤ h ≤ 5, -26 ≤ k ≤ 26, -14 ≤ l ≤ 14
Reflections collected	13285
Independent reflections	2341 [R_{int} = 0.2352, R_{sigma} = 0.2108]
Data/restraints/parameters	2341/0/146
Goodness-of-fit on F^2	0.957
Final R indexes [I>=2σ (I)]	R_1 = 0.0862, wR_2 = 0.1569
Final R indexes [all data]	R_1 = 0.2259, wR_2 = 0.2023
Largest diff. peak/hole / e Å^{-3}	0.26/-0.32

Crystal data and structure refinement for HL^{29}, 14srv219

Empirical formula	$C_{20}H_{15}N_3O$
Formula weight	313.35
Temperature/K	120.0
Crystal system	monoclinic
Space group	$P2_1/c$
a/Å	16.1462(11)
b/Å	6.0429(5)
c/Å	16.3394(15)
α/°	90.00
β/°	104.725(8)
γ/°	90.00
Volume/Å^3	1541.9(2)
Z	4
ρ_{calc}g/cm^3	1.350
μ/mm^{-1}	0.086
F(000)	656.0
Crystal size/mm^3	0.51 × 0.07 × 0.01
Radiation	MoKα (λ = 0.71073)
2Θ range for data collection/°	5.16 to 56
Index ranges	-21 ≤ h ≤ 21, -7 ≤ k ≤ 7, -21 ≤ l ≤ 21
Reflections collected	23998
Independent reflections	3711 [R_{int} = 0.0985, R_{sigma} = 0.0680]
Data/restraints/parameters	3711/0/277
Goodness-of-fit on F^2	1.033
Final R indexes [I>=2σ (I)]	R_1 = 0.0542, wR_2 = 0.0918
Final R indexes [all data]	R_1 = 0.0928, wR_2 = 0.1057
Largest diff. peak/hole / e Å^{-3}	0.23/-0.23

Crystal data and structure refinement for HL^{30}, 15srv130

Empirical formula	$C_{21}H_{17}N_3O$
Formula weight	327.38
Temperature/K	120.0
Crystal system	monoclinic
Space group	$P2_1/c$
a/Å	9.8507(5)
b/Å	8.5210(5)
c/Å	19.7284(10)
α/°	90.00
β/°	103.807(2)
γ/°	90.00
Volume/Å^3	1608.11(15)
Z	4
ρ_{calc}g/cm^3	1.352
μ/mm^{-1}	0.085
F(000)	688.0
Crystal size/mm^3	0.51 × 0.15 × 0.09
Radiation	MoKα (λ = 0.71073)
2Θ range for data collection/°	4.26 to 58
Index ranges	-13 ≤ h ≤ 13, -11 ≤ k ≤ 11, -26 ≤ l ≤ 26
Reflections collected	24051
Independent reflections	4279 [R_{int} = 0.0628, R_{sigma} = 0.0518]
Data/restraints/parameters	4279/0/294
Goodness-of-fit on F^2	1.021
Final R indexes [I>=2σ (I)]	R_1 = 0.0458, wR_2 = 0.1029
Final R indexes [all data]	R_1 = 0.0706, wR_2 = 0.1161
Largest diff. peak/hole / e Å^{-3}	0.27/-0.28

Crystal data and structure refinement for PtL^1Cl, 14srv227

Empirical formula	$C_{16}H_{11}ClN_2OPt \times CH_2Cl_2$
Formula weight	562.73
Temperature/K	120.0
Crystal system	triclinic
Space group	P-1
a/Å	7.8778(6)
b/Å	8.8726(8)
c/Å	13.2483(10)
α/°	75.787(7)
β/°	72.823(7)
γ/°	74.302(8)
Volume/$Å^3$	837.79(12)
Z	2
$\rho_{calc}g/cm^3$	2.231
μ/mm^{-1}	8.859
F(000)	532.0
Crystal size/mm^3	0.17 × 0.06 × 0.02
Radiation	MoKα (λ = 0.71073)
2Θ range for data collection/°	4.84 to 57
Index ranges	$-10 \le h \le 10$, $-11 \le k \le 11$, $-17 \le l \le 17$
Reflections collected	17866
Independent reflections	4252 [R_{int} = 0.0856, R_{sigma} = 0.0783]
Data/restraints/parameters	4252/0/217
Goodness-of-fit on F^2	0.990
Final R indexes [I>=2σ (I)]	R_1 = 0.0388, wR_2 = 0.0645
Final R indexes [all data]	R_1 = 0.0535, wR_2 = 0.0693
Largest diff. peak/hole / e $Å^{-3}$	1.23/-1.20

Crystal data and structure refinement for $PtL^1C{\equiv}C$-Ar, 16srv273

Empirical formula	$C_{26}H_{14}F_6N_2OPt$ x 2 C_2H_6OS
Formula weight	835.74
Temperature/K	120.0
Crystal system	monoclinic
Space group	$P2_1/c$
a/Å	16.5452(7)
b/Å	18.5441(7)
c/Å	9.7467(4)
α/°	90
β/°	91.0751(14)
γ/°	90
Volume/Å^3	2989.9(2)
Z	4
ρ_{calc}g/cm^3	1.857
μ/mm^{-1}	4.906
F(000)	1632.0
Crystal size/mm^3	0.11 × 0.1 × 0.06
Radiation	MoKα (λ = 0.71073)
2Θ range for data collection/°	4.392 to 60
Index ranges	-22 ≤ h ≤ 23, -26 ≤ k ≤ 26, -13 ≤ l ≤ 13
Reflections collected	65412
Independent reflections	8719 [R_{int} = 0.0488, R_{sigma} = 0.0328]
Data/restraints/parameters	8719/7/405
Goodness-of-fit on F^2	1.039
Final R indexes [I>=2σ (I)]	R_1 = 0.0243, wR_2 = 0.0399
Final R indexes [all data]	R_1 = 0.0389, wR_2 = 0.0429
Largest diff. peak/hole / e Å^{-3}	0.65/-0.63

Crystal data and structure refinement for PtL^6Cl, 16srv140

Empirical formula	$C_{13}H_{12}ClN_3OPt \times C_3H_7NO$
Formula weight	529.89
Temperature/K	120.0
Crystal system	monoclinic
Space group	$P2_1/c$
a/Å	14.4735(9)
b/Å	14.4419(9)
c/Å	8.3539(5)
α/°	90.00
β/°	96.170(2)
γ/°	90.00
Volume/Å^3	1736.06(18)
Z	4
ρ_{calc}g/cm^3	2.027
μ/mm^{-1}	8.253
F(000)	1016.0
Crystal size/mm^3	0.12 × 0.01 × 0.01
Radiation	MoKα (λ = 0.71073)
2Θ range for data collection/°	4 to 58
Index ranges	-19 ≤ h ≤ 19, -19 ≤ k ≤ 19, -11 ≤ l ≤ 11
Reflections collected	21653
Independent reflections	4619 [R_{int} = 0.0703, R_{sigma} = 0.0571]
Data/restraints/parameters	4619/0/220
Goodness-of-fit on F^2	1.026
Final R indexes [I>=2σ (I)]	R_1 = 0.0334, wR_2 = 0.0658
Final R indexes [all data]	R_1 = 0.0533, wR_2 = 0.0720
Largest diff. peak/hole / e Å^{-3}	2.65/-1.52

Crystal data and structure refinement for PtL^8Cl, 15srv223

Empirical formula	$C_{12}H_9ClN_4O_3Pt \times C_2H_6SO$
Formula weight	565.90
Temperature/K	120.0
Crystal system	monoclinic
Space group	$P2_1/n$
a/Å	7.0662(2)
b/Å	23.0266(5)
c/Å	11.1435(3)
α/°	90.00
β/°	106.773(2)
γ/°	90.00
Volume/Å^3	1736.02(8)
Z	4
ρ_{calc}g/cm^3	2.165
μ/mm^{-1}	8.384
F(000)	1080.0
Crystal size/mm^3	0.36 × 0.03 × 0.02
Radiation	MoKα (λ = 0.71073)
2Θ range for data collection/°	5.2 to 58
Index ranges	$-9 \le h \le 9$, $-31 \le k \le 31$, $-15 \le l \le 15$
Reflections collected	34017
Independent reflections	4619 [R_{int} = 0.0784, R_{sigma} = 0.0528]
Data/restraints/parameters	4619/0/228
Goodness-of-fit on F^2	1.204
Final R indexes [I>=2σ (I)]	R_1 = 0.0408, wR_2 = 0.0718
Final R indexes [all data]	R_1 = 0.0539, wR_2 = 0.0749
Largest diff. peak/hole / e Å^{-3}	1.47/-3.15

Crystal data and structure refinement for $PtL^{12}Cl$, 15srv232

Empirical formula	$C_{13}H_{14}ClN_3O_3Pt$
Formula weight	490.81
Temperature/K	120.0
Crystal system	triclinic
Space group	P-1
a/Å	8.5021(7)
b/Å	8.6034(7)
c/Å	10.4411(8)
α/°	66.850(2)
β/°	88.962(3)
γ/°	86.218(3)
Volume/Å^3	700.68(10)
Z	2
ρ_{calc}g/cm^3	2.326
μ/mm^{-1}	10.216
F(000)	464.0
Crystal size/mm^3	0.29 × 0.06 × 0.02
Radiation	MoKα (λ = 0.71073)
2Θ range for data collection/°	4.8 to 60
Index ranges	-11 ≤ h ≤ 11, -12 ≤ k ≤ 12, -14 ≤ l ≤ 14
Reflections collected	15145
Independent reflections	4080 [R_{int} = 0.0387, R_{sigma} = 0.0374]
Data/restraints/parameters	4080/0/194
Goodness-of-fit on F^2	1.059
Final R indexes [I>=2σ (I)]	R_1 = 0.0187, wR_2 = 0.0401
Final R indexes [all data]	R_1 = 0.0222, wR_2 = 0.0410
Largest diff. peak/hole / e Å^{-3}	1.77/-1.14

Crystal data and structure refinement for $PtL^{14}Cl$, 15srv096

Empirical formula	$C_{13}H_{12}ClN_3OPt$
Formula weight	456.80
Temperature/K	120.0
Crystal system	monoclinic
Space group	$P2_1/c$
a/Å	11.1945(5)
b/Å	9.5950(4)
c/Å	12.2845(5)
α/°	90.00
β/°	105.6722(14)
γ/°	90.00
Volume/$Å^3$	1270.44(9)
Z	4
$\rho_{calc}g/cm^3$	2.388
μ/mm^{-1}	11.248
F(000)	856.0
Crystal size/mm^3	0.16 × 0.09 × 0.06
Radiation	MoKα (λ = 0.71073)
2Θ range for data collection/°	5.46 to 60
Index ranges	$-15 \le h \le 15$, $-13 \le k \le 13$, $-17 \le l \le 17$
Reflections collected	27170
Independent reflections	3706 [R_{int} = 0.0275, R_{sigma} = 0.0158]
Data/restraints/parameters	3706/0/174
Goodness-of-fit on F^2	1.082
Final R indexes [I>=2σ (I)]	R_1 = 0.0114, wR_2 = 0.0232
Final R indexes [all data]	R_1 = 0.0142, wR_2 = 0.0240
Largest diff. peak/hole / e $Å^{-3}$	0.71/-0.48

Crystal data and structure refinement for $PtL^{17}Cl$, 15srv291

Empirical formula	$C_{13}H_{10}Cl_3N_3OPt \times C_3H_7NO$
Formula weight	598.78
Temperature/K	120.0
Crystal system	triclinic
Space group	P-1
a/Å	8.5082(7)
b/Å	8.8816(7)
c/Å	13.2120(11)
α/°	108.748(2)
β/°	100.964(3)
γ/°	97.584(3)
Volume/Å^3	907.91(13)
Z	2
ρ_{calc}g/cm^3	2.190
μ/mm^{-1}	8.189
F(000)	572.0
Crystal size/mm^3	0.19 × 0.04 × 0.01
Radiation	MoKα (λ = 0.71073)
2Θ range for data collection/°	4.96 to 60
Index ranges	-11 ≤ h ≤ 11, -12 ≤ k ≤ 12, -18 ≤ l ≤ 18
Reflections collected	18871
Independent reflections	5283 [R_{int} = 0.0418, R_{sigma} = 0.0460]
Data/restraints/parameters	5283/0/238
Goodness-of-fit on F^2	1.044
Final R indexes [I>=2σ (I)]	R_1 = 0.0230, wR_2 = 0.0457
Final R indexes [all data]	R_1 = 0.0296, wR_2 = 0.0474
Largest diff. peak/hole / e Å^{-3}	1.73/-1.59

Crystal data and structure refinement for $PtL^{19}Cl$, 16srv451

Empirical formula	$C_{14}H_{14}ClN_3O_2Pt$
Formula weight	486.82
Temperature/K	120.0
Crystal system	monoclinic
Space group	$P2_1/n$
a/Å	8.3913(5)
b/Å	8.2576(5)
c/Å	19.9601(11)
α/°	90
β/°	92.4713(19)
γ/°	90
Volume/Å^3	1381.79(14)
Z	4
ρ_{calc}g/cm^3	2.340
μ/mm^{-1}	10.355
F(000)	920.0
Crystal size/mm^3	0.11 × 0.05 × 0.02
Radiation	MoKα (λ = 0.71073)
2Θ range for data collection/°	5.19 to 59.994
Index ranges	-11 ≤ h ≤ 11, -11 ≤ k ≤ 11, -28 ≤ l ≤ 28
Reflections collected	22080
Independent reflections	4032 [R_{int} = 0.0527, R_{sigma} = 0.0432]
Data/restraints/parameters	4032/0/192
Goodness-of-fit on F^2	1.041
Final R indexes [I>=2σ (I)]	R_1 = 0.0268, wR_2 = 0.0427
Final R indexes [all data]	R_1 = 0.0465, wR_2 = 0.0461
Largest diff. peak/hole / e Å^{-3}	1.28/-0.88

Crystal data and structure refinement for PtL^{27}, 16srv209

Empirical formula	$C_{19}H_{15}N_3OPt \times C_2H_6SO$
Formula weight	574.56
Temperature/K	120.0
Crystal system	monoclinic
Space group	$P2_1/c$
a/Å	19.3076(8)
b/Å	19.5130(8)
c/Å	10.4261(5)
α/°	90
β/°	105.2760(10)
γ/°	90
Volume/Å^3	3789.2(3)
Z	8
ρ_{calc}g/cm^3	2.014
μ/mm^{-1}	7.539
F(000)	2224.0
Crystal size/mm^3	0.21 × 0.08 × 0.06
Radiation	MoKα (λ = 0.71073)
2Θ range for data collection/°	2.186 to 59.998
Index ranges	-27 ≤ h ≤ 27, -27 ≤ k ≤ 27, -14 ≤ l ≤ 14
Reflections collected	50787
Independent reflections	11044 [R_{int} = 0.0594, R_{sigma} = 0.0528]
Data/restraints/parameters	11044/0/511
Goodness-of-fit on F^2	1.034
Final R indexes [I>=2σ (I)]	R_1 = 0.0402, wR_2 = 0.0943
Final R indexes [all data]	R_1 = 0.0600, wR_2 = 0.1047
Largest diff. peak/hole / e Å^{-3}	3.49/-2.32

Crystal data and structure refinement for $PtL^{31}Cl$, 15srv149

Empirical formula	$C_{24}H_{22}ClN_3Opt$ (x 3 CH_3COOH?)
Formula weight	598.99
Temperature/K	120.0
Crystal system	triclinic
Space group	P-1
a/Å	10.0432(7)
b/Å	10.8058(7)
c/Å	13.7861(9)
α/°	71.4105(19)
β/°	71.8564(19)
γ/°	84.038(2)
Volume/Å^3	1347.55(16)
Z	2
ρ_{calc}g/cm^3	1.476
μ/mm^{-1}	5.322
F(000)	580.0
Crystal size/mm^3	0.16 × 0.05 × 0.01
Radiation	MoKα (λ = 0.71073)
2Θ range for data collection/°	4.26 to 55
Index ranges	-14 ≤ h ≤ 14, -15 ≤ k ≤ 15, -20 ≤ l ≤ 19
Reflections collected	24197
Independent reflections	6151 [R_{int} = 0.0708, R_{sigma} = 0.1241]
Data/restraints/parameters	6151/0/275
Goodness-of-fit on F^2	1.062
Final R indexes [I>=2σ (I)]	R_1 = 0.0424, wR_2 = 0.0882
Final R indexes [all data]	R_1 = 0.0569, wR_2 = 0.0911
Largest diff. peak/hole / e Å^{-3}	1.14/-2.15

Crystal data and structure refinement for [PtL^{29}]OTf, 16srv012

Empirical formula	$C_{23}H_{20}N_3O_2Pt$ x CF_3O_3S
Formula weight	714.58
Temperature/K	120.0
Crystal system	orthorhombic
Space group	Pbca
a/Å	10.5032(4)
b/Å	14.8938(5)
c/Å	30.1011(10)
α/°	90.00
β/°	90.00
γ/°	90.00
Volume/Å^3	4708.8(3)
Z	8
ρ_{calc}g/cm^3	2.016
μ/mm^{-1}	6.116
F(000)	2768.0
Crystal size/mm^3	0.53 × 0.07 × 0.02
Radiation	MoKα (λ = 0.71073)
2Θ range for data collection/°	4.72 to 56
Index ranges	-13 ≤ h ≤ 13, -19 ≤ k ≤ 19, -39 ≤ l ≤ 39
Reflections collected	73151
Independent reflections	5676 [R_{int} = 0.1696, R_{sigma} = 0.0678]
Data/restraints/parameters	5676/31/331
Goodness-of-fit on F^2	1.029
Final R indexes [I>=2σ (I)]	R_1 = 0.0556, wR_2 = 0.1362
Final R indexes [all data]	R_1 = 0.0825, wR_2 = 0.1564
Largest diff. peak/hole / e Å^{-3}	2.88/-1.54

Crystal data and structure refinement for $[Ir(dpyx)L^{15}]PF_6$, 16srv479

Empirical formula	$C_{32}H_{29}IrN_5O_2 \times PF_6 \times CH_3CN$
Formula weight	893.83
Temperature/K	120.0
Crystal system	monoclinic
Space group	$P2_1/c$
a/Å	11.4532(5)
b/Å	15.8034(7)
c/Å	18.1543(8)
α/°	90.00
β/°	95.0909(16)
γ/°	90.00
Volume/Å^3	3273.0(2)
Z	4
ρ_{calc}g/cm^3	1.814
μ/mm^{-1}	4.206
F(000)	1760.0
Crystal size/mm^3	0.25 × 0.21 × 0.08
Radiation	MoKα (λ = 0.71073)
2Θ range for data collection/°	4.8 to 60
Index ranges	-16 ≤ h ≤ 16, -22 ≤ k ≤ 22, -25 ≤ l ≤ 25
Reflections collected	71211
Independent reflections	9548 [R_{int} = 0.0310, R_{sigma} = 0.0174]
Data/restraints/parameters	9548/0/456
Goodness-of-fit on F^2	1.054
Final R indexes [I>=2σ (I)]	R_1 = 0.0161, wR_2 = 0.0348
Final R indexes [all data]	R_1 = 0.0214, wR_2 = 0.0367
Largest diff. peak/hole / e Å^{-3}	0.81/-1.01

Crystal data and structure refinement for H_2L^{36}, 16srv249

Empirical formula	$C_{20}H_{20}N_6O_2$
Formula weight	376.42
Temperature/K	120.0
Crystal system	monoclinic
Space group	I2/c
a/Å	15.5025(12)
b/Å	10.4734(8)
c/Å	11.3532(9)
α/°	90
β/°	93.231(7)
γ/°	90
Volume/Å^3	1840.4(3)
Z	4
ρ_{calc}g/cm^3	1.359
μ/mm^{-1}	0.092
F(000)	792.0
Crystal size/mm^3	0.32 × 0.1 × 0.06
Radiation	MoKα (λ = 0.71073)
2Θ range for data collection/°	4.696 to 57.986
Index ranges	-21 ≤ h ≤ 21, -14 ≤ k ≤ 14, -15 ≤ l ≤ 15
Reflections collected	15142
Independent reflections	2446 [R_{int} = 0.1019, R_{sigma} = 0.0686]
Data/restraints/parameters	2446/0/133
Goodness-of-fit on F^2	1.020
Final R indexes [I>=2σ (I)]	R_1 = 0.0565, wR_2 = 0.1088
Final R indexes [all data]	R_1 = 0.1101, wR_2 = 0.1299
Largest diff. peak/hole / e Å^{-3}	0.26/-0.22

Crystal data and structure refinement for H_2L^{38}, 16srv303

Empirical formula	$C_{36}H_{52}N_6O_2$
Formula weight	600.83
Temperature/K	120.0
Crystal system	triclinic
Space group	P-1
a/Å	12.1186(12)
b/Å	12.2241(10)
c/Å	12.9851(11)
α/°	72.172(3)
β/°	77.714(3)
γ/°	88.934(3)
Volume/Å^3	1787.0(3)
Z	2
ρ_{calc}g/cm^3	1.117
μ/mm^{-1}	0.070
F(000)	652.0
Crystal size/mm^3	0.32 × 0.11 × 0.05
Radiation	MoKα (λ = 0.71073)
2Θ range for data collection/°	4.79 to 58
Index ranges	-16 ≤ h ≤ 16, -16 ≤ k ≤ 16, -17 ≤ l ≤ 17
Reflections collected	28016
Independent reflections	9488 [R_{int} = 0.0442, R_{sigma} = 0.0629]
Data/restraints/parameters	9488/2/417
Goodness-of-fit on F^2	1.021
Final R indexes [I>=2σ (I)]	R_1 = 0.0556, wR_2 = 0.1208
Final R indexes [all data]	R_1 = 0.0964, wR_2 = 0.1369
Largest diff. peak/hole / e Å^{-3}	0.35/-0.32

Crystal data and structure refinement for $[Ir(dpyx)_2L^{36}]2PF_6$, 16srv305

Empirical formula	$C_{56}H_{48}Ir_2N_{10}O_2$ x 2 PF_6 x 4 CH_3CN
Formula weight	1731.60
Temperature/K	120.0
Crystal system	triclinic
Space group	P-1
a/Å	12.7200(11)
b/Å	14.3155(12)
c/Å	19.9170(17)
α/°	86.983(3)
β/°	79.538(3)
γ/°	78.218(2)
Volume/$Å^3$	3490.9(5)
Z	2
$\rho_{calc}g/cm^3$	1.647
μ/mm^{-1}	3.939
F(000)	1700.0
Crystal size/mm^3	0.12 × 0.09 × 0.02
Radiation	MoKα (λ = 0.71073)
2Θ range for data collection/°	4.216 to 55
Index ranges	-17 ≤ h ≤ 17, -19 ≤ k ≤ 19, -27 ≤ l ≤ 27
Reflections collected	74344
Independent reflections	16016 [R_{int} = 0.1680, R_{sigma} = 0.2280]
Data/restraints/parameters	16016/914/872
Goodness-of-fit on F^2	0.958
Final R indexes [I>=2σ (I)]	R_1 = 0.0735, wR_2 = 0.1514
Final R indexes [all data]	R_1 = 0.1517, wR_2 = 0.1700
Largest diff. peak/hole / e $Å^{-3}$	3.38/-1.40

Crystal data and structure refinement for $[Ir(dpyx)_2L^{37}]2PF_6$, 16srv324

Empirical formula	$2(C_{64}H_{64}Ir_2N_{10}O_2)$ x 3 (PF_6) x (CH_3OH) x 6 (CH_3CN)
Formula weight	3492.57
Temperature/K	120.0
Crystal system	triclinic
Space group	P-1
a/Å	12.2674(11)
b/Å	16.3422(15)
c/Å	21.227(2)
α/°	75.235(3)
β/°	76.582(3)
γ/°	87.493(3)
Volume/Å^3	4002.2(6)
Z	1
ρ_{calc}g/cm^3	1.449
μ/mm^{-1}	3.422
F(000)	1733.0
Crystal size/mm^3	0.16 × 0.15 × 0.06
Radiation	MoKα (λ = 0.71073)
2Θ range for data collection/°	4.24 to 57.998
Index ranges	-16 ≤ h ≤ 16, -22 ≤ k ≤ 22, -28 ≤ l ≤ 28
Reflections collected	83046
Independent reflections	21245 [R_{int} = 0.0351, R_{sigma} = 0.0362]
Data/restraints/parameters	21245/64/891
Goodness-of-fit on F^2	1.053
Final R indexes [I>=2σ (I)]	R_1 = 0.0484, wR_2 = 0.1054
Final R indexes [all data]	R_1 = 0.0674, wR_2 = 0.1166
Largest diff. peak/hole / e Å^{-3}	4.91/-3.05

7.3 X^2 values

Complex	X^2		
	Degassed	Aerated	77K
PtL^1Cl	0.993	1.038	1.170
PtL^2Cl	0.983	1.134	1.002
PtL^3Cl	0.952	1.044	1.176
PtL^4Cl	1.100	0.872	1.338
$PtL^1C{\equiv}C\text{-}Ar$	1.082	0.957	1.342
$PtL^{14}Cl$	1.078	1.042	1.324
$PtL^{15}Cl$	1.086	1.147	1.263
$PtL^{16}Cl$	0.947	0.932	1.159
$PtL^{17}Cl$	1.068	1.168	1.334
$PtL^{18}Cl$	0.995	1.034	1.329
$PtL^{19}Cl$	1.012	0.891	1.137
$PtL^{20}Cl$	1.039	1.169	1.206
$PtL^{14}C{\equiv}C\text{-}Ar$	1.028	1.065	1.258
a-$PtL^{22}Cl$	1.117	1.039	1.225
b-$PtL^{22}Cl$	0.977	1.049	1.139
$PtL^{23}Cl$	n/a	n/a	1.212
$PtL^{24}Cl$	n/a	n/a	0.977
$PtL^{25}Cl$	1.064	1.016	1.272
PtL^{27}	0.928	0.985	1.313
$PtL^{29}Cl$	0.997	1.222	n/a
$PtL^{30}Cl$	1.189	1.220	1.213
$PtL^{31}Cl$	0.968	0.980	1.279
$[Ir(dpyx)L^{14}]PF_6$	0.982	1.182	1.246
$[Ir(dpyx)L^{15}]PF_6$	1.110	1.034	1.303
$[Ir(dpyx)L^{16}]PF_6$	1.071	1.186	0.993
$[Ir(dpyx)L^{17}]PF_6$	1.279	1.043	1.234
a-$PtCl(\mu\text{-}L^{22})RuCl_2(PPh_3)_2$	n/a	n/a	1.025
[a-$PtCl(\mu\text{-}L^{22})Ir(ppy)_2$]$PF_6$	n/a	n/a	(496) 1.213 (659) 1.298
$[Ir(dpyx)HL^{36}]PF_6$	1.059	1.120	1.303
$[Ir(dpyx)HL^{37}]PF_6$	1.076	0.984	1.165
$[Ir(dpyx)HL^{38}]PF_6$	1.114	0.961	1.204
$[\{Ir(dpyx)\}_2L^{36}]2PF_6$	1.266	0.960	1.198
$[\{Ir(dpyx)\}_2L^{37}]2PF_6$	10.92	1.024	1.275

8 Bibliography

1 World Energy Council, *World Energy Resour.*, 2013, **23**.

2 T. R. Cook, D. K. Dogutan, S. Y. Reece, Y. Surendranath, T. S. Teets and D. G. Nocera, *Chem. Rev.*, 2010, **110**, 6474–6502.

3 B. D. Abbott, *IEEE*, 2010, **98**, 42–66.

4 J. R. Bolton and D. Hall, *Annu. Rev. Energy.*, 1979, **4**, 353–401.

5 D. A. J. Rand and R. M. Dell, *J. Power Sources*, 2005, **144**, 568–578.

6 BP Statistical Review of World Energy, 2016.

7 J. Cook, D. Nuccitelli, S. A. Green, M. Richardson, B. Winkler, R. Painting, R. Way, P. Jacobs and A. Skuce, *Environ. Res. Lett.*, 2013, **8**, 1–7.

8 D. G. Nocera and N. S. Lewis, *PNAS*, 2006, **104**, 15729–15735.

9 P. C. K. Vesborg, B. Seger and I. Chorkendorff, *J. Phys. Chem. Lett.*, 2015, **6**, 951–957.

10 B. Johnston, M. C. Mayo and A. Khare, *Technovation*, 2005, **25**, 569–585.

11 S. Dunn, *Worldwatch Paper #157: Hydrogen Futures: Toward a Sustainable Energy System*, 2001.

12 I. Kenney, *http://www.livestrong.com/article/128201-dangers-hydrogen-fuel-cells/*.

13 Fuel Cell & Hydrogen Energy Association, *https://static1.squarespace.com/static/53ab1feee4b0bef0179a1563/t/553e4940e4b0e47dfc339bd2/1430145344686/FCEV+and+H2+Myths.pdf*.

14 J. Barber and P. D. Tran, *J. R. Soc. Interface*, 2013, **10**, 1–16.

15 J. L. Dempsey, B. S. Brunschwig, J. R. Winkler and H. B. Gray, *Acc. Chem. Res.*, 2009, **42**, 1995–2004.

16 J. Barber, *Chem Soc Rev*, 2009, **38**, 185–196.

17 A. B. Laursen, S. Kegnæs, S. Dahl and I. Chorkendorff, *Energy Environ. Sci.*, 2012, **5**, 5577–5591.

18 E. S. Andreiadis, M. Chavarot-kerlidou, M. Fontecave and V. Artero, *Photochem. Photobiol.*, 2011, 946–964.

19 A. K. Jones, E. Sillery, S. P. J. Albracht and F. A. Armstrong, *Chem. Commun.*, 2002, 866–867.

20 M. Razavet, V. Artero and M. Fontecave, *Inorg. Chem.*, 2005, **44**, 4786–4795.

21 C. Baffert, V. Artero and M. Fontecave, *Inorg. Chem.*, 2007, **46**, 1817–1824.

22 V. Artero, M. Chavarot-Kerlidou and M. Fontecave, *Angew. Chemie - Int. Ed.*, 2011, **50**, 7238–7266.

23 N. Queyriaux, R. T. Jane, J. Massin, V. Artero and M. Chavarot-Kerlidou, *Coord. Chem. Rev.*, 2015, **304**–**305**, 3–19.

24 J. R. McKone, S. C. Marinescu, B. S. Brunschwig, J. R. Winkler and H. B. Gray, *Chem. Sci.*, 2014, **5**, 865–878.

25 J. L. Dempsey, J. R. Winkler and H. B. Gray, *J. Am. Chem. Soc.*, 2010, **132**, 16774–16776.

26 D. Mandal and B. D. Gupta, *Eur. J. Inorg. Chem.*, 2006, 4086–4095.

27 M. Bhuyan, M. Laskar and B. D. Gupta, *Organometallics*, 2008, **27**, 594–601.

28 T.-H. Chao and J. H. Espension, *J. Am. Chem. Soc.*, 1978, **100**, 129–133.

29 P. Connolly and J. H. Espenson, *Inorg. Chem.*, 1986, **25**, 2684–2688.

30 X. Hu, B. M. Cossairt, B. S. Brunschwig, N. S. Lewis and J. C. Peters, *Chem. Commun.*, 2005, **16**, 4723.

31 N. Kaeffer, M. Chavarot-Kerlidou and V. Artero, *Acc. Chem. Res.*, 2015, **48**, 1286–1295.

32 J. P. Bigi, T. E. Hanna, W. H. Harman, A. Chang and C. J. Chang, *Chem. Commun.*, 2010, **46**, 958–960.

33 R. S. Khnayzer, V. S. Thoi, M. Nippe, A. E. King, J. W. Jurss, K. A. El Roz, J. R. Long, C. J. Chang and F. N. Castellano, *Energy Environ. Sci.*, 2014, **7**, 1477.

34 L. Tong, R. Zong and R. P. Thummel, *J. Am. Chem. Soc.*, 2014, **136**, 4881–4884.

35 M. Nippe, R. S. Khnayzer, J. A. Panetier, D. Z. Zee, B. S. Olaiya, M. Head-Gordon, C. J. Chang, F. N. Castellano and J. R. Long, *Chem. Sci.*, 2013, **4**, 3934.

36 P. Banerjee, A. Company, T. Weyhermü, E. Bill and C. R. Hess, *Inorg. Chem.*, 2009, **48**, 2944–2955.

37 E. Mueller, G. Bernardinelli and A. Von Zelewsky, *Inorg. Chem.*, 1988, **27**, 4645–4651.

38 P. J. Chirik and K. Wieghardt, *Science (80-.).*, 2010, **327**, 794–795.

39 O. R. Luca and R. H. Crabtree, *Chem. Soc. Rev.*, 2013, **42**, 1440–1459.

40 J. Hawecker, J. M. Lehn and R. Ziessel, *Nouv J Chim*, 1983, **7**, 271–277.

41 E. V. Puttock, P. Banerjee, M. Kaspar, L. Drennen, D. S. Yufit, E. Bill, S. Sproules and C. R. Hess, *Inorg. Chem.*, 2015, **54**, 5864–5873.

42 M. D. Liptak and T. C. Brunold, *J. Am. Chem. Soc.*, 2006, **128**, 9144–56.

43 F. H. Allen, O. Kennard, D. G. Watson, L. Brammer, A. G. Orpen and R. Taylor, *J. Chem. Soc., Perkin Trans. 2*, 1987, S1–S19.

44 P. T. Kissinger and W. R. Heineman, *J. Chem. Educ.*, 1983, **60**, 9242–5.

45 A. L. Gavrilova and B. Bosnich, *Inorganica Chim. Acta*, 2003, **352**, 24–30.

46 D. Streich, *Uppsala Univ. Diss.*, 2013, 1–88.

47 X. Hu, B. S. Brunschwig and J. C. Peters, *J. Am. Chem. Soc.*, 2007, **129**, 8988–8998.

48 V. A. Benderskii, A. G. Krivenko and A. A. Ovchinnikov, *J. Electroanal. Chem. Interfacial Electrochem.*, 1980, **111**, 19–40.

49 J. P. Paris and W. W. Brandt, *J. Am. Chem. Soc.*, 1959, **81**, 5001–5002.

50 J. Kalinowski, V. Fattori, M. Cocchi and J. A. G. Williams, *Coord. Chem. Rev.*, 2011, **255**, 2401–2425.

51 J. A. G. Williams, *Chem. Soc. Rev.*, 2009, **38**, 1783–1801.

52 J. A. G. Williams, *Platin. Met. Rev.*, 2009, **53**, 45–47.

53 L. F. Gildea and J. A. G. Williams, *Iridium and platinum complexes for OLEDs*, 2013.

54 P.-T. Chou, Y. Chi, M.-W. Chung and C.-C. Lin, *Coord. Chem. Rev.*, 2011, **255**, 2653–2665.

55 S. J. Farley, D. L. Rochester, A. L. Thompson, J. A. K. Howard and J. A. G. Williams, *Inorg. Chem.*, 2005, **44**, 9690–9703.

56 B. Y. M. Kasha, *Discuss. Faraday Soc.*, 1950, **9**, 14–19.

57 L. Murphy and J. a G. Williams, *Molecular Organometallic Materials for Optics*, 2010, vol. 28.

58 A. Jabłoński, *Nature*, 1933, **131**, 839–840.

59 H. Kunkely and A. Vogler, *J. Am. Chem. Soc.*, 1990, **112**, 5625–5627.

60 J. Nishida, A. Maruyama, T. Iwata and Y. Yamashita, *Chem. Lett.*, 2005, **34**, 592–593.

61 S. Y. Chang, J. Kavitha, S. W. Li, C. S. Hsu, Y. Chi, Y. S. Yeh, P. T. Chou, G. H. Lee, A. J. Carty, Y. T. Tao and C. H. Chien, *Inorg. Chem.*, 2006, **45**, 137–146.

62 S. Huo, J. Carroll and D. A. K. Vezzu, *Asian J. Org. Chem.*, 2015, **4**, 1210–1245.

63 M. Velusamy, C. H. Chen, Y. S. Wen, J. T. Lin, C. C. Lin, C. H. Lai and P. T. Chou, *Organometallics*, 2010, **29**, 3912–3921.

64 N. Komiya, T. Kashiwabara, S. Iwata and T. Naota, *J. Organomet. Chem.*, 2013, **738**, 66–75.

65 V. Balzani and V. Carassiti, *J. Phys. Chem.*, 1968, **72**, 383–388.

66 G. T. Morgan and F. H. Burstall, *J. Chem. Soc*, 1934, 1498–1500.

67 H. Yip, L. Cheng, K. Cheung and C. Che, *J. Chem. Soc., Dalt. Trans.*, 1993, **2**, 2933–2938.

68 D. R. McMillin and J. J. Moore, *Coord. Chem. Rev.*, 2002, **229**, 113–121.

69 F. N. Castellano, I. E. Pomestchenko, E. Shikhova, F. Hua, M. L. Muro and N. Rajapakse, *Coord. Chem. Rev.*, 2006, **250**, 1819–1828.

70 K. M. C. Wong and V. W. W. Yam, *Coord. Chem. Rev.*, 2007, **251**, 2477–2488.

71 Z. Ji, A. Azenkeng, M. Hoffmann and W. Sun, *Dalton Trans.*, 2009, 7725–7733.

72 K. L. Garner, L. F. Parkes, J. D. Piper and J. a. Gareth Williams, *Inorg. Chem.*, 2010, **49**, 476–487.

73 E. C. Constable, R. P. G. Henney, T. A. Leese and D. A. Tocher, *J. Chem. Soc., Chem. Commun.*, 1990, **317**, 513–515.

74 T. Cheung and C. Che, *J. Chem. SOC., Dalt. Trans.,* 1996, **2**, 1645–1651.

75 W. Lu, B. X. Mi, M. C. W. Chan, Z. Hui, C. M. Che, N. Zhu and S. T. Lee, *J. Am. Chem. Soc.*, 2004, **126**, 4958–4971.

76 C. F. Harris, D. A. K. Vezzu, L. Bartolotti, P. D. Boyle and S. Huo, *Inorg. Chem.*, 2013, **52**, 11711–11722.

77 C.-C. Kwok, H. M. Y. Ngai, S.-C. Chan, I. H. T. Sham, C.-M. Che and N. Zhu, *Inorg. Chem.*, 2005, **44**, 4442–4.

78 D. J. Cárdenas, A. M. Echavarren and M. C. Ramírez de Arellano, *Organometallics*, 1999, **18**, 3337–3341.

79 J. A. G. Williams, A. Beeby, E. S. Davies, J. A. Weinstein and C. Wilson, *Inorg. Chem. Commun.*, 2003, **42**, 8609–8611.

80 D. A. K. Vezzu, D. Ravindranathan, A. W. Garner, L. Bartolotti, M. E. Smith, P. D. Boyle and S. Huo, *Inorg. Chem.*, 2011, **50**, 8261–8273.

81 S. C. F. Kui, F. F. Hung, S. L. Lai, M. Y. Yuen, C. C. Kwok, K. H. Low, S. S. Y. Chui and C. M. Che, *Chem. - A Eur. J.*, 2012, **18**, 96–109.

82 K. Feng, C. Zuniga, Y. D. Zhang, D. Kim, S. Barlow, S. R. Marder, J. L. Brédas and M. Weck, *Macromolecules*, 2009, **42**, 6855–6864.

83 D. A. K. Vezzu, J. C. Deaton, J. S. Jones, L. Bartolotti, C. F. Harris, A. P. Marchetti, M. Kondakova, R. D. Pike and S. Huo, *Inorg. Chem.*, 2010, **49**, 5107–5119.

84 D. A. K. Vezzu, J. C. Deaton, J. S. Jones, L. Bartolotti, C. F. Harris, A. P. Marchetti, M. Kondakova, R. D. Pike and S. Huo, *Inorg. Chem.*, 2010, **49**, 5107–5119.

85 S. Huo, C. F. Harris, D. A. K. Vezzu, J. P. Gagnier, M. E. Smith, R. D. Pike and Y. Li, *Polyhedron*, 2013, **52**, 1030–1040.

86 L. P. Ardasheva and G. A. Shagisultanova, *Russ. J. Inorg. Chem.*, 1998, **43**, 85–93.

87 K. Li, G. Cheng, C. Ma, X. Guan, W.-M. Kwok, Y. Chen, W. Lu and C.-M. Che, *Chem. Sci.*, 2013, **4**, 2630–2644.

88 S. C. F. Kui, P. K. Chow, G. S. M. Tong, S. L. Lai, G. Cheng, C. C. Kwok, K. H. Low, M. Y. Ko and C. M. Che, *Chem. - A Eur. J.*, 2013, **19**, 69–73.

89 G. Cheng, S. C. F. Kui, W.-H. Ang, M.-Y. Ko, P.-K. Chow, C.-L. Kwong, C.-C. Kwok, C. Ma, X. Guan, K.-H. Low, S.-J. Su and C.-M. Che, *Chem. Sci.*, 2014, **5**, 4819–4830.

90 J. a. G. Williams, A. J. Wilkinson and V. L. Whittle, *Dalt. Trans.*, 2008, 2081.

91 A. F. Henwood and E. Zysman-Colman, *Top. Curr. Chem.*, 2016, **374**, 1–41.

92 A. F. Henwood and E. Zysman-Colman, *Chem. Commun.*, 2017, **53**, 807–826.

93 L. Flamigni, A. Barbieri, C. Sabatini, B. Ventura and F. Barigelletti, *Photochem. Photophysics Coord. Compd. I*, 2007, **281**, 143–203.

94 K. P. S. Zanoni, R. L. Coppo, R. C. Amaral and N. Y. Murakami Iha, *Dalt. Trans.*, 2015, **44**, 14559–14573.

95 Y. Chi and P.-T. Chou, *Chem. Soc. Rev.*, 2010, **39**, 638–655.

96 Y. Chi, T.-K. Chang, P. Ganesan and P. Rajakannu, *Coord. Chem. Rev.*, 2016.

97 J.-P. Collin, I. M. Dixon, J.-P. Sauvage, J. A. G. Williams, F. Barrigelletti and L. Flamigni, *J. Am. Chem. Soc.*, 1999, **121**, 5009–5016.

98 A. J. Wilkinson, A. E. Goeta, C. E. Foster and J. A. G. Williams, *Inorg. Chem.*, 2004, **43**, 6513–6515.

99 L. L. Tinker and S. Bernhard, *Inorg. Chem.*, 2009, **48**, 10507–10511.

100 A. F. Rausch, L. Murphy, J. A. G. Williams and H. Yersin, *Inorg. Chem.*, 2012, **51**, 312–319.

101 H. Schiff, *Ann. Chem. Pharm.*, 1864, **131**, 118–124.

102 H.-F. Xiang, S.-C. Chan, C.-M. Che, P. T. Lai and P. C. Chui, *Proc. SPIE-Int. Soc. Opt. Eng.*, 2004, **5519**, 296–303.

103 C.-M. Che, S.-C. Chan, H.-F. Xiang, M. C. W. Chan, Y. Liu and Y. Wang, *Chem. Commun.*, 2004, 1484–1485.

104 J. M. Vila, M. T. Pereira, J. M. Ortigueira, D. Lata, M. López Torres, J. J. Fernández, A. Fernández and H. Adams, *J. Organomet. Chem.*, 1998, **566**, 93–101.

105 R. Gheorghe, M. Andruh, A. Müller and M. Schmidtmann, *Inorg. Chem.*, 2002, **41**, 5314–5316.

106 A. C. W. Leung, J. H. Chong, B. O. Patrick and M. J. MacLachlan, *Macromolecules*, 2003, **36**, 5051–5054.

107 X. Lü, W. Y. Wong and W. K. Wong, *Eur. J. Inorg. Chem.*, 2008, **2**, 523–528.

108 O. Lavastre, I. Illitchev, G. Jegou and P. H. Dixneuf, *J. Am. Chem. Soc.*, 2002, **124**, 5278–5279.

109 C. Godoy-Alcántar, A. K. Yatsimirsky and J.-M. Lehn, *J. Phys. Org. Chem.*, 2005, **18**, 979–985.

110 B. M. Dahl and O. Dahl, *Acta Chem. Scand.*, 1969, **23**, 1503–1513.

111 K. Takano, M. Takahashi, T. Fukushima, M. Takezaki, T. Tominaga, H. Akashi, H. Takagi and T. Shibahara, *Bull. Chem. Soc. Jpn.*, 2012, **85**, 1210–1221.

112 D. Ramakrishna and B. Ramachandra Bhat, *Inorg. Chem. Commun.*, 2010, **13**, 195–198.

113 C. A. Hunter and J. K. M. Sanders, *J. Am. Chem. Soc.*, 1990, **112**, 5525–5534.

114 G. Li, Z.-T. Zhang, L.-Y. Dai, Y.-L. Du and D. Xue, *Helv. Chim. Acta*, 2012, **95**, 989–997.

115 C. K. Seubert, Y. Sun and W. R. Thiel, *Dalton Trans.*, 2009, **2**, 4971–7.

116 J. C. Antilla, J. M. Baskin, T. E. Barder and S. L. Buchwald, *J. Org. Chem.*, 2004, **69**, 5578–5587.

117 J. Elguero, M. L. Jimeno and G. I. Yranzo, *Magn. Reson. Chem.*, 1990, **28**, 807–811.

118 D. J. Van Dijken, P. Kovaříček, S. P. Ihrig and S. Hecht, *J. Am. Chem. Soc.*, 2015, **137**, 14982–14991.

119 M. N. Chaur, D. Collado and J. M. Lehn, *Chem Eur J*, 2011, **17**, 248–258.

120 E. I. Lerner and S. J. Lippard, *J. Am. Chem. Soc.*, 1976, 5397–5398.

121 M. G. Cowan and S. Brooker, *Dalt. Trans.*, 2012, **41**, 1465–74.

122 M. G. Cowan and S. Brooker, *Coord. Chem. Rev.*, 2012, **256**, 2944–2971.

123 F. H. Case and E. Koft, 1959.

124 P. Paul, B. Tyagi, M. M. Bhadbhade and E. Suresh, *J. Chem. Soc., Dalt. Trans.*, 1997, 2273–2277.

125 V. S. Arvapalli, G. Chen, S. Kosarev, M. E. Tan, D. Xie and L. Yet, 2010, **51**, 284–286.

126 J. Clayden, N. Greeves, S. Warren and P. Wothers, *Organic Chemistry*, Oxford University Press, 2001.

127 P. Gros and Y. Fort, *J. Org. Chem.*, 2003, **68**, 2028–9.

128 I. I. Hunsberger, E. R. Shak, J. Fugger, R. Ketcham and D. Lednicer, *J. Org. Chem.*, 1955, **21**, 394–399.

129 S. Develay, O. Blackburn, A. L. Thompson and J. A. G. Williams, *Inorg. Chem.*, 2008, **47**, 11129–11142.

130 T. Arai, T. Araya, D. Sasaki, A. Taniguchi, T. Sato, Y. Sohma and M. Kanai, *Angew. Chem. Int. Ed.*, 2014, **53**, 8236–8239.

131 A. Mori, T. Suzuki, Y. Sunatsuki, A. Kobayashi, M. Kato, M. Kojima and K. Nakajima, *Eur. J. Inorg. Chem.*, 2014, 186–197.

132 E. Costa, P. G. Pringle and M. Ravetz, *Inorg. Synth.*, 1997, **31**, 284–286.

133 T. B. Peters, J. C. Bohling, Atta M. Arif and J. A. Gladysz, *Organometallics*, 1999, **18**, 3261–3263.

134 R. Muñoz-Rodríguez, E. Buñuel, N. Fuentes, J. a. G. Williams and D. J. Cárdenas, *Dalt. Trans.*, 2015, 8394–8405.

135 E. Rossi, A. Colombo, C. Dragonetti, S. Righetto, D. Roberto, R. Ugo, A. Valore, J. a G. Williams, M. G. Lobello, F. De Angelis, S. Fantacci, I. Ledoux-Rak, A. Singh and J. Zyss, *Chem. - A Eur. J.*, 2013, **19**, 9875–9883.

136 K. M. C. Wong, W. S. Tang, X. X. Lu, N. Zhu and V. W. W. Yam, *Inorg. Chem.*, 2005, **44**, 1492–1498.

137 J. S. Field, R. J. Haines, D. R. McMillin, O. Q. Munro and G. C. Summerton,

Inorganica Chim. Acta, 2005, **358**, 4567–4570.

138 P.-H. Lanoë, H. Le Bozec, J. a G. Williams, J.-L. Fillaut and V. Guerchais, *Dalton Trans.*, 2010, **39**, 707–710.

139 R. Ziessel and S. Diring, *Tetrahedron Lett.*, 2006, **47**, 4687–4692.

140 V. W. W. Yam, R. P. L. Tang, K. M. C. Wong and K. K. Cheung, *Organometallics*, 2001, **20**, 4476–4482.

141 M. Mohan, N. S. Gupta, L. Chandra and N. K. Jha, *J. Inorg. Biochem.*, 1987, **31**, 7–26.

142 A. Mori, T. Suzuki, Y. Nakatani, Y. Sunatsuki, M. Kojima and K. Nakajima, *Dalt. Trans.*, 2015, 15757–15760.

143 P. J. S. Miguel, M. Roitzsch, L. Yin, P. M. Lax, L. Holland, O. Krizanovic, M. Lutterneck, M. Schurmann, E. C. Fusch and B. Lippert, *Dalt. Trans.*, 2009, 10774–10786.

144 G. W. V Cave, N. W. Alcock and J. P. Rourke, *Organometallics*, 1999, **18**, 1801–1803.

145 M. Albrecht, *Chem. Rev.*, 2010, **110**, 576–623.

146 G. A. Morris, *eMagRes*, 2009, 1–13.

147 S. C. F. Kui, P. K. Chow, G. Cheng, C.-C. Kwok, C. L. Kwong, K.-H. Low and C.-M. Che, *Chem. Commun.*, 2013, **49**, 1497.

148 W. C. Harris and K. G. Stone, *J. Org. Chem.*, 1958, **23**, 2032–2034.

149 C. F. Harris, D. a K. Vezzu, L. Bartolotti, P. D. Boyle and S. Huo, *Inorg. Chem.*, 2013, **52**, 11711–22.

150 A. Wilkinson and H. Puschmann, *Inorg. …*, 2006, **45**, 8–10.

151 G. Asgedom, A. Sreedhara, J. Kivikoski, E. Kolehmainen and C. P. Rao, *J. Chem. Soc., Dalt. Trans.*, 1996, 93–97.

152 A. D. Becke, *J. Chem. Phys.*, 1986, **84**, 4524–4529.

153 A. D. Becke, *J. Chem. Phys.*, 1993, **98**, 5648–5652.

154 C. Lee, W. Yang and R. G. Parr, *Phys. Rev. B*, 1988, **37**, 785–789.

155 J. Frey, B. F. E. Curchod, R. Scopelliti, I. Tavernelli, U. Rothlisberger, M. K.

Nazeeruddin and E. Baranoff, *Dalton Trans.*, 2014, **43**, 5667–79.

156 L. P. Hammett, *J. Am. Chem. Soc.*, 1937, **59**, 96–103.

157 M. Chang, H. Horiki, K. Nakajima, A. Kobayashi, H.-C. Chang and M. Kato, *Bull. Chem. Soc. Jpn*, 2010, **83**, 905–910.

158 M. Chang, A. Kobayashi, H.-C. Chang, K. Nakajima and M. Kato, *Chem. Lett.*, 2011, **40**, 1335–1337.

159 A. Bacchi, M. Carcelli, M. Costa, A. Fochi, C. Monici, P. Pelagatti, C. Pelizzi, G. Pelizzi and L. M. Sanjuan Roca, *J. Organomet. Chem.*, 2000, **593**–**594**, 180–191.

160 C. Baik, W. S. Han, Y. Kang, S. O. Kang and J. Ko, *J. Organomet. Chem.*, 2006, **691**, 5912–5922.

161 F. Kitamura, K. Sawaguchi, A. Mori, S. Takagi, T. Suzuki, A. Kobayashi, M. Kato and K. Nakajima, *Inorg. Chem.*, 2015, **54**, 8436–8448.

162 S. F. Sousa, R. N. Sampaio, N. M. B. Neto, A. E. H. Machado and A. O. T. Patrocinio, *Photochem. Photobiol. Sci*, 2014, **13**, 1213–1224.

163 P. Brulatti, R. J. Gildea, J. a K. Howard, V. Fattori, M. Cocchi and J. a G. Williams, *Inorg. Chem.*, 2012, **51**, 3813–3826.

164 V. L. Whittle and J. A. G. Williams, *Inorg. Chem.*, 2008, **47**, 6596–6607.

165 A. M'hamedi, A. S. Batsanov, M. a. Fox, M. R. Bryce, K. Abdullah, H. a. Al-Attar and A. P. Monkman, *J. Mater. Chem.*, 2012, **22**, 13529.

166 X. Li, D. Zhang, W. Li, B. Chu, L. Han, T. Li, Z. Su, J. Zhu, Y. chen, Z. Hu, P. Lei and Z. Zhang, *Opt. Mater. (Amst).*, 2009, **31**, 1173–1176.

167 S. Bettington, M. Tavasli, M. R. Bryce, A. S. Batsanov, A. L. Thompson, H. A. Al Attar, F. B. Dias and A. P. Monkman, *J. Mater. Chem.*, 2006, **16**, 1046–1052.

168 S. Culham, P. H. Lanoë, V. L. Whittle, M. C. Durrant, J. A. G. Williams and V. N. Kozhevnikov, *Inorg. Chem.*, 2013, **52**, 10992–11003.

169 Y. Chi and P.-T. Chou, *Chem. Soc. Rev.*, 2010, **39**, 638–655.

170 S.-W. Lai, M. C.-W. Chan, T.-C. Cheung, S.-M. Peng and C.-M. Che, *Inorg. Chem.*, 1999, **38**, 4046–4055.

171 V. N. Kozhevnikov, M. C. Durrant and J. A. G. Williams, *Inorg. Chem.*, 2011, **50**, 6304–6313.

172 J. A. Bailey, V. M. Miskowski and H. B. Gray, *Inorg. Chem. Commun.*, 1993, **32**, 369–370.

173 S.-W. Lai, M. C. W. Chan, K.-K. Cheung, S.-M. Peng and C.-M. Che, *Organometallics*, 1999, **18**, 3991–3997.

174 B. Ma, J. Li, P. I. Djurovich, M. Yousufuddin, R. Bau and M. E. Thompson, *J. Am. Chem. Soc.*, 2005, **127**, 28–29.

175 B. Ma, P. I. Djurovich, S. Garon, B. Alleyne and M. E. Thompson, *Adv. Funct. Mater.*, 2006, **16**, 2438–2446.

176 S. Lai, H. Lam, W. Lu, K. Cheung and C. Che, *Organometallics*, 2002, **21**, 226.

177 S. Develay and J. A. G. Williams, *Dalton Trans.*, 2008, 4562–4564.

178 H. Houjou, Y. Hoga, Y.-L. Ma, H. Achira, I. Yoshikawa, T. Mutai and K. Matsumura, *Inorganica Chim. Acta*, 2017, **461**, 27–34.

179 V. Chandrasekhar, B. Mahanti, P. Bandipalli and K. Bhanuprakash, *Inorg. Chem.*, 2012, **51**, 10536–10547.

180 V. Chandrasekhar, N. Satumtira, O. Elbjeirami, M. a Omary, T. Hajra, J. K. Bera and S. M. W. Rahaman, *Inorg. Chem.*, 2012, **51**, 1319–1329.

181 D. G. Congrave, Y. Hsu, A. S. Batsanov, A. Beeby and M. R. Bryce, *Organometallics*, 2017, acs.organomet.6b00887.

182 X. Yang, Z. Feng, J. Zhao, J.-S. Dang, B. Liu, K. Zhang and G. Zhou, *ACS Appl. Mater. Interfaces*, 2016, **0**.

183 G. Turnbull, J. A. G. Williams and V. N. Kozhevnikov, *Chem. Commun.*, 2017, **53**, 2729–2732.

184 M. Biwu, P. I. Djurovich, M. Yousufuddin, R. Bau and M. E. Thompson, *J. Phys. Chem. C*, 2008, **112**, 8022–8031.

185 A. M. Prokhorov, A. Santoro, J. A. G. Williams and D. W. Bruce, *Angew. Chemie - Int. Ed.*, 2012, **51**, 95–98.

186 A. M. Soliman, D. Fortin, P. D. Harvey and E. Zysman-colman, *Chem. Commun.*, 2012, **48**, 1120–1122.

187 P.-H. Lanoë, C. M. Tong, R. W. Harrington, M. R. Probert, W. Clegg, J. A. G. Williams and V. N. Kozhevnikov, *Chem. Commun.*, 2014, **50**, 6831–6834.

188 A. Mori, T. Suzuki, Y. Sunatsuki, M. Kojima and K. Nakajima, *Bull. Chem. Soc. Jpn.*, 2015, **88**, 480–489.

189 J. L. Schmitt, A. M. Stadler, N. Kyritsakas and J. M. Lehn, *Helv. Chim. Acta*, 2003, **86**, 1598–1624.

190 K. Nakamaru, *Bull. Chem. Soc. Jpn*, 1982, **55**, 2697–2705.

191 A. M. Brouwer, *Pure Appl. Chem*, 2011, **83**, 2213–2228.

192 U. Resch-genger and K. Rurack, *Pure Appl. Chem*, 2013, **85**, 2005–2026.

193 J. N. Demas and G. A. Crosby, *J. Phys. Chem*, 1971, **75**, 991–1024.

194 W. Christian, M. Grabolle, J. Pauli, M. Spieles and U. Resch-genger, *Anal. Chem.*, 2011, **83**, 3431–3439.

195 L. Marcu, P. M. W. French and D. S. Elson, *Fluorescence Lifetime Spectroscopy and Imaging*, 2014.

196 G. R. Hanson, K. E. Gates, C. J. Noble, M. Griffin, A. Mitchell and S. Benson, *J. Inorg. Biochem.*, 2004, **98**, 903–916.

197 G. M. Sheldrick, *Acta Crystallogr. Sect. A Found. Crystallogr.*, 2007, **64**, 112–122.

198 O. V. Dolomanov, L. J. Bourhis, R. J. Gildea, J. A. K. Howard and H. Puschmann, *J. Appl. Cryst.*, 2009, **42**, 339–341.

199 S. Lohar, A. Sahana, A. Banerjee, A. Chattopadhyay, S. K. Mukhopadhyay, J. S. Matalobos and D. Das, *Inorganica Chim. Acta*, 2014, **412**, 67–72.

200 A. Sarkar and S. Pal, *Polyhedron*, 2006, **25**, 1689–1694.

201 K. Li and A. Tong, *Sensors Actuators, B Chem.*, 2013, **184**, 248–253.

202 M. Cushman, D. Nagarathnam, D. Gopal and R. L. Geahlen, *Bioorg. Med. Chem. Lett.*, 1991, **1**, 215–218.

203 S. Mukherjee, S. Chowdhury, A. Ghorai, U. Ghosh and H. Stoeckli-evans, *Polyhedron*, 2013, **51**, 228–234.

204 D. Leung and E. V Anslyn, *Org. Lett.*, 2011, **13**, 2298–2301.

205 A. Balbi, M. Anzaldi, C. Macciò, C. Aiello, M. Mazzei, R. Gangemi, P. Castagnola, M. Miele, C. Rosano and M. Viale, *Eur. J. Med. Chem.*, 2011, **46**, 5293–5309.

206 H. Chowdhury, S. H. Rahaman, R. Ghosh, S. K. Sarkar, H. K. Fun and B. K. Ghosh, *J. Mol. Struct.*, 2007, **826**, 170–176.

207 F. Lebon, M. Ledecq, M. Dieu, C. Demazy, J. Remacle, R. Lapouyade, O. Kahn and F. Durant, *J. Inorg. Biochem.*, 2001, **86**, 547–554.

208 L. Vandromme, H.-U. Reißig, S. Gröper and J. P. Rabe, *European J. Org. Chem.*, 2008, **2008**, 2049–2055.

209 M. S. Silva, L. M. P. M. Almeida and J. A. S. Cavaleiro, *Tetrahedron*, 1997, **53**, 11645–11658.

210 J. Catalan, F. Fabero, R. M. Claramunt, M. D. Santa Maria, M. de la C. Foces-Foces, F. Hernandez Cano, M. Martinez-Ripoll, J. Elguero and R. Sastre, *J. Am. Chem. Soc.*, 1992, **114**, 5039–5048.

211 Z. Y. Li, L. Li, Q. L. Li, K. Jing, H. Xu and G. W. Wang, *Chem. - A Eur. J.*, 2017, **23**, 3285–3290.

212 X. Q. Zhang, Y. M. Xie, Y. Zheng, F. Liang, B. Wang, J. Fan and L. S. Liao, *Org. Electron.*, 2016, **32**, 120–125.

213 Y. F. Wang, K. K. Toh, E. P. J. Ng and S. Chiba, *J. Am. Chem. Soc.*, 2011, **133**, 6411–6421.

214 A. D. Ostrowski and P. C. Ford, *Dalton Trans.*, 2009, 10660–10669.